Australian
National
University

Shape Engineering of InP Nanostructures for Optoelectronic Applications

Naiyin Wang

August 2020

A Dissertation Submitted for the Degree of Doctor of Philosophy
of the Australian National University

Department of Electronic Materials Engineering
Research School of Physics
College of Sciences
The Australian National University

Declaration

I certify that this dissertation does not incorporate, without acknowledgement, any material previously submitted for a degree or diploma in any university and that to the best of my knowledge, it does not contain any material previously published or written by another person except where due reference is made in the text. The work in this dissertation is my own, except for the contributions made by others as described in the Acknowledgements.

Naiyin Wang
August 2020

[redacted]

Acknowledgements

I would like to express the sincerest gratitude to many individuals and several organisations for the support and help during my PhD study. Without them, I could never make this far.

First of all, I would like to thank all my supervisors, Prof. Chennupati Jagadish, Prof. Hark Hoe Tan, Dr. Philippe Caroff, Prof. Lan Fu, and A/Prof. Jennifer Wong-Leung, for their guidance, encouragement and constant support during the past few years. I am deeply grateful to Prof. Jagadish who has been a great team leader and guided all of us to move forward on the right track by virtue of his broad knowledge, foresight and sagacity. Being a caring, generous and patient mentor, he is always available to his students and solve problems for us. I am extremely lucky to have Prof. Tan as my primary supervisor. He possesses profound knowledge and rigorous academic attitude, and set an excellent example for me. His continuous support and encouragement strengthen me even at the darkest moment during my PhD study. What is even more remarkable is that his sense of humour always makes it enjoyable to work with him. Dr. Caroff deserves very special thanks for not only his huge help and guidance in many aspects of my research, but also his trust and encouragement in my personal life, which I will never forget. He always surprises me with his knowledge and new ideas. I will miss those days when we spent countless hours on discussing scientific questions and talking about life. I also would like to express my great appreciation to Prof. Fu and A/Prof. Wong-Leung for their generous help in many occasions.

I am deeply thankful to A/Prof. Xiaoming Yuan from Central South University, China, who was also a former student of our group. He was one of my supervisors in a sense. My achievements during PhD study has greatly benefitted from his help and guidance. He has been a wonderful mentor and friend throughout the whole journey. Special thanks also go to Prof. Xu Zhang from Zhengzhou University, China and Mr. Wei Wen Wong from our group for their great contribution to modelling work in this thesis.

I would like to thank Ms. Bijun Zhao who has taught me a lot at the beginning of my PhD study and helped me in adapting to the new work environment. Bijun and her husband A/Prof. Xin Chen are two of my best friends and they are always beside me when I need them most. I

also thank Dr. Zhicheng Su for the optical study of the bilayer InP nanomembranes and Dr. Qian Gao for training me to prepare patterned substrates.

I have been working in a group full of amazing people. I would like to express my sincere thanks to all of them for their support, kindness and friendship, including Ms. Rowena Yew, Dr. Dipankar Chugh, Dr. Inseok Yang, Dr. Fajun Li, Dr. Parvathala Reddy Narangari, Mr. Fanlu Zhang, Mr. Yi Zhu, Dr. Vidur Raj, Mr. Ahmed Alabadla, Dr. Kun Peng, Ms. Zahra Azimi, Mr. Sonachand Adhikari, Ms. Anha Bhat, Mr. Josh Butson, Ms. Nikita Gagrani, Ms. Aswani Gopakumar, Ms. Shao Qi Lim, Ms. Xingshuo Huang, Ms. Huyen Pham, Mr. Mohammad Rashidi, Mr. Joshua Soo, Ms. Maria del Rocio Camacho Morales, Mr. Zhixiang Zhang, Dr. Xutao Zhang, Dr. Weizong Xu, Prof. Jiandong Ye, Prof. Fangfang Ren, Dr. Siva Karuturi, Dr. Ziyuan Li, A/Prof. Zhiqing Zhong, A/Prof. Jiaqin Liu, Dr. Julie Tournet, Dr. Tuomas Haggrén, Dr. Nian Jiang, Dr. Yan Li, Dr. Yong Hwan Lee, A/Prof. Yanxu Zhu, and this list can goes on and on.

This thesis would not have been possible without the experimental equipment and technical support from the ACT node of Australian National Fabrication Facility and ANU node of the Microscopy Australia (formerly the Australian Microscopy and Microanalysis Research Facility). Special thanks go to Dr. Li Li for helping with TEM lamella preparation, Dr. Mark Lockrey for CL measurements performed at both ANU and University of Technology Sydney, Dr. Mykhaylo Lysevych for helping with MOCVD growth, Dr. Felipe Kremer for TEM measurement as well as Dr. Kaushal Vora, Dr. Naeem Shahid, Mr. Chris Kafer, Dr. Fouad Karouta for their technical support in times of need. I also would like to extend my thanks to Drs. David Mitchell and Gilberto Casillas Garcia from the University of Wollongong for their assistance in TEM measurements.

I would like to express my sincere gratitude to Ms. Julie Arnold, Ms. Karen Nulty, Ms. Liudmila Mangos, Mrs. Sue Berkeley and Ms. Liz Micallef. They are definitely the best administrators I have ever met. Because of them, I can focus on my research and do not have to worry about too much paper works.

Living and studying far away from home is not easy. I am glad to have found some of my best friends in Canberra. I would like to thank Ms. Kunrong Yang, Mr. David Lockwood, Dr. Zhe Li, and Ms. Emma Yu for their precious friendship, unwavering support and tolerance for my unmeant caprice. Dr. Li Li deserves a special mention again since she and her husband Dr.

Xiangyuan Cui have always treated me as a family member. How lucky I am to have met all of you.

Lastly, and most importantly, I thank my parents, Qingshui Wang and Cuiyun Ge, little brother Fujun Wang, sister-in-law Na Chen, and girlfriend Na Kong for their love and support. They are the sources of my strength.

Abstract

III-V semiconductor nanostructures have been the research focus in the past two decades thanks to the superior properties of the materials themselves and the unique properties produced by reducing the dimension to the nanoscale. In particular, III-V nanowires have drawn much more attention and have been extensively applied in a wide range of devices including solar cells, light-emitting diodes, lasers, transistors, and photodetectors. Despite these great successes, these one-dimensional (1D) nanostructures still face many challenges in terms of synthesis, assembly, fabrication and the ability to form complex nanoarchitectures. Surprisingly, it has been demonstrated that nanostructures with more complex two- and three-dimensional (2D and 3D) shapes can provide possible solutions. These shape-engineered nanostructures can improve material properties and device functionality. Furthermore, recent intensive investigation of nanostructure networks shows a great demand on the shape flexibility, uniformity, structural and optical qualities of epitaxially grown III-V nanostructures.

This dissertation presents the shape engineering of InP-based nanostructures grown by metal organic chemical vapour deposition (MOCVD) from 1D nanowires to more sophisticated 2D and 3D shapes. Shape transformation mechanism, crystal structure and optical properties were thoroughly investigated to understand the growth mechanism of these complex III-V nanostructures for electronic and optoelectronic applications. Among the various growth techniques, selective area epitaxy (SAE) has the advantages of producing uniform nanostructure arrays with a high degree of controllability in pattern geometry, such as shape, dimension, site position and spacing, and thus has been used in this work.

InP nanostructures grown on {111}A InP substrates was first investigated. Two key growth parameters, temperature and V/III ratio, were studied to optimise the growth conditions. We found that a higher growth temperature was crucial to obtain high quality nanostructures. Under optimal growth conditions, the highly uniform arrays of wurtzite (WZ) InP nanostructures with tunable shapes, such as nanowires, nanomembranes, prism- and ring-like nanoshapes, were simultaneously achieved. Their side facets can be dominated by $\{10\bar{1}0\}$ and/or $\{11\bar{2}0\}$, making WZ InP a good candidate for tailoring the shape of the nanostructures. In-depth investigation of shape transformation with time and opening geometry/dimension revealed that the shape was essentially determined by pattern confinement and minimisation of total surface energy. A theoretical model was proposed to explain the observed behaviour. Structural and optical characterisation results demonstrated that all the different InP nanostructures grown under optimal conditions have perfect wurtzite (WZ) crystal structure regardless of their shape and strong and homogeneous photon emission.

Moreover, we investigated the shape evolution from branched nanowires to vertical/inclined nanomembranes and crystal structure of InP nanostructures grown on InP substrates of different orientations, including {100}, {110}, {111}B, {112}A and {112}B. Two growth models were proposed to explain these observations regarding shape transformation and phase transition. A strong correlation between the growth direction and crystal phase was revealed. Specifically, WZ and zinc-blende (ZB) phases form along the <111>A and <111>B directions, respectively, while crystal phase remains the same along other low-index directions. The polarity-induced crystal structure difference was explained by thermodynamic difference between the WZ and ZB phase nuclei on the {111}A and {111}B planes. Growth from the openings was essentially determined by pattern confinement and minimisation of the total surface energy, similar to growth on {111}A InP substrates. Accordingly, a novel type-II WZ/ZB nanomembrane homojunction array was obtained by tailoring growth directions through alignment of the openings along certain crystallographic orientations.

Finally, the incorporation of InAsP quantum well was carried out on pure WZ InP nanostructure templates grown on {111}A InP substrates with two different shapes, i.e. nanowires and nanomembranes. InAsP quantum wells grew both axially and laterally on the InP nanowires and nanomembranes. While the axial quantum well was of ZB phase, the lateral one grown on side facets had a WZ phase. When sidewalls of nanowires and nanomembranes were the nonpolar $\{1\bar{1}00\}$ facets, the radial quantum well selectively grew on the sidewall located at the semi-polar $<11\bar{2}>$A side of the axial quantum well, leading to the shape evolution of nanowires from hexagonal to triangular cross section and destroying the symmetry of nanomembranes. In comparison, nanomembranes with $\{11\bar{2}0\}$ sidewalls are shown to be an ideal template for growing InP/InAsP heterostructures thanks to the high symmetry and uniformity of quantum well nanomembrane array. EDX results showed that quantum well composition was highly dependent on the crystal facet. Moreover, quantum well nanomembranes with $\{11\bar{2}0\}$ sidewalls gave strong and uniform photon emission around 1.3 µm, showing superior optical properties compared with quantum wells incorporated in InP nanowires and nanomembranes with $\{1\bar{1}00\}$ facets.

Publications

Journal Articles

1. **Naiyin Wang,** Xiaoming Yuan, Xu Zhang, Qian Gao, Bijun Zhao, Li Li, Mark Lockery, Hark Hoe Tan, Chennupati Jagadish, and Philippe Caroff, "Shape engineering of InP nanostructures by selective area epitaxy", *ACS Nano* 13 (2019) 7261-7269.
2. Xiaoming Yuan,# **Naiyin Wang,**# Zhenzhen Tian, Fanlu Zhang, Li Li, Mark Lockrey, Jun He, Chennupati Jagadish, and Hark Hoe Tan, "Facet-dependent growth of InAsP quantum wells in InP nanowire and nanomembrane array", *Nanoscale Horizons* 5 (2020) 1530-1537. #These authors contributed equally to this work.
3. **Naiyin Wang,** Wei Wen Wong, Xiaoming Yuan, Li Li, Chennupati Jagadish, and Hark Hoe Tan, "Understanding Shape Evolution and Phase Transition in InP Nanostructures Grown by Selective Area Epitaxy", to be submitted.
4. Zhicheng Su, **Naiyin Wang,** Hark Hoe Tan, and Chennupati Jagadish, "2D carrier localization in novel layered wurtzite-zincblende InP nanomembranes", under review.
5. Bijun Zhao, Mark Nicolas Lockrey, **Naiyin Wang,** Philippe Caroff, Xiaoming Yuan, Li Li, Jennifer Wong-Leung, Hark Hoe Tan, Chennupati Jagadish, "Highly regular rosette-shaped cathodoluminescence in GaN self-assembled nanodisks and nanorods", *Nano Research* 13 (2020) 2500-2505.
6. Bijun Zhao, Mark Lockrey, Philippe Caroff, **Naiyin Wang,** Li Li, Jennifer Wong-Leung, Hark Hoe Tan and Chennupati Jagadish, "The effect of nitridation on the polarity and optical properties of GaN self-assembled nanorods", *Nanoscale* 10 (2018) 11205-11210.
7. Xiaoming Yuan, Lin Li, Ziyuan Li, Fan Wang, **Naiyin Wang,** Lan Fu, Jun He, Hark Hoe Tan, Chennupati Jagadish, "Unexpected benefits of stacking faults on electronic structure and optical emission in wurtzite GaAs/GaInP core/shell nanowires", *Nanoscale* 11 (2019) 9207-9215.

Conference papers

1. **Naiyin Wang**, Philippe Caroff, Qian Gao, Bijun Zhao, Li Li, Mark Lockery, Xiaoming

Yuan, Hark Hoe Tan, and Chennupati Jagadish, “Morphological control and characterization of InP nanostructures grown by selective area epitaxy”, ANFF - AMMRF Annual Research Showcase 2017, Sydney Australia.

2. **Naiyin Wang**, Philippe Caroff, Qian Gao, Bijun Zhao, Li Li, Mark Lockery, Hark Hoe Tan, and Chennupati Jagadish, “Morphological control and characterization of InP nanostructures grown by selective area epitaxy”, International Conference on Nanoscience and Nanotechnology (ICONN) 2018, Wollongong Australia.
3. **Naiyin Wang**, Philippe Caroff, Qian Gao, Bijun Zhao, Li Li, Mark Lockery, Xiaoming Yuan, Hark Hoe Tan, and Chennupati Jagadish, “Shape engineering of InP nanostructures grown by selective area epitaxy”, Conference on Optoelectronic and Microelectronic Materials and Devices (COMMAD) 2018, Perth Australia.
4. **Naiyin Wang,** Xiaoming Yuan, Philippe Caroff, Li Li, Hark Hoe Tan, Chennupati Jagadish, “Shape engineering of InP nanostructures grown by selective area epitaxy”, MRS Spring Meeting & Exhibit 2019, Phoenix, United States.

Acronyms and Symbols

1D	one-dimensional
2D	two-dimensional
3D	three-dimensional
AsH_3	arsine
BSEs	backscattered electrons
CCS	close coupled showerhead
CL	cathodoluminescence
Cs-STEM	aberration-corrected scanning transmission electron microscope
CVD	chemical vapour deposition
EBL	electron beam lithography
EDX	energy dispersive X-ray
FFT	fast Fourier transform
FIB	focused ion beam
HAADF	high angle annular dark field
HMDS	hexamethyldisilazane
HRTEM	high resolution transmission electron microscopy
IPA	isopropyl alcohol
LEDs	light emitting diodes
MOCVD	metal-organic chemical vapour deposition
MOVPE	metal-organic vapour phase epitaxy
PECVD	plasma-enhanced chemical vapour deposition
PH_3	phosphine
PL	photoluminescence
QDs	quantum dots
QDs	quantum dots
QWRs	quantum wires
QWs	quantum wells
QWs	quantum wells

RF	radio frequency
RIE	reactive ion etching
SADP	selective area diffraction pattern
SAE	selective area epitaxy
SA-MOCVD	selective-area metal-organic chemical vapour deposition
sccm	standard cubic centimeters per minute
SEM	scanning electron microscopy
SEs	secondary electrons
slm	standard litres per minute
SST	susceptor surface temperature
STEM	scanning transmission electron microscopy
TEM	transmission electron microscopy
TMAl	trimethylaluminium
TMGa	trimethylgallium
TMIn	trimethylindium
TRPL	time-resolved photoluminescence spectroscopy
VLS	vapour-liquid-solid
WZ	wurtzite
ZB	zinc-blende
γ	surface energy

Contents

List of Figures

List of Tables

CHAPTER 1

Introduction

1.1. III-V semiconductor nanostructures

Most of group III-V semiconductors are key components of modern electronics and optoelectronics thanks to their superior electronic and optoelectronic properties, such as high carrier mobility, direct bandgap and band structure engineering capability.[1, 2] The relevant devices have been widely applied in many aspects of our daily life, from general lighting to satellite communications. In the past two decades, nanoscience and nanotechnology have developed rapidly where reducing material dimension to the nanometre level brings many unique properties. III-V semiconductor nanostructures, especially the quasi-one-dimensional (1D) nanowires, have drawn great attention with the rise of material synthesis and device fabrication at the nanoscale.

III-V nanowires generally have a diameter at the nanometre scale and a height at the micrometre level. The small size and unique geometry give them tremendous advantages over their planar counterparts. For instance, the material consumption and cost can be reduced in devices made of III-V nanowires.[3] Small feature size allows a lot of nanowires to integrate into a tiny single chip,[4] and thus realises complex functionalities and miniaturises devices. Quantum confinement can occur in the radial direction of nanowires with a sufficiently small diameter, which leads to the reverse relationship between band gap and diameter,[5] and significantly affects the optical and electronic properties.[6-10] In addition to zinc-blende (ZB) phase that is commonly observed in bulk III-V semiconductors, the metastable wurtzite (WZ) phase could form in III-V nanowires depending on the growth conditions.[11-16] The ability to form these two crystal structures enables phase engineering which provides more possibilities for tailoring nanomaterial structures and properties,[17] such as the formation of WZ/ZB homojunctions with type-II band alignment and unusual WZ GaP nanowires with a direct band gap.[18-20] Both single nanowire and nanowire array can greatly enhance light absorption, making them attractive candidates for applications such as solar cells, light emitting diodes (LEDs) and solar water splitting.[3, 21-25] Krogstrup *et al.*[21] reported a single GaAs nanowire solar cell with efficiency beyond the Shockley-Queisser limit partly because of enhanced light absorption due to an antenna-like self-concentration effect. Wallentin *et al.*[3] achieved an InP nanowire array solar cell with 13.8% efficiency surpassing the ray optics limit thanks to the resonant light trapping of nanowires. Carrier collection efficiency is significantly improved in nanowires with a radial p-n junction due to the decoupling of light absorption and carrier collection pathways.[26] Moreover, nanowires also possess high surface-to-volume ratio, high aspect ratio and excellent mechanical flexibility, and thus demonstrate great potential in sensing, flexible electronics, and nanogenerators.[27-36] In addition to device applications, nanowires have also demonstrated great significance in fundamental science.[37-39]

The quasi-1D geometry of nanowires implies that heterostructures could form axially and/or radially, providing extra freedom of material synthesis and device fabrication compared with planar structures where only axial heterostructures can be formed.[40-43] For instance, the nonpolar $\{10\bar{1}0\}$ sidewalls of c-axis oriented GaN nanowires offer a platform for growing radial InGaN quantum wells on non/semi-polar facets where the quantum-confined Stark effect can be eliminated. This kind of InGaN/GaN nanowire heterostructures have been widely applied to light-emitting diodes, solar cells and lasers in consideration of its great significance of improving quantum efficiency and mitigating efficiency droop.[44-48] Axial nanowire heterostructures have a much higher tolerance for lattice mismatch than planar heterostructures due to the extremely reduced lateral dimension of nanowires which can relieve lattice mismatch induced strain.[49-53] Thus, heterogeneous semiconductors with a big lattice difference are more likely to form high quality heterostructures even without dislocations in the nanowire form. In short, nanowires make it possible to form heterostructures by combining more dissimilar semiconductors, which provides more possibilities for device applications.

Based on these unique properties mentioned above, III-V nanowires are revolutionising modern electronics and optoelectronics.[54, 55] Amongst them, InP-based nanowires are of particular research interest due to superior properties of InP, such as direct band gap, high electron mobility, low surface recombination velocity, and lattice matched with a wide range of ternary and quaternary III-V semiconductors.[56-58] Thus, InP-based nanowires have been widely applied in various applications, including light-emitting diodes,[59-61] lasing,[62-65] solar cells,[3, 66-70] photodetectors,[71-74] field-effect transistors,[75-77] terahertz detectors,[78, 79] single-photon detectors,[80] and solar water splitting.[81-83]

1.2. Significance of expanding research interests from 1D nanowires to higher-order 2D/3D nanostructures

Despite the superior properties and great successes of III-V nanowires mentioned above, they still face many challenges or inadequacies, such as in terms of synthesis, assembly, fabrication, and functionality, which are caused by the quasi-1D geometry of nanowires themselves.[84] Nanowire morphologies, such as tapering and cross-section shape, have been extensively investigated since they play important role in determining their properties and applications.[85-91] For example, Foster *et al*.[92] reported the highly linearly polarized photon emission of an embedded InGaAs quantum dot in a GaAs nanowire with an elongated cross section, showing promise for realising linearly polarized single photon emission. More surprisingly, there is an increasing number of reports that nanostructures with a higher-order two- and three-dimensional (2D and 3D) shapes can provide possible solutions for the challenges and inadequacies of nanowires.

1.2.1. Epitaxial growth

Twin-free GaAs nanowires grown by metal-seeded vapour-liquid-solid (VLS) technique have been extensively reported[93-95] whereas those grown by catalyst-free selective area epitaxy (SAE) remain challenging since planar defects can be easily formed in nanowires grown by the latter technique.[96-98] Twinning defects are an inherent feature of SAE grown GaAs nanowires, and twin-free ones are yet to be reported. In contrast, by fabricating nanoslot openings with a proper orientation ($<11\bar{2}>$) instead of round nanoholes for SAE, twin-free GaAs nanostructures with a 2D sheet-like shape have been successfully grown at a range of growth conditions due to the formation of two vertical $\{1\bar{1}0\}$ side facets because of nanoslot confinement.[97]

Much efforts have been devoted to growing III-V nanostructures on Si(100) wafers in consideration of the great prospect offered by the integration of advanced III-V optoelectronic nanodevices with modern microelectronic technology.[85, 99-106] A vertical configuration is of particular interest but remains challenging.[107, 108] Till now, as-grown vertical III-V nanowires epitaxially grown on Si(100) by either VLS or SAE techniques have not been reported. Fortunately, the vertical III-V nanostructures with 2D shapes including V-shaped InAs nanomembranes and GaAs nanospades have been reported by Morral *et al.*,[107, 109-111] showing a breakthrough in this research area. V-shaped InAs nanomembranes with flat {110} walls are grown by catalyst-free SAE as a result of growth along two opposite <111>B directions,[109-111] while GaAs nanospades with a virtually defect-free bicrystalline structure have been grown by selective-area self-catalyst VLS.[107]

In addition, the metastable WZ phase III-As/P nanowires occur only at the nano/micrometre scale since they become unstable and even switch to ZB phase with diameter exceeding a critical value. However, WZ III-V semiconductors with a large size are sometimes desired for supporting optical modes and reducing detrimental surface recombination.[112] Staudinger *et al*.[112, 113] demonstrated a large size WZ InP film/micro-disk as a result of a zipper-induced epitaxial lateral overgrowth originating from six <110>-oriented nanoslots connected in the centre. The dimensions of this kind of 2D structure can exceed 100 μm^2 beyond nanowire size constraints, providing a good platform for light-emitting devices and photonics.

Due to the great significance of epitaxially grown III-V nanostructures with higher-order dimensional shapes, the understanding of shape transformation mechanism is important, especially for those grown by SAE technique,[97, 111, 112, 114] which is therefore the focus of this dissertation.

1.2.2. Fabrication and assembly

It has been shown that 1D nanowires, limited by the geometry, have unavoidable difficulty in device fabrication and certain types of measurements, such as Hall effect especially when multiple terminals are required.[115, 116] In comparison, 2D nanomembranes with an extra spatial dimension can significantly ease the fabrication process and enable complex device design with multiple contacts and gates, as demonstrated by GaAs nanosheets,[117] InAs nanofins,[118] and InSb nanosheets/nanosails.[119-121] For instance, the rectangular InAs nanofins grown by SAE have been fabricated into a sophisticated device consisting of a number of contacts, global back-gate and local top-gate after being mechanically transferred to another substrate with a high accuracy and yield.[118] Particularly, this device can measure the mobility with carrier density, demonstrating a superior contact design and fabrication over nanowires where the field-effect mobility is generally measured limited by contacts.[116] Furthermore, the performance of nanodevices based on III-V nanomembranes may benefit from the direct contact of the active layer and gate stack enabled by the 2D nature of nanomembranes.[84, 122]

Assembly of epitaxially grown nanowires into a highly ordered horizontal array has potential for the scalable fabrication of electronic and photonic nanodevices. However, the postgrowth processing (e.g. contact printing) is required,[123, 124] which generally causes alignment fluctuation. Xu *et al*.[125] demonstrated an alternative solution for achieving scalable fabrication of nanodevices based on ordered core-shell nanostructures, that is growing surface-guided CdS-CdSe core-shell nanowalls. They fabricated photodetectors using this kind of nanostructures without the need of transfer, alignment and selective etching of the shells. In addition to the convenience, the nanowall geometry has positive effect on device performance because of enhanced charge-separation efficiency and 3D trigate configuration.[125, 126] Besides, highly ordered arrays of InAs nanofins,[106, 118] GaN nanosheets/nanowalls/fins,[127-132] and GaAs nanosheets[97] grown by SAE technique should also be suitable for fabricating devices at the wafer-scale, similar to the CdS-CdSe nanowalls. Similar InP nanostructures grown by SAE have not been reported until our publication regarding the work discussed in Chapter 4.[112, 133]

1.2.3. Property, functionality and application

Many superior properties of nanowires reviewed in Section 1.1 are actually shared by nanostructures including those with complex shapes. Moreover, the higher-order nanostructures with sophisticated shapes can also have some unique properties, such as twin-free GaAs nanosheets, vertical V-shaped InAs nanomembranes and GaAs nanospades on Si(100), and Cds-CdSe nanowalls discussed earlier in Sections 1.2.1 and 1.2.2. The shape-engineered nanostructures with outstanding and/or unique properties are drawing a lot of attention as a way to achieve improved or even new device functionality.

For instance, twin-free GaAs nanosheets[97] have been shown to have superior electronic and optical properties, such as substantially longer minority carrier diffusion length than their nanowire counterparts,[117] complex 2D asymmetric optical cavity,[134] and high optical quality and homogeneous emission over a large scale without a capping layer.[135] Surface passivation is generally needed to improve optoelectronic properties (e.g. photoluminescence intensity and carrier lifetime) of GaAs nanosheets,[136, 137] but it may cause a negative effect, such as a shift and broadening of the exciton peak,[135] which makes InP nanomembranes an attractive alternative because of their low surface recombination velocity. An example is the gold-catalysed InP nanoflag consisting of a nanowire “flagpole” and a high quality WZ nanomembrane.[138] This specially shaped InP nanostructure shows a high degree of linear polarization (up to 90%), directional radiation pattern, enhanced electric field intensity, and more interestingly, encapsulating the active nanoemitter with a nanoantenna.[138, 139]

There is an early report of free-standing InAs nanoplates in which carrier density can be reduced to zero, making them useful for studying electron transport.[140] V-shaped InAs nanomembranes grown on Si(100) demonstrated enhanced light scattering as a result of their distinctive shape-dependent optical resonance[111] and enhanced second harmonic generation.[141] More works related to 2D free-standing InAs nanostructures with high quality have been reported, including wafer-scale nanosheets grown on various substrates (Si, MgO, sapphire, GaAs, etc.) with outstanding electrical and optical properties,[122] pure ZB phase nanobelts,[142] WZ phase nanosheets with $\{11\bar{2}0\}$ surfaces,[143] and bicrystalline nanoleaves.[144] Recently, narrow band gap InSb nanostructures with nanosail, nanosheet, nanoflag, and nanocube shapes have also been intensively investigated due to their intrinsic properties and great potential in electronics, infrared optoelectronics, and especially quantum applications.[120, 121, 145-148] For instance, Mata *et al*.[121] demonstrated high electron mobility (over 12000 $\mathrm{cm^2V^{-1}S^{-1}}$) at room temperature and quantized conductance in a quantum point contact in a InSb nanosail quantum system. Xu *et al*. successfully grew pure ZB InSb nanosheets on InAs nanowire stems by VLS method, and revealed that they have a high electron mobility, 2D electronic states and strong spin-orbit coupling, which together with their 2D geometry makes them a good platform for constructing complex topological circuits.

GaN nanowalls, also known as nanofins and nanosheets, with large nonpolar $\{1\bar{1}00\}$ or $\{11\bar{2}0\}$ surfaces have been extensively reported because of their ability to mitigate quantum-confined Stark effect and efficiency droop as well as reducing dislocation density and edge effects, providing an ideal template to grow InGaN/GaN quantum well structures and thus a versatile platform for optoelectronic devices, such as light-emitting diodes and lasers.[127-132, 149] Heterostructures are vital to further improving the functionality of III-V nanostructures and realise advanced devices. In addition to InGaN/GaN nanowalls, GaAs/AlGaAs quantum well nanomembranes have also been reported.[150] However, there is relatively less studies on the incorporation of quantum heterostructures in free-standing 2D/3D nanostructures. In Chapter 6 of this dissertation, an in-depth investigation of InAsP/InP quantum well nanomembranes is presented.

The IBM research group in Zürich achieved room-temperature lasing from both GaAs microdisks monolithically integrated on Si(100)[151, 152] and WZ InP microdisks on InP substrate[113] grown by SAE technique benefitting from high crystal and optical qualities, thus showing the prospect for optoelectronic applications and Si photonics. Besides, III-V ring-like nano/microstructures merit a special mention. Kuo *et al*.[153, 154] demonstrated that the emission wavelength from a nanoring micro-LED can be tuned from green to blue because of strain-induced effects which can then facilitate the realisation of a full-colour monolithic hybrid micro-LED device. III-V semiconductor nano/microring lasers have been widely investigated.[155-160] However, ring-like structures are generally fabricated by etching since the direct epitaxial growth is still challenging.[159, 161]

Out-of-plane 2D/3D nanostructures consisting of interconnected 1D nanowires, such as nanotrees[162] and nanocrosses/networks,[163-172] can greatly expand functionalities and applications, as demonstrated by multifunctional all-optical logic gates formed by InP and AlGaAs nanowire networks[163] and InSb network quantum device.[167] Still, there are higher demands on the flexibility of geometry, uniformity, structural and optical qualities of nanostructures grown by the bottom-up approach. As an alternative, in-plane networks grown by SAE with or without catalyst are of particular interest recently because of the ability to form nanoarchitectures with extremely high uniformity in large scale and complex shapes for fundamental science and diverse quantum applications.[173-179]

The discussion above has been focused on III-V semiconductors in addition to CdS-CdSe core-shell nanowalls reported by Xu *et al*.[125] More broadly, the advantages of shape engineering also motivate the exploration of 2D/3D nanostructure shapes of other free-standing materials, such as ZnS nanobelts for ultraviolet-light sensors,[180, 181] CdSSe heterostructure nanosheets for two-colour lasing,[182] CdS-CdSeS nanoribbon and GaTe nanosheets for high performance photodetectors,[183, 184] ZnTe nanosheets,[185] II-VI tripods,[186] Pd, AuPd, and Au nanoplates.[187]

1.3. Techniques for synthesis of III-V nanoshapes

There are two techniques, generally categorised as top-down and bottom-up, to achieve the synthesis of III-V nanostructures. While top-down approach creates nanostructures using bulk materials through a series of processing (lithography, etching, mechanical exfoliation, etc.), bottom-up approach grows them using chemical reactions.

Top-down approach is an attractive route[84, 161] but requires rather complex technological processing and further processing steps to remove the unavoidable surface damage which can deteriorate the material properties.[157, 158, 188] Moreover, this approach has difficulties in forming complex heterostructures in all three dimensions. In comparison, bottom-up growth provides a promising alternative to obtaining free-standing III-V nanostructures with diverse shapes while maintaining many advantages such as strain relaxation between highly lattice-mismatched interface, formation of metastable crystal phase, heterostructures in both axial and radial directions and atomically sharp surfaces. Metal-seeded growth and SAE are two commonly used bottom-up methods.[189] Specifically, the former has been used to grow 2D/3D nanowire networks[167] and membrane-like nanostructures by manipulating the catalyst shape and position, the introduction of structural defects (lateral twins, mirror twins) and/or tuning the growth conditions.[120, 121, 138-140, 144, 148] However this method has very limited controllability of the nanostructure geometry and position, with poor yield and uniformity. Instead, SAE is more suitable for growing III-V nanostructure arrays with high controllability in terms of shape, dimension, site position, and directionality as well as uniformity and potential for scalability, as demonstrated by twin-free GaAs nanosheets[97, 135] rectangle InAs nanofins,[118] and various networks.[173, 174, 176]

1.4. Thesis synopsis

This dissertation presents a detailed investigation of various shape-engineered InP nanostructures, including nanostructure growth by catalyst-free SAE technique, mechanism study, and heterostructure incorporation towards the realisation of optoelectronic applications. Prior to that, some basic concepts and knowledge related to III-V nanostructures are given in Chapter 2 while a number of experimental techniques involving substrate preparation and nanostructure characterisation are introduced in Chapter 3.

In Chapter 4, InP nanostructures with diverse shapes, including nanowires, nanomembranes, nanoprisms, and nanorings, grown on {111}A InP substrates are investigated since substrates of {111} surfaces are most commonly used for growing vertical III-V nanowires. The design of openings on the mask plays a key role in controlling the nanostructure shapes. Growth optimisation is conducted by studying the effect of two key growth parameters (temperature and V/III ratio) on nanostructure morphology and optical properties. After optimisation, the morphology, structural and optical properties of 2D/3D nanoshapes are examined, showing high uniformity, pure WZ phase structure, and strong and homogeneous photon emission. In addition to pattern confinement, shape transformation mechanism is also determined by minimisation of total surface energy, as confirmed by a proposed model.

Chapter 5 further expands the investigation of InP nanostructures to InP substrates of other orientations, in order to systematically understand the growth mechanism and explore new nanostructures. Shape evolution from branched nanowires to nanomembranes with the elongation of openings along specific orientations are investigated on substrates of various orientations. Shape transformation mechanism is studied through a proposed growth model, which can also be attributed to minimisation of total surface energy. Moreover, the link between crystal phase and growth direction is analysed and explained with the help of a nucleation-based model. A novel double layered InP nanomembrane with WZ/ZB homojunction is achieved.

In Chapter 6, the growth of InAsP quantum well in InP nanowire with $\{1\bar{1}00\}$ side facets and nanomembranes with either $\{1\bar{1}00\}$ or $\{11\bar{2}0\}$ side facets are investigated. An asymmetric incorporation of quantum well is observed in both nanowires and nanomembranes with $\{1\bar{1}00\}$ side facets. In-depth analysis shows that lateral quantum well has a WZ phase and grows on $\{1\bar{1}00\}$ side facets of $<11\bar{2}>$A side of axial ZB quantum well, eventually leading to the asymmetry. On the other hand, nanomembranes with $\{11\bar{2}0\}$ side facets allow the formation of highly uniform quantum well on both sides. Optical results acquired from cathodoluminescence (CL) spectroscopy of these quantum well nanostructures are presented and compared, showing nanomembranes with $\{11\bar{2}0\}$ facets are better platform for future optoelectronic applications.

Finally, Chapter 7 summarises the main contributions in this dissertation and gives some suggestions for future works.

References

1. B. Gil. *III-nitride semiconductors and their modern devices*. Oxford University Press: New York, 2013.
2. M. Bosi, and C. Pelosi. The potential of III-V semiconductors as terrestrial photovoltaic devices. *Progress in Photovoltaics: Research and Applications* 2007, vol. 15, no. 1, pp. 51-68.
3. J. Wallentin, N. Anttu, D. Asoli, M. Huffman, I. Aberg, M. H. Magnusson, G. Siefer, P. Fuss-Kailuweit, F. Dimroth, B. Witzigmann, H. Q. Xu, L. Samuelson, K. Deppert, and M. T. Borgstrom. InP nanowire array solar cells achieving 13.8% efficiency by exceeding the ray optics limit. *Science* 2013, vol. 339, no. 6123, pp. 1057-1060.
4. T. Bryllert, L.-E. Wernersson, T. Löwgren, and L. Samuelson. Vertical wrap-gated nanowire transistors. *Nanotechnology* 2006, vol. 17, no. 11, pp. S227-S230.
5. H. Yu, J. Li, R. A. Loomis, L.-W. Wang, and W. E. Buhro. Two- versus three-dimensional quantum confinement in indium phosphide wires and dots. *Nature Materials* 2003, vol. 2, p. 517.
6. A. D. Yoffe. Low-dimensional systems: quantum size effects and electronic properties of semiconductor microcrystallites (zero-dimensional systems) and some quasi-two-dimensional systems. *Advances in Physics* 1993, vol. 42, no. 2, pp. 173-262.
7. A. L. Efros, and M. Rosen. The electronic structure of semiconductor nanocrystals. *Annual Review of Materials Science* 2000, vol. 30, no. 1, pp. 475-521.

8. M. S. Gudiksen, J. Wang, and C. M. Lieber. Size-dependent photoluminescence from single indium phosphide nanowires. *The Journal of Physical Chemistry B* 2002, vol. 106, no. 16, pp. 4036-4039.
9. Z. Zanolli, M.-E. Pistol, L. Fröberg, and L. Samuelson. Quantum-confinement effects in InAs–InP core–shell nanowires. *Journal of Physics: Condensed Matter* 2007, vol. 19, no. 29, p. 295219.
10. M. Alemany, X. Huang, M. L. Tiago, L. Gallego, and J. R. Chelikowsky. The role of quantum confinement in p-type doped indium phosphide nanowires. *Nano Letters* 2007, vol. 7, no. 7, pp. 1878-1882.
11. D. Jacobsson, F. Yang, K. Hillerich, F. Lenrick, S. Lehmann, D. Kriegner, J. Stangl, L. R. Wallenberg, K. A. Dick, and J. Johansson. Phase transformation in radially merged wurtzite GaAs nanowires. *Crystal Growth & Design* 2015, vol. 15, no. 10, pp. 4795-4803.
12. K. Ikejiri, Y. Kitauchi, K. Tomioka, J. Motohisa, and T. Fukui. Zinc blende and wurtzite crystal phase mixing and transition in indium phosphide nanowires. *Nano Letters* 2011, vol. 11, no. 10, pp. 4314-4318.
13. Y. Kitauchi, Y. Kobayashi, K. Tomioka, S. Hara, K. Hiruma, T. Fukui, and J. Motohisa. Structural transition in indium phosphide nanowires. *Nano Letters* 2010, vol. 10, no. 5, pp. 1699-1703.
14. H. J. Joyce, J. Wong-Leung, Q. Gao, H. H. Tan, and C. Jagadish. Phase perfection in zinc Blende and Wurtzite III-V nanowires using basic growth parameters. *Nano Letters* 2010, vol. 10, no. 3, pp. 908-915.
15. J. Johansson, K. A. Dick, P. Caroff, M. E. Messing, J. Bolinsson, K. Deppert, and L. Samuelson. Diameter dependence of the wurtzite– zinc blende transition in InAs nanowires. *The Journal of Physical Chemistry C* 2010, vol. 114, no. 9, pp. 3837-3842.
16. G. Patriarche, F. Glas, M. Tchernycheva, C. Sartel, L. Largeau, J.-C. Harmand, and G. E. Cirlin. Wurtzite to zinc blende phase transition in GaAs nanowires induced by epitaxial burying. *Nano Letters* 2008, vol. 8, no. 6, pp. 1638-1643.
17. Y. Chen, Z. Lai, X. Zhang, Z. Fan, Q. He, C. Tan, and H. Zhang. Phase engineering of nanomaterials. *Nature Reviews Chemistry* 2020, vol. 4, no. 5, pp. 243-256.
18. K. A. Dick, C. Thelander, L. Samuelson, and P. Caroff. Crystal phase engineering in single InAs nanowires. *Nano Letters* 2010, vol. 10, no. 9, pp. 3494-3499.
19. K. Pemasiri, M. Montazeri, R. Gass, L. M. Smith, H. E. Jackson, J. Yarrison-Rice, S. Paiman, Q. Gao, H. H. Tan, C. Jagadish, X. Zhang, and J. Zou. Carrier dynamics and

quantum confinement in type II ZB-WZ InP nanowire homostructures. *Nano Letters* 2009, vol. 9, no. 2, pp. 648-654.

20. S. Assali, I. Zardo, S. Plissard, D. Kriegner, M. A. Verheijen, G. Bauer, A. Meijerink, A. Belabbes, F. Bechstedt, J. E. M. Haverkort, and E. P. A. M. Bakkers. Direct band gap wurtzite gallium phosphide nanowires. *Nano Letters* 2013, vol. 13, no. 4, pp. 1559-1563.
21. P. Krogstrup, H. I. Jørgensen, M. Heiss, O. Demichel, J. V. Holm, M. Aagesen, J. Nygard, and A. Fontcuberta i Morral. Single-nanowire solar cells beyond the Shockley–Queisser limit. *Nature Photonics* 2013, vol. 7, no. 4, pp. 306-310.
22. M. Heiss, E. Russo-Averchi, A. Dalmau-Mallorquí, G. Tütüncüoğlu, F. Matteini, D. Rüffer, S. Conesa-Boj, O. Demichel, E. Alarcon-Lladó, and A. Fontcuberta i Morral. III–V nanowire arrays: growth and light interaction. *Nanotechnology* 2013, vol. 25, no. 1, p. 014015.
23. C. Hahn, Z. Zhang, A. Fu, C. H. Wu, Y. J. Hwang, D. J. Gargas, and P. Yang. Epitaxial growth of InGaN nanowire arrays for light emitting diodes. *ACS Nano* 2011, vol. 5, no. 5, pp. 3970-3976.
24. A. Standing, S. Assali, L. Gao, M. A. Verheijen, D. Van Dam, Y. Cui, P. H. Notten, J. E. Haverkort, and E. P. Bakkers. Efficient water reduction with gallium phosphide nanowires. *Nature communications* 2015, vol. 6, no. 1, pp. 1-7.
25. P. Varadhan, H.-C. Fu, D. Priante, J. R. D. Retamal, C. Zhao, M. Ebaid, T. K. Ng, I. Ajia, S. Mitra, and I. S. Roqan. Surface passivation of GaN nanowires for enhanced photoelectrochemical water-splitting. *Nano Letters* 2017, vol. 17, no. 3, pp. 1520-1528.
26. C. Tong. *Introduction to materials for advanced energy systems*. Springer Nature Switzerland AG: Cham, 2019.
27. Z. Fan, J. C. Ho, T. Takahashi, R. Yerushalmi, K. Takei, A. C. Ford, Y. L. Chueh, and A. Javey. Toward the development of printable nanowire electronics and sensors. *Advanced Materials* 2009, vol. 21, no. 37, pp. 3730-3743.
28. T. Takahashi, K. Takei, J. C. Ho, Y.-L. Chueh, Z. Fan, and A. Javey. Monolayer resist for patterned contact printing of aligned nanowire arrays. *Journal of the American Chemical Society* 2009, vol. 131, no. 6, pp. 2102-2103.
29. T. Takahashi, K. Takei, E. Adabi, Z. Fan, A. M. Niknejad, and A. Javey. Parallel array InAs nanowire transistors for mechanically bendable, ultrahigh frequency electronics. *ACS Nano* 2010, vol. 4, no. 10, pp. 5855-5860.

30. X. Liu, Y.-Z. Long, L. Liao, X. Duan, and Z. Fan. Large-scale integration of semiconductor nanowires for high-performance flexible electronics. *ACS Nano* 2012, vol. 6, no. 3, pp. 1888-1900.
31. M. Fang, N. Han, F. Wang, Z.-x. Yang, S. Yip, G. Dong, J. J. Hou, Y. Chueh, and J. C. Ho. III–V nanowires: Synthesis, property manipulations, and device applications. *Journal of Nanomaterials* 2014, vol. 2014, p. 702859.
32. Z. Liu, I. Papadimitriou, M. Castillo-Rodríguez, C. Wang, G. Esteban-Manzanares, X. Yuan, H. H. Tan, J. M. Molina-Aldareguía, and J. Llorca. Mechanical behavior of InP twinning superlattice nanowires. *Nano Letters* 2019, vol. 19, no. 7, pp. 4490-4497.
33. A. Gao, N. Lu, Y. Wang, P. Dai, T. Li, X. Gao, Y. Wang, and C. Fan. Enhanced sensing of nucleic acids with silicon nanowire field effect transistor biosensors. *Nano Letters* 2012, vol. 12, no. 10, pp. 5262-5268.
34. P. Ambhorkar, Z. Wang, H. Ko, S. Lee, K.-i. Koo, K. Kim, and D.-i. D. Cho. Nanowire-based biosensors: From growth to applications. *Micromachines* 2018, vol. 9, no. 12, p. 679.
35. Z. L. Wang, and J. Song. Piezoelectric nanogenerators based on zinc oxide nanowire arrays. *Science* 2006, vol. 312, no. 5771, pp. 242-246.
36. Q. Wan, Q. H. Li, Y. J. Chen, T. H. Wang, X. L. He, J. P. Li, and C. L. Lin. Fabrication and ethanol sensing characteristics of ZnO nanowire gas sensors. *Applied Physics Letters* 2004, vol. 84, no. 18, pp. 3654-3656.
37. P. Yang, R. Yan, and M. Fardy. Semiconductor nanowire: what's next? *Nano Letters* 2010, vol. 10, no. 5, pp. 1529-1536.
38. V. Mourik, K. Zuo, S. M. Frolov, S. Plissard, E. P. Bakkers, and L. P. Kouwenhoven. Signatures of Majorana fermions in hybrid superconductor-semiconductor nanowire devices. *Science* 2012, vol. 336, no. 6084, pp. 1003-1007.
39. L. Tizei, A. Craven, L. Zagonel, M. Tencé, O. Stéphan, T. Chiaramonte, M. Cotta, and D. Ugarte. Enhanced Eshelby twist on thin wurtzite InP nanowires and measurement of local crystal rotation. *Physical Review Letters* 2011, vol. 107, no. 19, p. 195503.
40. W. Lu, and C. M. Lieber. Semiconductor nanowires. *Journal of Physics D: Applied Physics* 2006, vol. 39, no. 21, pp. R387-R406.
41. L. J. Lauhon, M. S. Gudiksen, D. Wang, and C. M. Lieber. Epitaxial core–shell and core–multishell nanowire heterostructures. *Nature* 2002, vol. 420, no. 6911, pp. 57-61.
42. J. Johansson, and K. A. Dick. Recent advances in semiconductor nanowire heterostructures. *CrystEngComm* 2011, vol. 13, no. 24, pp. 7175-7184.

43. J. K. Hyun, S. Zhang, and L. J. Lauhon. Nanowire heterostructures. *Annual Review of Materials Research* 2013, vol. 43, no. 1, pp. 451-479.

44. T.-W. Yeh, Y.-T. Lin, L. S. Stewart, P. D. Dapkus, R. Sarkissian, J. D. O'Brien, B. Ahn, and S. R. Nutt. InGaN/GaN multiple quantum wells grown on nonpolar facets of vertical GaN nanorod arrays. *Nano Letters* 2012, vol. 12, no. 6, pp. 3257-3262.

45. R. Koester, J.-S. Hwang, D. Salomon, X. Chen, C. Bougerol, J.-P. Barnes, D. L. S. Dang, L. Rigutti, A. de Luna Bugallo, G. Jacopin, M. Tchernycheva, C. Durand, and J. Eymery. M-plane core–shell InGaN/GaN multiple-quantum-wells on GaN wires for electroluminescent devices. *Nano Letters* 2011, vol. 11, no. 11, pp. 4839-4845.

46. Y.-H. Ra, R. Navamathavan, H.-I. Yoo, and C.-R. Lee. Single nanowire light-emitting diodes using uniaxial and coaxial InGaN/GaN multiple quantum wells synthesized by metalorganic chemical vapor deposition. *Nano Letters* 2014, vol. 14, no. 3, pp. 1537-1545.

47. J. J. Wierer Jr, Q. Li, D. D. Koleske, S. R. Lee, and G. T. Wang. III-nitride core–shell nanowire arrayed solar cells. *Nanotechnology* 2012, vol. 23, no. 19, p. 194007.

48. C. Li, J. B. Wright, S. Liu, P. Lu, J. J. Figiel, B. Leung, W. W. Chow, I. Brener, D. D. Koleske, T.-S. Luk, D. F. Feezell, S. R. J. Brueck, and G. T. Wang. Nonpolar InGaN/GaN core–shell single nanowire lasers. *Nano Letters* 2017, vol. 17, no. 2, pp. 1049-1055.

49. H. J. Joyce. Growth and characterisation of III-V semiconductor nanowires for optoelectronic device applications. Ph.D. thesis, Australian National University, 2009.

50. S. Luryi, and E. Suhir. New approach to the high quality epitaxial growth of lattice-mismatched materials. *Applied Physics Letters* 1986, vol. 49, no. 3, pp. 140-142.

51. L. C. Chuang, M. Moewe, C. Chase, N. P. Kobayashi, C. Chang-Hasnain, and S. Crankshaw. Critical diameter for III-V nanowires grown on lattice-mismatched substrates. *Applied Physics Letters* 2007, vol. 90, no. 4, p. 043115.

52. M. de la Mata, C. Magén, P. Caroff, and J. Arbiol. Atomic scale strain relaxation in axial semiconductor III–V nanowire heterostructures. *Nano Letters* 2014, vol. 14, no. 11, pp. 6614-6620.

53. N. Jiang. Growth and characterisation of GaAs/AlGaAs core-shell nanowires for optoelectronic device applications. Ph.D. thesis, Australia National University, 2015.

54. X. Duan, Y. Huang, Y. Cui, J. Wang, and C. M. Lieber. Indium phosphide nanowires as building blocks for nanoscale electronic and optoelectronic devices. *Nature* 2001, vol. 409, no. 6816, p. 66.

55. Z. Wang, B. Tian, M. Pantouvaki, W. Guo, P. Absil, J. Van Campenhout, C. Merckling, and D. Van Thourhout. Room-temperature InP distributed feedback laser array directly grown on silicon. *Nature Photonics* 2015, vol. 9, no. 12, p. 837.
56. H. A. Fonseka. Growth and characterisation of InP nanowires and nanowire-based heterostructures for future optoelectronic device applications. Ph.D. thesis, Australia National University, 2015.
57. Q. Gao. InP nanowires grown by selective-area metalorganic vapour phase epitaxy. Ph.D. thesis, Australian National University, 2016.
58. H. J. Joyce, J. Wong-Leung, C. K. Yong, C. J. Docherty, S. Paiman, Q. Gao, H. H. Tan, C. Jagadish, J. Lloyd-Hughes, L. M. Herz, and M. B. Johnston. Ultralow surface recombination velocity in InP nanowires probed by terahertz spectroscopy. *Nano Letters* 2012, vol. 12, no. 10, pp. 5325-5330.
59. E. D. Minot, F. Kelkensberg, M. Van Kouwen, J. A. Van Dam, L. P. Kouwenhoven, V. Zwiller, M. T. Borgström, O. Wunnicke, M. A. Verheijen, and E. P. Bakkers. Single quantum dot nanowire LEDs. *Nano Letters* 2007, vol. 7, no. 2, pp. 367-371.
60. I. Yang, S. Kim, M. Niihori, A. Alabadla, Z. Li, L. Li, M. N. Lockrey, D.-Y. Choi, I. Aharonovich, J. Wong-Leung, H. H. Tan, C. Jagadish, and L. Fu. Highly uniform InGaAs/InP quantum well nanowire array-based light emitting diodes. *Nano Energy* 2020, vol. 71, p. 104576.
61. I. Yang, Z. Li, J. Wong-Leung, Y. Zhu, Z. Li, N. Gagrani, L. Li, M. N. Lockrey, H. Nguyen, and Y. Lu. Multiwavelength single nanowire InGaAs/InP quantum well light-emitting diodes. *Nano Letters* 2019, vol. 19, no. 6, pp. 3821-3829.
62. Q. Gao, D. Saxena, F. Wang, L. Fu, S. Mokkapati, Y. Guo, L. Li, J. Wong-Leung, P. Caroff, and H. H. Tan. Selective-area epitaxy of pure wurtzite InP nanowires: high quantum efficiency and room-temperature lasing. *Nano Letters* 2014, vol. 14, no. 9, pp. 5206-5211.
63. W.-Z. Xu, F.-F. Ren, D. Jevtics, A. Hurtado, L. Li, Q. Gao, J. Ye, F. Wang, B. Guilhabert, and L. Fu. Vertically emitting indium phosphide nanowire lasers. *Nano Letters* 2018, vol. 18, no. 6, pp. 3414-3420.
64. K. Li, H. Sun, F. Ren, K. W. Ng, T.-T. D. Tran, R. Chen, and C. J. Chang-Hasnain. Tailoring the optical characteristics of microsized InP nanoneedles directly grown on silicon. *Nano Letters* 2014, vol. 14, no. 1, pp. 183-190.
65. S. W. Eaton, A. Fu, A. B. Wong, C.-Z. Ning, and P. Yang. Semiconductor nanowire lasers. *Nature Reviews Materials* 2016, vol. 1, no. 6, p. 16028.

66. H. Goto, K. Nosaki, K. Tomioka, S. Hara, K. Hiruma, J. Motohisa, and T. Fukui. Growth of core–shell InP nanowires for photovoltaic application by selective-area metal organic vapor phase epitaxy. *Applied Physics Express* 2009, vol. 2, no. 3, p. 035004.
67. M. Heurlin, P. Wickert, S. Falt, M. T. Borgstrom, K. Deppert, L. Samuelson, and M. H. Magnusson. Axial InP nanowire tandem junction grown on a silicon substrate. *Nano Letters* 2011, vol. 11, no. 5, pp. 2028-2031.
68. Z. Zhong, Z. Li, Q. Gao, Z. Li, K. Peng, L. Li, S. Mokkapati, K. Vora, J. Wu, and G. Zhang. Efficiency enhancement of axial junction InP single nanowire solar cells by dielectric coating. *Nano Energy* 2016, vol. 28, pp. 106-114.
69. Y. C. Cui, J. Wang, S. R. Plissard, A. Cavalli, T. T. T. Vu, R. P. J. van Veldhoven, L. Gao, M. Trainor, M. A. Verheijen, J. E. M. Haverkort, and E. Bakkers. Efficiency enhancement of InP nanowire solar cells by surface cleaning. *Nano Letters* 2013, vol. 13, no. 9, pp. 4113-4117.
70. G. Otnes, E. Barrigón, C. Sundvall, K. E. Svensson, M. Heurlin, G. Siefer, L. Samuelson, I. Åberg, and M. T. Borgström. Understanding InP nanowire array solar cell performance by nanoprobe-enabled single nanowire measurements. *Nano Letters* 2018, vol. 18, no. 5, pp. 3038-3046.
71. J. F. Wang, M. S. Gudiksen, X. F. Duan, Y. Cui, and C. M. Lieber. Highly polarized photoluminescence and photodetection from single indium phosphide nanowires. *Science* 2001, vol. 293, no. 5534, pp. 1455-1457.
72. V. Jain, A. Nowzari, J. Wallentin, M. T. Borgstrom, M. E. Messing, D. Asoli, M. Graczyk, B. Witzigmann, F. Capasso, L. Samuelson, and H. Pettersson. Study of photocurrent generation in InP nanowire-based p(+)-i-n(+) photodetectors. *Nano Research* 2014, vol. 7, no. 4, pp. 544-552.
73. H. Pettersson, I. Zubritskaya, N. T. Nghia, J. Wallentin, M. T. Borgstrom, K. Storm, L. Landin, P. Wickert, F. Capasso, and L. Samuelson. Electrical and optical properties of InP nanowire ensemble p(+)-i-n(+) photodetectors. *Nanotechnology* 2012, vol. 23, no. 13, p. 135201.
74. Z. Li, J. Allen, M. Allen, H. H. Tan, C. Jagadish, and L. Fu. Review on III-V semiconductor single nanowire-based room temperature infrared photodetectors. *Materials* 2020, vol. 13, no. 6, p. 1400.
75. J. Wallentin, M. Ek, L. R. Wallenberg, L. Samuelson, and M. T. Borgstrom. Electron trapping in InP nanowire FETs with stacking faults. *Nano Letters* 2012, vol. 12, no. 1, pp. 151-155.

76. B. Ganjipour, J. Wallentin, M. T. Borgstrom, L. Samuelson, and C. Thelander. Tunnel field-effect transistors based on InP-GaAs heterostructure nanowires. *ACS Nano* 2012, vol. 6, no. 4, pp. 3109-3113.
77. T. Y. Duan, C. N. Liao, T. Chen, N. Yu, Y. Liu, H. Yin, Z. J. Xiong, and M. Q. Zhu. Single crystalline nitrogen-doped InP nanowires for low-voltage field-effect transistors and photodetectors on rigid silicon and flexible mica substrates. *Nano Energy* 2015, vol. 15, pp. 293-302.
78. K. Peng, P. Parkinson, J. L. Boland, Q. Gao, Y. C. Wenas, C. L. Davies, Z. Y. Li, L. Fu, M. B. Johnston, H. H. Tan, and C. Jagadish. Broadband phase-sensitive single InP nanowire photoconductive terahertz detectors. *Nano Letters* 2016, vol. 16, no. 8, pp. 4925-4931.
79. K. Peng, D. Jevtics, F. Zhang, S. Sterzl, D. A. Damry, M. U. Rothmann, B. Guilhabert, M. J. Strain, H. H. Tan, L. M. Herz, L. Fu, M. D. Dawson, A. Hurtado, C. Jagadish, and M. B. Johnston. Three-dimensional cross-nanowire networks recover full terahertz state. *Science* 2020, vol. 368, no. 6490, pp. 510-513.
80. S. J. Gibson, B. van Kasteren, B. Tekcan, Y. Cui, D. van Dam, J. E. M. Haverkort, E. Bakkers, and M. E. Reimer. Tapered InP nanowire arrays for efficient broadband high-speed single-photon detection. *Nature nanotechnology* 2019, vol. 14, no. 5, pp. 473-479.
81. L. Gao, Y. C. Cui, J. Wang, A. Cavalli, A. Standing, T. T. T. Vu, M. A. Verheijen, J. E. M. Haverkort, E. Bakkers, and P. H. L. Notten. Photoelectrochemical hydrogen production on InP nanowire arrays with molybdenum sulfide electrocatalysts. *Nano Letters* 2014, vol. 14, no. 7, pp. 3715-3719.
82. N. Kornienko, N. A. Gibson, H. Zhang, S. W. Eaton, Y. Yu, S. Aloni, S. R. Leone, and P. D. Yang. Growth and photoelectrochemical energy conversion of wurtzite indium phosphide nanowire arrays. *ACS Nano* 2016, vol. 10, no. 5, pp. 5525-5535.
83. J. Wong-Leung, I. Yang, Z. Li, S. K. Karuturi, L. Fu, H. H. Tan, and C. Jagadish. Engineering III–V semiconductor nanowires for device applications. *Advanced Materials* 2020, vol. 32, no. 18, p. 1904359.
84. J. A. Rogers, M. G. Lagally, and R. G. Nuzzo. Synthesis, assembly and applications of semiconductor nanomembranes. *Nature* 2011, vol. 477, no. 7362, pp. 45-53.
85. H. A. Fonseka, P. Caroff, J. Wong-Leung, A. S. Ameruddin, H. H. Tan, and C. Jagadish. Nanowires grown on InP (100): growth directions, facets, crystal structures, and relative yield control. *ACS Nano* 2014, vol. 8, no. 7, pp. 6945-6954.
86. M. A. Verheijen, R. E. Algra, M. T. Borgström, G. Immink, E. Sourty, W. J. P. van Enckevort, E. Vlieg, and E. P. A. M. Bakkers. Three-dimensional morphology of

GaP−GaAs nanowires revealed by transmission electron microscopy tomography. *Nano Letters* 2007, vol. 7, no. 10, pp. 3051-3055.

87. S.-K. Kim, R. W. Day, J. F. Cahoon, T. J. Kempa, K.-D. Song, H.-G. Park, and C. M. Lieber. Tuning light absorption in core/shell silicon nanowire photovoltaic devices through morphological design. *Nano Letters* 2012, vol. 12, no. 9, pp. 4971-4976.
88. Y. Calahorra, A. Kelrich, S. Cohen, and D. Ritter. Catalyst shape engineering for anisotropic cross-sectioned nanowire growth. *Scientific Reports* 2017, vol. 7, p. 40891.
89. Y.-S. No, L. Xu, M. N. Mankin, and H.-G. Park. Shape-controlled assembly of nanowires for photonic elements. *ACS Photonics* 2016, vol. 3, no. 12, pp. 2285-2290.
90. G. Bulgarini, M. E. Reimer, M. Bouwes Bavinck, K. D. Jöns, D. Dalacu, P. J. Poole, E. P. A. M. Bakkers, and V. Zwiller. Nanowire waveguides launching single photons in a Gaussian mode for ideal fiber coupling. *Nano Letters* 2014, vol. 14, no. 7, pp. 4102-4106.
91. A. P. Foster, J. K. Maguire, J. P. Bradley, T. P. Lyons, A. B. Krysa, A. M. Fox, M. S. Skolnick, and L. R. Wilson. Tuning nonlinear mechanical mode coupling in GaAs nanowires using cross-section morphology control. *Nano Letters* 2016, vol. 16, no. 12, pp. 7414-7420.
92. A. P. Foster, J. P. Bradley, K. Gardner, A. B. Krysa, B. Royall, M. S. Skolnick, and L. R. Wilson. Linearly polarized emission from an embedded quantum dot using nanowire morphology control. *Nano Letters* 2015, vol. 15, no. 3, pp. 1559-1563.
93. H. J. Joyce, Q. Gao, H. H. Tan, C. Jagadish, Y. Kim, M. A. Fickenscher, S. Perera, T. B. Hoang, L. M. Smith, H. E. Jackson, J. M. Yarrison-Rice, X. Zhang, and J. Zou. High purity GaAs nanowires free of planar defects: Growth and characterization. *Advanced Functional Materials* 2008, vol. 18, no. 23, pp. 3794-3800.
94. B. A. Wacaser, K. Deppert, L. S. Karlsson, L. Samuelson, and W. Seifert. Growth and characterization of defect free GaAs nanowires. *Journal of Crystal Growth* 2006, vol. 287, no. 2, pp. 504-508.
95. J.-H. Kang, Q. Gao, H. J. Joyce, H. H. Tan, C. Jagadish, Y. Kim, Y. Guo, H. Xu, J. Zou, and M. A. Fickenscher. Defect-free GaAs/AlGaAs core–shell nanowires on Si substrates. *Crystal Growth & Design* 2011, vol. 11, no. 7, pp. 3109-3114.
96. K. Ikejiri, T. Sato, H. Yoshida, K. Hiruma, J. Motohisa, S. Hara, and T. Fukui. Growth characteristics of GaAs nanowires obtained by selective area metal-organic vapour-phase epitaxy. *Nanotechnology* 2008, vol. 19, no. 26, p. 265604.

97. C. Y. Chi, C. C. Chang, S. Hu, T. W. Yeh, S. B. Cronin, and P. D. Dapkus. Twin-free GaAs nanosheets by selective area growth: implications for defect-free nanostructures. *Nano Letters* 2013, vol. 13, no. 6, pp. 2506-2515.
98. H. Yoshida, K. Ikejiri, T. Sato, S. Hara, K. Hiruma, J. Motohisa, and T. Fukui. Analysis of twin defects in GaAs nanowires and tetrahedra and their correlation to GaAs(111)B surface reconstructions in selective-area metal organic vapour-phase epitaxy. *Journal of Crystal Growth* 2009, vol. 312, no. 1, pp. 52-57.
99. M. Borg, H. Schmid, K. E. Moselund, G. Signorello, L. Gignac, J. Bruley, C. Breslin, P. Das Kanungo, P. Werner, and H. Riel. Vertical III–V nanowire device integration on Si (100). *Nano Letters* 2014, vol. 14, no. 4, pp. 1914-1920.
100. B. Kunert, Y. Mols, M. Baryshniskova, N. Waldron, A. Schulze, and R. Langer. How to control defect formation in monolithic III/V hetero-epitaxy on (100) Si? A critical review on current approaches. *Semiconductor Science and Technology* 2018, vol. 33, no. 9, p. 093002.
101. S. Y. Li, X. L. Zhou, X. T. Kong, M. K. Li, J. P. Mi, M. Q. Wang, and J. Q. Pan. Strain-driven synthesis of < 112 > direction InAs nanowires in V-grooved trenches on Si using InP/GaAs buffer layers. *Journal of Crystal Growth* 2016, vol. 449, pp. 5-9.
102. S. Y. Li, X. L. Zhou, X. T. Kong, M. K. Li, J. P. Mi, and J. Q. Pan. Catalyst-free growth of InP nanowires on patterned Si (001) substrate by using GaAs buffer layer. *Journal of Crystal Growth* 2016, vol. 440, pp. 81-85.
103. Z. Wang, B. Tian, M. Paladugu, M. Pantouvaki, N. Le Thomas, C. Merckling, W. Guo, J. Dekoster, J. Van Campenhout, and P. Absil. Polytypic InP nanolaser monolithically integrated on (001) silicon. *Nano Letters* 2013, vol. 13, no. 11, pp. 5063-5069.
104. K. Naji, G. Saint-Girons, J. Penuelas, G. Patriarche, L. Largeau, H. Dumont, P. Rojo-Romeo, and M. Gendry. Influence of catalyst droplet diameter on the growth direction of InP nanowires grown on Si(001) substrate. *Applied Physics Letters* 2013, vol. 102, no. 24.
105. H. Khmissi, K. Naji, M. H. H. Alouane, N. Chauvin, C. Bru-Chevallier, B. Ilahi, G. Patriarche, and M. Gendry. InAs/InP nanowires grown by catalyst assisted molecular beam epitaxy on silicon substrates. *Journal of Crystal Growth* 2012, vol. 344, no. 1, pp. 45-50.
106. C.-W. Hsu, Y.-F. Chen, and Y.-K. Su. Dislocation reduction of InAs nanofins prepared on Si substrate using metal-organic vapor-phase epitaxy. *Nanoscale Research Letters* 2012, vol. 7, no. 1, pp. 1-6.

107. L. Guniat, S. Marti-Sanchez, O. Garcia, M. Boscardin, D. Vindice, N. Tappy, M. Friedl, W. Kim, M. Zamani, L. Francaviglia, A. Balgarkashi, J. B. Leran, J. Arbiol, and I. M. A. Fontcuberta. III-V integration on si(100): Vertical nanospades. *ACS Nano* 2019, vol. 13, no. 5, pp. 5833-5840.

108. E. Russo-Averchi, J. Vukajlovic Plestina, G. z. Tütüncüoglu, F. Matteini, A. Dalmau-Mallorquí, M. De La Mata, D. Rüffer, H. A. Potts, J. Arbiol, and S. Conesa-Boj. High yield of GaAs nanowire arrays on Si mediated by the pinning and contact angle of Ga. *Nano Letters* 2015, vol. 15, no. 5, pp. 2869-2874.

109. E. Russo-Averchi, G. Tütüncüoglu, A. Dalmau-Mallorqui, I. C. Mundet, M. De La Mata, D. Rüffer, J. Arbiol, S. Conesa-Boj, and A. F. i Morral. Bottom-up engineering of InAs at the nanoscale: From V-shaped nanomembranes to nanowires. *Journal of Crystal Growth* 2015, vol. 420, pp. 47-56.

110. E. Russo-Averchi, A. Dalmau-Mallorquí, I. Canales-Mundet, G. Tütüncüoğlu, E. Alarcon-Llado, M. Heiss, D. Rüffer, S. Conesa-Boj, P. Caroff, and A. Fontcuberta i Morral. Growth mechanisms and process window for InAs V-shaped nanoscale membranes on Si[001]. *Nanotechnology* 2013, vol. 24, no. 43, p. 435603.

111. S. Conesa-Boj, E. Russo-Averchi, A. Dalmau-Mallorqui, J. Trevino, E. F. Pecora, C. Forestiere, A. Handin, M. Ek, L. Zweifel, L. R. Wallenberg, D. Ruffer, M. Heiss, D. Troadec, L. Dal Negro, P. Caroff, and A. Fontcuberta i Morral. Vertical "III-V" V-shaped nanomembranes epitaxially grown on a patterned Si[001] substrate and their enhanced light scattering. *ACS Nano* 2012, vol. 6, no. 12, pp. 10982-10991.

112. P. Staudinger, K. E. Moselund, and H. Schmid. Exploring the size limitations of wurtzite III-V film growth. *Nano Letters* 2020, vol. 20, no. 1, pp. 686-693.

113. P. Staudinger, S. Mauthe, N. V. Triviño, S. Reidt, K. E. Moselund, and H. Schmid. Wurtzite InP microdisks: from epitaxy to room-temperature lasing. *Nanotechnology* 2021, vol. 32, no. 07, p. 075605.

114. M. Albani, L. Ghisalberti, R. Bergamaschini, M. Friedl, M. Salvalaglio, A. Voigt, F. Montalenti, G. Tutuncuoglu, A. F. I. Morral, and L. Miglio. Growth kinetics and morphological analysis of homoepitaxial GaAs fins by theory and experiment. *Physical Review Materials* 2018, vol. 2, no. 9, p. 093404.

115. K. Storm, F. Halvardsson, M. Heurlin, D. Lindgren, A. Gustafsson, P. M. Wu, B. Monemar, and L. Samuelson. Spatially resolved Hall effect measurement in a single semiconductor nanowire. *Nature Nanotechnology* 2012, vol. 7, no. 11, p. 718.

116. C. Blömers, T. Grap, M. Lepsa, J. Moers, S. Trellenkamp, D. Grützmacher, H. Lüth, and T. Schäpers. Hall effect measurements on InAs nanowires. *Applied Physics Letters* 2012, vol. 101, no. 15, p. 152106.

117. C. C. Chang, C. Y. Chi, C. C. Chen, N. F. Huang, S. Arab, J. Qiu, M. L. Povinelli, P. D. Dapkus, and S. B. Cronin. Carrier dynamics and doping profiles in GaAs nanosheets. *Nano Research* 2014, vol. 7, no. 2, pp. 163-170.

118. J. Seidl, J. G. Gluschke, X. Yuan, S. Naureen, N. Shahid, H. H. Tan, C. Jagadish, A. P. Micolich, and P. Caroff. Regaining a spatial dimension: Mechanically transferrable two-dimensional InAs nanofins grown by selective area epitaxy. *Nano Letters* 2019, vol. 19, no. 7, pp. 4666-4677.

119. J. Xue, Y. Chen, D. Pan, J.-Y. Wang, J. Zhao, S. Huang, and H. Xu. Gate defined quantum dot realized in a single crystalline InSb nanosheet. *Applied Physics Letters* 2019, vol. 114, no. 2, p. 023108.

120. D. Pan, D. X. Fan, N. Kang, J. H. Zhi, X. Z. Yu, H. Q. Xu, and J. H. Zhao. Free-standing two-dimensional single-crystalline InSb nanosheets. *Nano Letters* 2016, vol. 16, no. 2, pp. 834-841.

121. M. de la Mata, R. Leturcq, S. R. Plissard, C. Rolland, C. Magen, J. Arbiol, and P. Caroff. Twin-induced InSb nanosails: a convenient high mobility quantum system. *Nano Letters* 2016, vol. 16, no. 2, pp. 825-833.

122. D. Pan, J.-Y. Wang, W. Zhang, L. Zhu, X. Su, F. Fan, Y. Fu, S. Huang, D. Wei, L. Zhang, M. Sui, A. Yartsev, H. Xu, and J. Zhao. Dimension engineering of high-quality InAs nanostructures on a wafer scale. *Nano Letters* 2019, vol. 19, no. 3, pp. 1632-1642.

123. Z. Fan, J. C. Ho, Z. A. Jacobson, R. Yerushalmi, R. L. Alley, H. Razavi, and A. Javey. Wafer-scale assembly of highly ordered semiconductor nanowire arrays by contact printing. *Nano Letters* 2008, vol. 8, no. 1, pp. 20-25.

124. Y. Huang, X. Duan, Q. Wei, and C. M. Lieber. Directed assembly of one-dimensional nanostructures into functional networks. *Science* 2001, vol. 291, no. 5504, pp. 630-633.

125. J. Xu, K. Rechav, R. Popovitz-Biro, I. Nevo, Y. Feldman, and E. Joselevich. High-gain 200 ns photodetectors from self-aligned CdS–CdSe core–shell nanowalls. *Advanced Materials* 2018, vol. 30, no. 20, p. 1800413.

126. J. Xu, E. Oksenberg, R. Popovitz-Biro, K. Rechav, and E. Joselevich. Bottom-up tri-gate transistors and submicrosecond photodetectors from guided CdS nanowalls. *Journal of the American Chemical Society* 2017, vol. 139, no. 44, pp. 15958-15967.

127. J. Hartmann, F. Steib, H. Zhou, J. Ledig, L. Nicolai, S. Fündling, T. Schimpke, A. Avramescu, T. Varghese, and A. Trampert. Study of 3D-growth conditions for selective area MOVPE of high aspect ratio GaN fins with non-polar vertical sidewalls. *Journal of Crystal Growth* 2017, vol. 476, pp. 90-98.

128. T. W. Yeh, Y. T. Lin, B. Ahn, L. S. Stewart, P. D. Dapkus, and S. R. Nutt. Vertical nonpolar growth templates for light emitting diodes formed with GaN nanosheets. *Applied Physics Letters* 2012, vol. 100, no. 3, p. 033119.

129. A. K. Rishinaramangalam, M. N. Fairchild, S. D. Hersee, G. Balakrishnan, and D. F. Feezell. Three-dimensional GaN templates for molecular beam epitaxy of nonpolar InGaN/GaN coaxial light-emitting diodes. *Journal of Vacuum Science & Technology B* 2013, vol. 31, no. 3, p. 03C107.

130. A. K. Rishinaramangalam, M. N. Fairchild, S. M. U. Masabih, D. M. Shima, G. Balakrishnan, and D. F. Feezell. *Selective-area growth of III-nitride core-shell nanowalls for light-emitting and laser diodes*. 2014 Conference on Lasers and Electro-Optics (CLEO) - Laser Science to Photonic Applications, San Jose, CA, USA, 8-13 June 2014, pp. 1-2.

131. A. K. Rishinaramangalam, S. M. Ul Masabih, M. N. Fairchild, J. B. Wright, D. M. Shima, G. Balakrishnan, I. Brener, S. R. J. Brueck, and D. F. Feezell. Controlled growth of ordered III-nitride core–shell nanostructure arrays for visible optoelectronic devices. *Journal of Electronic Materials* 2015, vol. 44, no. 5, pp. 1255-1262.

132. J. Hartmann, F. Steib, H. Zhou, J. Ledig, S. Fundling, F. Albrecht, T. Schimpke, A. Avramescu, T. Varghese, H. H. Wehmann, M. Strassburg, H. J. Lugauer, and A. Waag. High aspect ratio GaN fin microstructures with nonpolar sidewalls by continuous mode metalorganic vapor phase epitaxy. *Crystal Growth & Design* 2016, vol. 16, no. 3, pp. 1458-1462.

133. N. Wang, X. Yuan, X. Zhang, Q. Gao, B. Zhao, L. Li, M. Lockrey, H. H. Tan, C. Jagadish, and P. Caroff. Shape engineering of InP nanostructures by selective area epitaxy. *ACS Nano* 2019, vol. 13, no. 6, pp. 7261-7269.

134. S. Arab, P. D. Anderson, C. Y. Chi, P. D. Dapkus, M. L. Povinelli, and S. B. Cronin. Observation of asymmetric nanoscale optical cavity in GaAs nanosheets. *ACS Photonics* 2015, vol. 2, no. 8, pp. 1124-1128.

135. Z. Yang, A. Surrente, G. Tutuncuoglu, K. Galkowski, M. Cazaban-Carraze, F. Amaduzzi, P. Leroux, D. K. Maude, I. M. A. Fontcuberta, and P. Plochocka. Revealing large-scale homogeneity and trace impurity sensitivity of GaAs nanoscale membranes. *Nano Letters* 2017, vol. 17, no. 5, pp. 2979-2984.

136. S. Arab, C. Y. Chi, M. Yao, C.-C. Chang, P. D. Dapkus, and S. B. Cronin. *Optical and electrical characterization of surface passivated GaAs nanostructures*. Proc. SPIE 8996, Quantum Dots and Nanostructures: Synthesis, Characterization, and Modeling XI, San Francisco, California, United States, 19 February 2014, p. 89960G.

137. S. Arab, C.-Y. Chi, T. Shi, Y. Wang, D. P. Dapkus, H. E. Jackson, L. M. Smith, and S. B. Cronin. Effects of surface passivation on twin-free GaAs nanosheets. *ACS Nano* 2015, vol. 9, no. 2, pp. 1336-1340.

138. A. Kelrich, O. Sorias, Y. Calahorra, Y. Kauffmann, R. Gladstone, S. Cohen, M. Orenstein, and D. Ritter. InP nanoflag growth from a nanowire template by in situ catalyst manipulation. *Nano Letters* 2016, vol. 16, no. 4, pp. 2837-2844.

139. O. Sorias, A. Kelrich, R. Gladstone, D. Ritter, and M. Orenstein. Epitaxial nanoflag photonics: Semiconductor nanoemitters grown with their nanoantennas. *Nano Letters* 2017, vol. 17, no. 10, pp. 6011-6017.

140. M. Aagesen, E. Johnson, C. B. Sorensen, S. O. Mariager, R. Feidenhans'l, E. Spiecker, J. Nygard, and P. E. Lindelof. Molecular beam epitaxy growth of free-standing plane-parallel InAs nanoplates. *Nature Nanotechnology* 2007, vol. 2, no. 12, pp. 761-764.

141. E. F. Pecora, G. F. Walsh, C. Forestiere, A. Handin, E. Russo-Averchi, A. Dalmau-Mallorqui, I. Canales-Mundet, I. M. A. Fontcuberta, and L. Dal Negro. Enhanced second harmonic generation from InAs nano-wing structures on silicon. *Nanoscale* 2013, vol. 5, no. 21, pp. 10163-10170.

142. Q. Sun, H. Gao, X. Zhang, X. Yao, K. Zheng, P. Chen, W. Lu, and J. Zou. Free-standing InAs nanobelts driven by polarity in MBE. *ACS Applied Materials & Interfaces* 2019, vol. 11, no. 47, pp. 44609-44616.

143. Q. Sun, H. Gao, X. Zhang, X. Yao, S. Xu, K. Zheng, P. Chen, W. Lu, and J. Zou. High-quality epitaxial wurtzite structured InAs nanosheets grown in MBE. *Nanoscale* 2020, vol. 12, no. 1, pp. 271-276.

144. M. T. Soo, K. Zheng, Q. Gao, H. H. Tan, C. Jagadish, and J. Zou. Mirror-twin induced bicrystalline InAs nanoleaves. *Nano Research* 2016, vol. 9, no. 3, pp. 766-773.

145. V. Isha, Z. Valentina, R. Francesca, E. Daniele, B. Fabio, and S. Lucia. Morphology control of single-crystal InSb nanostructures by tuning the growth parameters. *Nanotechnology* 2020, vol. 31, no. 38, p. 384002.

146. J. H. Zhi, N. Kang, F. F. Su, D. X. Fan, S. Li, D. Pan, S. P. Zhao, J. H. Zhao, and H. Q. Xu. Coexistence of induced superconductivity and quantum Hall states in InSb nanosheets. *Physical Review B* 2019, vol. 99, no. 24, p. 245302.

147. J. Zhi, N. Kang, S. Li, D. Fan, F. Su, D. Pan, S. Zhao, J. Zhao, and H. Xu. Supercurrent and multiple Andreev reflections in InSb nanosheet SNS junctions. *Physica Status Solidi (B)* 2019, vol. 256, no. 6, p. 1800538.

148. N. Kang, D. Fan, J. Zhi, D. Pan, S. Li, C. Wang, J. Guo, J. Zhao, and H. Xu. Two-dimensional quantum transport in free-standing InSb nanosheets. *Nano Letters* 2019, vol. 19, no. 1, pp. 561-569.

149. J. Hartmann, I. Manglano Clavero, L. Nicolai, C. Margenfeld, H. Spende, J. Ledig, H. Zhou, F. Steib, A. Jaros, and A. Avramescu. 3D GaN fins as a versatile platform for a-plane-based devices. *Physica Status Solidi (B)* 2019, vol. 256, no. 4, p. 1800477.

150. G. Tutuncuoglu, M. de la Mata, D. Deiana, H. Potts, F. Matteini, J. Arbiol, and A. Fontcuberta i Morral. Towards defect-free 1-D GaAs/AlGaAs heterostructures based on GaAs nanomembranes. *Nanoscale* 2015, vol. 7, no. 46, pp. 19453-19460.

151. S. Wirths, B. F. Mayer, H. Schmid, M. Sousa, J. Gooth, H. Riel, and K. E. Moselund. Room-temperature lasing from monolithically integrated GaAs microdisks on silicon. *ACS Nano* 2018, vol. 12, no. 3, pp. 2169-2175.

152. B. F. Mayer, S. Wirths, S. Mauthe, P. Staudinger, M. Sousa, J. Winiger, H. Schmid, and K. E. Moselund. Microcavity lasers on silicon by template-assisted selective epitaxy of microsubstrates. *IEEE Photonics Technology Letters* 2019, vol. 31, no. 13, pp. 1021-1024.

153. S.-W. Huang Chen, C.-C. Shen, T. Wu, Z.-Y. Liao, L.-F. Chen, J.-R. Zhou, C.-F. Lee, C.-H. Lin, C.-C. Lin, C.-W. Sher, P.-T. Lee, A.-J. Tzou, Z. Chen, and H.-C. Kuo. Full-color monolithic hybrid quantum dot nanoring micro light-emitting diodes with improved efficiency using atomic layer deposition and nonradiative resonant energy transfer. *Photonics Research* 2019, vol. 7, no. 4, pp. 416-422.

154. S.-W. Wang, K.-B. Hong, Y.-L. Tsai, C.-H. Teng, A.-J. Tzou, Y.-C. Chu, P.-T. Lee, P.-C. Ku, C.-C. Lin, and H.-C. Kuo. Wavelength tunable InGaN/GaN nano-ring LEDs via nano-sphere lithography. *Scientific Reports* 2017, vol. 7, no. 1, p. 42962.

155. F. Fan, Y. Yu, S. E. H. Amiri, D. Quandt, D. Bimberg, and C. Z. Ning. Fabrication and room temperature operation of semiconductor nano-ring lasers using a general applicable membrane transfer method. *Applied Physics Letters* 2017, vol. 110, no. 17, p. 171105.

156. S. Park, S.-S. Kim, L. Wang, and S.-T. Ho. InGaAsP-InP nanoscale waveguide-coupled microring lasers with submilliampere threshold current using Cl2-N2-based high-density plasma etching. *IEEE Journal of Quantum Electronics* 2005, vol. 41, no. 3, pp. 351-356.

157. K. Amarnath, R. Grover, S. Kanakaraju, and P.-T. Ho. Electrically pumped InGaAsP-InP microring optical amplifiers and lasers with surface passivation. *IEEE Photonics Technology Letters* 2005, vol. 17, no. 11, pp. 2280-2282.

158. M. Shih, M. Hu, M. Freiler, M. Levy, R. Scarmozzino, R. Osgood Jr, I. Tao, and W. Wang. Fabrication of an InGaAs single quantum well circular ring laser by direct laser patterning. *Applied Physics Letters* 1995, vol. 66, no. 20, pp. 2608-2610.

159. T. Cockerill, M. Osowski, R. Lammert, and J. Coleman. *A strained-layer InGaAs-GaAs buried heterostructure circular ring laser with integrated y-coupled passive waveguide by selective-area metalorganic chemical vapor deposition*. Proceedings of IEEE 14th International Semiconductor Laser Conference, Maui, HI, USA, 19-23 September 1994, IEEE, pp. 195-196.

160. P. Hansen, G. Raybon, M.-D. Chien, U. Koren, B. Miller, M. Young, J.-M. Verdiell, and C. Burrus. A 1.54-um monolithic semiconductor ring laser: CW and mode-locked operation. *IEEE Photonics Technology Letters* 1992, vol. 4, no. 5, pp. 411-413.

161. S. H. Kim, P. K. Mohseni, Y. Song, T. Ishihara, and X. Li. Inverse metal-assisted chemical etching produces smooth high aspect ratio InP nanostructures. *Nano Letters* 2014, vol. 15, no. 1, pp. 641-648.

162. K. A. Dick, K. Deppert, M. W. Larsson, T. Mårtensson, W. Seifert, L. R. Wallenberg, and L. Samuelson. Synthesis of branched 'nanotrees' by controlled seeding of multiple branching events. *Nature Materials* 2004, vol. 3, no. 6, pp. 380-384.

163. H. Yang, V. Khayrudinov, V. Dhaka, H. Jiang, A. Autere, H. Lipsanen, Z. Sun, and H. Jussila. Nanowire network–based multifunctional all-optical logic gates. *Science Advances* 2018, vol. 4, no. 7, p. eaar7954.

164. F. Krizek, T. Kanne, D. Razmadze, E. Johnson, J. Nygård, C. M. Marcus, and P. Krogstrup. Growth of InAs wurtzite nanocrosses from hexagonal and cubic basis. *Nano Letters* 2017, vol. 17, no. 10, pp. 6090-6096.

165. J.-H. Kang, M. Galicka, P. Kacman, and H. Shtrikman. Wurtzite/Zinc-blende ‘k’-shape InAs nanowires with embedded two-dimensional wurtzite plates. *Nano Letters* 2017, vol. 17, no. 1, pp. 531-537.

166. J. Gooth, M. Borg, H. Schmid, V. Schaller, S. Wirths, K. Moselund, M. Luisier, S. Karg, and H. Riel. Ballistic one-dimensional InAs nanowire cross-junction interconnects. *Nano Letters* 2017, vol. 17, no. 4, pp. 2596-2602.

167. S. Gazibegovic, D. Car, H. Zhang, S. C. Balk, J. A. Logan, M. W. A. de Moor, M. C. Cassidy, R. Schmits, D. Xu, G. Wang, P. Krogstrup, R. L. M. Op Het Veld, K. Zuo, Y.

Vos, J. Shen, D. Bouman, B. Shojaei, D. Pennachio, J. S. Lee, P. J. van Veldhoven, S. Koelling, M. A. Verheijen, L. P. Kouwenhoven, C. J. Palmstrom, and E. Bakkers. Epitaxy of advanced nanowire quantum devices. *Nature* 2017, vol. 548, no. 7668, pp. 434-438.

168. E. M. Fadaly, H. Zhang, S. Conesa-Boj, D. Car, O. n. Gül, S. b. R. Plissard, R. L. Op het Veld, S. Kölling, L. P. Kouwenhoven, and E. P. Bakkers. Observation of conductance quantization in InSb nanowire networks. *Nano Letters* 2017, vol. 17, no. 11, pp. 6511-6515.
169. T. Rieger, D. Rosenbach, D. Vakulov, S. Heedt, T. Schäpers, D. Grützmacher, and M. I. Lepsa. Crystal phase transformation in self-assembled InAs nanowire junctions on patterned Si substrates. *Nano Letters* 2016, vol. 16, no. 3, pp. 1933-1941.
170. D. Car, J. Wang, M. A. Verheijen, E. P. Bakkers, and S. R. Plissard. Rationally designed single-crystalline nanowire networks. *Advanced Materials* 2014, vol. 26, no. 28, pp. 4875-4879.
171. S. R. Plissard, I. Van Weperen, D. Car, M. A. Verheijen, G. W. Immink, J. Kammhuber, L. J. Cornelissen, D. B. Szombati, A. Geresdi, and S. M. Frolov. Formation and electronic properties of InSb nanocrosses. *Nature Nanotechnology* 2013, vol. 8, no. 11, p. 859.
172. J.-H. Kang, Y. Cohen, Y. Ronen, M. Heiblum, R. Buczko, P. Kacman, R. Popovitz-Biro, and H. Shtrikman. Crystal structure and transport in merged InAs nanowires MBE grown on (001) InAs. *Nano Letters* 2013, vol. 13, no. 11, pp. 5190-5196.
173. R. L. M. Op het Veld, D. Xu, V. Schaller, M. A. Verheijen, S. M. E. Peters, J. Jung, C. Tong, Q. Wang, M. W. A. de Moor, B. Hesselmann, K. Vermeulen, J. D. S. Bommer, J. Sue Lee, A. Sarikov, M. Pendharkar, A. Marzegalli, S. Koelling, L. P. Kouwenhoven, L. Miglio, C. J. Palmstrøm, H. Zhang, and E. P. A. M. Bakkers. In-plane selective area InSb–Al nanowire quantum networks. *Communications Physics* 2020, vol. 3, no. 1, p. 59.
174. S. M. Frolov, M. J. Manfra, and J. D. Sau. Topological superconductivity in hybrid devices. *Nature Physics* 2020, vol. 16, no. 7, pp. 718-724.
175. P. Aseev, G. Wang, L. Binci, A. Singh, S. Marti-Sanchez, M. Botifoll, L. J. Stek, A. Bordin, J. D. Watson, F. Boekhout, D. Abel, J. Gamble, K. Van Hoogdalem, J. Arbiol, L. P. Kouwenhoven, G. de Lange, and P. Caroff. Ballistic InSb nanowires and networks via metal-sown selective area growth. *Nano Letters* 2019, vol. 19, no. 12, pp. 9102-9111.
176. P. Aseev, A. Fursina, F. Boekhout, F. Krizek, J. E. Sestoft, F. Borsoi, S. Heedt, G. Wang, L. Binci, S. Marti-Sanchez, T. Swoboda, R. Koops, E. Uccelli, J. Arbiol, P. Krogstrup, L. P. Kouwenhoven, and P. Caroff. Selectivity map for molecular beam epitaxy of advanced III-V quantum nanowire networks. *Nano Letters* 2019, vol. 19, no. 1, pp. 218-227.

177. S. Vaitiekenas, A. M. Whiticar, M. T. Deng, F. Krizek, J. E. Sestoft, C. J. Palmstrom, S. Marti-Sanchez, J. Arbiol, P. Krogstrup, L. Casparis, and C. M. Marcus. Selective-area-grown semiconductor-superconductor hybrids: A basis for topological networks. *Physical Review Letters* 2018, vol. 121, no. 14, p. 147701.

178. F. Krizek, J. E. Sestoft, P. Aseev, S. M. S. Anchez, S. Vaitiekenas, L. Casparis, S. A. Khan, Y. Liu, T. Stankevic, A. M. Whiticar, A. Fursina, F. Boekhout, R. Koops, E. Uccelli, L. P. Kouwenhoven, C. M. Marcus, J. Arbiol, and P. Krogstrup. Field effect enhancement in buffered quantum nanowire networks. *Physical Review Materials* 2018, vol. 2, no. 9, p. 093401.

179. M. Friedl, K. Cerveny, P. Weigele, G. Tutuncuoglu, S. Marti-Sanchez, C. Huang, T. Patlatiuk, H. Potts, Z. Sun, M. O. Hill, L. Guniat, W. Kim, M. Zamani, V. G. Dubrovskii, J. Arbiol, L. J. Lauhon, D. M. Zumbuhl, and I. M. A. Fontcuberta. Template-assisted scalable nanowire networks. *Nano Letters* 2018, vol. 18, no. 4, pp. 2666-2671.

180. X. Fang, Y. Bando, M. Liao, U. K. Gautam, C. Zhi, B. Dierre, B. Liu, T. Zhai, T. Sekiguchi, and Y. J. A. M. Koide. Single-crystalline ZnS nanobelts as ultraviolet-light sensors. *Advanced Materials* 2009, vol. 21, no. 20, pp. 2034-2039.

181. X. Fang, Y. Bando, M. Liao, T. Zhai, U. K. Gautam, L. Li, Y. Koide, and D. Golberg. An efficient way to assemble ZnS nanobelts as ultraviolet-light sensors with enhanced photocurrent and stability. *Advanced Functional Materials* 2010, vol. 20, no. 3, pp. 500-508.

182. F. Fan, Z. Liu, L. Yin, P. L. Nichols, H. Ning, S. Turkdogan, and C.-Z. Ning. Simultaneous two-color lasing in a single CdSSe heterostructure nanosheet. *Semiconductor Science and Technology* 2013, vol. 28, no. 6, p. 065005.

183. P. Guo, W. Hu, Q. Zhang, X. Zhuang, X. Zhu, H. Zhou, Z. Shan, J. Xu, and A. Pan. Semiconductor alloy nanoribbon lateral heterostructures for high-performance photodetectors. *Advanced Materials* 2014, vol. 26, no. 18, pp. 2844-2849.

184. Z. Wang, M. Safdar, M. Mirza, K. Xu, Q. Wang, Y. Huang, F. Wang, X. Zhan, and J. He. High-performance flexible photodetectors based on GaTe nanosheets. *Nanoscale* 2015, vol. 7, no. 16, pp. 7252-7258.

185. Y. Wang, H. Li, T. Yang, Z. Zou, Z. Qi, L. Ma, and J. Chen. Space-confined physical vapour deposition of high quality ZnTe nanosheets for optoelectronic application. *Materials Letters* 2019, vol. 238, pp. 309-312.

186. M. I. B. Utama, Q. Zhang, S. Jia, D. Li, J. Wang, and Q. Xiong. Epitaxial II–VI tripod nanocrystals: A generalization of van der Waals epitaxy for nonplanar polytypic nanoarchitectures. *ACS Nano* 2012, vol. 6, no. 3, pp. 2281-2288.

187. Y. Yoo, S. I. Kim, J. Kim, and B. Kim. Geometry-tailored freestanding epitaxial Pd, AuPd, and Au nanoplates driven by surface interactions. *Nanoscale* 2020, vol. 12, no. 11, pp. 6537-6544.

188. J.-Y. Kim, K. S. Kwak, J. S. Kim, B. Kang, and O. D. Kwon. Fabrication of photonic quantum ring laser using chemically assisted ion beam etching. *Journal of Vacuum Science & Technology B: Microelectronics and Nanometer Structures Processing, Measurement, and Phenomena* 2001, vol. 19, no. 4, pp. 1334-1338.

189. B. Mandl, J. Stangl, E. Hilner, A. A. Zakharov, K. Hillerich, A. W. Dey, L. Samuelson, G. Bauer, K. Deppert, and A. Mikkelsen. Growth mechanism of self-catalyzed group III− V nanowires. *Nano Letters* 2010, vol. 10, no. 11, pp. 4443-4449.

CHAPTER 2

Basic concepts of III-V nanostructures

2.1. Introduction

In this chapter, some key concepts and background knowledge related to III-V nanostructures are provided, including the mechanisms underlying MOCVD and selective area epitaxy in Section 2.2, crystal structures and planar defects in Section 2.3, crystal facets and polarity in Section 2.4, and semiconductor hetero/homostructures in Section 2.5. These contents are helpful to better understand the epitaxial growth and characterisation of InP and InP/InAsP nanostructures which is the dissertation of this thesis.

2.2. Selective-area MOCVD of III-V nanostructures

The mechanisms of MOCVD and selective area growth are first discussed here due to their importance in epitaxial growth of III-V nanostructures which is the first step for all three projects (Chapters 4-6). As a mainstream technique, MOCVD is widely used to synthesize III-V and II-VI compound semiconductors in academic research and industry. More details related to MOCVD system will be discussed later in Chapter 3.3. Basically, crystal growth is achieved using MOCVD technique by flowing a carrier gas (e.g. H_2 and N_2) and gas precursors (i.e. organometallics and hydrides) over a heated substrate wafer where the highly controlled phase transition between gas reactants and target solid crystal takes place at given conditions.[1, 2] Thus, MOCVD is a vapour phase epitaxy and also referred to as MOVPE. Here, the terminology "epitaxy" indicates that the growing crystal is in registry with the underlying crystalline substrate and can be divided into homoepitaxy and heteroepitaxy depending on whether the growing crystal is the same material with the substrate or not. The processes involved in the crystal growth of III-V semiconductors, such as InP, InAs and InAsP, in a MOCVD reactor are extremely complicated, but they can be ideally expressed as:

$$(CH_3)_3In + PH_3 \rightarrow InP + 3CH_4 \tag{2.1}$$

$$(CH_3)_3In + AsH_3 \rightarrow InAs + 3CH_4 \tag{2.2}$$

$$(CH_3)_3In + xAsH_3 + (1-x)PH_3 \rightarrow InAs_xP_{1-x} + 3CH_4 \tag{2.3}$$

where the intermediate steps and by-products are ignored, as schematically depicted in Figure 2.1a. Note that the gas flow can be either vertically or horizontally introduced into the MOCVD reactor (see Chapter 3.3 for more details). In both cases, the gas reactants diffuse toward the surface of a heated substrate through a laminar boundary layer with a temperature gradient (see Figure 2.1a).[3-5] During the diffusion or mass transport under typical MOCVD conditions, the organometallics (e.g. group III alkyls) are predominantly decomposed by removing methyl radicals (Figure 2.1a) while only some hydrides containing group V elements are decomposed because of their higher thermal stability. Their pyrolysis mainly occurs at the substrate surface thanks to the catalysis of III-V crystals.[6-11] The crystal growth reactions take place at the suitable site of substrate surface (Figure 2.1a).

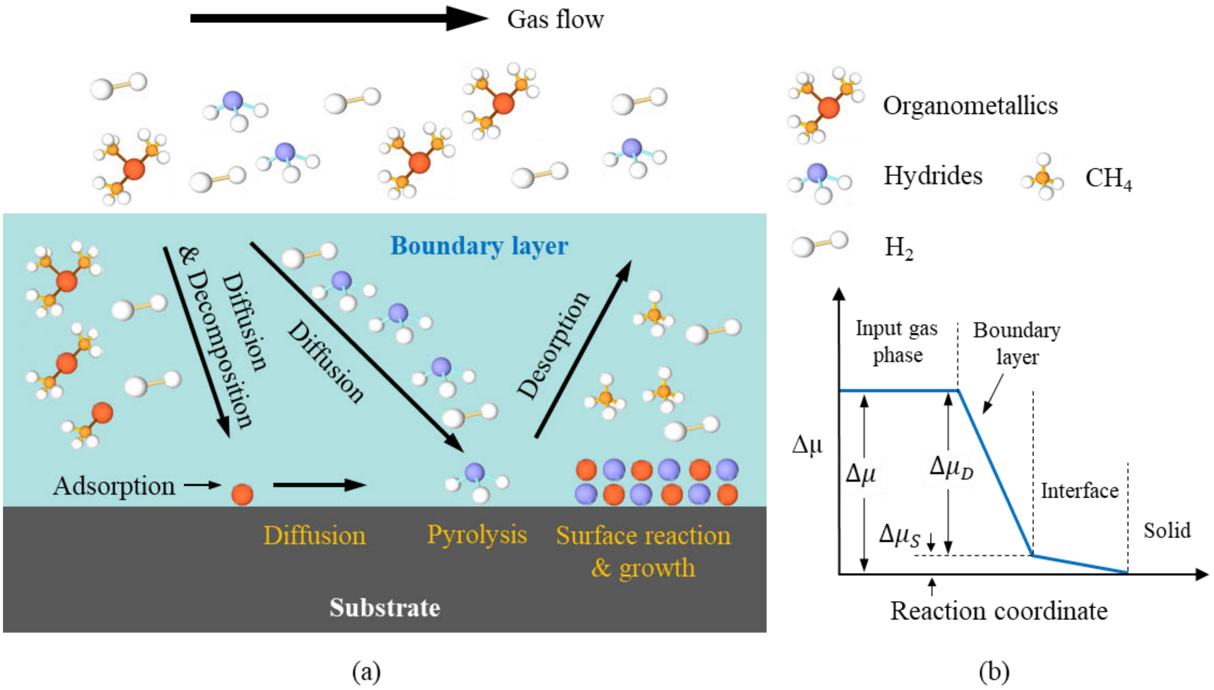

Figure 2.1: Schematic illustration of (a) simplified processes during MOCVD growth and (b) chemical potential difference as a function of reaction coordinate. (b), which is reproduced from Stringfellow[6] indicates that the chemical potential difference, as a thermodynamic force, drives the processes in MOCVD growth with equal rates.

MOCVD processes are not at equilibrium as a result of the continuous gas precursors being introduced with an amount more than is needed to keep equilibrium with the substrate. Thus, the thermodynamic force to restore the equilibrium drives the crystal growth (e.g. III-V compound semiconductors),[12-15] which can be described as the chemical potential difference between the reactants and grown solid with relatively higher and lower chemical potentials, respectively:[16]

$$\Delta\mu = \mu_{III}^{v} + \mu_{V}^{v} - \mu_{III-V}^{s} = RT\, ln \frac{P_{III}P_{V}}{P_{III}^{e}P_{V}^{e}} \qquad (2.4)$$

where the terms in the middle represent the chemical potentials of corresponding gas reactants and grown solid III-V semiconductors; R and T are the ideal gas constant and temperature, respectively; $\mathrm{P_{III}}(\mathrm{P_{III}^{e}})$ and $P_V(\mathrm{P_{V}^{e}})$ are the partial pressures of group III and group V reactants where the superscript e denotes the partial pressures at equilibrium. The maximum growth rate is determined by the thermodynamics and total gas flow of reactants used for crystal growth. In theory, it can be achieved in the case when all the supersaturated reactants form crystals and the equilibrium state is restored. However, in practice, the growth rate is much smaller than the maximum value due to the kinetic factors, i.e. the limited mass transport and surface reaction rates. Figure 2.1b schematically shows the chemical potential drop to drive the mass transport through the boundary layer ($\Delta\mu_D$) and surface reactions ($\Delta\mu_S$). Furthermore, while the surface reaction rate is much faster than the mass transport process, chemical potential difference (i.e. thermodynamic driving force) is predominantly used to promote the mass transport process, $\Delta\mu_D \gg \Delta\mu_S$, as demonstrated in Figure 2.1b. In this case, the crystal growth is in the mass transport- or diffusion-limited growth region.[1] Epitaxial growth of III-V semiconductors is often carried out in this situation thanks to the highly efficient, superior epitaxial layer and insensitivity of growth rate to the temperature and substrate orientation.[1] In addition, at temperatures lower than the transport-limited growth region, crystal growth is limited by surface kinetics due to the incomplete pyrolysis of precursors and the growth rate increases with the increase of temperature. In contrast, at higher temperatures, the growth rate decreases with the increase of temperature which is attributed to desorption of reactants and parasitic growth in the gas phase.[6] Despite the highly non-equilibrium MOCVD processes ($\Delta\mu \gg 0$), the near-equilibrium conditions may appear at the interface between vapour and solid phases in the mass transport-limited situations. This equilibrium approximation allows the thermodynamic analysis of III-V compound semiconductors in terms of composition, stoichiometry, and defects, etc.[1]

Prior to growth, the substrate is partially covered by a dielectric layer (e.g. SiO_x and SiN_x), referred to as the mask layer. As the name indicates, selective area epitaxy allows the epitaxial growth to occur only on the exposed regions of the underlying substrate and not on the dielectric mask layer itself. Typically, a high-quality dielectric layer with smooth surface and relatively higher growth temperatures are required to increase the selectivity between the exposed regions and the mask. The details of substrate preparation will be discussed later in Chapter 3.2. Figure 2.2a,b schematically illustrates the mass transport processes consisting of vapour phase diffusion and surface diffusion during the SA-MOCVD growth of nanostructures.[17] Basically, there are three diffusion fluxes of reaction species contributing to nanostructure growth: reaction species that directly diffuse to openings or nanostructure top surface (route 1), adsorb on mask layer and diffuse to the openings or nanostructures (route 2), adsorb on nanostructure side facets (route 3).[18] At the early stage of growth, reaction species from routes 1 and 2 lead to the nucleation and filling up of the openings. For the crystal growth outside of openings, nanostructures tend to be bound by low-index facets where crystal facet difference (such as growth rate, adatom diffusion length, thermal stability) play an important role in the crystal structure and geometry.[19-21] III-V nanostructures normally prefer to grow along the <111>A (InP) and <111>B (GaAs and InAs) directions, which leads to the formation of vertical nanowires with a high aspect ratio on {111} substrates. More interestingly, the facets of the nanostructures can be altered by changing the growth conditions, substrate orientation, and pattern design on substrate, making the control over of crystal structures and shapes possible.

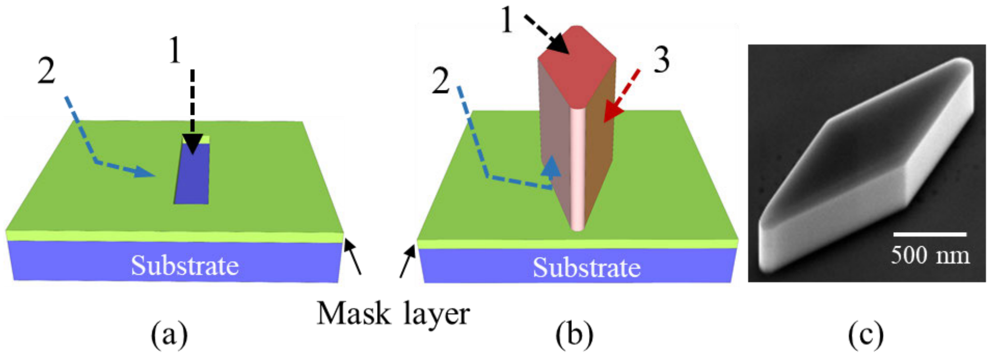

Figure 2.2: Schematic illustration of mass transport processes during SA-MOCVD growth: (a) nucleation and filling up inside of the opening; (b) nanostructure growth outside of opening. (c) 30° tilted SEM image of a prism-like InP nanostructure, the same as the schematic diagram in (b), grown on InP {111}A substrate by SA-MOCVD.

2.3. Crystal structures and planar defects

The above discussion in Section 2.2 is helpful to understand the epitaxial growth of III-V nanostructures. Once III-V nanostructures are grown, their crystal structure needs to be investigated. This section gives an overview of the WZ and ZB crystal structures. Crystal structure describes the unique arrangement of the ordered atoms in various crystalline materials. Despite the diverse crystal structures revealed in III-V semiconductors, only two main types, hexagonal wurtzite (WZ) and cubic zinc blende (ZB) structures, are observed in our nanostructures and therefore discussed here. While III-As and III-P semiconductors in the bulk form are generally of ZB structure, at the nanometre or micrometre forms they can exist in both ZB and WZ crystal structures.[19, 22-25]

Taking InP for an example, Figure 2.3 and Figure 2.4 schematically demonstrate the atomic stacking sequence of ZB and WZ crystal structures. Along the <111> or <0001> crystal direction, the bilayers consisting of a group III (In) layer and a group V (P) layer stack on each one another following the ABCABCABC sequence in ZB structure and ABABAB sequence in WZ structure (see Figure 2.3). Besides, for ZB structure, group III atoms take positions P2, P3 and P1 in the bilayer A, B, and C, respectively (Figure 2.4a-c). In contrast, group III atoms in WZ structure take positions P1 and P2 in the bilayers A and B, respectively (Figure 2.4d,e). In other words, group III or V atoms in WZ structure always sit on top of the second nearest group V or III atoms along the <111> direction.[26]

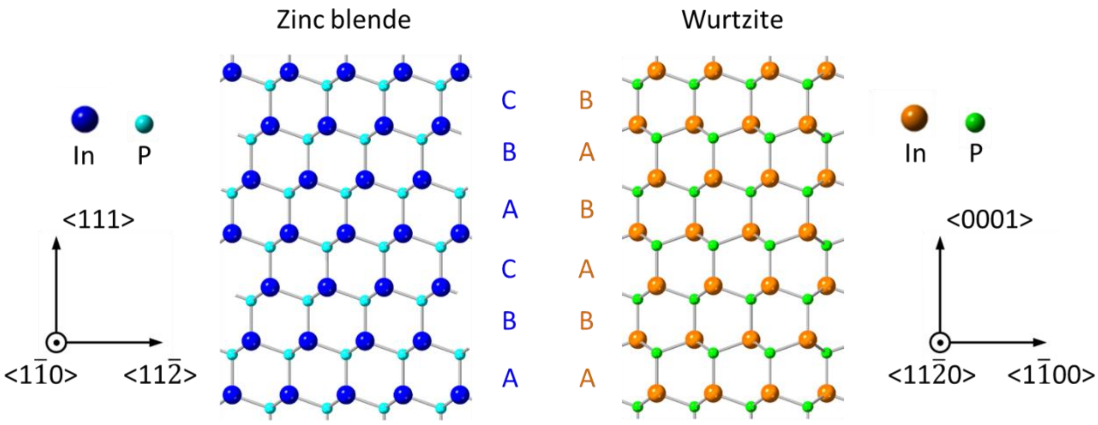

Figure 2.3: Schematic illustrations of the atomic stacking sequence of (left panel) zinc blende and (right panel) wurtzite crystal structures.

Planar defects form when the regular stacking sequence of the bilayers (i.e. ABCABC for ZB structure and ABAB for WZ structure) is interrupted. Twin plane and stacking fault are the two most commonly found planar defects in III-V nanostructures. For example, after the regular stacking pattern ABCA in the ZB structure, if the next bilayer is C instead of B, and followed by bilayers B and A in turn, the stacking sequence would be ABC$\underline{\text{A}}$CBA. The stacking sequence of the bilayers on the both side of $\underline{\text{A}}$ presents a mirror symmetry, and thus a twin plane is created at the $\underline{\text{A}}$ bilayer. Moreover, the C$\underline{\text{A}}$C can be treated as a thin WZ structure since it is the stacking pattern in WZ structure (i.e. CACACA). From this perspective, all bilayers in WZ structure can be treated as a twin plane.[27] The phase transition from ZB to WZ structures is accompanied by the formation of a twin plane. In addition, if a bilayer C is faultily stacked in the regular ABABAB WZ structure and leads to the occurrence of ABABCAB stacking sequence, this bilayer C is a stacking fault. And the ABCA part can be treated as a thin ZB segment in the faulted WZ structure.

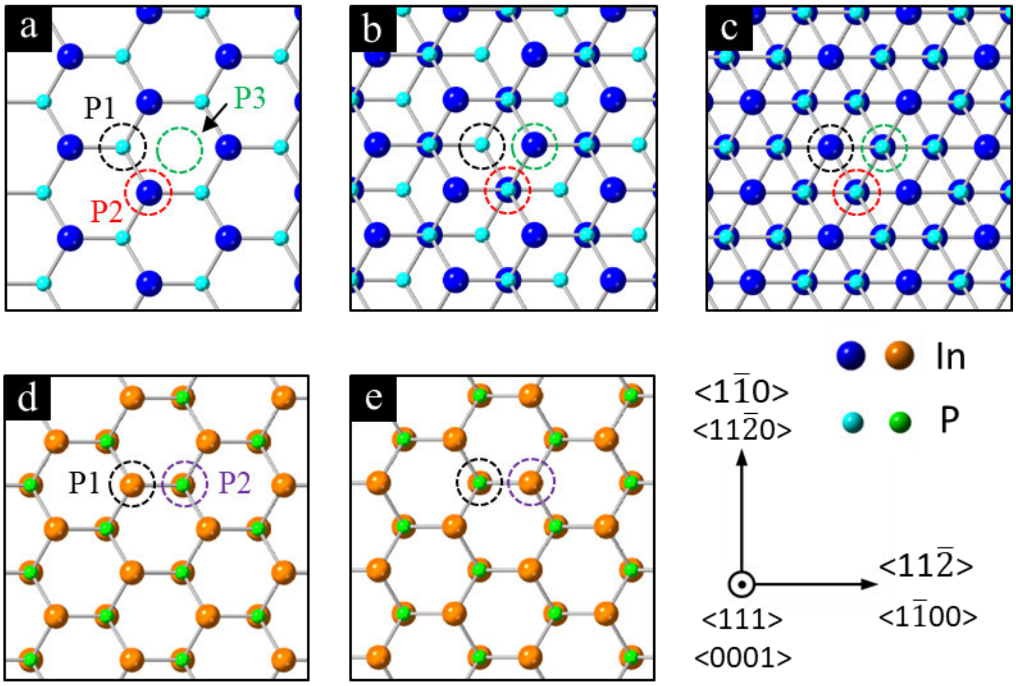

Figure 2.4: Schematic illustrations of (a-c) ZB and (d,e) WZ structures viewed along the <111> and <0001> directions, respectively. (a-c) show the stacking of one bilayer A, two bilayers AB, and three bilayers ABC, respectively. Three atom positions 1-3 in the ZB structures are indicated by the coloured circles. (d,e) shows the stacking of one bilayer A and two bilayers AB, respectively, where two atom positions are also indicated by the coloured circles.

The atomic stacking sequence can be easily distinguished by examining along the <1$\bar{1}$0> or <11$\bar{2}$0> direction. Thus, III-V nanostructures are commonly viewed along the <1$\bar{1}$0> or <11$\bar{2}$0> zone axis using atomically-resolved transmission electron microscopy to investigate the crystal structures and planar defects. The band structure and optoelectronic properties of III-V semiconductor compounds are dependent on their crystal structures,[28-31] which makes the relevant investigations (i.e. crystal structure or phase engineering) significant, including phase perfection,[32, 33] phase transition,[34-38] type-II band alignment[29, 39, 40] and twinning superlattice[40, 41]. In general, twins and stacking faults occur during growth along the <111> or <0001> direction. Since the substrates of III-V semiconductors are of ZB structure, the WZ III-V nanostructures grow along the <111> or <0001> direction. On the other hand, this provides a route to grow planar defect-free ZB structure by tailoring growth directions away from the <111> direction, as reported in InP nanowires grown by gold-assisted method along the <001> direction,[42-45] InP films along the <001> direction,[46] and GaAs nanowires along the <110> direction.[47] The planar defect-free ZB regions of InP nanostructures discussed in Chapter 5 are attributed to the non-<111>/<0001> oriented growth direction.

2.4. Crystal facets of III-V nanostructures and their polarity

In addition to crystal structures, crystal facets and polarity are important for aspects in the nanostructure formation as will be discussed in detail in Chapters 4 and 5. III-V nanostructures tend to be bound by low-index facets due to their higher thermal stability compared to high-index facets. Extensive reports in the literature show that these low-index facets generally include $\{111\}$, $\{1\bar{1}0\}$, $\{11\bar{2}\}$, $\{100\}$ in ZB nanowires and $\{0001\}$, $\{1\bar{1}00\}$, $\{11\bar{2}0\}$ in WZ nanowires. A variety of combinations have been observed to form nanowire side facets, which strongly affect the morphology and optoelectronic properties.[27, 44, 49-52] More details of the possible morphologies induced by different side facets of conventional <111>/<0001> oriented nanowires can be found in theses by Joyce and Fonseka.[27, 48] These low-index facets are also predominantly observed in the various In(As)P nanostructures involved in this dissertation. For example, as will be demonstrated in Chapter 4, all InP nanostructures with different wire-, membrane-, prism- and ring-like shapes are of WZ structure and mainly bound with the top facets of $\{0001\}$ and side facets of $\{1\bar{1}00\}$ and/or $\{11\bar{2}0\}$. Note that the competition of the side facets $\{1\bar{1}00\}$ and $\{11\bar{2}0\}$ plays an important role in shape transformation of InP nanostructures since SAE is significantly governed by the formation of facets during growth.[21] In addition to the expected $\{1\bar{1}00\}$ and $\{11\bar{2}0\}$ side facets, high-index facets could largely form as well in some nanostructures with non-equilibrium shape due to the confinement effect of patterned openings, such as the inner side facets of ring-like nanostructures and side facets of non-low-index oriented nanomembranes with a long length (see Figures 4.13c and 4.19). For InP nanostructures grown on substrates of different orientations (see Chapter 5) and InP/InAsP quantum well nanostructures (see Chapter 6), their crystal facets are still dominated by these low-index facets but of relatively complicated combinations due to the coexistence of both WZ and ZB crystal phases and insertion of InAsP quantum well, which will be discussed in the specific chapters.

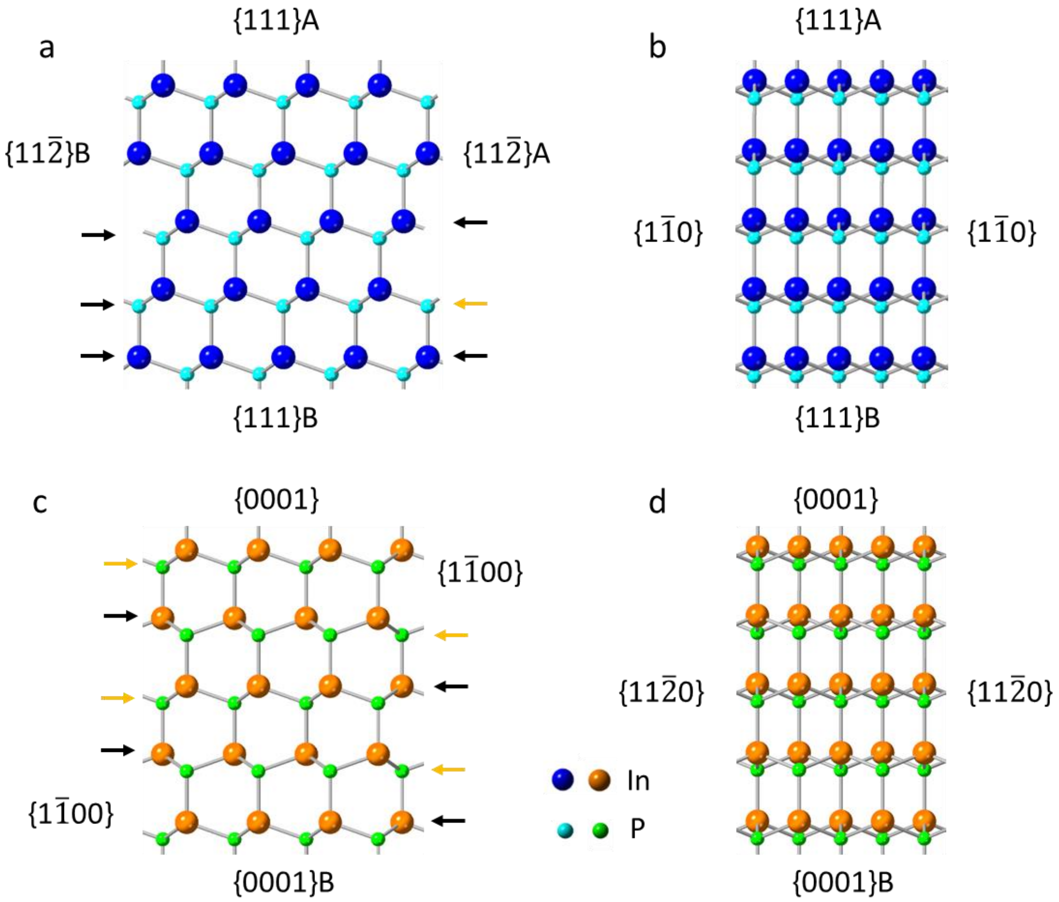

Figure 2.5: Schematic illustrations of (a,b) ZB and (c,d) WZ structures viewed along different crystallographic directions, showing the atomic arrangement of low-index {111}, {1$\bar{1}$0}, {11$\bar{2}$}, {0001}, {1$\bar{1}$00}, and {11$\bar{2}$0} facets.

III-V compound semiconductors (e.g. InP) have a partially ionic character due to the different electronegativity between group III and V elements where electronegativity indicates the ability of an atom to attract electrons.[49] Group III and V elements in the III-V compounds are generally of net positive and negative charges, respectively, which leads to the polar nature of III-V ZB and WZ structures.[50] Consequently, the polarities of all {111} (or {0001}) facets which are completely terminated with either group III or V atoms are not identical. The {111} (or {0001}) facets terminated with group III atoms are commonly named as A-polar, i.e. {111}A (or {0001}A) while those with group V atoms are B-polar, denoted as {111}B (or {0001}B), as shown in Figure 2.5a,c. Taking ZB InP structure for example, the {111}A and {111}B can be also expressed as {111}In and {111}P, respectively.

In contrast, all the {1$\bar{1}$0} facets consist of an equal number of group III and V surface atoms (see Figure 2.5b), and thus they are nonpolar and equivalent, which explains the appearance of the regular hexagonal cross-section of ZB GaAs and InAs nanowires.[20, 51, 52]

Likewise, the $\{1\bar{1}00\}$ and $\{11\bar{2}0\}$ facets are nonpolar (see Figure 2.5c,d), and often the regular hexagonal cross-section is observed in WZ InP nanowires bound with six equivalent $\{1\bar{1}00\}$ side facets.[53, 54]

For the $\{11\bar{2}\}$ facets, the ratio of the number of group III and V surface atoms are either 2 or ½, as shown in Figure 2.5a. Thus, the $\{11\bar{2}\}$ facets are polar and can be divided into $\{11\bar{2}\}$A and $\{11\bar{2}\}$B with more group III and V atoms, respectively. More precisely, the $\{11\bar{2}\}$ facets are partially polar which is different from the above {111} facets since they consist of both group III and V atoms rather than a single kind of atoms. The presence of crystal facet polarity plays a key role in epitaxial growth of III-V nanostructures due to the significant effects on surface properties, such as surface energy and growth rate.[55-60] For instance, Lehmann *et al.*[61] reported that pure ZB and WZ InP nanowires are simultaneously grown along the <111>A and <111>B directions, respectively. In addition, Zou *et al.*[62] found that the lateral growth rate of GaAs nanowires on $\{11\bar{2}\}$A side facet is faster than that on $\{11\bar{2}\}$B side facets under the adopted growth conditions, which leads to the formation of truncated triangular nanowire cross-section. In Chapters 5 and 6, the effect of polarity on In(As)P nanostructure growth (crystal phase, morphology, etc.) will be discussed in detail.

2.5. Semiconductor heterostructures and homostructures

As will be shown in Chapter 5, InP nanomembranes with type-II WZ/ZB homojunction are grown. Moreover, to further extend the optical properties and practical functionality of InP nanostructures, InAsP quantum wells and quantum dots are incorporated. In this section, some basic knowledge with respect to semiconductor heterostructures and homostructures is discussed to better understand the growth of type-II WZ/ZB homojunction in Chapter 5 and the corporation of InAsP in Chapter 6. Semiconductor heterostructures consist of two or more dissimilar semiconductors with different band gaps in which heterojunctions are formed at the interfaces. Heterostructures provide an advantage in controlling/modifying properties of the semiconductors, making them the key component in many optoelectronic devices, such as solar cells, light emitting diodes, lasers, and transistors.[63] In particular, the band discontinuity caused by the difference in energy bands enables electrons and holes to be spatially confined in a desired manner. Based on the difference in energy band alignment, semiconductor heterostructures generally can be divided into three types that are type-I with a straddling gap and represented by InP/InAsP and GaAs/AlGaAs, type-II with a staggered gap and represented by InP/InSb, and type-III with a broken/misaligned gap and represented by GaSb/InAs, as schematically illustrated in Figure 2.6a-c.

Potential wells can be formed in the conduction and valence bands of semiconductor heterostructures thanks to band offsets of the different semiconductors. Taking InP/InAsP (type-I heterostructure) for example, potential wells in both conduction and valence bands exist in InAsP layer which is sandwiched by InP layers with a relatively large band gap, leading to electrons and holes being trapped in InAsP layer (see Figure 2.6d). Furthermore, when the thickness of semiconductor layers where potential wells occur are reduced to be comparable with the de Broglie wavelength of carriers, quantum size effectss become significant.[64, 65] These thin sandwiched semiconductor layers are referred to as quantum wells (QWs) in which the carriers are confined in one dimension, leading to the quantisation of energy levels that carriers can occupy. Quantum confinement of carriers is important for heterostructure-based devices, such as improving luminescence efficiency and modulating emission wavelength. In addition to the above QWs, there commonly exists another two quantum structures according to the number of confined dimensions: quantum wires (QWRs) and quantum dots (QDs). Specifically, in QWRs, carriers are confined in two dimensions, and thus can only move without restrictions in one dimension; in contrast, carriers in QDs are completely confined and cannot freely move in all three dimensions. Sharp interfaces are highly required for quantum heterostructures due to that the embedded quantum structures are extremely small. Normally, MOCVD and molecular beam epitaxy are used to grow these heterostructures.

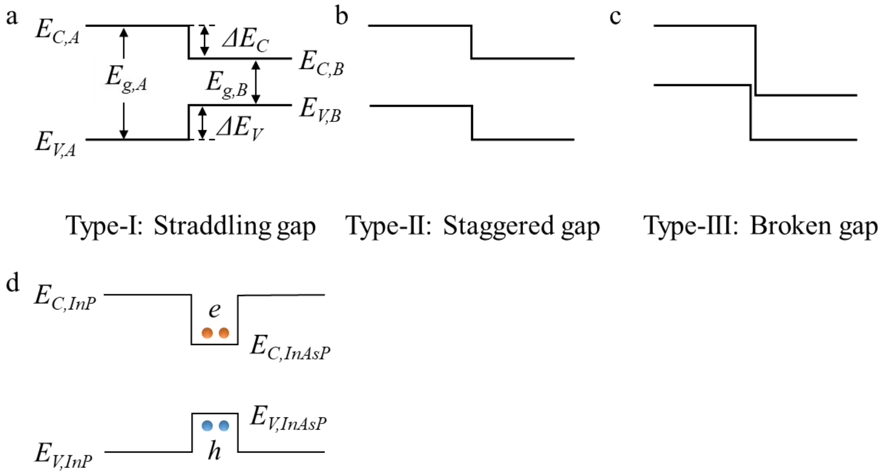

Figure 2.6: Schematic diagrams of (a-c) three types of band alignment of semiconductor heterostructures and (d) energy band diagram of InP/InAsP quantum well. (a-c) are reproduced from Zhang *et al.*[66]

The incorporation of quantum structures in III-V nanowires is more flexible compared to that in the planar structures thanks to their three dimensional geometries. Also, the nano-scale size reduces lattice mismatch limitation and therefore enables more semiconductors to form high-quality heterostructures.[67] QWs, QWRs and QDs heterostructures have been achieved in a variety of III-V nanowires by the controlling axial and radial growth, demonstrating great potentials in fundamental science and device applications.[68-70] For the free-standing nanomembranes, both top and side facets can be used for growing quantum heterostructures, similar to that as nanowires.

Compared with semiconductor heterostructures made of different materials, semiconductor homostructures are defined as structures consisting of the same semiconductors but with different band gaps. As mentioned in Section 2.3 above, III-V nanostructures can be formed in the WZ or ZB phase with different band structures. Although both WZ and ZB InP have direct band gaps, the WZ band gap is approximately 80 meV larger than the ZB counterpart.[30, 71] Thus, the nanostructures consisting of InP ZB/WZ sections can be treated as homostructures. In particular, some of III-V homostructures, such as InP, InAs and GaAs, have type-II band alignment, as shown in Figure 2.6b. Electrons and holes in these type-II semiconductor homostructures tend to be confined in ZB and WZ layers, respectively, which leads to unique electronic and optical properties.[29, 72, 73]

2.6. Summary

Some basic knowledge for understanding experimental results of InP and InAsP nanostructures in the next few chapters has been reviewed in this chapter. The general MOCVD processes, driving force caused by chemical potential difference, and SAE processes were first discussed, followed by the description of crystallographic knowledge with the emphasis on crystal phases, defects, facets and polarities. Finally, some key concepts related to homostructures and heterostructures are introduced. All these basics are useful to understand the InP and InAsP nanostructures from various aspects, such as growth behaviours, structural and optical properties.

References

1. G. B. Stringfellow. *Organometallic vapor-phase epitaxy: theory and practice*. 2nd ed., Academic Press: San Diego, 1999.

2. J. L. Zilko. Metal organic chemical vapor deposition: technology and equipment. In *Handbook of thin film deposition processes and techniques*. Elsevier: 2001, pp. 151-203.
3. T. F. Kuech. III-V compound semiconductors: Growth and structures. *Progress in Crystal Growth and Characterization of Materials* 2016, vol. 62, no. 2, pp. 352-370.
4. M. Ludowise. Metalorganic chemical vapor deposition of III-V semiconductors. *Journal of Applied Physics* 1985, vol. 58, no. 8, pp. R31-R55.
5. F. H. Yang. Modern metal-organic chemical vapor deposition (MOCVD) reactors and growing nitride-based materials. In *Nitride semiconductor light-emitting diodes (LEDs)*. J. Huang; H.-C. Kuo; S.-C. Shen, Eds. Woodhead Publishing: 2014, pp. 27-65.
6. G. B. Stringfellow. A critical appraisal of growth mechanisms in MOVPE. *Journal of Crystal Growth* 1984, vol. 68, no. 1, pp. 111-122.
7. J. Nishizawa. On the reaction mechanism of GaAs MOCVD. *Journal of the Electrochemical Society* 1983, vol. 130, no. 2, p. 413.
8. G. Stringfellow. Organometallic vapor-phase epitaxial growth of III-V semiconductors. *Semiconductors and Semimetals* 1985, vol. 22, p. 209.
9. I. Frolov, E. Kiteav, B. Druz, and E. Sokolov. Kinetics of the thermal decomposition of arsine in a stream. *Journal of Physical Chemistry* 1977, vol. 51, p. 591.
10. J. Duchemin, J. Hirtz, M. Razeghi, M. Bonnet, and S. Hersee. GaInAs and GaInAsP materials grown by low pressure MOCVD for microwave and optoelectronic applications. *Journal of Crystal Growth* 1981, vol. 55, no. 1, pp. 64-73.
11. M. R. Leys, and H. Veenvliet. A study of the growth mechanism of epitaxial GaAs as grown by the technique of metal organic vapour phase epitaxy. *Journal of Crystal Growth* 1981, vol. 55, no. 1, pp. 145-153.
12. G. B. Stringfellow. Fundamental aspects of MOVPE. In *Metalorganic vapor phase epitaxy (MOVPE): growth, materials properties, and applications*. S. Irvine; P. Capper, Eds. John Wiley & Sons Ltd: 2020, pp. 19-69.
13. G. B. Stringfellow. Fundamental aspects of organometallic vapor phase epitaxy. *Materials Science and Engineering: B* 2001, vol. 87, no. 2, pp. 97-116.
14. G. B. Stringfellow. Thermodynamic aspects of OMVPE. *Journal of Crystal Growth* 1984, vol. 70, no. 1, pp. 133-139.
15. G. B. Stringfellow. Thermodynamic aspects of organometallic vapor phase epitaxy. *Journal of Crystal Growth* 1983, vol. 62, no. 2, pp. 225-229.
16. G. B. Stringfellow. Fundamentals of vapor phase epitaxial growth processes. *AIP Conference Proceedings* 2007, vol. 916, no. 1, pp. 48-68.

17. D. G. Coronell, and K. F. Jensen. Analysis of MOCVD of GaAs on patterned substrates. *Journal of Crystal Growth* 1991, vol. 114, no. 4, pp. 581-592.
18. H. Joyce. III-V nanowires and related nanostructures: from nitrides to antimonides. In *Metalorganic vapor phase epitaxy (MOVPE): growth, materials properties, and applications*. S. Irvine; P. Capper, Eds. John Wiley & Sons Ltd.: 2019, pp. 217-239.
19. K. Tomioka, K. Ikejiri, T. Tanaka, J. Motohisa, S. Hara, K. Hiruma, and T. Fukui. Selective-area growth of III-V nanowires and their applications. *Journal of Materials Research* 2011, vol. 26, no. 17, pp. 2127-2141.
20. K. Ikejiri, T. Sato, H. Yoshida, K. Hiruma, J. Motohisa, S. Hara, and T. Fukui. Growth characteristics of GaAs nanowires obtained by selective area metal-organic vapour-phase epitaxy. *Nanotechnology* 2008, vol. 19, no. 26, p. 265604.
21. K. Ikejiri, J. Noborisaka, S. Hara, J. Motohisa, and T. Fukui. Mechanism of catalyst-free growth of GaAs nanowires by selective area MOVPE. *Journal of Crystal Growth* 2007, vol. 298, pp. 616-619.
22. K. W. Ng, W. S. Ko, F. Lu, and C. J. Chang-Hasnain. Metastable growth of pure wurtzite InGaAs microstructures. *Nano Letters* 2014, vol. 14, no. 8, pp. 4757-4762.
23. P. Staudinger, K. E. Moselund, and H. Schmid. Exploring the size limitations of wurtzite III-V film growth. *Nano Letters* 2020, vol. 20, no. 1, pp. 686-693.
24. Q. Gao, D. Saxena, F. Wang, L. Fu, S. Mokkapati, Y. Guo, L. Li, J. Wong-Leung, P. Caroff, and H. H. Tan. Selective-area epitaxy of pure wurtzite InP nanowires: high quantum efficiency and room-temperature lasing. *Nano Letters* 2014, vol. 14, no. 9, pp. 5206-5211.
25. T. T. T. Vu, T. Zehender, M. A. Verheijen, S. R. Plissard, G. W. G. Immink, J. E. M. Haverkort, and E. Bakkers. High optical quality single crystal phase wurtzite and zincblende InP nanowires. *Nanotechnology* 2013, vol. 24, no. 11, p. 115705.
26. Y. Kitauchi, Y. Kobayashi, K. Tomioka, S. Hara, K. Hiruma, T. Fukui, and J. Motohisa. Structural transition in indium phosphide nanowires. *Nano Letters* 2010, vol. 10, no. 5, pp. 1699-1703.
27. H. J. Joyce. Growth and characterisation of III-V semiconductor nanowires for optoelectronic device applications. Ph.D. thesis, Australian National University, 2009.
28. A. Maharjan, K. Pemasiri, P. Kumar, A. Wade, L. M. Smith, H. E. Jackson, J. M. Yarrison-Rice, A. Kogan, S. Paiman, Q. Gao, H. H. Tan, and C. Jagadish. Room temperature photocurrent spectroscopy of single zincblende and wurtzite InP nanowires. *Applied Physics Letters* 2009, vol. 94, no. 19.

29. K. Pemasiri, M. Montazeri, R. Gass, L. M. Smith, H. E. Jackson, J. Yarrison-Rice, S. Paiman, Q. Gao, H. H. Tan, C. Jagadish, X. Zhang, and J. Zou. Carrier dynamics and quantum confinement in type II ZB-WZ InP nanowire homostructures. *Nano Letters* 2009, vol. 9, no. 2, pp. 648-654.
30. A. Mishra, L. Titova, T. Hoang, H. Jackson, L. Smith, J. Yarrison-Rice, Y. Kim, H. Joyce, Q. Gao, and H. Tan. Polarization and temperature dependence of photoluminescence from zincblende and wurtzite InP nanowires. *Applied Physics Letters* 2007, vol. 91, no. 26, p. 263104.
31. T. Cheiwchanchamnangij, and W. R. Lambrecht. Band structure parameters of wurtzite and zinc-blende GaAs under strain in the GW approximation. *Physical Review B* 2011, vol. 84, no. 3, p. 035203.
32. D. Pan, M. Fu, X. Yu, X. Wang, L. Zhu, S. Nie, S. Wang, Q. Chen, P. Xiong, S. von Molnár, and J. Zhao. Controlled synthesis of phase-pure InAs nanowires on Si(111) by diminishing the diameter to 10 nm. *Nano Letters* 2014, vol. 14, no. 3, pp. 1214-1220.
33. H. J. Joyce, J. Wong-Leung, Q. Gao, H. H. Tan, and C. Jagadish. Phase perfection in zinc Blende and Wurtzite III-V nanowires using basic growth parameters. *Nano Letters* 2010, vol. 10, no. 3, pp. 908-915.
34. T. Rieger, D. Rosenbach, D. Vakulov, S. Heedt, T. Schäpers, D. Grützmacher, and M. I. Lepsa. Crystal phase transformation in self-assembled InAs nanowire junctions on patterned Si substrates. *Nano Letters* 2016, vol. 16, no. 3, pp. 1933-1941.
35. D. Jacobsson, F. Yang, K. Hillerich, F. Lenrick, S. Lehmann, D. Kriegner, J. Stangl, L. R. Wallenberg, K. A. Dick, and J. Johansson. Phase transformation in radially merged wurtzite GaAs nanowires. *Crystal Growth & Design* 2015, vol. 15, no. 10, pp. 4795-4803.
36. S. Assali, L. Gagliano, D. S. Oliveira, M. A. Verheijen, S. R. Plissard, L. Feiner, and E. P. Bakkers. Exploring crystal phase switching in GaP nanowires. *Nano Letters* 2015, vol. 15, no. 12, pp. 8062-8069.
37. H. Zheng, J. Wang, J. Y. Huang, J. Wang, Z. Zhang, and S. X. Mao. Dynamic process of phase transition from wurtzite to zinc blende structure in InAs nanowires. *Nano Letters* 2013, vol. 13, no. 12, pp. 6023-6027.
38. K. Ikejiri, Y. Kitauchi, K. Tomioka, J. Motohisa, and T. Fukui. Zinc blende and wurtzite crystal phase mixing and transition in indium phosphide nanowires. *Nano Letters* 2011, vol. 11, no. 10, pp. 4314-4318.
39. N. Akopian, G. Patriarche, L. Liu, J. C. Harmand, and V. Zwiller. Crystal phase quantum dots. *Nano Letters* 2010, vol. 10, no. 4, pp. 1198-1201.

40. L. J. Zhang, J. W. Luo, A. Zunger, N. Akopian, V. Zwiller, and J. C. Harmand. Wide InP nanowires with wurtzite/zincblende superlattice segments are type-II whereas narrower nanowires become type-I: an atomistic pseudopotential calculation. *Nano Letters* 2010, vol. 10, no. 10, pp. 4055-4060.

41. R. E. Algra, M. A. Verheijen, M. T. Borgström, L.-F. Feiner, G. Immink, W. J. van Enckevort, E. Vlieg, and E. P. Bakkers. Twinning superlattices in indium phosphide nanowires. *Nature* 2008, vol. 456, no. 7220, pp. 369-372.

42. J. Wang, S. R. Plissard, M. A. Verheijen, L. F. Feiner, A. Cavalli, and E. Bakkers. Reversible switching of InP nanowire growth direction by catalyst engineering. *Nano Letters* 2013, vol. 13, no. 8, pp. 3802-3806.

43. H. A. Fonseka, P. Caroff, J. Wong-Leung, A. S. Ameruddin, H. H. Tan, and C. Jagadish. Nanowires grown on InP (100): growth directions, facets, crystal structures, and relative yield control. *ACS Nano* 2014, vol. 8, no. 7, pp. 6945-6954.

44. J. Wang, S. Plissard, M. Hocevar, T. T. Vu, T. Zehender, G. G. Immink, M. A. Verheijen, J. Haverkort, and E. P. Bakkers. Position-controlled [100] InP nanowire arrays. *Applied Physics Letters* 2012, vol. 100, no. 5, p. 053107.

45. U. Krishnamachari, M. Borgstrom, B. Ohlsson, N. Panev, L. Samuelson, W. Seifert, M. Larsson, and L. Wallenberg. Defect-free InP nanowires grown in [001] direction on InP (001). *Applied Physics Letters* 2004, vol. 85, no. 11, pp. 2077-2079.

46. P. Staudinger, S. Mauthe, K. E. Moselund, and H. Schmid. Concurrent zinc-blende and wurtzite film formation by selection of confined growth planes. *Nano Letters* 2018, vol. 18, no. 12, pp. 7856-7862.

47. M. Knoedler, N. Bologna, H. Schmid, M. Borg, K. E. Moselund, S. Wirths, M. D. Rossell, and H. Riel. Observation of twin-free GaAs nanowire growth using template assisted selective epitaxy. *Crystal Growth & Design* 2017, vol. 17, no. 12, pp. 6297-6302.

48. H. A. Fonseka. Growth and characterisation of InP nanowires and nanowire-based heterostructures for future optoelectronic device applications. Ph.D. thesis, Australia National University, 2015.

49. S. Luryi, and E. Suhir. New approach to the high quality epitaxial growth of lattice-mismatched materials. *Applied Physics Letters* 1986, vol. 49, no. 3, pp. 140-142.

50. J. E. Ayers, T. Kujofsa, P. Rago, and J. Raphael. *Heteroepitaxy of semiconductors: theory, growth, and characterization*. 2nd ed., CRC Press: 2016.

51. J. Motohisa, J. Noborisaka, J. Takeda, M. Inari, and T. Fukui. Catalyst-free selective-area MOVPE of semiconductor nanowires on (111)B oriented substrates. *Journal of Crystal Growth* 2004, vol. 272, no. 1, pp. 180-185.
52. K. Tomioka, P. Mohan, J. Noborisaka, S. Hara, J. Motohisa, and T. Fukui. Growth of highly uniform InAs nanowire arrays by selective-area MOVPE. *Journal of Crystal Growth* 2007, vol. 298, pp. 644-647.
53. Y. Ding, J. Motohisa, B. Hua, S. Hara, and T. Fukui. Observation of microcavity modes and waveguides in InP nanowires fabricated by selective-area metalorganic vapor-phase epitaxy. *Nano Letters* 2007, vol. 7, no. 12, pp. 3598-3602.
54. Q. Gao, V. G. Dubrovskii, P. Caroff, J. Wong-Leung, L. Li, Y. Guo, L. Fu, H. H. Tan, and C. Jagadish. Simultaneous selective-area and vapor-liquid-solid growth of InP nanowire arrays. *Nano Letters* 2016, vol. 16, no. 7, pp. 4361-4367.
55. S. H. Jones, L. K. Seidel, K. M. Lau, and M. Harold. Patterned substrate epitaxy surface shapes. *Journal of Crystal Growth* 1991, vol. 108, no. 1, pp. 73-88.
56. O. Kayser. Selective growth of InP/GaInAs in LP-MOVPE and MOMBE/CBE. *Journal of Crystal Growth* 1991, vol. 107, no. 1, pp. 989-998.
57. M. A. Verheijen, R. E. Algra, M. T. Borgström, G. Immink, E. Sourty, W. J. van Enckevort, E. Vlieg, and E. P. Bakkers. Three-dimensional morphology of GaP− GaAs nanowires revealed by transmission electron microscopy tomography. *Nano Letters* 2007, vol. 7, no. 10, pp. 3051-3055.
58. C. E. Dreyer, A. Janotti, and C. G. Van de Walle. Absolute surface energies of polar and nonpolar planes of GaN. *Physical Review B* 2014, vol. 89, no. 8, p. 081305.
59. X. Yuan, P. Caroff, J. Wong-Leung, L. Fu, H. H. Tan, and C. Jagadish. Tunable Polarity in a III–V Nanowire by Droplet Wetting and Surface Energy Engineering. *Advanced Materials* 2015, vol. 27, no. 40, pp. 6096-6103.
60. M. Paladugu, J. Zou, Y.-N. Guo, X. Zhang, H. J. Joyce, Q. Gao, H. H. Tan, C. Jagadish, and Y. Kim. Polarity driven formation of InAs/GaAs hierarchical nanowire heterostructures. *Applied Physics Letters* 2008, vol. 93, no. 20, p. 201908.
61. S. Lehmann, J. Wallentin, E. K. Martensson, M. Ek, K. Deppert, K. A. Dick, and M. T. Borgstrom. Simultaneous growth of pure wurtzite and zinc blende nanowires. *Nano Letters* 2019, vol. 19, no. 4, pp. 2723-2730.
62. J. Zou, M. Paladugu, H. Wang, G. J. Auchterlonie, Y. N. Guo, Y. Kim, Q. Gao, H. J. Joyce, H. H. Tan, and C. Jagadish. Growth mechanism of truncated triangular III–V nanowires. *Small* 2007, vol. 3, no. 3, pp. 389-393.

63. Z. I. Alferov. The history and future of semiconductor heterostructures. *Semiconductors* 1998, vol. 32, no. 1, pp. 1-14.
64. R. Dingle, W. Wiegmann, and C. H. Henry. Quantum states of confined carriers in very thin AlxGa1-xAs-GaAs-AlxGa1-xAs heterostructures. *Physical Review Letters* 1974, vol. 33, no. 14, pp. 827-830.
65. N. Holonyak, R. Kolbas, R. Dupuis, and P. Dapkus. Quantum-well heterostructure lasers. *IEEE Journal of Quantum Electronics* 1980, vol. 16, no. 2, pp. 170-186.
66. J. Zhang, M. Zhang, R.-Q. Sun, and X. Wang. A facile band alignment of polymeric carbon nitride semiconductors to construct isotype heterojunctions. *Angewandte Chemie International Edition* 2012, vol. 51, no. 40, pp. 10145-10149.
67. K. A. Dick, S. Kodambaka, M. C. Reuter, K. Deppert, L. Samuelson, W. Seifert, L. R. Wallenberg, and F. M. Ross. The morphology of axial and branched nanowire heterostructures. *Nano Letters* 2007, vol. 7, no. 6, pp. 1817-1822.
68. L. J. Lauhon, M. S. Gudiksen, and C. M. Lieber. Semiconductor nanowire heterostructures. *Philosophical Transactions of the Royal Society A* 2004, vol. 362, no. 1819, pp. 1247-1260.
69. J. Johansson, and K. A. Dick. Recent advances in semiconductor nanowire heterostructures. *CrystEngComm* 2011, vol. 13, no. 24, pp. 7175-7184.
70. J. K. Hyun, S. Zhang, and L. J. Lauhon. Nanowire heterostructures. *Annual Review of Materials Research* 2013, vol. 43, pp. 451-479.
71. M. Mattila, T. Hakkarainen, M. Mulot, and H. Lipsanen. Crystal-structure-dependent photoluminescence from InP nanowires. *Nanotechnology* 2006, vol. 17, no. 6, p. 1580.
72. K. A. Dick, C. Thelander, L. Samuelson, and P. Caroff. Crystal phase engineering in single InAs nanowires. *Nano Letters* 2010, vol. 10, no. 9, pp. 3494-3499.
73. D. Spirkoska, J. Arbiol, A. Gustafsson, S. Conesa-Boj, F. Glas, I. Zardo, M. Heigoldt, M. Gass, A. L. Bleloch, and S. Estrade. Structural and optical properties of high quality zinc-blende/wurtzite GaAs nanowire heterostructures. *Physical Review B* 2009, vol. 80, no. 24, p. 245325.

CHAPTER 3

Experimental techniques

3.1. Introduction

In this chapter, the detailed procedures of sample preparation for selective area epitaxy and the principles of the key equipment used for sample preparation, epitaxial growth and characterisation are discussed. Many of these experimental techniques are complex and thus, to some extent, only the fundamentals relevant to this dissertation are discussed.

3.2. Substrate preparation for selective area epitaxy

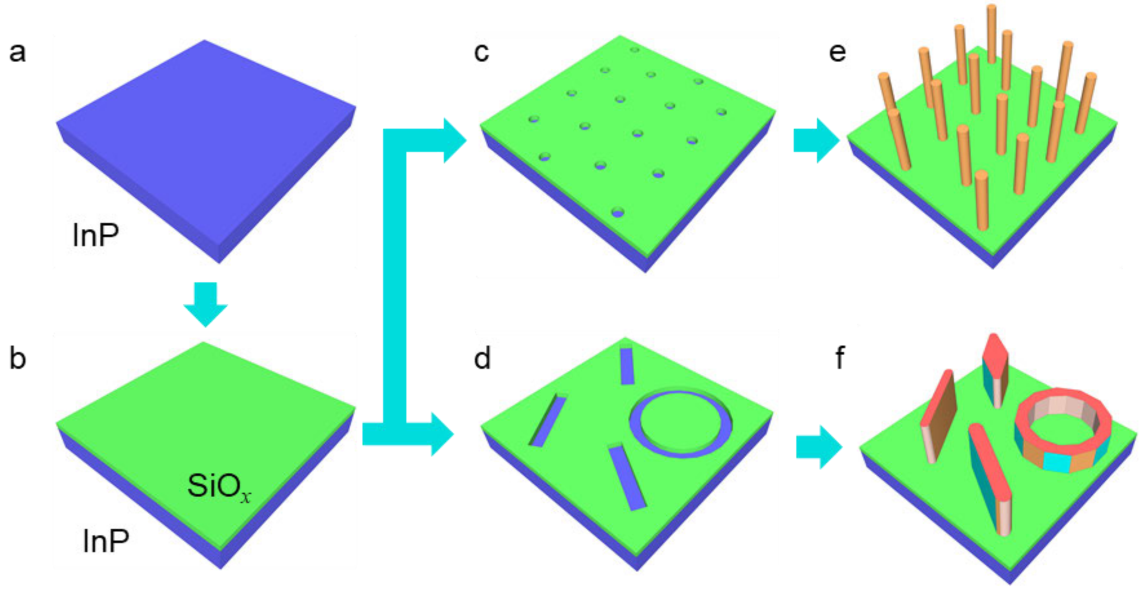

Figure 3.1: Schematic of patterning substrate for growing InP nanostructures using SAE technique. (a) InP substrate. (b) Deposition of 30 nm-thick SiO_x on InP substrate as a mask. (c,d) Fabricating SiO_x mask to create openings with various geometries, such as (c) conventional holes, (d) slots and rings. (e,f) InP nanostructures grown from the corresponding openings on the patterned InP substrates. Note that the morphology of grown InP nanostructures is dependent on substrate orientation which will be discussed in Chapter 5.

Figure 3.1 schematically shows the key processing steps for SAE growth of nanostructures. To grow nanostructures at selective areas and of desired geometries, first we need to prepare patterned substrates using a top-down etching technique. Below, the details of substrate preparation are discussed step by step.

Step 1: Substrate selection (Figure 3.1a)**.**

All substrates used in this dissertation are single-side polished epi-ready InP wafers with a diameter of 50.8 mm from AXT, Inc. Their surface orientation is vital to the growth of nanostructures (see Chapters 4 and 5). {111}A, {111}B, {100} and {110} oriented InP substrates are used. However, the growth dependence on the doping and conductivity type of substrates is not observed. Nevertheless, semi-insulating iron-doped substrates are preferred since they have lower photoluminescence and cathodoluminescence intensity and interfere less with the optical signals from the nanostructures.

Step 2: Deposition of SiO_x mask (Figure 3.1b)**.**

An approximate 30 nm-thick SiO_x layer is deposited on the selected InP substrates using an Oxford Plasmalab 100 Dual Frequency Plasma-Enhanced Chemical Vapour Deposition (PECVD) system featuring a load-lock. As a well-established technique, PECVD has been widely used to deposit various thin films (SiO_x, SiN_x, etc.) with high uniformity and rate (tens of nm per minute) at a relatively lower temperature compared with conventional CVD. Here, "*x*" is utilised in the chemical formula of silicon oxide and silicon nitride in consideration that these PECVD deposited thin films are rarely stoichiometric.[1] The chamber has two parallel electrodes (Figure 3.2). The upper electrode is connected with two plasma generators operated at 13.56 MHz and 50-450 kHz respectively, while the lower electrode is electrically grounded and worked as a sample holder. The ability to use mixed high and low frequencies allows control over the stress of film. During deposition, the lower electrode is heated to 300 °C to improve the density and quality of the film and the pressure is maintained at 650 mTorr. Source gases SiH_4 and N_2O and carrier gas N_2 are introduced into the chamber with the flow of 9, 710 and 161 sccm, respectively. The plasma of reactant gases is generated by capacitive coupling discharge between two electrodes under the radio frequency power of 20 watts. After a series of chemical reactions, the reaction product of SiO_x is deposited on InP substrate. Deposition time is less than 1 min to obtain a 30 nm-thick SiO_x film. A JA Woollam M-2000D ellipsometer is used to measure the thickness of deposited SiO_x on InP substrate.

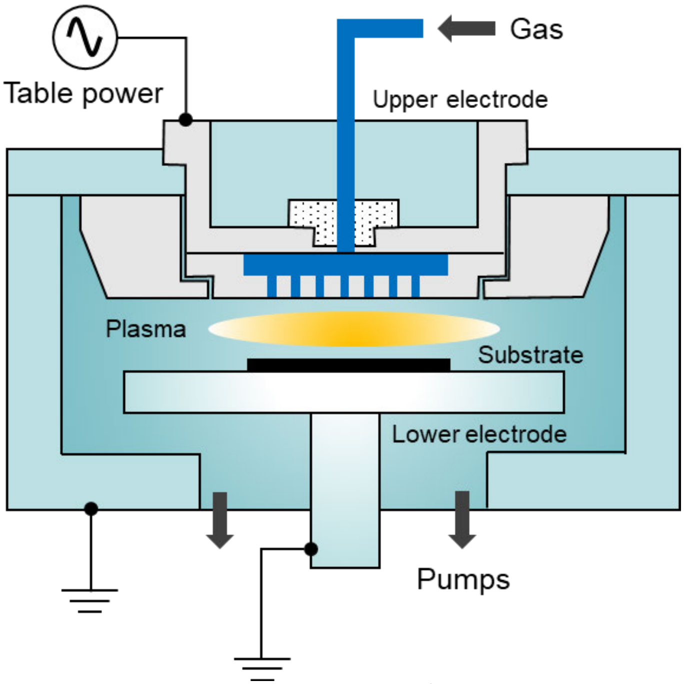

Figure 3.2: Schematic of a PECVD process chamber.[2]

Step 3: Spin-coating of electron beam resist.

Two thin layers of hexamethyldisilazane (HMDS) and diluted ZEP520A (volume ratio of ZEP520A and Anisole, 1:2) are spin-coated on the SiO_x/InP substrate in turn using a spin coater at 500 rpm for 5 seconds and 4000 rpm for 45 seconds. ZEP520A is a high-resolution positive electron beam resist (e-resist) and has a high resistance to dry etching. HMDS is used to improve the adhesion between SiO_x and e-resist. To minimise the contamination of substrate, we recommend carrying out this step as soon as possible after the deposition of SiO_x. The thickness of spin-coated polymer is approximately 80 nm, measured by the ellipsometer.

Step 4: Baking.

After spin-coating, the substrate is baked in an oven at 170 °C for 30 min.

Step 5: Electron beam lithography.

Electron beam lithography is a versatile technique that uses an electron beam (e-beam) to expose electron-sensitive resist and then create extremely fine patterns. It has been widely used in nanofabrication thanks to its high-resolution and flexibility in creating arbitrary patterns. EBL system derives from scanning electron microscopy in the middle of the last century.[3] It is a very complex instrument, but the basic components are far less, as schematically illustrated in Figure 3.3. Basically, in a high vacuum column, electrons are first generated by an electron gun (thermionic or field emission) and accelerated by an electrostatic field. Subsequently, these electrons are modulated by passing through electron-optics consisting of electromagnetic lenses and deflection coils etc., and finally focused on the e-resist covered substrate. The deflection coils are used to deflect e-beam for writing designed patterns without moving substrate. The area that e-beam can be reached by the deflection system is referred to as “write field”, which is different in different EBL systems. When a designed pattern is larger than write field, generally substrate needs to be moved, which could be realised by mounting substrate on a high-precision stage. Within a write field, there are different ways, such as raster scanning and vector scanning, for scanning of the e-beam across the e-resist surface. By turning on/off the e-beam based on the designed patterns during scanning, the e-resist is selectively exposed. For example, three different geometries are exposed in this thesis, as shown in Figure 3.3b.

The resolution of optical lithography is fundamentally limited by the diffraction limit to approximately half the wavelength of the light used.[4] For EBL, the diffraction limit is no longer an issue since high-energy electrons have much shorter wavelengths (0.012 nm at 10 keV). Therefore the EBL resolution is ultimately related to the spot size of focused e-beam and scattering of electrons in the resist and substrate.[5] In a dedicated EBL system, the spot size can be focused to as small as 1 nm.[6] As electrons penetrate the resist, they scatter forward with small angles (forward scattering), which broaden the beam diameter. Additionally, some of electrons scatter at large angles as they pass through the resist into substrate (backscattering), which leads to that the region receiving extra electrons from nearby ones during exposure (i.e., proximity effect).[7] Despite of these limitations, EBL has the ability to produce patterns at the nanoscale, with feature size of 10 nm or smaller. For example, Manfrinato *et al*. reported 2 nm isolated features and 5 nm half-pitch fabricated by a EBL system with an aberration corrected scanning transmission electron microscope.[8] In addition, the electron dose, defined as (dwell time × beam current)/area, is a key parameter for fabricating the desired pattern arrays. Dose values between 40 and 104 $\mu C/cm^2$ are used in this work.

In this thesis, a Raith150 EBL operated at 10 keV is used to write the required patterns on the e-resist film.

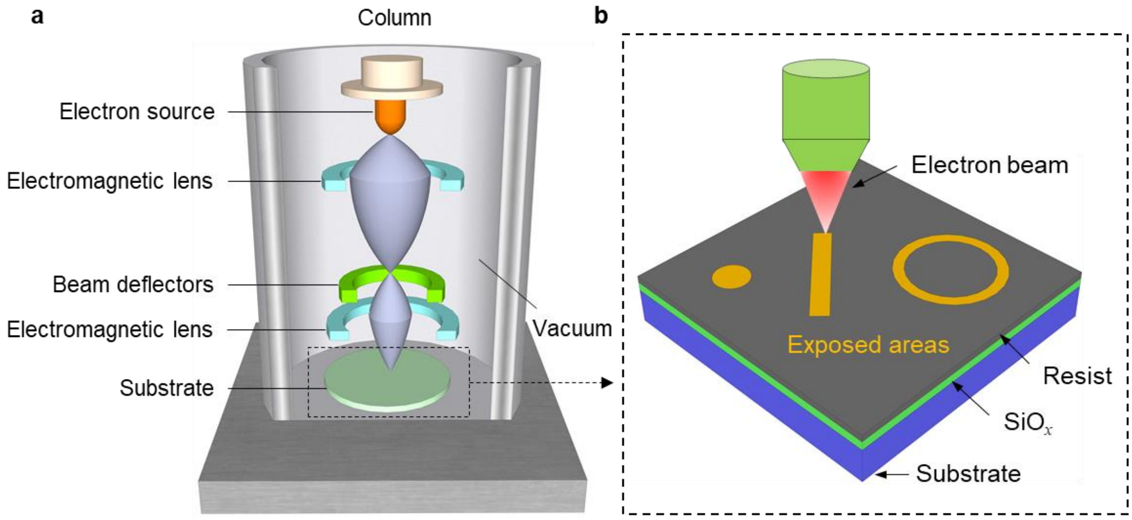

Figure 3.3: Schematic diagram of electron beam lithography.

Step 6: Development.

E-resist is chemically altered with irradiation by electrons. As a result, the exposed areas of positive resist or unexposed areas of negative resist can be dissolved in an appropriate chemical solution (developer). In our case, after EBL patterning, samples are dipped in the developer (n-Amyl acetate) for 30 s to remove the electron irradiated areas, in order to expose the underlying SiO$_x$, and then rinsed by IPA (isopropyl alcohol) for 30 s. Samples are dried using a N$_2$ gun. Finally, to ensure that e-resist is completely removed in the exposed areas, oxygen plasma cleaning is carried out using a PVA TePla barrel etcher. 300 sccm oxygen is introduced to the chamber while the system is operated at 600 Watts for a few seconds and then 100 Watts for approximately 2 min.

Step 7: Reactive ion etching

In this step, we use a dry etching method, reactive ion etching (RIE) to remove the underlying SiO$_x$ layer that is exposed after the removal of the e-resist. RIE is a plasma-based etching process and widely applied in micro- and nano-fabrication thanks to the higher accuracy and directional (or anisotropic) etching ability compared with solution-based wet etching. RIE system consists of a pair of parallel plates built in a vacuum chamber. The top plate (anode) is grounded while the bottom one (cathode), on which samples are mounted, is connected to the coupling capacitor and radio frequency (RF) source (generally at 13.56 MHz). By applying RF power, the gas between two plates is ionized under low pressure, generating a plasma consisting of electrons, ions, and energetic radicals. A high concentration of electrons soon accumulate on the capacitively coupled electrode (bottom plate) because of high mobility, forming a DC bias.

On one hand, the chemically reactive species in plasma react with the materials to be etched, such as SiO_x layer, and produce volatile reaction products. On the other hand, the positive ions being accelerated by the DC bias bombard the sample downward and etch materials by sputtering. The vertical etching rate is much higher than lateral etching rate due to the directional physical bombardment, which contributes to the anisotropic characteristic of the etched profiles, regardless of the crystal orientations of the substrate.

In this thesis, the SiO_x layer is etched using an Oxford Plasmalab 80Plus RIE system with the active gas CHF_3 at a flow of 25 sccm, pressure of 30 mTorr, RF power of 100 Watts. Under the above optimized conditions, the etching rate for the PECVD deposited SiO_x is approximately 15 nm/min.

Step 8: Remove e-resist

After RIE, the surface of remaining e-resist is damaged by high-energy ion bombardment. We first use oxygen plasma to clean the damaged layer, and then immerse the samples into the ZEP remover (dimethylacetamide) solution overnight. Samples are then dried by a N_2 gun and cleaned again using oxygen plasma. Both oxygen plasma treatments are carried out in a PVA TePla barrel etcher under the conditions given in step 6. Figure 3.1c,d shows the patterned substrates after removing e-resist where openings with various geometries are created in the SiO_x layer.

Step 9: Trim etching

Consider that InP substrates can be damaged during the deposition and etching of the SiO_x layer, the last step of sample preparation, i.e. trim etching, is performed to obtain a high quality InP surface suitable for epitaxial growth. 30% H_2O_2 solution is used to oxidize a superficial InP layer for 2 min which is then removed by a diluted H_3PO_4 solution (20 ml 85% H_3PO_4 solution and 130 ml deionized water) for 2 min.[9] These two steps are repeated ten times and samples are rinsed using deionized water in between. After trim etching, the patterned substrates are immediately loaded into the metalorganic chemical vapour deposition (MOCVD) reactor for the subsequent epitaxial growth.

3.3. Epitaxial growth

Two different Aixtron MOCVD reactors, i.e. the 200/4 horizontal flow reactor and close coupled showerhead (CCS) reactor, are used to grow In(As)P nanostructures investigated in this dissertation. MOCVD is also known as metalorganic vapour phase epitaxy (MOVPE), OMCVD and OMVPE, of which MO (metalorganic) represents the precursor molecules and CVD (chemical vapour deposition) indicates the growth mechanism.[10] MOCVD research can be traced back to the patent (September, 1954) filed by Scott *et al*. and rapidly developed in the early 1970s thanks to the significant contributions made by Manasevit and co-workers in the late 1960s.[10-12] More details of the MOCVD technique are available in the book written by Stringfellow.[10] In addition, MOCVD is capable of growing compound semiconductor materials with ultra-high purity and atomically abrupt interface over wafer scale and a high growth rate, which make it widely applied in the industry and academic research. Till now, this technique can produce almost all III-V and II-VI compound semiconductors covering binary, ternary and quaternary materials.

Some InP nanostructures in Chapter 4 and all in Chapter 5 were grown by a horizontal flow MOCVD system, as shown in Figure 3.4a,b. The rest of InP nanostructures in Chapter 4 and InP/InAsP nanostructures in Chapter 6 were grown by a CCS MOCVD system. The main purpose of using these two reactors is to demonstrate the growth of our InP nanostructures can be ported between different growth systems relatively easily. The major difference between these two systems is the reactor chamber where epitaxial growth takes place. Both reactor chambers have a silicon carbide coated graphite susceptor accommodating three two-inch substrates. While the reactant gases are introduced from one side with the laminar flow parallel to the substrates in the horizontal reactor (see Figure 3.4b), they are vertically injected into the CCS reactor through an array of small gas channels in the top ceiling like a bathroom showerhead (see Figure 3.4c).[13] Both susceptors are rotatable, which together with the elaborately designed reactors make the reactant gases evenly distribute over all substrate wafers. In addition, the susceptor temperature is controllably heated up and maintained by a three-zone infrared lamp and three-zone resistive heating coils in the horizontal and CCS reactors, respectively, to ensure that the temperature is evenly distributed across the susceptor. The uniform distributions of gaseous reactants and temperature are vital in achieving high uniformity and reproducibility for epitaxial growth.

The MOCVD system is extremely complex. In despite of the difference in reactors, the horizontal and CCS MOCVD systems are similar to each other in many aspects. Briefly, highly purified H_2, being filtered by a palladium-silver membrane, is used as the carrier gas. To grow III-V compound semiconductors, metalorganic (metal alkyl) precursors, such as trimethylindium ($In(CH_3)_3$, TMIn), trimethylgallium ($Ga(CH_3)_3$, TMGa) and trimethylaluminium ($Al(CH_3)_3$, TMAl), are used to provide group III elements of In, Ga and

Al, respectively. They are stored in sealed stainless steel cylinders and kept under controlled temperature and pressure. These precursors are transported to reactors by flowing H_2 which acts as a carrier gas. In contrast, group V elements are provided by hydrides, such as AsH_3 for As and PH_3 for P. They are stored in pressurized cylinders and transported to reactors in the lines different from metalorganics to avoid pre-reaction before reaching the reactors. The amounts of precursors being delivered to reactors can be precisely controlled by electronic mass flow controllers. As can be seen in Figure 3.4b, the pipelines for delivering metalorganics and hydrides consist of run and vent lines, through which precursors are transported to the reactor and exhaust, respectively. This design aims to stabilize the gases before entering the reactor and avoid fluctuation and turbulence. Note that the total flows for metalorganic lines and hydride lines are fixed at 5 and 10 standard litres per minute (slm), respectively, in the horizontal MOCVD system while that are maintained equally at 5 slm in the CCS MOCVD system.

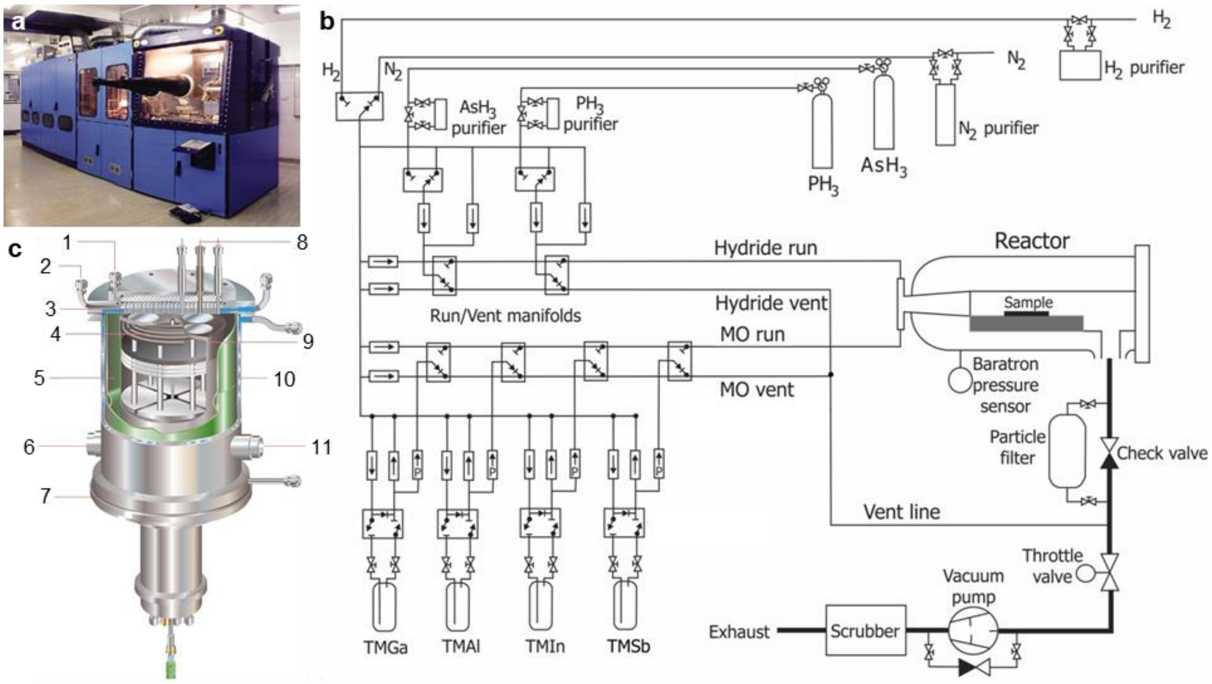

Labels in (c): 1- Precursors top plenum; 2- Precursors bottom plenum; 3- Water cooled injector surface; 4- Three zone heater; 5- Quartz liner; 6- Exhaust; 7- Sealing flange; 8- Optical probe; 9- SiC coated graphite susceptor; 10- Water cooled chamber; 11- Exhaust.

Figure 3.4: (a) Photo and (b) schematic illustration of the Aixtron 200/4 horizontal MOCVD system used in this work.[14] (c) Schematic diagram of a the CCS MOCVD reactor used in this work.[15]

Both reactors are operated at a low pressure (100 mbar). The relatively low pressure helps to eliminate parasitic nucleation in the gas phase and improve interface sharpness, etc.[16] After the metalorganics and hydrides reach the substrates placed on a heated susceptor, epitaxial growth occurs. Although the overall growth process is highly complicated, it can be simplified as the pyrolysis of precursors and the reactions of the pyrolysis products.[10] For example, $In(CH_3)_3 + PH_3 \rightarrow InP + 3CH_4$ describes the formation of InP. The exhaust including unreacted precursors, reaction by-products and carrier gas are passed through a scrubber filled with activated carbon to remove toxics before being disposed. The effect of growth parameters, such as growth temperature, amount of precursors, on the morphology and property of the material deposited will be discussed in later chapters.

3.4. Electron microscopy

In this section, several characterization techniques related to electron microscopy are employed to systematically analyse In(As)P nanostructures grown by SAE method in terms of morphology, structure, luminescence, and composition.

3.4.1. Interaction between electrons and matter

We see small things with the aid of an optical microscope by collecting light generated or reflected from them. In this process, photons with the wavelength in the visible ranges (approximately 400-700 nm) act as the media. However, the resolution, defined as the least distance between two objects that can be resolved, of the optical microscope is limited to about 200 nm because of diffraction limit. To see smaller things, such as the nanostructures discussed in this dissertation, a beam of electrons having the wave-like nature with extremely short wavelength can be used instead of visible light.

Electron microscopy is a powerful technique which uses an electron beam to illuminate a specimen and create its image at high resolution and magnification. More interestingly, one can obtain a wealth of information in addition to small features of the specimen by collecting and analysing the electron-excited signals. Figure 3.5 schematically illustrates the interaction of an incident electron beam with the specimen and lists some of produced signals, such as Auger electrons, secondary electrons (SEs), backscattered electrons (BSEs), cathodoluminescence (CL) and characteristic X-rays. Note that if the specimen is very thin, electrons may pass through the specimen without interruption or after experiencing a series of elastic and inelastic scattering. Those electrons are referred to as transmitted, elastic and inelastic electrons, respectively, as shown in Figure 3.5.

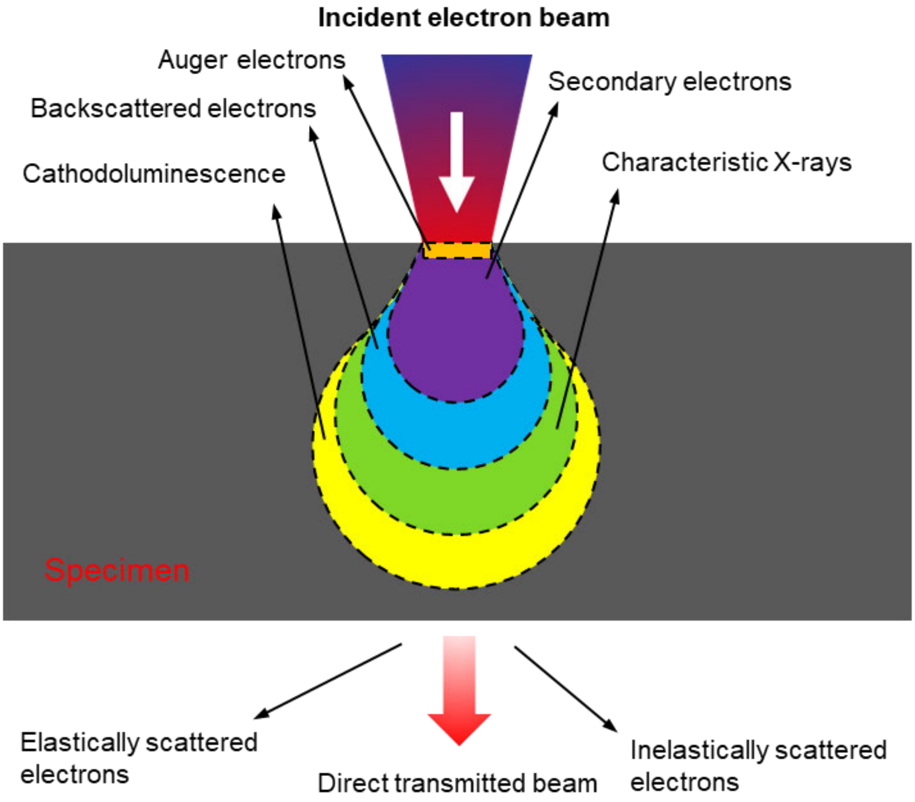

Figure 3.5: Schematic illustration of signals generated by the interaction of an electron beam and a specimen.

If an inner-shell electron of an atom is removed by the incident electron beam, a higher-energy electron fills up the vacancy while the released energy could eject an outer-shell electron, forming an Auger electron. Auger electrons originate from the specimen surface (within 1 nm) and carry compositional information. SEs are electrons ejected from the outer-shell of atoms because of the inelastic interaction between the primary incident electrons and the specimen. Since they are low-energy electrons (typically <50 eV), only those close to the specimen surface (depth within 5-50 nm) can escape without being re-absorbed in the specimen. The produced SEs are highly related to the topography of the specimen and therefore can be used for morphology characterization. Some of the incident electrons could be elastically scattered by the specimen atoms backward, which are knowns as BSEs. Compared with SEs, BSEs have generally higher energy and therefore deeper escape depth (see Figure 3.5). The possibility of electrons being elastically backscattered away from the specimen increases with the increase of atomic number, which leads to elements with higher atomic number appearing brighter. In addition to the compositional variation, BSEs can provide more information related to topography and crystallography. Instead of Auger electrons, characteristic X-rays can be produced when the outer-shell electrons of an atom jump to fill up the vacancy in the inner-shell as a result of inelastic scattering. The frequencies of these X-rays are determined by the energy difference between the two shells, which makes them characteristic to each element. Thus, characteristic X-rays can be used to analyse the chemical composition of the specimen. When the incident electrons interact with the specimen, electron-hole pairs can also be generated as a result of electron transition from the valence band to the conduction band. The radiative recombination may occur which leads to emission of photons with the wavelength varying from ultra-violet to infrared ranges. CL signals provide the optical and electronic information of the specimen. If the specimen is very thin (approximately <200 nm), some electrons pass through it and can be collected to obtain the information respect to the internal crystal structure of the specimen.

3.4.2. Scanning electron microscopy (SEM)

In this dissertation, an FEI Verios 460 SEM system is used for morphology characterization to acquire the information of the nanostructures, such as shape, dimension (length, height, thickness, etc.), surface quality, crystal facet, and uniformity. Additionally, an FEI Helios Nanolab FIB system with basic SEM functionality is occasionally utilized for the same purpose. In SEM, SEs are generated by scanning (rastering) a focused electron beam onto the sample which are then collected for imaging. Samples should have decent conductivity, otherwise, deposition of a thin conductive film (Au or C) is needed to decrease the impact of charging. Since the semiconductor samples involved in our work are reasonably conductive, such a coating is not required.

Figure 3.6 shows the simplified ray diagram of an SEM system for basic imaging functionality. In the vacuum column, electrons are generated from an electron source (field emission tip in our case) and accelerated with an accelerating voltage (typically 1-30 keV), forming a coherent electron beam. The electron beam is shaped and finally focused on the specimen surface like a probe after passing through a series of electromagnetic lenses and steerers, and apertures. The resolution of SEM images is limited by the electron beam diameter on the surface with smaller diameter improving the resolution.

The number of SEs produced is related to the topography of the specimen surface. In short, the number is the smallest when the incident electron beam is perpendicular to the surface while it increases with the increase of the angle between the incident electron beam and surface normal. The generated SEs are collected in synchrony with the raster scanning of a focused electron beam and further processed for producing a greyscale image on the viewing screen. The SEM images are essentially created based on the strength variation of secondary electron signals and reflect the topographical difference of the specimen.

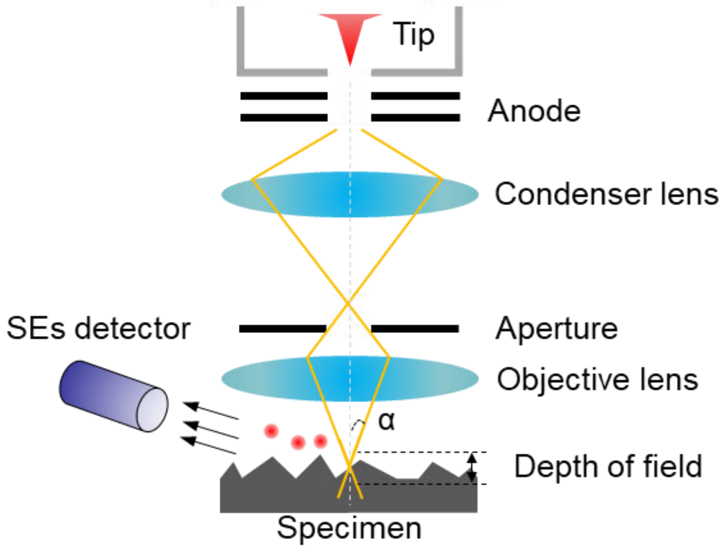

Figure 3.6: Schematic diagram of an SEM system for imaging purpose using SEs.

The depth of field, defined as the height of a specimen being imaged in focus, of an SEM system is more than 300 times than that of an optical microscope. This advantage makes the SEM better to image nanostructures. The use of smaller aperture can reduce the convergence angle (i.e. α, see Figure 3.6), and hence increases the depth of field. But, it also decreases the number of SEs. We have to make a trade-off between them. Besides, to acquire a high-quality SEM image, some parameters need to be optimized, such as accelerating voltage, beam current, and working distance (distance between the bottom column and specimen surface).

3.4.3. Cathodoluminescence

Cathodoluminescence (CL) is a non-destructive technique commonly used to investigate the optical and electronic properties of inorganic solids, such as semiconductors.[17] Compared to photoluminescence, CL has a higher spatial resolution (sub-50 nm) and can apply to semiconductor materials with a large bandgap (> 3 eV). The former makes it the dominant method for optical characterisation in this dissertation. CL measurement is predominantly carried out in an SEM environment equipped with various components such as a luminescence collection mirror, spectrometer and detectors. CL in Chapters 4 and 5 as well as the nanowire CL in Chapter 6 were obtained on an FEI Verios 460 SEM system equipped with a Gatan MonoCL4 Elite CL spectroscopic system at the Australia National University while the nanomembrane CL results in Chapter 6 were acquired on an FEI Quanta 200 ESEM with CL Spectroscopy and Moran Scientific CL Mapping System at the University of Technology Sydney.

The CL measurements carried out at The Australian National University only involve emission in the wavelength range of approximate 800-1000 nm, as schematically illustrated in Figure 3.7. A parabolic mirror made of aluminium is inserted into the SEM chamber to efficiently collect the emitted CL signals. A precise alignment is required to ensure that the specimen is placed at the focal point of the parabolic mirror and the collected light is collimated before entering the spectrometer or detector. This is done to maximise the collection efficiency. In operation, two different modes, panchromatic and parallel, were implemented to produce panchromatic and spectral images, respectively, depending on the selected light path. For panchromatic imaging, all photons effectively collected by the mirror are introduced to a Si photomultiplier tube (PMT) with detecting range from UV to approximately 1000 nm. The panchromatic image is an intensity map of emitted photons regardless of their wavelength over the scanning area, which can be used to analyse the crystal quality, emission intensity and uniformity of nanostructures (see the bottom light path in Figure 3.7). Alternatively, the light can be dispersed by a grating and then detected by a Si-based CCD in parallel (see the top light path in Figure 3.7), finally producing the spectral images. Each pixel in the spectral image contains both spatial and spectral information. After post-processing, a lot of information about the investigated nanostructures can be obtained, such as spectrum at any arbitrary position, emission intensity distribution within a specified wavelength range, and distribution of CL peak wavelength. Since the bandgap of wurtzite InP is approximately 80 meV higher than that of zinc-blende InP,[18] the distribution of CL peak wavelength, i.e. CL peak wavelength image, can be used to indicate the distribution of the crystal phase.

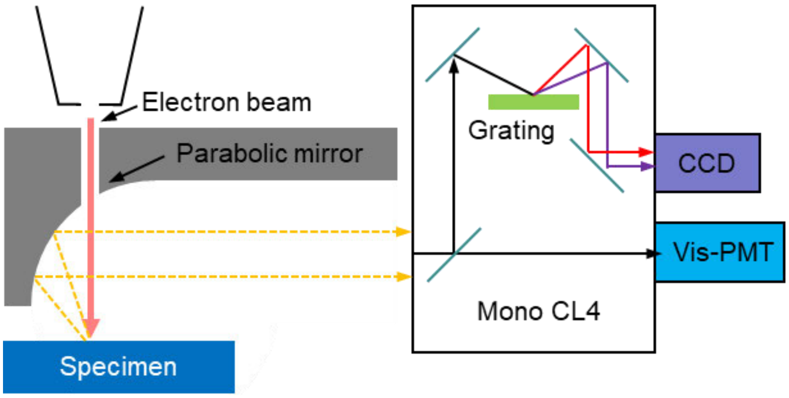

Figure 3.7: Schematic of the Gatan MonoCL4 Elite CL spectroscopic system equipped on the FEI Verios 460 SEM system. The set-up shows panchromatic and parallel operation modes.

In Chapter 6, CL emission of InP/InAsP quantum well nanomembranes in the wavelength ranges of approximate 800-1000 nm and 1100-1600 nm are separately characterised using an FEI Quanta 200 ESEM with CL system. This system has the similar configuration for light collection as shown in Figure 3.7. However, an optical fibre is utilised to guide the collected light into the QE6500+ spectrometer or the Oriel MS257 monochromator connected to the specified detectors. CL spectral images are finally created within the two different wavelength ranges. More details of the set-ups in this system can be found in the doctoral thesis of Dr. Mark Lockrey.[19] Note that all CL results in this thesis were acquired at the room temperature.

3.4.4. Transmission electron microscopy

Transmission electron microscopy (TEM) is a powerful technique for microanalysis in the field of materials science. While a beam of high energy electrons (hundreds of kV) is shaped and directed to illuminate the specimen, electrons exiting from the back side are used to acquire various internal information about the specimen, such as crystal structure and defects. In addition to the high accelerating voltage, there is a great demand on the specimen thickness (typically <200 nm) to ensure that the sufficient electrons are passed through the specimen, as illustrated in Figure 3.5.

In this dissertation, only a few nanowires and nanomembranes are thin enough for the direct TEM examination after being mechanically transferred to a holey carbon coated copper grid. Preparation of thin TEM lamellae is required for the majority of nanostructures. All TEM lamellae are prepared by milling the nanostructures along specific orientations using a focused ion beam (FIB). This is carried out by an FEI Helios 600 Nanolab Dual-beam FIB/SEM system.

Firstly, Pt is mildly deposited using an electron beam (2-3 kV and 2.7 nA) to cover the nanostructures and fill up the gaps in between to protect them from ion milling damage. Moreover, the electron beam can be used to monitor the whole processing by SEs imaging. Subsequently, the redundant parts on both sides of the area of interest (AOI) are alternately removed by a focused Ga ion beam. A strong FIB (30 kV and 6.5 nA) is used at the beginning to roughly mill materials around the AOI with a high rate. As the milling proceeds, both accelerating voltage and beam current of the FIB are gradually dropped to reduce the damage of the AOI. The final TEM lamellae in this dissertation generally have the thickness less than 100 nm which is suitable for the atomically-resolved imaging. These lamellae are attached to holey carbon coated copper grids or FIB lift-out grids for TEM examination.

In a TEM system, a beam of high energy electrons is shaped by the condenser lens system before illuminating the specimen. Figure 3.8 shows the simplified ray diagrams of the basic diffraction and image modes when the incident electrons are parallel (i.e. parallel beam illumination). As described in Figure 3.5, electrons can penetrate the specimen in different ways, forming the directly transmitted beam parallel with the incident electron beam and the elastically/inelastically scattered beams. All these electrons carrying the specimen information pass through the objective lens and then form an image or diffraction pattern at the intermediate image plane and back focal plane, respectively (see Figure 3.8). The image and diffraction pattern can be alternatively projected on the fluorescent screen or CCD camera through the intermediate lens with an adjustable strength and projector lens. A selective area aperture (SAD) is available at the intermediate image plane to select the area of the specimen from where the diffraction pattern is formed. The objective aperture is used to choose the electron beam for imaging.

Diffraction pattern is caused by Bragg scattering when electrons are passed through the crystalline specimen. It is related to the crystal structure and incident angle of the electron beam with respect to the crystal planes. In this dissertation, the diffraction pattern is frequently used to align TEM lamellae and determine the ZB and WZ crystal phases. Furthermore, diffraction pattern can be used to investigate defects, strain, and composition. Based on the different types of electrons selected by the objective aperture at the back focal plane for imaging, i.e. directly transmitted (unscattered) electrons or scattered electrons, either a bright field or dark field image can be formed. The background in the bright and dark field images is bright and dark, respectively. Bright field images provide better contrast since the areas in the crystal specimen which are thicker or have higher mass density appear darker compared to the other areas. On the other hand, the dark field images show the crystal defects more clearly.

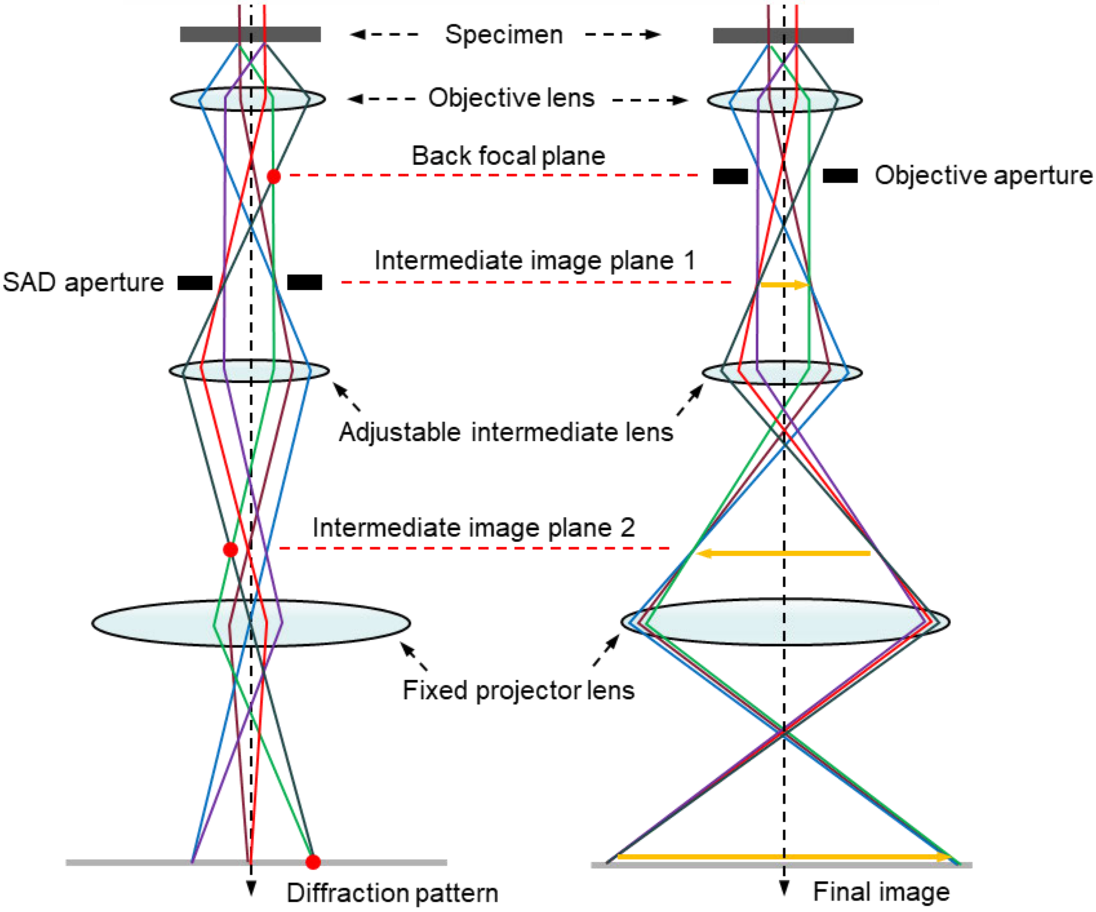

Figure 3.8: Ray diagrams of diffraction mode (left panel) and imaging mode (right panel) in a TEM system.[20]

High resolution TEM (HRTEM) imaging is a powerful mode in the modern TEM system which uses the interference between the transmitted and scattered electron beams to form phase contrast images referred to as HRTEM images. HRTEM images are acquired at an extremely high magnification with the incident electron beam along the low-index orientations (<1$\bar{1}$0> or <11$\bar{2}$0> zone axis in our case). These images have the ability to provide information at the atomic scale.

TEM can also be operated when the incident electron beam is focused to a fine spot and scanned onto the specimen in a raster way, which is known as scanning TEM (STEM). In the STEM operation mode, there are two types of detectors which are typically used for imaging, i.e. bright field detectors and annular dark field detectors. The former collects directly transmitted electrons over a disc-like area while the latter collects the scattered electrons with high scattering angles over an annular area. The images are referred to as bright field and high angle annular dark field (HAADF) images, respectively. The scattering of electrons as they pass through the specimen is strongly affected by the atomic number, which makes HAADF imaging capable of distinguishing different atoms which are displayed in the images with the different intensities. In addition to the imaging of STEM, energy dispersive X-ray (EDX) spectroscopy can be performed by detecting the characteristic X-rays for compositional analysis, which will be discussed in Section 3.4.5.

A JEOL JEM-ARM200F aberration-corrected STEM at the University of Wollongong and a JEOL 2100F TEM at the Australian National University are used for structural characterisation in this dissertation. Both systems were operated at 200 kV. At 200 kV, they feature extremely high resolutions of <0.08 nm and 0.23 nm, respectively. Moreover, the EDX analysis of InP/InAsP nanomembranes discussed in Chapter 6 is carried out by the aberration-corrected STEM system.

3.4.5. Energy dispersive X-ray spectroscopy

In this dissertation, an energy dispersive X-ray spectroscopy, referred to as EDX, EDS, or XEDS, equipped in a JEOL JEM-ARM200F aberration-corrected STEM system at the University of Wollongong is used to analyse the chemical composition of InAsP quantum structures in Chapter 6. Although EDX can also be carried out in an SEM system, the spatial resolution in a TEM system is higher because of the high accelerating voltage and thin specimen, which makes it better for analysing quantum structures at the nanometre scale.

As mentioned in Section 3.4.1, X-rays are the by-products of the interaction between an incident electron beam and atoms in the specimen. More specifically, it is the interaction of an incident electron with an inner-shell electron of an atom in the specimen resulting in its removal and leaving a vacancy in the inner-shell. The ionised atom is unstable and thus, an electron from the outer-shell transfers to fill the vacancy while a X-ray photon is generated with the energy the same as the energy difference between the inner- and outer-shells.[21] The process of X-ray emission is schematically shown in Figure 3.9. The underlying mechanism for identifying elements using the emitted X-ray signals is that the energy difference between two shells of each element is unique. Note that EDX technique is applicable to elements with atomic number >3 (>11 for quantitative analysis) and capable of detecting the minor elements as low as approximately 0.01-0.1 weight percentages in the TEM environment.[21] The Siegbahn notation is generally used to name a specific Characteristic X-ray, for example "In Kα" where the element (In), inner-shell (K) from where an electron is ejected by an incident electron, and relative outer-shell from where an electron fills the vacancy in the inner-shell, respectively. α represents that the electron used to fill the vacancy is from the closest outer-shell, followed by β from the second closest outer-shell. In addition to characteristic X-ray, Bremsstrahlung X-rays, also known as continuum or background X-rays, can be generated with the deceleration of incident electrons because of inelastic scattering with atoms in the specimen (see Figure 3.9).

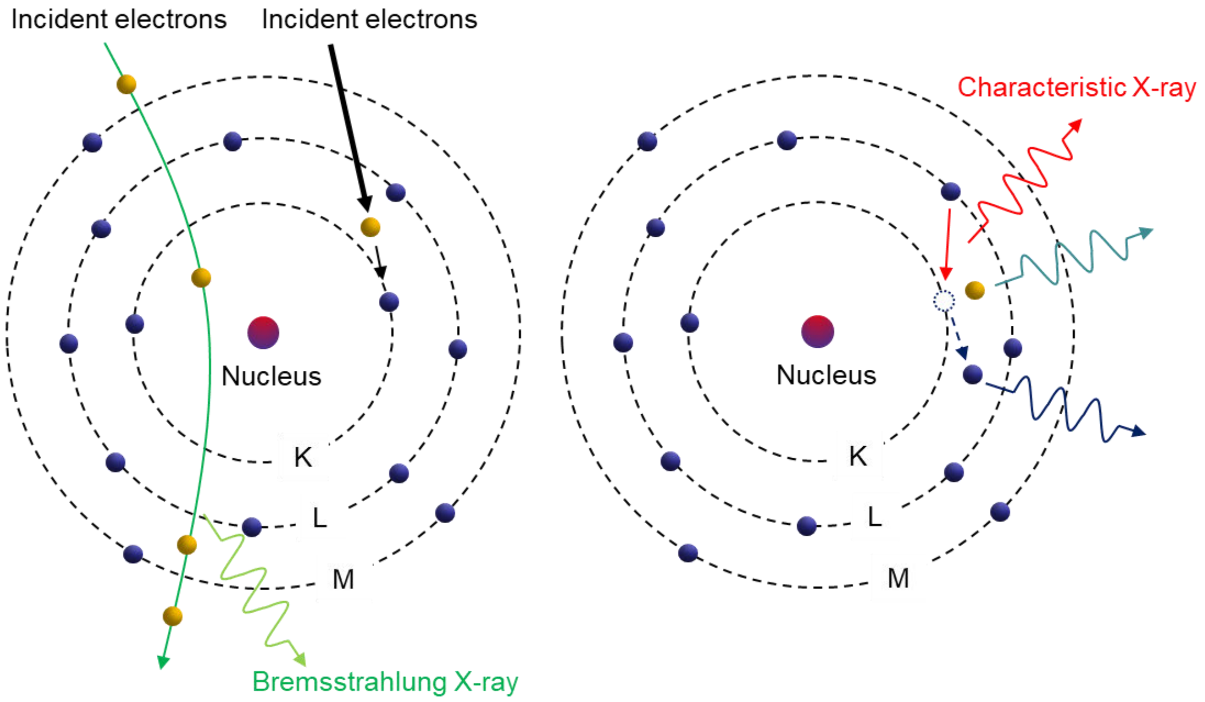

Figure 3.9: Schematic diagram of X-rays emission as a result of interaction with incident energetic electrons.

In operation, EDX analysis is carried out in STEM mode with a focused electron beam illuminating the specimen. The generated X-ray photons are detected by a JEOL Centurio SDD detector and then further processed before displaying as a spectrum of count (intensity) versus energy of the characteristic X-rays. Point-scan, line-scan and mapping are three common ways to analyse the elemental distributions at the point, line and area of interest, respectively. EDX technique is capable of both qualitative and quantitative analysis of chemical composition. The quantitative analysis of InAsP quantum structures can be realised by comparing the relative intensity of P element with the binary InP reference.

3.5. Time-resolved photoluminescence spectroscopy

Photoluminescence (PL) is the emission of light from materials as a result of the illumination with photons. The main difference between PL and CL is that the radiation source of PL is photons rather than electrons in CL. In semiconducting materials illuminated by photons with the energy higher than their band gaps, electrons in the valence band can be excited to the conduction band, generating electron-hole pairs. PL arises from the radiative recombination of these carriers. PL emission carries a wealth of information about the materials being investigated, such as band gaps, crystal phases, electronic states, crystal qualities, and impurities.[22-24] PL spectroscopy is an efficient and non-destructive technique used to investigate the electronic structures and optical properties of the target materials.

PL spectroscopy has various variants and therefore different functionalities thanks to the flexibility in changing configurations. Figure 3.10 schematically illustrates the time-resolved PL spectroscopy (TRPL) at the Australian National University that is used for investigating the optical properties and crystal qualities of InP nanostructures in this dissertation by measuring the decay of the PL signal at a certain wavelength and extracting carrier lifetimes. The TRPL system is constructed based on a Nikon Eclipse L150 optical microscope where two 100× Nikon objective lenses with the numerical apertures of 0.9 and 0.7 are used to focus the laser beam to a small spot, which enables the measurement of individual nanostructures on the sub-micrometre scale. Thus, this system also acts a micro-PL.

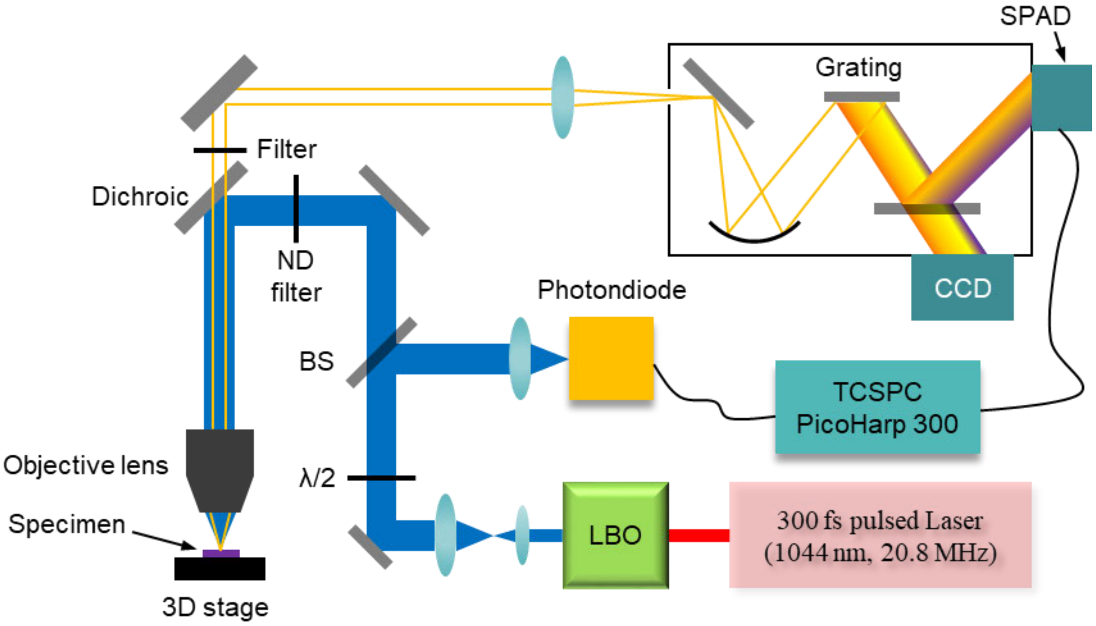

Figure 3.10: Schematic diagram of the TRPL system used in this dissertation.

As shown in Figure 3.10, 300 fs laser pulses are generated from a diode pumped solid-state laser (femtoTRAIN IC-Yb-2000, 1044nm, 20.8 MHz) and frequency doubled to 522 nm by a LBO frequency doubling crystal. Subsequently, the 522 nm pulsed laser beam is split into two by a beam splitter. The first beam is modulated and passed through the objective lens, forming a focused beam spot to excite the individual nanostructures. The PL emission from the specimen is collected by the same objective lens and directed into a spectrometer (Acton, SpectraPro 2750). After being spectrally dispersed, the PL signal can be detected by a CCD camera (Princeton Instruments, PIXIS) and form the PL spectrum as a plot of wavelength versus intensity. To acquire carrier lifetimes, we first used the time-correlated single photon counting (TCSPC) technique to measure the PL decay. The second split beam is directed into a photodiode which generates the signal for starting photon counting. In the spectrometer, the PL emission at a selected wavelength is directed into a single photon avalanche diode (SPAD) and generates a signal for stopping the photon counting. Both “start” and “stop” signals are generated within the same cycle of the pulsed laser (approximate 48 ns in our case). The time interval between the excitation and photon generation in a pulsed cycle is recorded by the TCSPC system (PicoHarp 300). After many cycles, a histogram of the emitted photon counts versus time interval is obtained, showing the PL decay. Carrier lifetimes can be extracted from the PL decay curves and serves as an important indicator of the crystal quality of InP nanostructures.

The TRPL system is capable of measuring the specimen at low temperatures (down to approximately 10 K), which is achieved by placing the specimen in a continuous flow He cryostat. A 100× objective lens with a numerical aperture of 0.7 is utilised in this case since it has a long working distance.

3.6. Summary

In this chapter, the basic operations and principles of experimental techniques related to this thesis are described. In Section 3.2, the detailed procedures of preparing patterned substrates for SAE and the equipment used, such as PECVD, EBL RIE, are discussed. In Section 3.3, the two MOCVD systems used for growing nanostructures presented in this dissertation are outlined, while in Sections 0 and 3.5, various characterisation techniques including SEM, CL, TEM, EDX, and TRPL are discussed which are used for morphological, structural, compositional and optical analysis of the nanostructures.

References

1. F. Karouta, K. Vora, J. Tian, and C. Jagadish. Structural, compositional and optical properties of PECVD silicon nitride layers. *Journal of Physics D: Applied Physics* 2012, vol. 45, no. 44, p. 445301.
2. G. Zhang, M. Takiguchi, K. Tateno, T. Tawara, M. Notomi, and H. Gotoh. Telecom-band lasing in single InP/InAs heterostructure nanowires at room temperature. *Science Advances* 2019, vol. 5, no. 2, p. eaat8896.
3. K. C. A. Smith, and C. W. Oatley. The scanning electron microscope and its fields of application. *British Journal of Applied Physics* 1955, vol. 6, no. 11, pp. 391-399.
4. E. Abbe. Beiträge zur Theorie des Mikroskops und der mikroskopischen Wahrnehmung. *Archiv für Mikroskopische Anatomie* 1873, vol. 9, no. 1, pp. 413-468.
5. Y. Xia, J. A. Rogers, K. E. Paul, and G. M. Whitesides. Unconventional methods for fabricating and patterning nanostructures. *Chemical Reviews* 1999, vol. 99, no. 7, pp. 1823-1848.
6. C. Vieu, F. Carcenac, A. Pepin, Y. Chen, M. Mejias, A. Lebib, L. Manin-Ferlazzo, L. Couraud, and H. Launois. Electron beam lithography: resolution limits and applications. *Applied Surface Science* 2000, vol. 164, no. 1, pp. 111-117.
7. T. Chang. Proximity effect in electron-beam lithography. *Journal of Vacuum Science Technology* 1975, vol. 12, no. 6, pp. 1271-1275.

8. V. R. Manfrinato, L. Zhang, D. Su, H. Duan, R. G. Hobbs, E. A. Stach, and K. K. Berggren. Resolution limits of electron-beam lithography toward the atomic scale. *Nano Letters* 2013, vol. 13, no. 4, pp. 1555-1558.

9. A. Mouton, C. S. Sundararaman, H. Lafontaine, S. Poulin, and J. F. Currie. Etching of InP by H3PO4, H2O2 Solutions. *Japanese Journal of Applied Physics* 1990, vol. 29, no. 10, pp. 1912-1913.

10. G. B. Stringfellow. *Organometallic vapor-phase epitaxy: theory and practice*. 2nd ed., Academic Press: San Diego, 1999.

11. H. M. Manasevit, and W. I. Simpson. The use of metal-organics in the preparation of semiconductor materials: I. Epitaxial gallium-V compounds. *Journal of the Electrochemical Society* 1969, vol. 116, no. 12, p. 1725.

12. H. M. Manasevit. Single-crystal gallium arsenide on insulating substrates. *Applied Physics Letters* 1968, vol. 12, no. 4, pp. 156-159.

13. J. Zhang, M. Zhang, R.-Q. Sun, and X. Wang. A facile band alignment of polymeric carbon nitride semiconductors to construct isotype heterojunctions. *Angewandte Chemie International Edition* 2012, vol. 51, no. 40, pp. 10145-10149.

14. H. J. Joyce. Growth and characterisation of III-V semiconductor nanowires for optoelectronic device applications. Ph.D. thesis, Australian National University, 2009.

15. https://www.britannica.com/science/polarity-chemistry.

16. M. Razeghi. *The MOCVD challenge: a survey of GaInAsP-InP and GaInAsP-GaAs for photonic and electronic device applications*. 2nd ed., CRC Press: Boca Raton, 2010.

17. B. G. Yacobi, and D. B. Holt. *Cathodoluminescence microscopy of inorganic solids*. Plenum Press: New York, 1990.

18. A. Mishra, L. Titova, T. Hoang, H. Jackson, L. Smith, J. Yarrison-Rice, Y. Kim, H. Joyce, Q. Gao, and H. Tan. Polarization and temperature dependence of photoluminescence from zincblende and wurtzite InP nanowires. *Applied Physics Letters* 2007, vol. 91, no. 26, p. 263104.

19. M. N. Lockrey. Investigation into the effects of electron-beam irradiation on III-nitride based LED devices. Ph.D. thesis, University of Technology Sydney, 2015.

20. D. B. Williams, and C. B. Carter. *Transmission electron microscopy*. 2nd ed., Springer US: New York, 2009.

21. J. K. Hyun, S. Zhang, and L. J. Lauhon. Nanowire heterostructures. *Annual Review of Materials Research* 2013, vol. 43, pp. 451-479.

22. F. Wang, Q. Gao, K. Peng, Z. Li, Z. Li, Y. Guo, L. Fu, L. M. Smith, H. H. Tan, and C. Jagadish. Spatially resolved doping concentration and nonradiative lifetime profiles in single Si-doped InP nanowires using photoluminescence mapping. *Nano Letters* 2015, vol. 15, no. 5, pp. 3017-3023.

23. G. D. Gilliland. Photoluminescence spectroscopy of crystalline semiconductors. *Materials Science and Engineering: R: Reports* 1997, vol. 18, no. 3, pp. 99-399.

24. M. Mattila, T. Hakkarainen, M. Mulot, and H. Lipsanen. Crystal-structure-dependent photoluminescence from InP nanowires. *Nanotechnology* 2006, vol. 17, no. 6, pp. 1580-1583.

CHAPTER 4

Shape engineering of InP nanostructures grown by selective area epitaxy on {111}A InP substrates

4.1. Introduction

The extensive research of group III-V semiconductors at the nanometer scale in the last two decades has revolutionized nanoelectronics and nanophotonics.[1, 2] Recently, greater demand for III-V nanostructures with more sophisticated geometries other than one-dimensional nanowires is expected, as discussed in Chapter 1. Unfortunately, systematic investigation of manipulating the desired shapes and understanding the transformation mechanism of nanostructures is still missing. In this chapter, we thoroughly investigate SAE of higher order of InP nanostructures (two- and three-dimensional shapes) on {111}A InP substrates which are commonly used for growing vertical nanowires. The growth parameters (*i.e.*, V/III ratio and temperature) are optimized by analyzing their effects on morphological and optical properties of InP nanostructures. After optimization, we achieve highly uniform arrays of WZ InP nanostructures with membrane-, prism- and ring-like geometries. The morphological changes of nanostructures with V/III ratio, growth temperature, pattern dimension, and growth time are discussed in details. Based on these experimental results, we explore the shape transformation mechanism of these nanostructures with the help of a thermodynamic model. This also provides underlying theoretical concepts for designing and achieving nanostructures of other shapes. All InP nanostructures grown under optimal conditions show perfect WZ crystal structure regardless of their geometries. Moreover, CL results show strong and highly homogeneous emission from both ensemble and single elements of these nanostructures, indicating their excellent optical properties. This chapter shows the possibilities of obtaining other functional nanostructures using a bottom-up pathway to produce shape-engineered devices.

4.2. Experimental methods

All InP nanostructures discussed in this chapter were grown on {111}A InP substrates by the SAE technique. Prior to growth, the substrates with a 30 nm-thick SiO_x mask were patterned using the procedure detailed in Chapter 3.2. As for openings, various geometries were designed, with a focus on nanoslots and nanorings to grow membrane- and ring-like nanostructures, respectively. We designed directions of nanoslots along $<10\bar{1}>$, $<11\bar{2}>$, and θ off (*i.e.,* the angle between nanoslot direction and $<10\bar{1}>$ is θ) orientations. Moreover, a large range of nanoslot lengths and nanoring diameters were considered to investigate the shape evolution of InP nanostructures and understand their formation mechanism. After trim etching, the patterned substrates were immediately loaded into the MOCVD reactor for epitaxial growth.

In this chapter, two different MOCVD reactors, a CCS reactor (Aixtron 3×2'') and a horizontal flow reactor (Aixtron 200/4), were utilized. The CCS reactor was used to optimize the growth conditions in terms of temperature and V/III ratio. Then, we used the horizontal reactor to test epitaxial reproducibility and carry out the time-dependent growth. The same nanostructures could be grown in the different types of reactors, suggesting the high reproducibility of our work. Both CCS and horizontal reactors operated at a low pressure of 100 mbar and used ultrahigh purity H_2 as a carrier gas with a total flow of 10 l/min and 15 l/min, respectively. Trimethylindium (TMIn) and phosphine (PH_3) were used as precursors for In and P elements, respectively. All substrates were first annealed in PH_3 ambient at the susceptor surface temperature (SST) of 658 °C in the CCS reactor or at the temperature of 750 °C in the horizontal reactor. Note that the SST in the CCS rector is measured by the *in situ* EpiTT while the temperature in the horizontal reactor was measured *via* a thermocouple imbedded in the susceptor. After 10 min annealing, epitaxial growth was carried out once the reactors reached the target conditions. Specifically, the molar fractions of PH_3 for CCS and horizontal reactors were $1.90\text{-}2.80\times10^{-3}$ and 2.67×10^{-3} while those of TMIn were set to be 9.41×10^{-6} and 9.07×10^{-6}, respectively. The SST of CCS reactor was changed from 593 to 680 °C while the temperature of the horizontal reactor varied from 650 to 750 °C. The growth time of InP nanostructures grown by CCS reactor was fixed at 3 min. Furthermore, two different growth times, 7 and 14 min, were implemented in the horizontal reactor.

The morphology of InP nanostructures was characterized using an FEI Verios 460 SEM. A Gatan MonoCL4 Elite CL spectroscopic system equipped in the SEM and a time-resolved photoluminescence (TRPL) system were used to investigate their optical properties. For structural characterization, an FEI Helios Nanolab FIB system was used to prepare the lamellae by cutting the nanostructures along the specific crystallographic orientations. The lamellae were examined by a JEOL JEM-ARM200f aberration-corrected scanning transmission electron microscope (Cs-STEM).

4.3. Optimization of growth parameters

4.3.1. V/III ratio

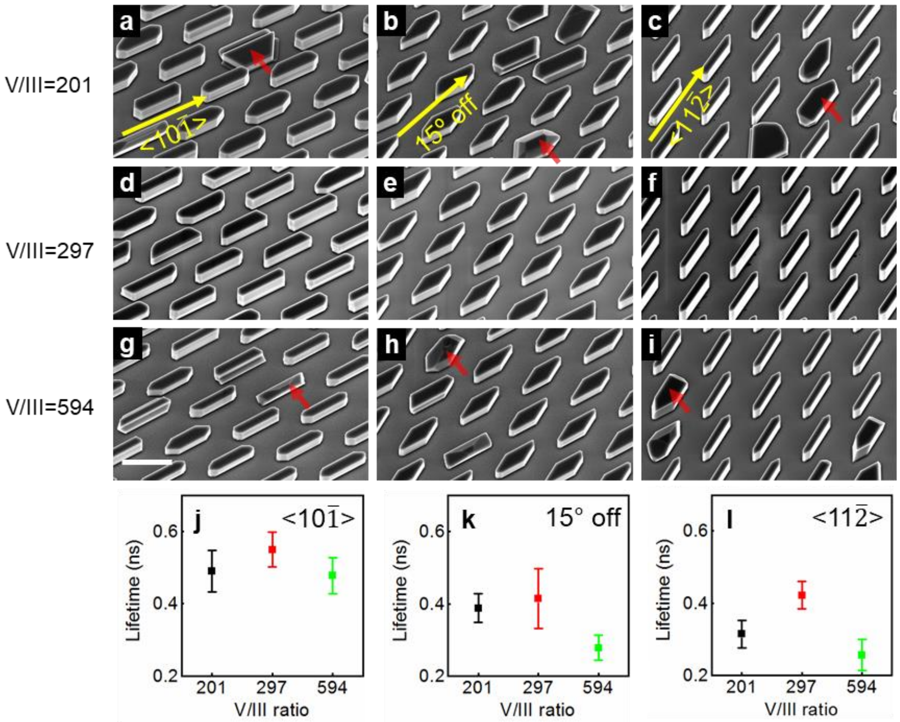

Figure 4.1: (a-i) SEM images and (j-l) room temperature minority carrier lifetimes of InP nanostructures grown at the fixed temperature of 636 °C but different V/III ratios using the CCS reactor. The V/III ratios are (a-c) 201, (d-f) 297 and (g-j) 594, respectively. The directions of nanoslots in left, middle and right columns are <10$\bar{1}$>, 15° off and <11$\bar{2}$>, respectively. The scale bar in (g) is 2 µm and applies to all SEM images. Carrier lifetimes are extracted from TRPL measurements and averaged over 45 nanostructures.

To optimize the growth conditions in the CCS reactor, we first investigated V/III ratio under the fixed growth temperature of 636 °C. The molar fraction of TMIn was fixed (9.41×10^{-6}), and hence, by changing molar fraction of PH_3 ($1.90\text{-}2.80\times10^{-3}$) V/III ratio was increased from 201 to 594. Figure 4.1a-i shows SEM images of InP nanostructures grown under those parameters. It is clear that the arrays grown at V/III ratio of 297 have less irregular shapes and therefore much better uniformity as compared to their counterparts formed with V/III ratios of 201 and

594, regardless of the nanoslot directions (the irregular shapes are representatively marked by the red arrows).

Furthermore, we extracted minority carrier lifetimes (τ_{mc}) of the InP nanostructures, defined as $1/\tau_{mc} = 1/\tau_{nr} + 1/\tau_r$, by fitting the measured room temperature TRPL spectra (see Figure 4.1j-l). Here τ_{nr} and τ_r are nonradiative and radiative carrier lifetimes, respectively. The room temperature τ_{mc} is limited by τ_{nr} at low excitation power densities[3] and strongly affected by defect density and surface quality. As shown in Figure 4.1j-l, the relatively longer τ_{mc} of InP nanostructures grown at V/III of 297 indicates that they may have less bulk defects and better surface quality (lower surface recombination velocity).[4] Overall, based on the morphologies and optical properties of InP nanostructures, the V/III ratio of 297 is better than 201 and 594 at the growth temperature of 636 °C. Note that although only three different V/III ratios are investigated, a clear trend is observed.

4.3.2. Growth temperature

Based on the findings in the previous section, we further optimized growth temperature which is also a key parameter for epitaxy. While V/III ratio is fixed at 297, we changed the growth temperatures from 593 to 680 °C. Figure 4.2 and Figure 4.3 show SEM images at different views of the InP nanostructures. As shown in Figure 4.2 with a low magnification, their morphologies become more regular and uniform on a larger scale with the increase of growth temperature. Besides, high-resolution SEM images taken at high magnifications illustrate that the side facets of nanostructures grown at higher temperatures are much smoother than that grown at lower temperatures probably due to the reduction of defect density (Figure 4.3). We also observe the trenches on the top facets at low temperatures which are marked by the red arrows, however they disappear as the growth temperature increases (Figure 4.3j-o). Since surface diffusion of indium adatoms from side facets plays a key role in the axial growth, the occurrence of the trenches can be attributed to inefficient diffusion of indium towards the centre of the top facet because of low temperatures. Here, a model is proposed to understand the formation of these trenches as follow.

Axial growth of nanostructures is contributed by two kinetic pathways of indium influx: direct impingement onto top facets and surface diffusion from side facets. Indium adatoms diffusing from the side facets arrive at the edges of the top facet and then migrate to the centre area, leading to higher indium concentration near the edges. Thus, the axial growth rate near the edges is higher than that at centre area. Depending on the diffusion length of indium adatoms, the difference in growth rates could lead to the uneven profile of the top facets. The stationary adatom concentration n_f of indium on the top facets satisfy the diffusion equation[5]

$$D_f \frac{d^2 n_f}{dx^2} + J - \frac{n_f}{\tau_f} = 0 \tag{4-1}$$

where D_f is the diffusion coefficient of indium adatoms on the top facets, J is the impinging flux, τ_f is the effective lifetime of adatoms before desorption, and x is the in-plane coordinate along the lateral direction perpendicular to the nanoslots. The general solution for n_f is expressed as

$$n_f(x) = J\tau_f + a_1 \cosh\frac{x}{\lambda} + a_2 \sinh\frac{x}{\lambda} \tag{4-2}$$

where a_1 and a_2 are constants, λ is the diffusion length of indium adatoms, which is sensitive to the growth temperature. The boundary conditions are given by

$$J_{diff} = -2(L+W)D_f \left(\frac{dn_f}{dx}\right)_{x=0} = 2(L+W)\lambda J, \left(\frac{dn_f}{dx}\right)_{x=c} = 0 \tag{4-3}$$

Here J_{diff} is the diffusion flux of indium adatoms towards top surface; L and W are the length and width of nanomembranes, respectively; $x = 0$ and $x = c$ represent the edge and the middle position of the top surface, respectively. Thus, the boundary conditions indicate that the diffusion flux at the edge is equal to the diffusion flux from the sidewalls while the flux at the centre is zero. The axial growth rate of nanostructures is expressed as $H(x) = \frac{\Omega n_f(x)}{\tau_f} t$, where t is the growth time and Ω is the volume of bi-atom pair in the solid. Upon solving equation (4-2) with the boundary conditions, the relative profile of the top facets along the lateral direction could be expressed as

$$\frac{H_{(x)}}{H_{x=0}} = \frac{\cosh\frac{c-x}{\lambda} + \sinh\frac{c}{\lambda}}{\cosh\frac{c}{\lambda} + \sinh\frac{c}{\lambda}} \tag{4-4}$$

Here λ is set to be 220 and 620 nm under the growth temperatures of 593 and 680 °C, respectively. As the fitting parameters, they are obtained by calculating the length and width of nanomembranes grown under different temperatures. Through the calculations, the relative profile of the top facets along the lateral direction is plotted in the Figure 4.4, showing the formation of trenches on the top facets under the low growth temperature. However, at higher growth temperature, the formation of the trenches in the middle regions is significantly reduced.

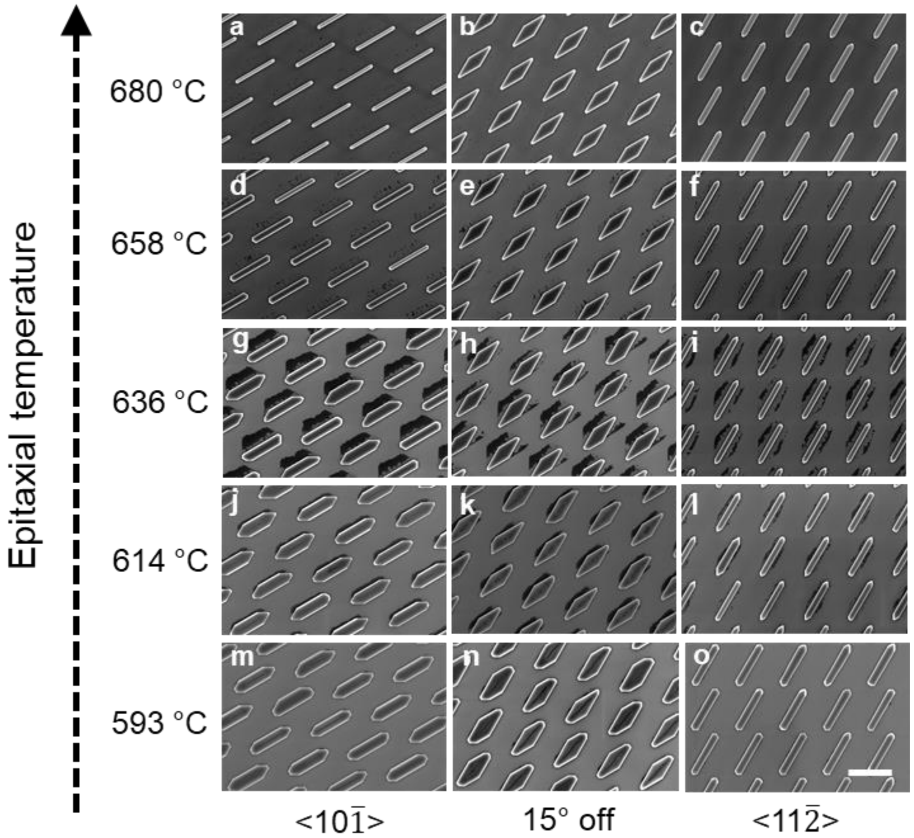

Figure 4.2: Top view low magnification SEM images of InP nanostructures grown at different temperatures with V/III ratio of 294 using the CCS reactor. The nanoslot directions in the left, middle and right columns are along <10$\bar{1}$>, 15° off and <11$\bar{2}$>, respectively. The scale bar in (o) is 2 µm and applies to all SEM images.

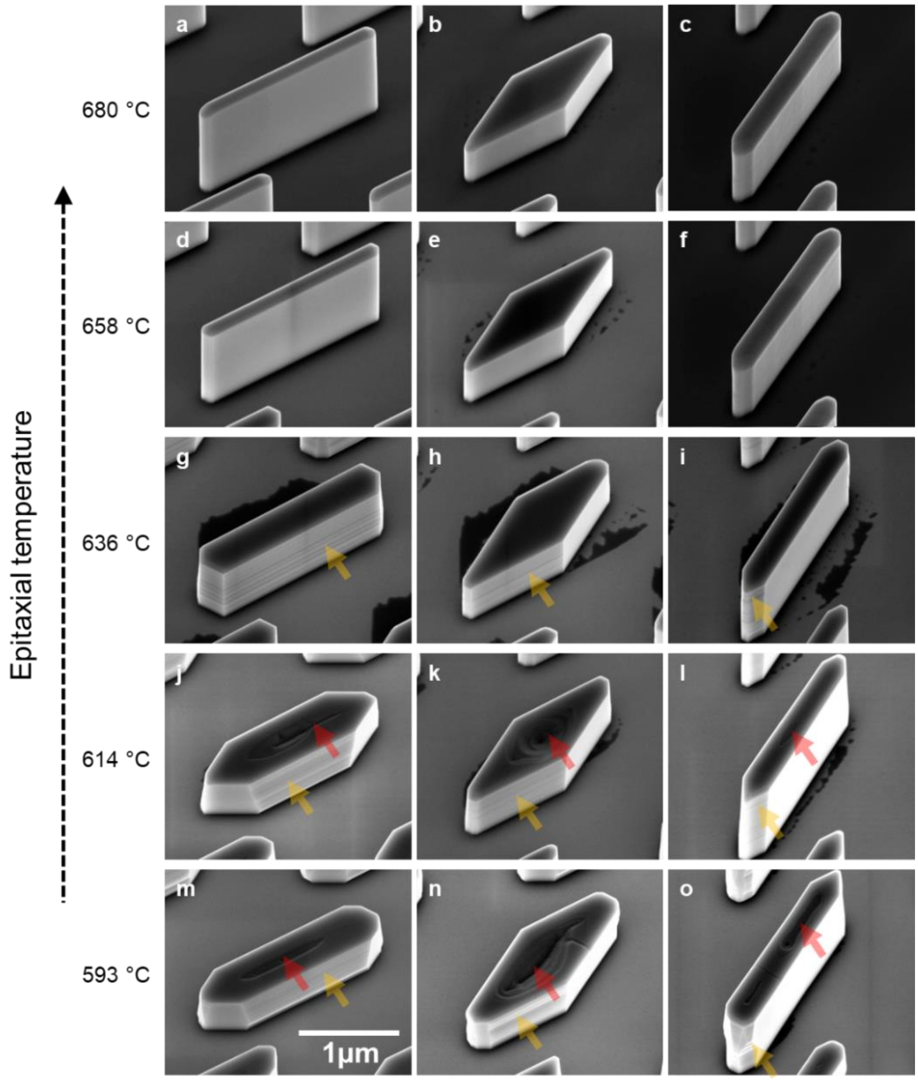

Figure 4.3: High magnification SEM images taken at 30° tilted view of InP nanostructures grown at different temperatures with V/III ratio of 294 using the CCS reactor. The nanoslot directions in the left, middle and right columns are along <10$\bar{1}$>, 15° off and <11$\bar{2}$>, respectively. The red and orange arrows highlight the trenches on top facets and uneven side facets, respectively. The scale bar in (m) is 1 µm and applies to all SEM images.

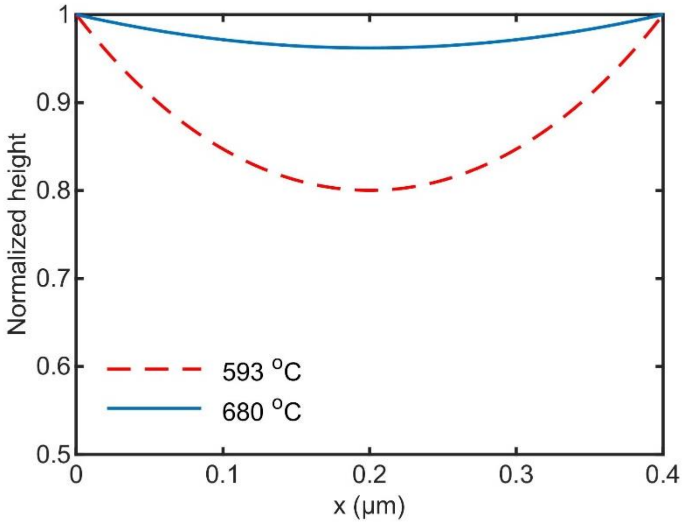

Figure 4.4: Normalized height of nanostructure cross-section along the direction perpendicular to underlying nanoslot under the two different temperatures.

Apart from the morphological characterization, we also investigated the effect of growth temperature on optical properties of the nanostructures using TRPL and CL. Figure 4.5 depicts the minority carrier lifetimes of the InP nanomembranes grown along the <$10\bar{1}$> and <$11\bar{2}$> oriented nanoslots, showing that the lifetime generally increases with the increase of growth temperature. Besides, the luminescence of the prism- and membrane-like nanostructures grown from 15° off and <$11\bar{2}$> oriented nanoslots at higher temperature is significantly uniform compared to that at lower temperature, confirmed by the panchromatic CL images shown in Figure 4.6. Overall, all these observations indicate the significance of increasing growth temperature in improving the morphology, crystalline and optical quality of the InP nanostructures, which is also consistent with the SAE of InP nanowires.[4] We also carried out the structural examination on nanostructures grown at 680 °C, demonstrating that they all have pure wurtzite structure, regardless of their shapes, which will be further discussed in the Section 4.6. Thus, the V/III ratio of 297 and growth temperature of 680 °C are the optimized parameters for epitaxial growth of InP nanostructures in the CCS reactor.

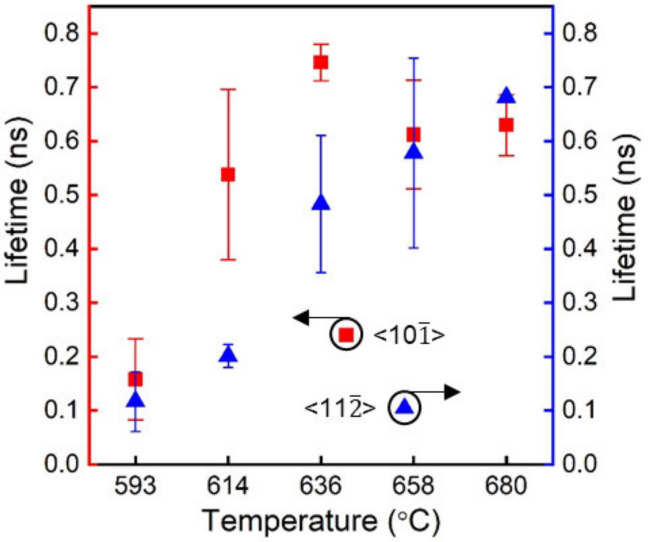

Figure 4.5: Minority carrier lifetimes of the InP nanomembranes grown from <10$\bar{1}$> and <11$\bar{2}$> oriented nanoslots at different temperatures in the CCS reactor. V/III ratio for all the nanomembranes is 297.

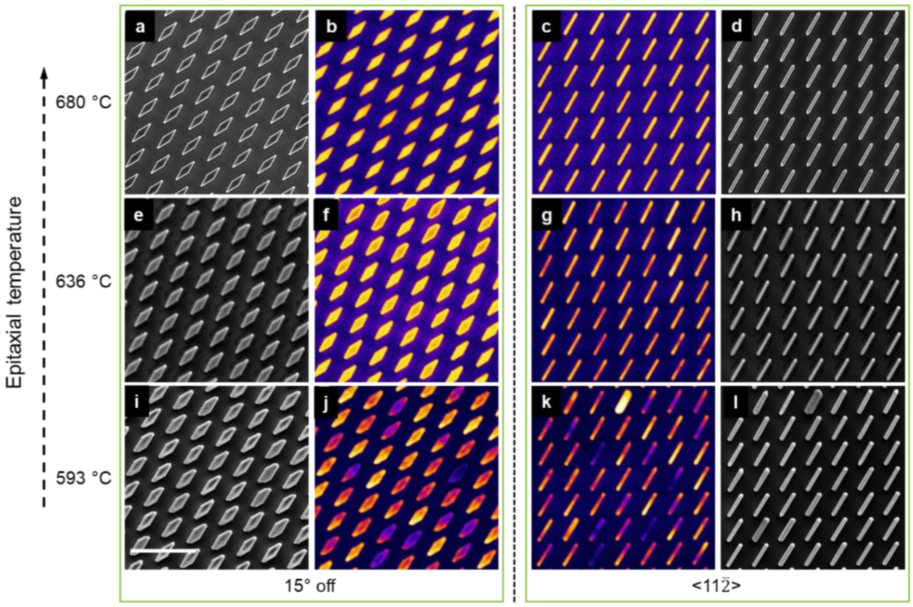

Figure 4.6: Top view SEM and corresponding panchromatic CL images of InP nanostructures grown under different temperatures in the CCS reactor. The nanoslot directions are 15° off (left) and <11$\bar{2}$> (right), respectively. The scale bar in (i) is 5 µm and applies to all SEM and CL images.

4.4. Membrane- and prism-like InP nanostructures

In this section, an in-depth investigation of membrane- and prism-like InP nanostructures grown from nanoslots at the optimal conditions are carried out. We first discuss the effects of orientation and dimension of nanoslots on the morphology and facets of nanostructures. We then propose a thermodynamic model to explain the mechanism for shape transformation of these nanostructures.

4.4.1. InP nanostructures grown from nanoslots with the identical length but different orientations and widths

In this section, all InP nanostructures are grown from nanoslots with a length of 2 μm. To investigate the effect of nanoslots direction, their widths are fixed to be approximately 120 nm. Figure 4.7a schematically illustrates the SAE InP nanostructures grown from the patterned nanoslots of three different orientations. As will be shown and discussed in Section 4.6, the nanostructures are all of WZ crystal structure, and hence we refer to them using the corresponding 4-index scheme. Mainly bounded by $\{10\bar{1}0\}$ and/or $\{11\bar{2}0\}$ side facets, they all grow vertically along the [0001] direction. Depending on the direction of nanoslots, the cross-sections of nanostructures may not fully inherit the geometries of the underlying patterns in spite of their confinement in the lateral directions. The morphologies of the nanostructures grown from the $<10\bar{1}>$, 15° off and $<11\bar{2}>$ oriented nanoslots are shown in Figure 4.7b-d, respectively. For $<10\bar{1}>$ and $<11\bar{2}>$ oriented nanoslots, the facets confined by the pattern correspond to $\{10\bar{1}0\}$ and $\{11\bar{2}0\}$ planes, respectively. They both are the dominant side facets in Figure 4.7b,d, respectively, leading to the formation of nanomembranes. We observe that the $<10\bar{1}>$ oriented nanomembranes are thinner than the $<11\bar{2}>$ oriented nanomembranes. Since thinner membranes are taller, surface diffusion is playing a role in this difference of geometry, but as we will discuss in Section 4.4.3, the difference in surface energy and radial growth of the $\{10\bar{1}0\}$ and $\{11\bar{2}0\}$ facets also play a substantial role. When the nanoslot does not correspond to any low-index direction, for instance the 15° off nanoslot, the sidewalls of nanostructure predominantly consist of both $\{10\bar{1}0\}$ and $\{11\bar{2}0\}$ facets (see Figure 4.7c). Instead of a nanomembrane, the nanostructure is grown in the shape of a parallelogram prism. This coexistence of $\{10\bar{1}0\}$ and $\{11\bar{2}0\}$ facets in WZ InP would increase the possibilities for engineering the shapes of InP nanostructures. More interestingly, the highly uniform arrays of InP nanostructures with different shapes can be simultaneously achieved in the same growth run by simply adjusting nanoslot directions.

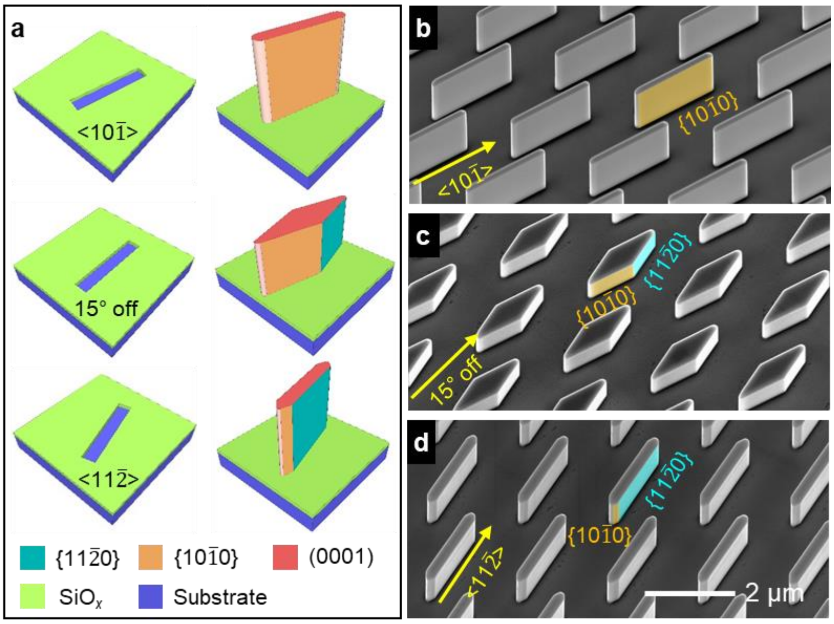

Figure 4.7: InP nanostructures grown from the patterned nanoslots with different directions. (a) Schematics of the designed nanoslots and grown InP nanostructures. The nanoslots are along the <10$\bar{1}$>, 15° off (with respect to <10$\bar{1}$>) and <11$\bar{2}$> directions of the (111)A InP substrate. 30° tilted SEM images of InP nanostructure arrays with the nanoslots along (b) <10$\bar{1}$>, (c) 15° off, and (d) <11$\bar{2}$> directions. The {10$\bar{1}$0} and {11$\bar{2}$0} side facets are representatively highlighted by orange and aqua colours, respectively. The scale bar in (d) is 2 μm and applies to all SEM images.

We also investigate the effect of nanoslot width on nanomembranes grown from the <10$\bar{1}$> and <11$\bar{2}$> oriented nanoslots. While nanoslot length and growth time are fixed at 2 μm and 3 min, respectively, the nanoslot widths vary from approximately 76 to 325 nm. Figure 4.8a shows the height and thickness of membrane-like nanostructures as a function of the underlying nanoslot width. Meanwhile, for better visual comparison, Figure 4.8b-e shows tilted SEM images of the representative nanomembranes whose nanoslots are of minimum and maximum widths. It can be seen that the thickness of both <10$\bar{1}$> and <11$\bar{2}$> oriented nanomembranes increases approximately linearly with nanoslot width with the <11$\bar{2}$> oriented nanomembranes always thicker than their <10$\bar{1}$> counterparts, which suggests that the nanomembranes with {11$\bar{2}$0} side facets encourages more lateral growth than those with {10$\bar{1}$0} side facets. The difference in lateral growth is due to {10$\bar{1}$0} facet being more stable than {11$\bar{2}$0} facet under the current growth conditions. More details will be discussed later in Section 4.4.3. In addition, the height of nanomembranes with <10$\bar{1}$> oriented nanoslots decreases monotonously while that with <11$\bar{2}$> oriented nanoslots fluctuates only slightly and is less dependent on nanoslots width. The reaction species contributing to the axial growth could be divided into two parts, as schematically illustrated in Figure 2.2b: those that directly impinge on the top surface and those that adsorb on the mask layer and nanostructure side facets, and then diffuse to the top surface. In case of thinner slots, the axial growth of InP nanomembranes is dominated by species diffusing from the side facets and mask layer. With increasing slot width, more species are consumed by the lateral growth, leading to the rapid decrease of <$10\bar{1}$> oriented nanostructure height. In contrast, in case of thicker slots, the axial growth is predominantly due to the species which are directly deposited on nanostructure top surface, therefore leading to an axial growth rate that is less dependent on slot width. Thus, although the height of the <$10\bar{1}$> oriented nanostructures decreases with increasing the slot width, the difference becomes smaller. It also explains the similar heights of the <$10\bar{1}$> and <$11\bar{2}$> oriented nanomembranes with slot width approximately 325 nm. As for the height of <$11\bar{2}$> oriented nanomembranes which is less dependent on slot width, it can be attributed to their higher lateral growth rate even when slots are narrow.

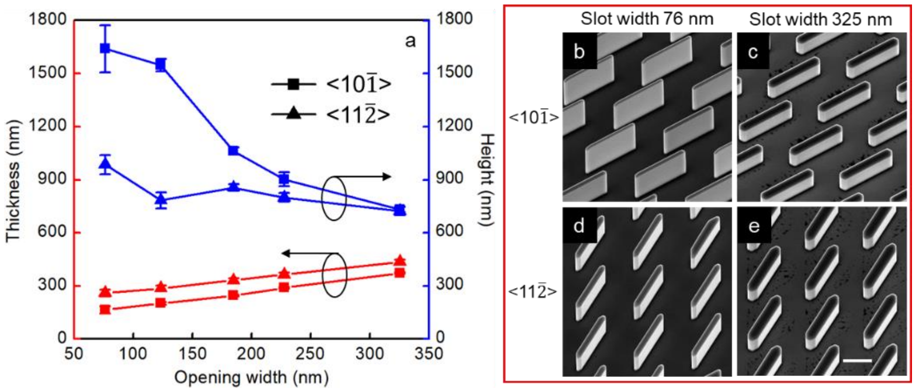

Figure 4.8: (a) Average thickness and height of InP nanomembranes grown from the <$10\bar{1}$> and <$11\bar{2}$> oriented nanoslots as a function of nanoslots width. The error bars represent the standard deviation of thickness and height from 350 individual nanomembranes. (b-e) 30º tilted SEM images of InP nanomembranes with nanoslots width of approximately (b,d) 76 and (c,e) 325 nm. The scale bar in (e) is 1 µm and applies to all SEM images.

4.4.2. Shape evolution from nanowire to membrane- and prism-like nanostructures

The shape of SAE InP nanostructures is determined by growth conditions, duration, and designed pattern including geometry, dimension and orientation. In this section, we investigate the shape transformation of InP nanostructures by changing growth time and nanoslot length. It not only demonstrates the ability to engineer nanostructure shapes, but also provides deeper insight into the understanding of growth mechanism.

In case of the <$10\bar{1}$> and <$11\bar{2}$> oriented nanoslots, when growth time is 7 min we observed the shape evolution from nanowires to nanomembranes with the increase of nanoslot length, as shown in Figure 4.9d-f and Figure 4.10d-f. All nanostructures grown from the <$10\bar{1}$> oriented nanoslots are mainly bounded by {$10\bar{1}0$} side facets, independent of the nanoslot length (Figure 4.9d-f). In comparison, only InP nanostructures grown from the very short <$11\bar{2}$> oriented nanoslots mainly consist of {$10\bar{1}0$} side facets, showing a prism-like shape. As the nanoslots become longer, they start to confine lateral growth and {$11\bar{2}0$} facets start to appear and become more dominant (Figure 4.10d-f). Even when both oriented nanoslots are up to 50 µm in length, the nanomembranes follow the trend discussed above, as shown in Figure 4.11a,b. Furthermore, these long nanomembranes present uniform and regular morphologies. With increasing growth time, nanomembranes with <$10\bar{1}$> oriented nanoslots grow taller and slightly thicker, but maintain the same dominant side facets and geometries (Figure 4.9a-c). In contrast, the nanomembranes with <$11\bar{2}$> oriented nanoslots transform into prism-like nanostructures due to the replacement of {$11\bar{2}0$} side facets with {$10\bar{1}0$} (Figure 4.10a-c). The shape of a crystal usually reflects the stability of its facets.[6, 7] Thus, the above observations suggest that although both {$11\bar{2}0$} and {$10\bar{1}0$} facets are formed during the SAE of InP, {$10\bar{1}0$} facets are more stable under the current growth conditions.

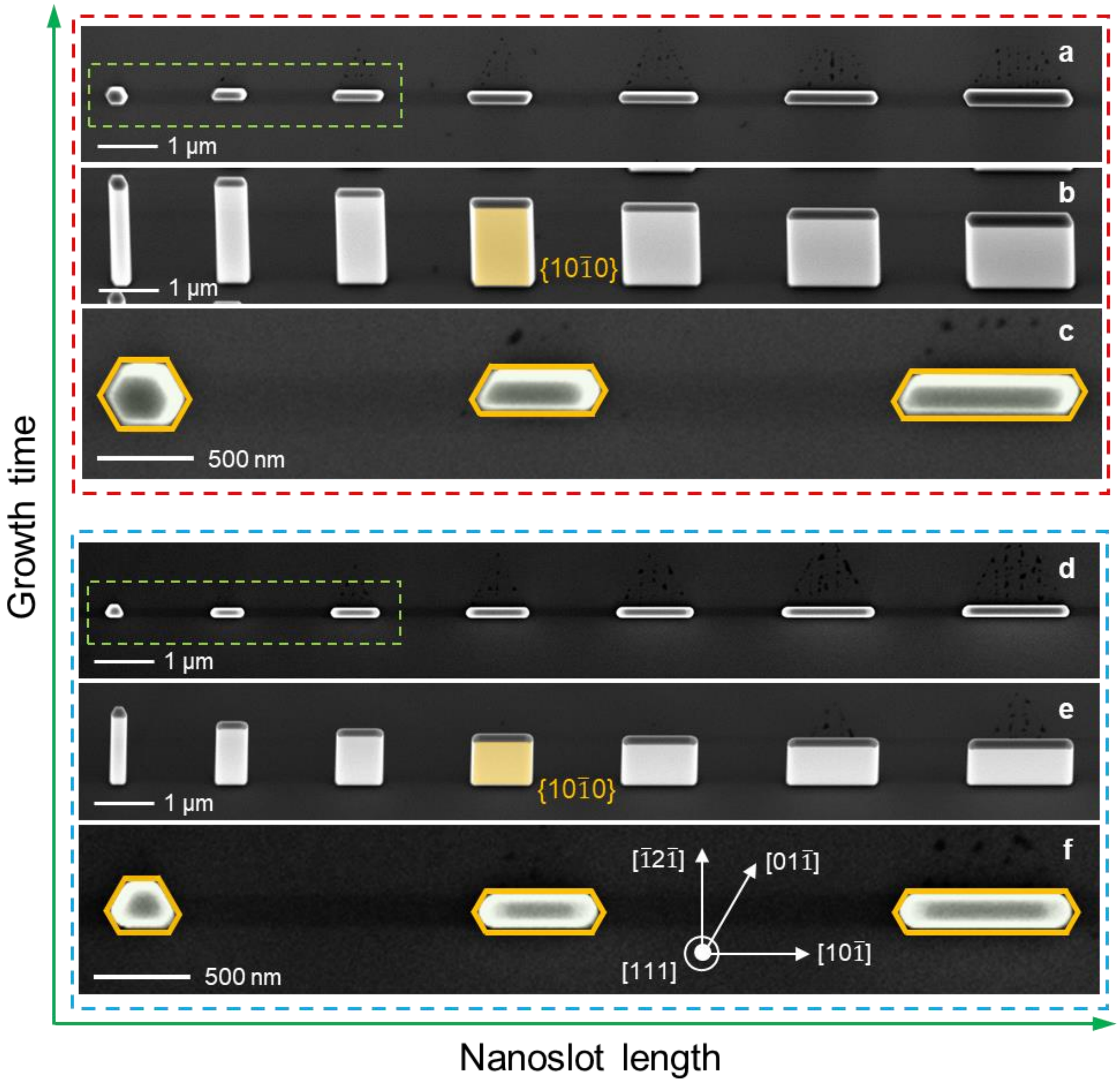

Figure 4.9: (a-f) SEM images of InP nanostructures grown in the horizontal reactor, showing the shape evolution from nanowire to nanomembrane with the increase of nanoslot length along the $<10\bar{1}>$ direction. Growth times for nanostructures shown in lower and upper panels are 7 and 14 min respectively. (a,c,d,f) top view; (b,e) 15° tilted view. High magnification SEM images from the highlighted area in (a) and (d) are shown in (c) and (f), respectively. The orange solid lines in (c,f) and orange areas in (b,e) are corresponding to $\{10\bar{1}0\}$ side facets.

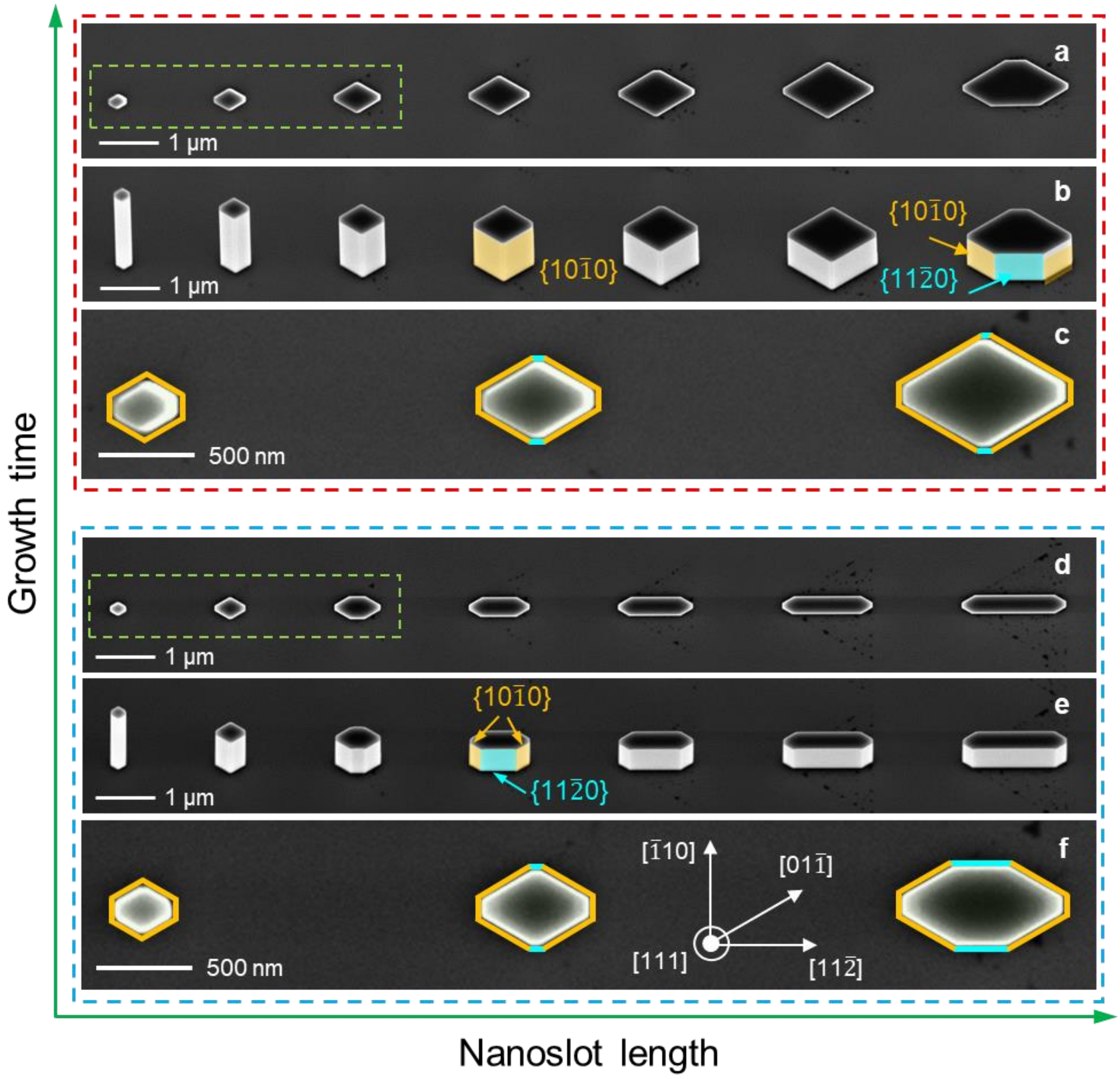

Figure 4.10: (a-f) SEM images of InP nanostructures grown from the <11$\bar{2}$> oriented nanoslots with increasing lengths. The growth took place under the optimal growth conditions in the horizontal reactor for (a-c) 14 and (d-f) 7 min, respectively. (a,c,d,f) top view; (b,e) 15° tilted view. High magnification SEM images from the highlighted area in (a) and (d) are shown in (c) and (f) respectively. The orange and aqua coloured regions and lines indicate {10$\bar{1}$0} and {11$\bar{2}$0} side facets, respectively.

According to both time and nanoslot length dependent investigation of nanostructures grown from the <11$\bar{2}$> oriented nanoslots, the shape evolution determined by facet stability can be observed either by extending growth time or decreasing nanoslot length (Figure 4.10). In other words, nanostructures grown on shorter slots have seen more material deposition, and their growth has evolved more in comparison to those grown on longer nanoslots. This also applies to the case of nanoslots along any crystal directions. Taking 15° off direction for example, the experimental results are shown in Figure 4.11c and Figure 4.12. By analyzing their evolution of side facets with the decrease of nanoslots length, we found the growth process can be divided into four stages, each of which has different shapes, as schematically illustrated in Figure 4.13. At the earlier stage after nucleation and filling up of the opening, shape I is formed (see Figure 4.11c for SEM image), followed by the transformation towards shapes II, III and IV (see Figure 4.13). Specifically, due to the confinement effect of the nanoslots, high-index facets appear at the initial stage I, but they are not thermodynamically stable and tend to be replaced by a combination of the metastable $\{11\bar{2}0\}$ facets and the stable $\{10\bar{1}0\}$ facets, leading to the formation of shape II. The evolution continues with the gradual replacement of the $\{11\bar{2}0\}$ facets by the $\{10\bar{1}0\}$ facets (stage III), and eventually reaches the stage IV with the equilibrium prism-like shape when the $\{11\bar{2}0\}$ facets completely disappear.

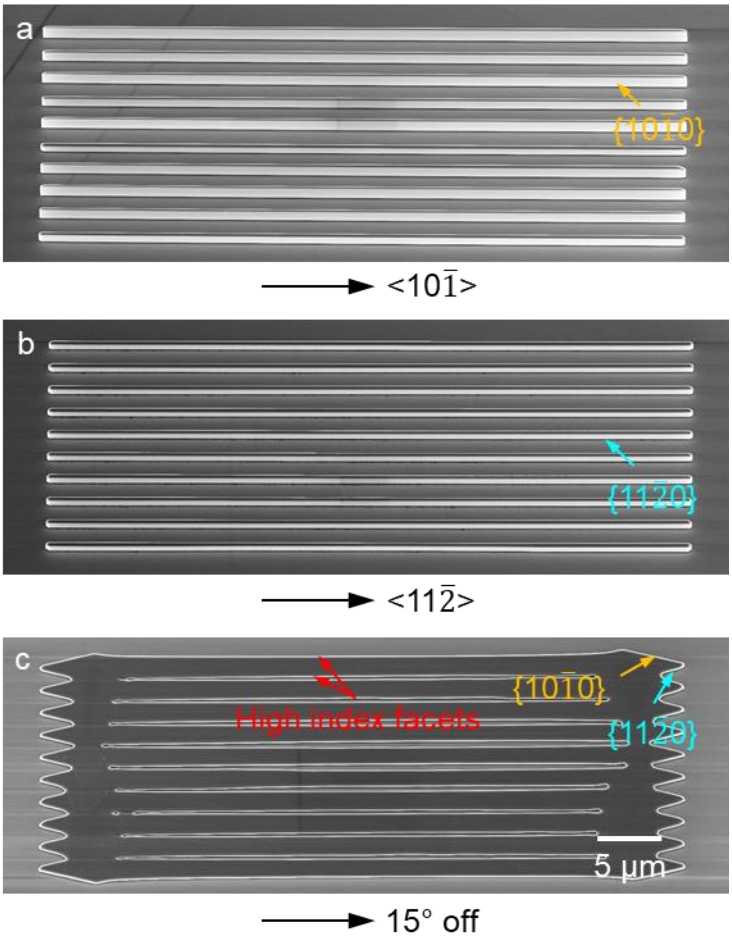

Figure 4.11: 30° tilted SEM images of InP nanostructures grown from the $<10\bar{1}>$, $<11\bar{2}>$ and 15° off nanoslots with a length of 50 µm. The scale bar in (c) applies to all SEM images.

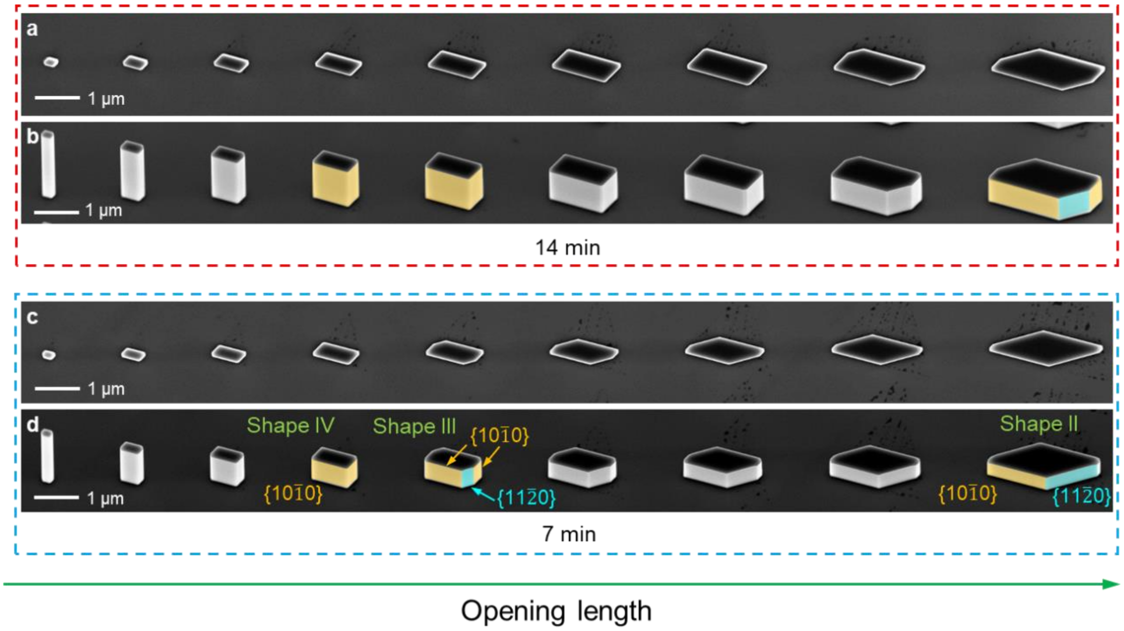

Figure 4.12: SEM images of InP nanostructures with increasing nanoslot length along 15° off direction grown at 750 °C using the horizontal reactor. The growth times are (a,b) 14 min and (c,d) 7 min, respectively. (a,c) top view; (b,d) 15° tilted view. The facets highlighted by orange and aqua areas in (b) and (d) are {10$\bar{1}$0} and {11$\bar{2}$0}, respectively.

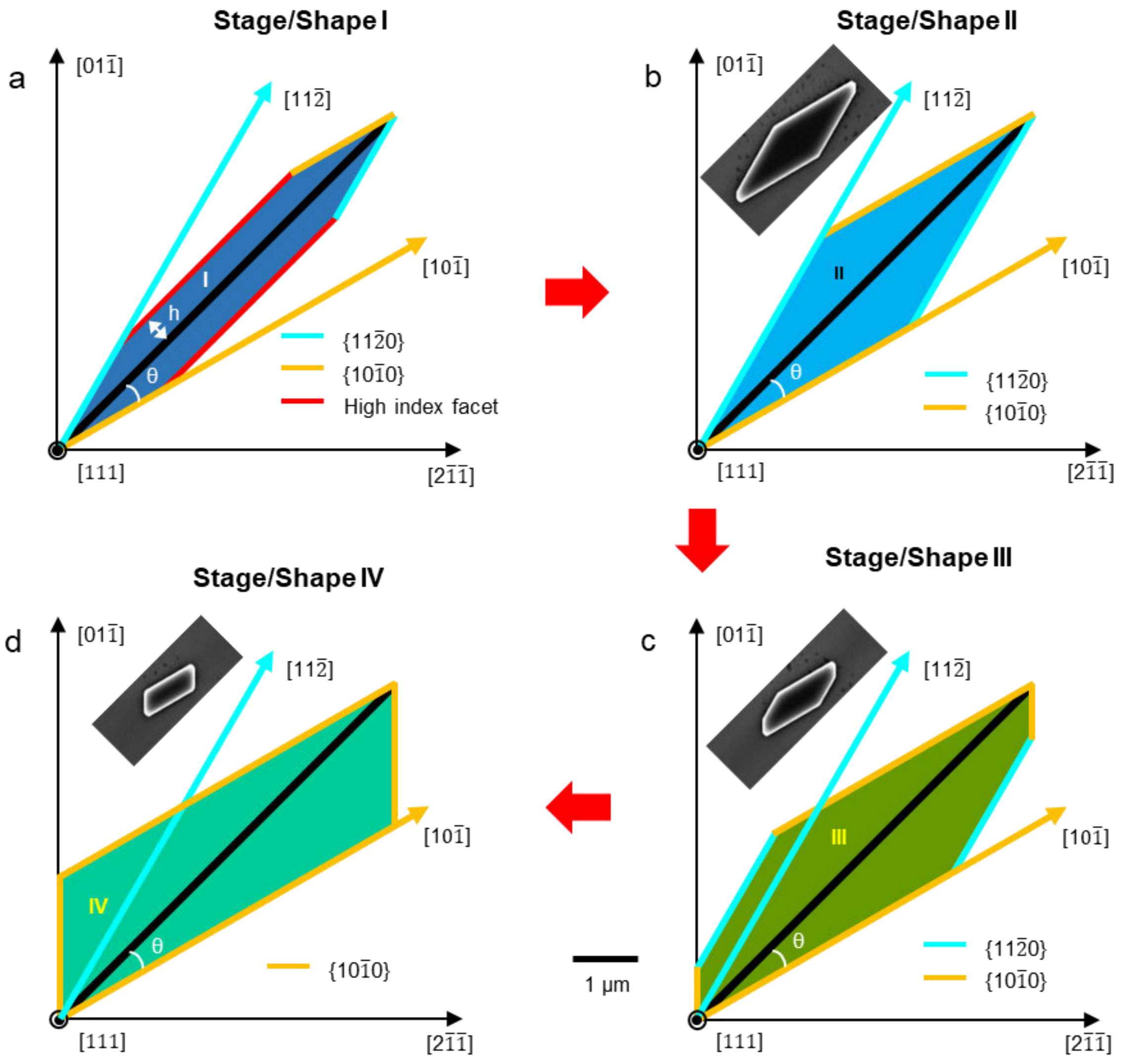

Figure 4.13: Schematics of shape evolution of InP nanostructures with the nanoslot direction θ between $[10\bar{1}]$ and $[11\bar{2}]$. SEM images show the representative nanostructures with the corresponding geometries taking the 15° off oriented samples for example.

4.4.3. Study of growth mechanisms

The concept of shape engineering expands the research field from traditional nanowires to nanostructures with many types of possible geometries. These novel nanostructures play a significant role in applications, such as metamaterials and meta-optics which demand accurate control of homogeneity and geometry. The understanding of mechanisms for the shape transformation is a vital step in achieving these applications. Considering crystal symmetry, we only need to consider nanoslot directions of $[10\bar{1}]$, $[11\bar{2}]$ and θ off where $0° < \theta < 30°$ is the angle between nanoslot direction and $[10\bar{1}]$. Furthermore, since nanostructures which are grown from $\langle 10\bar{1}\rangle$ oriented nanoslots remain a membrane-like shape regardless of nanoslot dimension and growth time (see Figure 4.9), only nanostructures with $\langle 11\bar{2}\rangle$ oriented nanoslots are discussed as a special case. In this section, we will discuss the transformative mechanism of nanostructures with a special <11$\bar{2}$> and any high-index oriented (θ off) nanoslots.

4.4.3.1. Study of nanostructures grown from in-plane <11$\bar{2}$> oriented nanoslots

To understand mechanism behind the transformation of InP nanostructures, a thermodynamic growth model is proposed. According to the growth results in Figure 4.10, we observed morphological transformation from membrane-like to prism-like shapes with the increase of growth time, which are schematically plotted in Figure 4.14. The total surface energy of the prism-like nanostructure is expressed as

$$G_P = \frac{4}{\sqrt{3}}\gamma_{\{10\bar{1}0\}}H_P L_P + \frac{{L_P}^2}{2\sqrt{3}}\Delta\gamma \qquad (4\text{-}5)$$

where $\gamma_{\{10\bar{1}0\}}$ is the surface energy of $\{10\bar{1}0\}$ facet, H_P is the height, and L_P is the length for both nanoslots and nanostructures. $\Delta\gamma = \gamma_{top} + \gamma_i - \gamma_s$, where γ_{top}, γ_i and γ_s are the top facet surface energy, interfacial energy between substrate and grown nanostructure, and substrate surface energy, respectively. In the case of homoepitaxy, $\Delta\gamma$ is equal to zero. Thus, the equation (4-5) could be simplified as

$$G_P = \frac{4}{\sqrt{3}}\gamma_{\{10\bar{1}0\}}H_P L_P \qquad (4\text{-}6)$$

Likewise, we obtain the total surface energy of membrane-like nanostructure

$$G_M = 2\gamma_{\{11\bar{2}0\}}\left(L_M - \sqrt{3}W_M\right)H_M + 4\gamma_{\{10\bar{1}0\}}W_M H_M \qquad (4\text{-}7)$$

where $\gamma_{\{11\bar{2}0\}}$ is the $\{11\bar{2}0\}$ facet surface energy, L_M is the length for both nanoslots and nanostructures, H_M is the height, and $W_M = kL_M$, $(0 < k < \sqrt{3}/3)$ represents the width. k is a geometric factor depending on the shape. With the increase of k, the nanostructures transform from a membrane-like to a prism-like shape. At $k = \sqrt{3}/3$, the transformation is completed. The volumes of the membrane-like and prism-like shapes are $V_M = \left(k - \sqrt{3}k^2/2\right){L_M}^2 H_M$ and $V_P = {L_P}^2 H_P/2\sqrt{3}$, respectively. At $L_P = L_M$, we assume that the volumes of these two shapes grown under the same conditions are equal. Therefore, we have $H_P = (2\sqrt{3}k - 3k^2)H_M$. By substituting them into equations (4-6) and (4-7), we obtain

$$\frac{G_M}{G_P} = \frac{1}{4k - 2\sqrt{3}k^2}\left[\left(1 - \sqrt{3}k\right)\frac{\gamma_{\{11\bar{2}0\}}}{\gamma_{\{10\bar{1}0\}}} + 2k\right],\ 0 < k < \sqrt{3}/3 \qquad (4\text{-}8)$$

Taking $\gamma_{\{11\bar{2}0\}} = 1.38\,J/m^2$ and $\gamma_{\{10\bar{1}0\}} = 1.19\,J/m^2$,[8] G_M/G_P is calculated and plotted as a function of k as shown in Figure 4.15. We found that the ratio of G_M/G_P decreases exponentially with k but is always larger than 1. It suggests that, under the scenario described above, the prism-like nanostructure has the lowest total surface energy and therefore the transformation from membrane-like shape to this prism-like shape is energetically favourable. Overall, at the early stage of epitaxial growth, the metastable $\{11\bar{2}0\}$ facet is dominant over the stable $\{10\bar{1}0\}$ facet due to the confinement of the <11$\bar{2}$> nanoslot, leading to the formation of nanostructure with a membrane-like geometry. As the epitaxial growth continues, to minimize the total surface energy, the membrane-like shape transforms to the prism-like shape by the replacement of $\{11\bar{2}0\}$ facets with $\{10\bar{1}0\}$ facets.

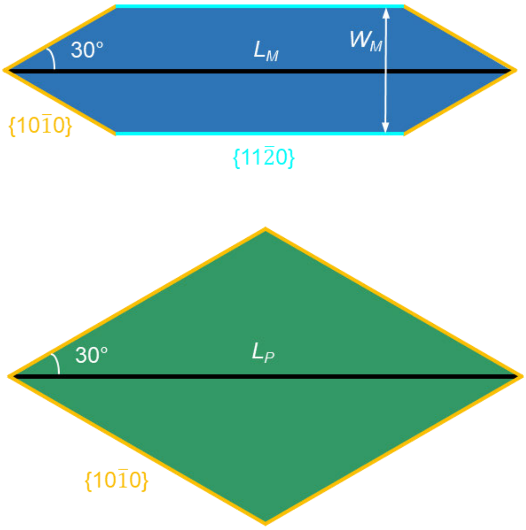

Figure 4.14: Top view schematic of a membrane-like and prism-like shape of InP nanostructures with <11$\bar{2}$> oriented nanoslot.

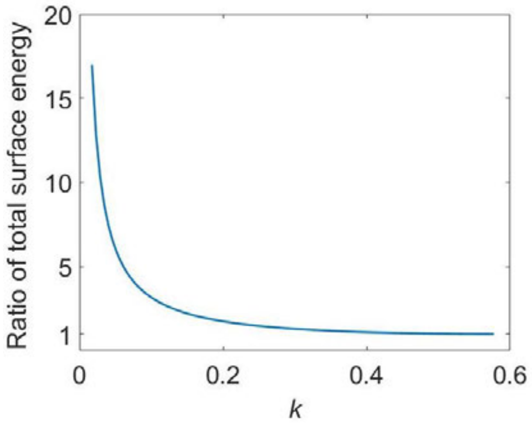

Figure 4.15: The ratio of the total surface energy between the membrane-like and prism-like nanostructures, G_M/G_P as a function of k where k $(0 < k < \sqrt{3}/3)$ is the ratio of membrane-like nanostructure width and length.

4.4.3.2. Study of nanostructures grown from nanoslots along any high-index direction

As shown in Figure 4.13, the shape evolution of nanostructures with θ off oriented nanoslots during epitaxy can be divided into four stages with respective shapes labelled as I-IV. The total surface energy of shapes I, II and IV are expressed as

$$G_I = \left\{\frac{2h}{\sin(\pi/6-\theta)}\gamma_{\{11\bar{2}0\}} + \frac{2h}{\sin\theta}\gamma_{\{10\bar{1}0\}} + 2\left[L - \frac{h}{\sin 2(\theta+\pi/6)-\sqrt{3}/2}\right]\gamma_{HI}\right\}H_I,\ 0 < h < \left[\sin 2(\theta + \pi/6) - \sqrt{3}/2\right]L \qquad \text{(4-9)}$$

$$G_{II} = \left\{\frac{2L\left[\sin 2(\theta+\pi/6)-\sqrt{3}/2\right]}{\sin(\pi/6-\theta)}\gamma_{\{11\bar{2}0\}} + \frac{2L\left[\sin 2(\theta+\pi/6)-\sqrt{3}/2\right]}{\sin\theta}\gamma_{\{10\bar{1}0\}}\right\}H_{II} \qquad \text{(4-10)}$$

$$G_{IV} = \left\{\frac{2L[\sin(2\theta+\pi/6)-1/2]}{\sqrt{3}\cos(\theta+\pi/6)}\gamma_{\{10\bar{1}0\}} + \frac{2L[\sin(2\theta+\pi/6)-1/2]}{\sqrt{3}\sin\theta}\gamma_{\{10\bar{1}0\}}\right\}H_{IV} \qquad \text{(4-11)}$$

where L is the nanoslot length; h is the half width of shape I nanostructure; γ_{HI} is the surface energy of the high index facets and satisfy $\gamma_{\{10\bar{1}0\}} < \gamma_{\{11\bar{2}0\}} < \gamma_{HI}$. The volumes of shapes I, II, and IV are given by

$$V_I = \left\{2L - h/\left[\sin 2(\theta + \pi/6) - \sqrt{3}/2\right]\right\}hH_I \qquad \text{(4-12)}$$

$$V_{II} = \left[\sin 2(\theta + \pi/6) - \sqrt{3}/2\right]L^2H_{II} \qquad \text{(4-13)}$$

$$V_{IV} = [\sin(2\theta + \pi/6) - 1/2]L^2H_{IV}/\sqrt{3} \qquad \text{(4-14)}$$

Under the assumption that the shapes I, II and IV have the same volume, we obtain

$$H_{IV} = \sqrt{3}\frac{\sin 2(\theta+\pi/6)-\sqrt{3}/2}{\sin(2\theta+\pi/6)-1/2}H_{II} = \sqrt{3}\frac{2L-h/\left[\sin 2(\theta+\pi/6)-\sqrt{3}/2\right]}{[\sin(2\theta+\pi/6)-1/2]L^2}hH_I \qquad \text{(4-15)}$$

Through the calculation, we found $G_I/G_{IV} > G_{II}/G_{IV} > 1$ at a preset value of $h = \left[\sin 2(\theta + \pi/6) - \sqrt{3}/2\right]L/2$, independent of length and direction of the nanoslots. It suggests that, the epitaxial stages I-II are energetically unfavourable and therefore shape I induced initially by the pattern confinement effect evolves to shape II and eventually to the final equilibrium shape IV, *via* another intermediate shape III, due to minimization of the total surface energy. In particular, the area ratio of $\{11\bar{2}0\}/\{10\bar{1}0\}$ facets at the stage II increases monotonously with θ from 0° - 30° and equals to 1 at θ = 15°.

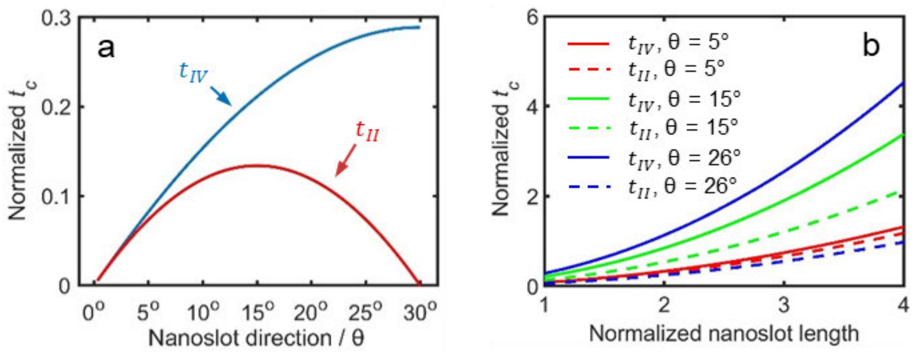

Figure 4.16: Relative transformation time of nanostructures as a function of nanoslot (a) direction and (b) length.

The dynamic shape evolution process provides a “roadmap” for tuning the shape of InP nanostructures. For more precise shape engineering, the relation between time (t_c) required to reach the critical shapes II and IV and pattern design including orientation and dimension need to be established since we have already observed this strong correlation as shown in Figure 4.10d,e and Figure 4.12c,d. For simplicity, we assume the growth of nanostructures is dominated by diffusion of indium adatoms from the substrate/SiO$_x$ mask with a diffusion length of λ_s. The feeding area is either directly proportional to dL (when $\lambda_s > d$) or $\lambda_s L$ (when $\lambda_s < d$) where d is the distance between two nearby nanoslots in the perpendicular direction. Accordingly, the growth rate of the nanostructures is equal to $\lambda_s L v$ or dLv=constant where v (nm/s) is the deposition rate. t_c could be expressed as

$$t_c = \frac{\rho L^2 f(\theta)}{\lambda_s v} \text{ or } t_c = \frac{\rho L^2 f(\theta)}{dv} \tag{4-16}$$

where $\rho = H/L$ is the ratio of nanostructure height and length, $f(\theta) = \sin(2\theta + \pi/3) - \sqrt{3}/2$ and $f(\theta) = [\sin(2\theta + \pi/6) - 1/2]\sqrt{3}/3$ ($0° < \theta \leq 30°$) are the geometric factor of the top facet area of shapes II and IV, respectively. Particularly, at $\theta = 30°$ (*i.e.* the $[11\bar{2}]$ direction), shape I with high-index facets does not exist and shapes II and IV correspond to the membrane- and prism-like shapes, respectively. The calculation results are plotted in Figure 4.16. Figure 4.16a indicates that, at a fixed nanoslot length, the time needed to form shape II increases with the nanoslot direction away from $[10\bar{1}]$ and $[11\bar{2}]$ directions and reaches a maximum at 15° off direction. On the other hand, the transformation time for achieving the final shape IV monotonously increases when the nanoslot direction gradually rotates from $[10\bar{1}]$ to $[11\bar{2}]$. Figure 4.16b shows that three representative directions are identified in the calculations. At a fixed nanoslot direction, the shorter the nanoslot is, the sooner the shape transformation into the intermediate shape II and final shape IV could be completed (see the dotted and solid curves in Figure 4.16b, respectively). Thus, at a fixed growth time and nanoslot direction, the nanostructures with different nanoslot length are at the different stages of transformation, which is responsible for the observed shape evolution of the nanostructures with the decrease of nanoslots length along <$11\bar{2}$> and 15° off directions (Figure 4.10 and Figure 4.11).

4.5. Ring-like InP nanostructures

The above analysis of prism- and membrane-like nanostructures shows the possibility of InP in forming nanostructures with more complex shapes. In this section, we will discuss ring-like shape which is a desired geometry for optical signal processing and lasing applications.[9-11] In the first subsection, we investigate the side facets and geometries of ring-like nanostructures under the optimized growth conditions; in the second subsection, we focus on the stability change of side facets with growth temperatures.

4.5.1. Diameter-dependent study under the optimal growth conditions

Figure 4.17a-e shows SEM images of InP nanostructures grown from ring openings with diameters varying from approximately 2 to 9 µm at the optimal conditions in the CCS reactor. It can be seen that InP nanostructures cannot fully inherit the geometry of the underlying patterns due to the unlikely formation of curved facets but present a multi-faceted ring-like shape consisting of {$11\bar{2}0$} and {$10\bar{1}0$} side facets. The confinement effect of the patterned nanoring on the formation of these two facets is equivalent, which makes the investigation of the actual morphology of ring-like nanostructures more interesting in terms of understanding the growth behaviour.

Under optimal growth conditions (higher growth temperature), the area ratio of {$11\bar{2}0$}/{$10\bar{1}0$} side facets gets larger but is always smaller than 1 with the increase of diameter (Figure 4.17f), leading to the transformation of nanostructures from hexagon-like to dodecagon-like shapes (Figure 4.17a-d). The ring size is essentially a snapshot in time of the growth evolution that is occurring. As the rings size becomes smaller, growth around the rings has evolved more and as a result {$10\bar{1}0$} facets are more dominant. Conversely, for larger diameter rings, growth is less evolved and hence both {$10\bar{1}0$} and {$11\bar{2}0$} facets are dominant. Thus, the metastable {$11\bar{2}0$} facets will gradually evolve to {$10\bar{1}0$} facets with further growth, eventually leading to the formation of the hexagon-like equilibrium crystal shape, confirmed by the time-dependent growth results (see Figure 4.18). These results are consistent with the earlier analysis of nanostructures grown from nanoslots that {$10\bar{1}0$} facet is more stable than {$11\bar{2}0$} facet.

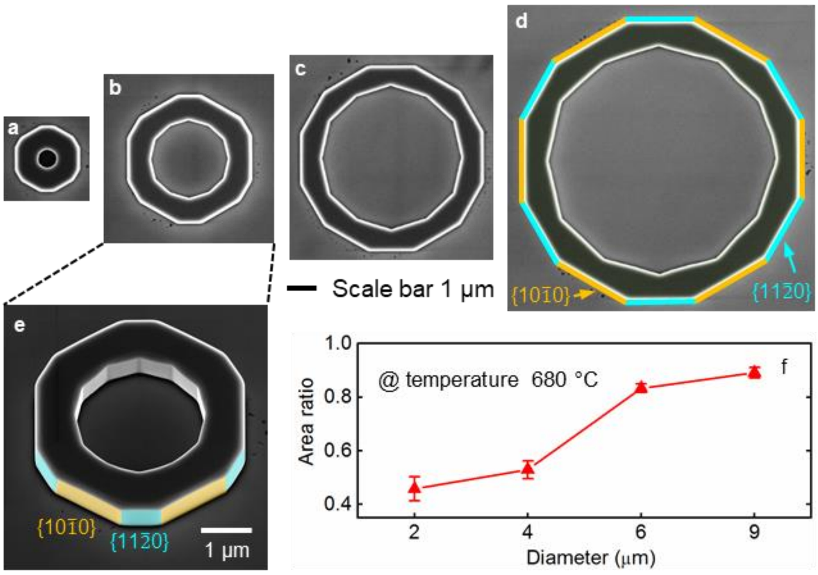

Figure 4.17: (a-d) Top view SEM images of ring-like InP nanostructures with different diameters grown at the optimal conditions in the CCS reactor. (e) 3D view of the ring-like nanostructure shown in (b). (d,e) The orange and aqua coloured regions and lines indicate $\{10\bar{1}0\}$ and $\{11\bar{2}0\}$ side facets, respectively. (f) shows the relation of the area ratio of $\{11\bar{2}0\}/\{10\bar{1}0\}$ side facets with diameter.

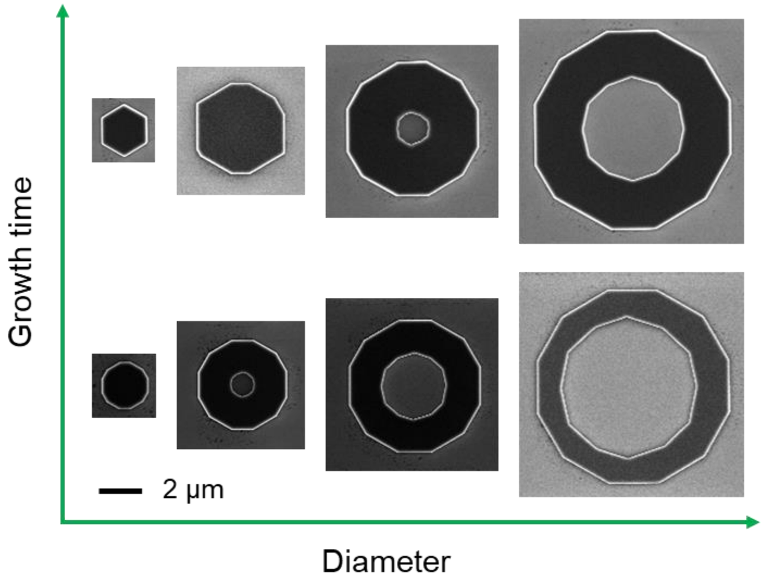

Figure 4.18: Top view SEM images of InP ring-like nanostructures with different diameters grown at the optimal conditions in the horizontal reactor. Growth time is 14 min (top) and 7 min (bottom), respectively.

4.5.2. Facet stability and morphological transformation under different growth temperatures

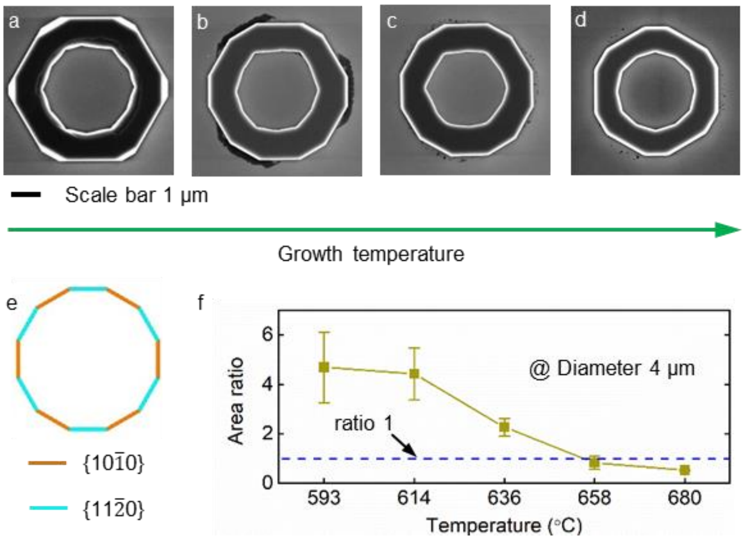

Figure 4.19: (a-d) Top view SEM images of ring-like InP nanostructures with 4 μm diameter grown at different temperatures in the CCS reactor. Growth temperature is (a) 593, (b) 636, (c) 658 and (d) 680 °C. Side facets of nanostructures in (a-d) parallel to the aqua and orange lines in (e) are $\{11\bar{2}0\}$ and $\{10\bar{1}0\}$ side facets, respectively. (f) shows the relation of the area ratio of $\{11\bar{2}0\}/\{10\bar{1}0\}$ side facets with growth temperature.

The role of growth temperature on facet stability and shape evolution is investigated by analyzing ring-like nanostructures with 4 μm diameter (Figure 4.19a-d). The regular dodecagon with two different coloured sides shown in Figure 4.19e is used to determine $\{11\bar{2}0\}$ and $\{10\bar{1}0\}$ side facets of these nanostructures. The area ratio of $\{11\bar{2}0\}/\{10\bar{1}0\}$ side facets monotonously decreases from 4.7 to 0.53 as the temperature increases from 593 to 680 °C (see Figure 4.19g). This shows that while $\{11\bar{2}0\}$ facets are dominant at the low growth temperature, gradually the $\{10\bar{1}0\}$ facets dominate with the increase of temperature, suggesting the relative facet stability and nanostructure shapes are tunable by controlling the growth conditions. This also indicates that although the shape evolution is predominantly driven by the growth thermodynamics which is explained by the modeling in Section 4.4.3, growth kinetics may play a role too.

The phenomenon of $\{11\bar{2}0\}$ facet being more stable at the low temperature is also observed during the growth of nanomembranes. Figure 4.20 shows the top view SEM images of InP nanostructures with different nanoslot directions grown at a lower temperature of 593 °C. In the cases of short $<10\bar{1}>$ and 15° off nanoslots, the nanostructures are only bounded by $\{11\bar{2}0\}$ side facets. $\{10\bar{1}0\}$ side facets start to appear and gradually become larger with the increase of nanoslot length. In comparison, nanostructures with $<11\bar{2}>$ oriented nanoslots mainly consist of $\{11\bar{2}0\}$ side facets, independent of the nanoslot length. These results suggest that $\{11\bar{2}0\}$ facet is more stable than $\{10\bar{1}0\}$ facet under the current growth conditions at lower temperature. $\{11\bar{2}0\}$ side facet is therefore playing the dominant role that $\{10\bar{1}0\}$ facet is playing at high temperature in determining shapes of nanostructures.

Generally the stability of the crystal facets is inversely proportional to their surface energy (γ), thus our results indicate that $\{10\bar{1}0\}$ facets have a lower surface energy at higher temperatures while the reverse is true for $\{11\bar{2}0\}$ facets. More precisely, the temperature effect on the surface energy is probably because of the effect of temperature on the percentage decomposition of PH_3 precursor[12] and therefore the phosphorus chemical potential plays a key role in determining the facet surface energy.[13, 14] Nanostructure shapes are affected by growth temperature, particularly at lower temperature where there are some unwanted effects such as irregular shape, rough surface and non-uniformity (see Figure 4.2, Figure 4.3, Figure 4.19a, and Figure 4.20).

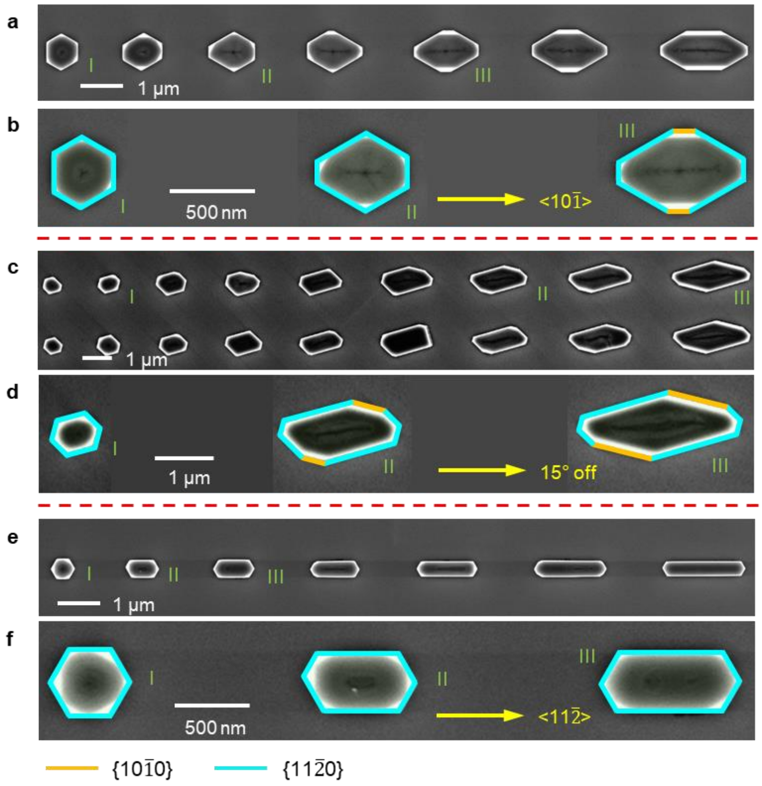

Figure 4.20: Top view SEM images of InP nanostructures grown at 593 °C in the CCS reactor. The directions of nanoslots are along (a,b) $<10\bar{1}>$, (c,d) 15° off and (e,f) $<11\bar{2}>$. The high magnification SEM images of nanostructures I, II and III in (a), (c) and (e) are shown in (b), (d) and (f), respectively. $\{10\bar{1}0\}$ and $\{11\bar{2}0\}$ side facets are indicated by the orange and aqua solid lines, respectively, in (b), (d) and (f).

4.6. Structural and optical studies of InP nanostructures

In this section, we will examine structural and optical properties of InP nanostructures with membrane-, prism- and ring-like shapes grown at the optimal conditions in the CCS reactor.

4.6.1. Structural study

So far, we have demonstrated good morphology of SAE InP nanostructures with different shapes grown under the optimal conditions. Still, there is a very high requirement on their crystalline quality for device applications since it has been shown that relevant figures of merit such as quantum efficiency is directly affected by the presence of crystalline defects.[4]

For <11$\bar{2}$> orientated nanomembranes (Figure 4.21a), the dominant side facets are perpendicular to <11$\bar{2}$0> zone axis which is an ideal incident direction for an electron beam for planar defects investigation. Selective area diffraction pattern (SADP) confirms that they are of WZ phase (Figure 4.21b). Atomically-resolved high-angle annular dark-field (HAADF) image taken at the interface shows a twin-plane above the ZB substrate at the start of WZ growth and a stacking fault, as indicated by white arrows (Figure 4.21c). Except for this single stacking fault, all subsequent atomic layers follow the WZ stacking sequence without observation of any misaligned layer along [0001] direction until end of the membrane, evidenced by the atomically-resolved HAADF images taken from the middle and top sections (Figure 4.21d,e).

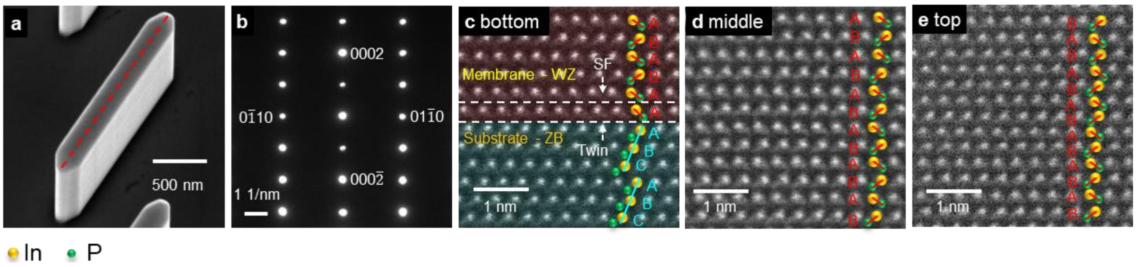

Figure 4.21: (a) 30° tilted SEM image, (b) SADP, atomic-resolved HAADF images taken along <11$\bar{2}$0> zone axis from the (c) bottom, (d) middle and (e) top sections of the <11$\bar{2}$> oriented nanomembrane. The dotted red line in (a) indicates the direction and position where the TEM lamellas were prepared by the FIB system.

Structural analysis for <10$\bar{1}$> oriented nanomembranes is more challenging since the TEM lamella needs to be rotated 30° to the <11$\bar{2}$0> zone axis, which weakens the quality of TEM images. Still, careful TEM examinations confirm that the <10$\bar{1}$> nanomembrane shows a pure WZ structure without twins and stacking faults (see Figure 4.22).

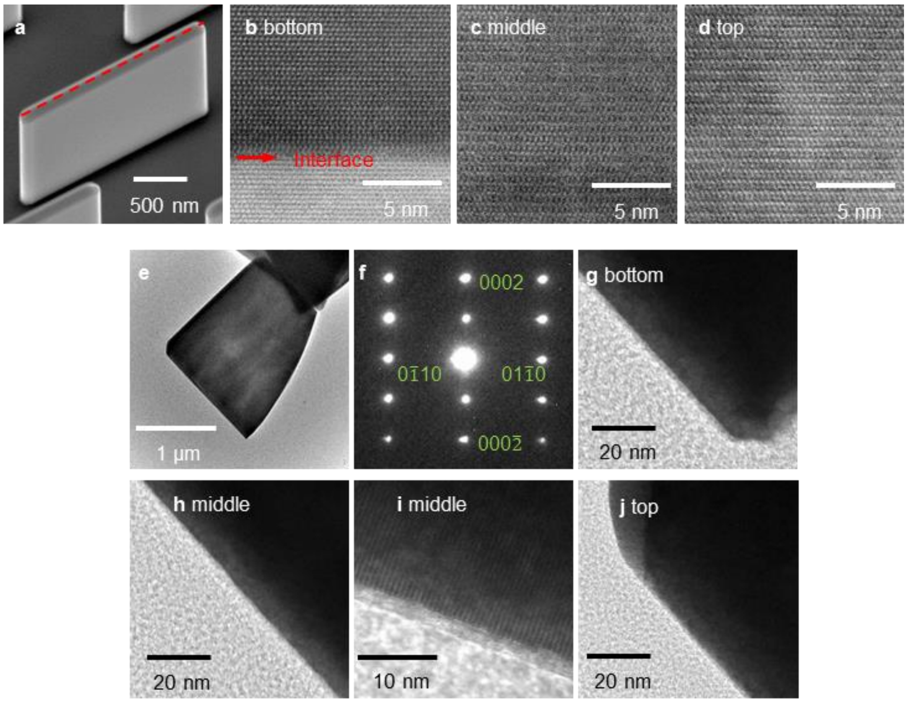

Figure 4.22: Electron micrographs of $<10\bar{1}>$ oriented nanomembranes. (a) 30° tilted SEM image, high resolution HAADF images taken along $<11\bar{2}0>$ zone axis from the (b) bottom, (c) middle and (d) top sections of a nanomembrane. Dotted red line in (a) indicates the direction and position where the TEM lamella was prepared by FIB. (e) Low magnification TEM image, (f) SADP, high resolution TEM images also taken along $<11\bar{2}0>$ zone axis from the (g) bottom, (h,i) middle and (j) top regions of another nanomembrane.

Besides, the prism-like nanostructure grown from a 15° off oriented nanoslot (Figure 4.23a-e) and the ring-like nanostructure (Figure 4.23f-j) also have a perfect WZ structure except at the bottom sections. A stacking fault close to the interface is found in the prism-like nanostructure, but WZ phase starts from the first layer, showing an atomically sharp interface for the phase transformation (Figure 4.23c). As for the ring-like nanostructures, the initial stage of epitaxy (*i.e.* nucleation and filling up of opening) seems more complicated since nine layers of ZB segments with the rotational twinning planes are formed inside of patterned opening (Figure 4.23g,i). In addition to the geometric factor of the patterns, the minor fluctuation caused by the unstable growth conditions at the beginning of epitaxy might be responsible for the formation of these defects. After the initial growth stage, crystal stacking sequence of all examined nanostructures becomes stable, growing as pure WZ phase. Basically, the above structural investigations indicate that all nanoshapes have a perfect WZ crystal structure.

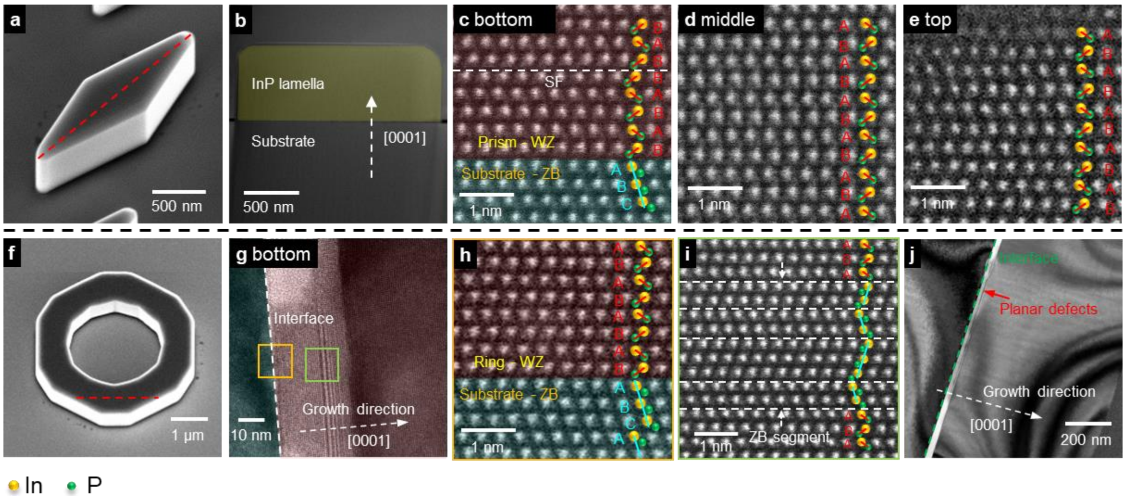

Figure 4.23: (a) 30° tilted SEM image, (b) low magnification TEM image, high-resolution HAADF images taken along $\langle 11\bar{2}0\rangle$ zone axis from (c) bottom, (d) middle and (e) top regions of the prism-like nanostructure with 15° off oriented nanoslot. (f) 30° tilted SEM image and (g) TEM image taken along $\langle 11\bar{2}0\rangle$ zone axis from bottom of the InP ring-like nanostructure. (h) and (i) show high-resolution HAADF images from the highlighted area marked by orange and green boxes in (g), respectively. (j) $\langle 11\bar{2}0\rangle$ zone axis bright field TEM image indicates that planar defects only can be found next to the interface and do not penetrate the whole layer. Dotted red lines in (a) and (f) indicate the direction and position where the TEM lamellas were prepared by FIB.

We also noticed that planar defects at bottom section of the ring-like nanostructure disappear somewhere instead of penetrating the whole layer (Figure 4.23j).[15] Since the dimension of patterned openings can be larger than adatom diffusion length,[4] multiple nuclei are most likely formed in the initial stages, which subsequently expand and merge with each other to form a single crystal. The merging of nuclei could interrupt the spread of those planar defects.

4.6.2. Optical study

Figure 4.24 shows SEM and panchromatic CL images of highly ordered arrays of InP nanostructures with membrane-, prism-, and ring-like shapes. Strong and uniform luminescence from each element is observed for all the nanostructure arrays regardless of their geometries, which is also confirmed by intensity profiles along the dashed lines (see inserts in Figure 4.24d-f). More surprisingly, InP nanomembranes show uniform emission even when their length is up to 50 µm (Figure 4.25). Thus, in addition to the excellent crystalline structure, superior optical properties as the prerequisite for photonic applications are achieved. Room-temperature photoluminescence spectra have a sharp emission peak at 871 nm for all the different nanoshapes, consistent with the bandgap of WZ crystal structure (Figure 4.26).

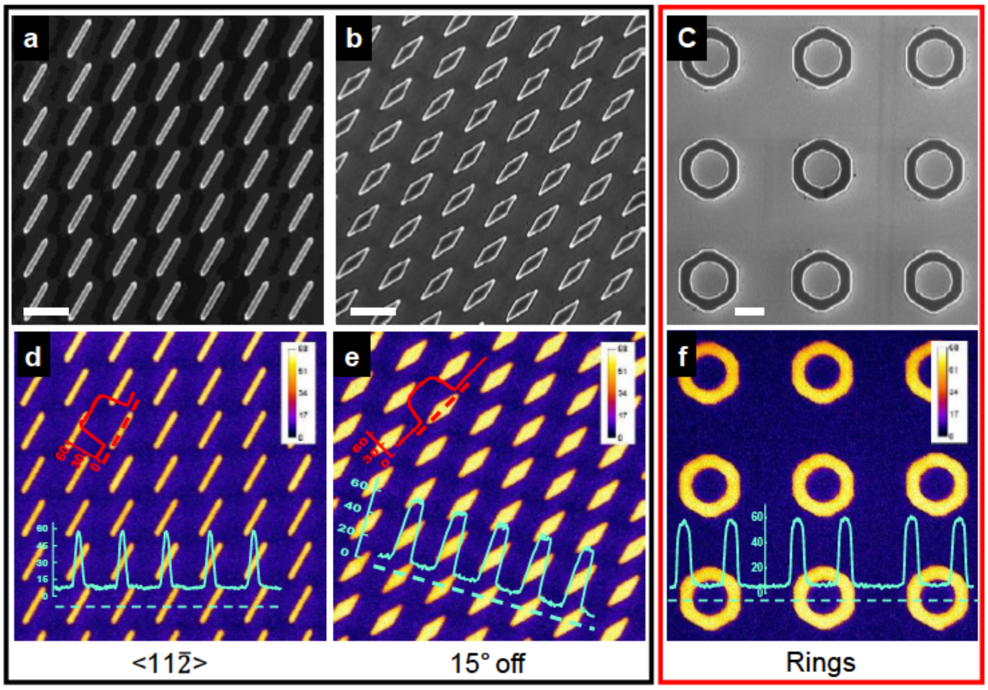

Figure 4.24: Strong and uniform photon emission from InP nanostructures with different shapes. (a-c) Top-view SEM and (d-f) corresponding panchromatic CL images of InP nanostructure arrays. The overlays in (d-f) show emission intensity profiles along the dash lines. Scale bars 2 μm.

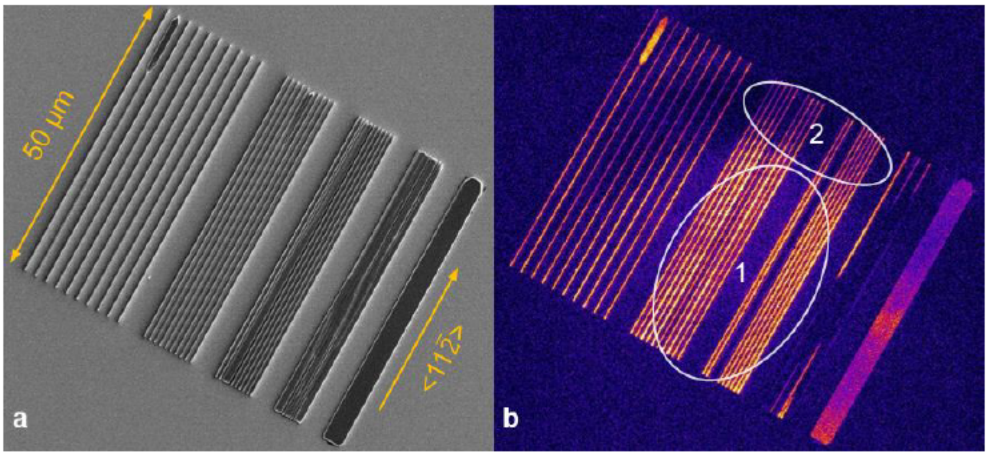

Figure 4.25: (a) SEM and (b) panchromatic CL images of <11$\bar{2}$> oriented InP nanomembranes grown under the optimal conditions in the CCS reactor, showing the ability to obtain uniform luminescence in a very long nanomembranes. The non-uniform luminescence among different areas, for example area 1 and area 2, is due to the limited collection area of the system rather than variation of optical quality.

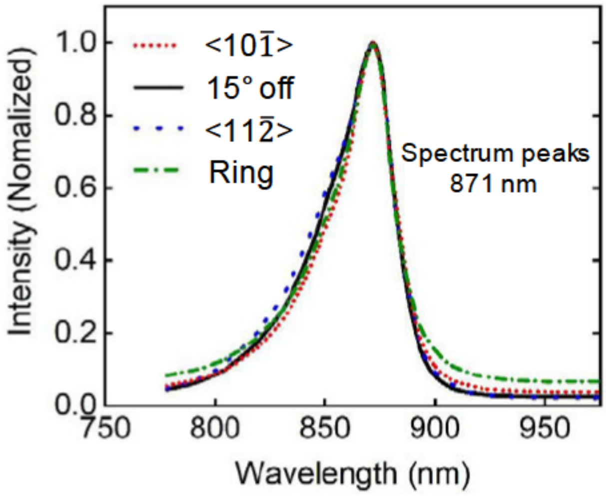

Figure 4.26: PL spectra of nanostructures grown from <10$\bar{1}$>, 15° off, <11$\bar{2}$> oriented nanoslots and nanoring, showing peaks at 871 nm at room temperature.

4.7. Summary

We optimize the growth conditions and then demonstrate InP nanostructures with membrane-, prism- and ring-like shapes grown by the catalyst-free SAE technique, expanding the research field from 1-D nanowires to more sophisticated 2-D and 3-D nanostructures. WZ InP is a good candidate for shape engineering since we found that $\{10\bar{1}0\}$ and $\{11\bar{2}0\}$ facets are able to be formed at the same time. The in-depth study of shape evolution with time, dimension and temperature indicates that the shape is determined by the designed pattern (geometry, dimension, orientation) and growth parameters (temperature, time *etc.*). A proposed thermodynamic model confirms that the driving force of the shape transformation is the minimization of the total surface energy during growth. We also found that the stability of $\{10\bar{1}0\}$ and $\{11\bar{2}0\}$ facets varies with the growth conditions. The $\{10\bar{1}0\}$ ($\{11\bar{2}0\}$) facet is more stable at the higher (lower) growth temperature which we attribute to the change of their surface energy. Under the optimal conditions at high temperature, highly uniform arrays of InP nanostructures can be obtained with excellent WZ crystal structure. Moreover, panchromatic CL results show the strong luminescence in the nanostructure arrays with high homogeneity for each nanostructure element in the array. The understanding of growth mechanism is crucial to designing and growing nanostructures with the desired geometries. Our results represent the important steps towards shape engineering of nanostructures to realize advanced optoelectronic and electronic devices based on sophisticated and controllable geometries.

References

1. X. Duan, Y. Huang, Y. Cui, J. Wang, and C. M. Lieber. Indium phosphide nanowires as building blocks for nanoscale electronic and optoelectronic devices. *Nature* 2001, vol. 409, no. 6816, p. 66.
2. Z. Wang, B. Tian, M. Pantouvaki, W. Guo, P. Absil, J. Van Campenhout, C. Merckling, and D. Van Thourhout. Room-temperature InP distributed feedback laser array directly grown on silicon. *Nature Photonics* 2015, vol. 9, no. 12, p. 837.
3. R. Ahrenkiel. Measurement of minority-carrier lifetime by time-resolved photoluminescence. *Solid-State Electronics* 1992, vol. 35, no. 3, pp. 239-250.
4. Q. Gao, D. Saxena, F. Wang, L. Fu, S. Mokkapati, Y. Guo, L. Li, J. Wong-Leung, P. Caroff, H. H. Tan, and C. Jagadish. Selective-area epitaxy of pure wurtzite InP nanowires: high quantum efficiency and room-temperature lasing. *Nano Letters* 2014, vol. 14, no. 9, pp. 5206-5211.
5. V. Dubrovskii, N. Sibirev, G. Cirlin, I. Soshnikov, W. Chen, R. Larde, E. Cadel, P. Pareige, T. Xu, and B. Grandidier. Gibbs-Thomson and diffusion-induced contributions to the growth rate of Si, InP, and GaAs nanowires. *Physical Review B* 2009, vol. 79, no. 20, p. 205316.
6. K. Ikejiri, Y. Kitauchi, K. Tomioka, J. Motohisa, and T. Fukui. Zinc blende and wurtzite crystal phase mixing and transition in indium phosphide nanowires. *Nano Letters* 2011, vol. 11, no. 10, pp. 4314-4318.
7. X. Yuan, J. Yang, J. He, H. H. Tan, and C. Jagadish. Role of surface energy in nanowire growth. *Journal of Physics D: Applied Physics* 2018, vol. 51, no. 28, p. 283002.
8. N. Sibirev, M. Timofeeva, A. Bol’shakov, M. Nazarenko, and V. Dubrovskiĭ. Surface energy and crystal structure of nanowhiskers of III–V semiconductor compounds. *Physics of the Solid State* 2010, vol. 52, no. 7, pp. 1531-1538.
9. T. A. Ibrahim, R. Grover, L. Kuo, S. Kanakaraju, L. Calhoun, and P. Ho. All-optical AND/NAND logic gates using semiconductor microresonators. *IEEE Photonics Technology Letters* 2003, vol. 15, no. 10, pp. 1422-1424.
10. K. Amarnath, R. Grover, S. Kanakaraju, and P.-T. Ho. Electrically pumped InGaAsP-InP microring optical amplifiers and lasers with surface passivation. *IEEE Photonics Technology Letters* 2005, vol. 17, no. 11, pp. 2280-2282.
11. B. E. Little, J. S. Foresi, G. Steinmeyer, E. R. Thoen, S. T. Chu, H. A. Haus, E. P. Ippen, L. C. Kimerling, and W. Greene. Ultra-compact Si-SiO2 microring resonator optical channel dropping filters. *IEEE Photonics Technology Letters* 1998, vol. 10, no. 4, pp. 549-551.
12. G. Stringfellow. A critical appraisal of growth mechanisms in MOVPE. *Journal of Crystal Growth* 1984, vol. 68, no. 1, pp. 111-122.

13. M. Fahed, L. Desplanque, C. Coinon, D. Troadec, and X. Wallart. Impact of P/In flux ratio and epilayer thickness on faceting for nanoscale selective area growth of InP by molecular beam epitaxy. *Nanotechnology* 2015, vol. 26, no. 29, p. 295301.

14. Q. Liu, N. Moll, M. Scheffler, and E. Pehlke. Equilibrium shapes and energies of coherent strained InP islands. *Physical Review B* 1999, vol. 60, no. 24, p. 17008.

15. A. M. Sanchez, Y. Zhang, E. W. Tait, N. D. Hine, H. Liu, and R. Beanland. Nonradiative step facets in semiconductor nanowires. *Nano Letters* 2017, vol. 17, no. 4, pp. 2454-2459.

CHAPTER 5

Understanding shape transformation and phase transition of InP nanostructures grown on substrates of various orientations

5.1. Introduction

In the previous chapter, we have demonstrated SAE of highly uniform InP nanostructure arrays with pure WZ phase on InP {111}A substrates, such as nanowires, nanomembranes, and nanorings. InP {111}A substrates were preferentially chosen considering that {111} substrates are most commonly used for III-V epitaxy of nanowires due to the preferred growth direction along the <111> direction. However, in the quest for exploration of complex nanostructures and improved functionalities, substrates of other orientations have been used to grow nanostructures with desired morphology and phase as well as fabricate advanced devices.[1-20] For example, Gazibegovic *et al.*[8] demonstrated the direct formation of InSb networks on InP {100} substrates with exposed {111}B facets and their applications in quantum devices. ZB and WZ phase films with a thickness of a few nanometers and area up to 50 μm^2 were simultaneously grown on InP {100} substrates by controlling the crystal growth directions, showing the possibility of phase transitions in a large area.[3]

Understanding growth mechanisms is the cornerstone for III-V epitaxy. Till now, the mechanism studies of SAE of III-V nanostructures are largely limited to nanowires and only a few focus on those with more complex geometries.[21-23] Furthermore, SAE of 2D and 3D nanostructures may have different growth mechanisms, as reported in the formation of twin-free GaAs nanosheets[24] and large size pure WZ InP nanomembranes.[25] The lack of a unified model or understanding for SAE of III-V nanostructures with different shapes seriously impedes the advances in the growth of these nanostructures, which is increasingly required for advanced device applications.

In this chapter, InP nanostructures grown by the SAE technique on InP {100}, {110}, {111}B, {112}A and {112}B substrates are investigated and discussed in Section 5.3. Two growth models are proposed in Section 5.4 to explain the experimental observations in Section 5.3. Through systematic analyses, we build a unified fundamental understanding for SAE of InP nanostructures with various geometries and both crystal phases regardless of substrate orientation. Specifically, by using carefully designed patterns in the mask layer, shape evolution of InP nanostructures from nanowire to nanomembrane on substrates of different orientations was investigated. Our in-depth analysis of the morphology and crystal structure reveals the dependence of nucleus formation on substrate orientation, the correlation between crystal phase and growth direction as well as the mechanism for morphology transformation. The polarity difference leads to different WZ and ZB phase formation during nucleation on A/B-polar substrates and growth along A/B-polar directions, respectively, which could be explained by a nucleation-based model. Meanwhile, the crystal phase remains the same during nucleation on non-{111} low-index substrates and growth along non-<111> low-index directions, leading to pure ZB phase formation. Our findings provide a pathway to simultaneously tailor the shape and crystal phase of nanostructures. For instance, WZ/ZB homojunction with type-II band alignment is demonstrated in a layered nanomembrane form. In addition to the confinement effect imposed by various opening arrays, shape transformation is essentially driven by the minimization of total surface energy. The understanding gained from this chapter lays the foundation for the design and fabrication of advanced III-V semiconductor devices based on complex geometrical nanostructures.

5.2. Experimental methods

A ~30 nm-thick SiO_x layer was deposited on InP substrates with different orientations, including {111}A, {111}B, {100}, {110}, {112}A and {112}B substrates, where various patterned openings were fabricated through a series of processing steps (see Chapter 3.2 for the details). These openings consist of different dimensions and geometries. Moreover, they were carefully designed based on the crystallographic nature of substrates for investigating growth fundamentals and achieving novel nanomembranes. More details will be provided in the later sections.

All InP nanostructures discussed in this chapter were grown in the same run via a horizontal flow reactor of Aixtron 200/4 MOCVD system with a low pressure of 100 mbar and total flow of 15 L/min. Trimethylindium (TMIn) and phosphine (PH_3) were used as precursors while ultrahigh purity H_2 was used as the carrier gas. Prior to growth, the patterned substrates were annealed at 750 °C in PH_3 ambient for 10 minutes to remove the possible contaminants. The optimized growth conditions for SAE of WZ phase InP array on InP {111}A substrate as discussed in Chapter 4 were used here, i.e., growth temperature of 750 °C, growth duration of 7 min, PH_3 mole fraction of 2.67×10^{-3}, and TMIn mole fraction of 9.07×10^{-6}.[26]

The morphology of InP nanostructures was characterized by an FEI Verios 460 SEM system operated at a voltage and current of 5 kV and 200 pA, respectively. CL mapping was carried out in the FEI Verios 460 SEM system equipped with a Gatan MonoCL4 Elite module. TEM lamellae were prepared by an FEI Helios Nanolab FIB system and subsequently examined by a JEOL JEM-ARM200f Cs-corrected STEM and a JEOL 2100F TEM.

5.3. Studies of InP nanostructures grown on InP substrates of different orientations

5.3.1. InP {100} substrate

InP nanostructures grown on InP {100} substrates are first investigated since this substrate orientation has been widely used for epitaxy of III-V nanostructures and in the Si-based industry. In addition to conventional nanoholes, low-index oriented nanoslot patterns are carefully designed for possible formation of the corresponding nanostructures along low-index planes. For instance, Figure 5.1a schematically illustrates arrays of openings in the SiO_x mask consisting of holes and slots along the low-index $\langle 10\bar{1}\rangle_{\perp}$ and $\langle 10\bar{1}\rangle_{\parallel}$ directions on InP {100} substrate. Note that although in-plane <10$\bar{1}$> orientation is non-polar, they could be recognized as two different $\langle 10\bar{1}\rangle_{\perp}$ and $\langle 10\bar{1}\rangle_{\parallel}$ directions in consideration of their relationship with the {111}A and {111}B side planes shown in Figure 5.1a, which leads to different growth behaviours. The low-index planes closest to {100} top surface are indicated to clarify the crystalline facets and/or orientations of the nanoslots and grown nanostructures (Figure 5.1a). Both WZ and ZB phases are formed in our InP nanostructures, thus the crystalline facets and orientations are named using the three-index scheme for simplicity unless specified otherwise.

For the $\langle 10\bar{1}\rangle_{\perp}$ oriented opening array, nanostructure geometry evolves from V-shaped nanowire to V-shaped nanomembrane with the increase in slot length (Figure 5.1b,c). The branches of V-shaped nanowires grow along the <111>A directions, which can be determined by the angles between them and the substrate (see lower panel in Figure 5.1c). Structural characterization demonstrates WZ phase in the main body of the branched nanowires but ZB phase at the intersection region, as shown in Figure 5.2. By increasing the openings from nanoholes to nanoslots along the $\langle 10\bar{1}\rangle_{\perp}$ direction, V-shaped nanomembranes are formed (see

Figure 5.1b,c). The two branches of V-shaped nanomembranes grow along the <111>A directions as well, as confirmed by the angles between them and the substrate (Figure 5.3a-c). CL spectral peak mapping indicates that the nanomembrane branches are of WZ phase while their intersection is ZB phase (see upper panel in Figure 5.1c). The atomistic model in Figure 5.3d illustrates the crystal phase distribution of the cross-sectional V-shaped nanomembranes. Apparently, the crystallography of V-shaped nanomembranes is similar to V-shaped nanowires, which suggests the same growth behaviour of these two kinds of V-shaped nanostructures.

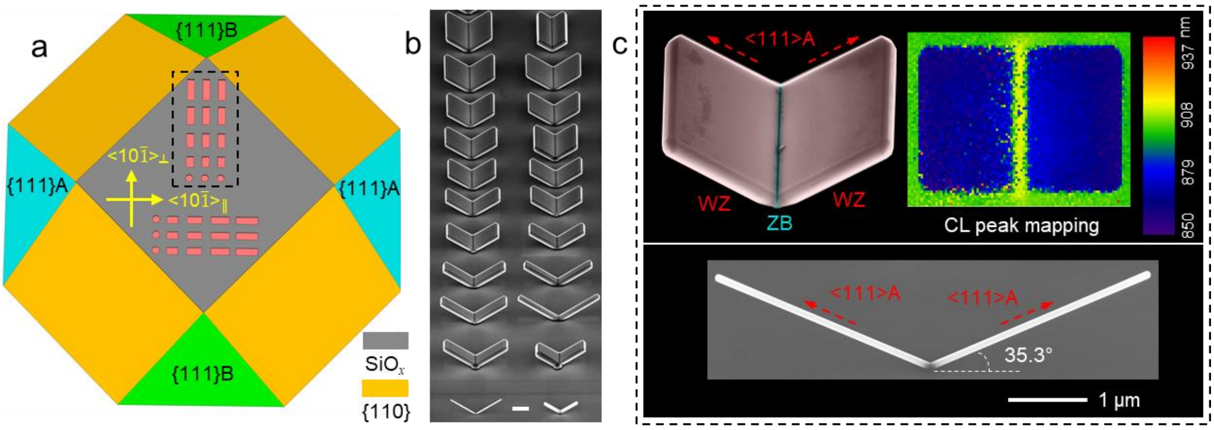

Figure 5.1: (a) Schematic of the designed openings on InP {100} substrate and low-index {111}A, {111}B, {110} planes closest to substrate top surface. (b) 54° tilted SEM image of the nanostructures grown from $\langle 10\bar{1}\rangle_{\perp}$ oriented openings, showing the evolution from V-shaped nanowires to V-shaped nanomembranes with the increase of slot length. (c) 30° tilted SEM images of a V-shaped nanowire (lower panel) and a V-shaped nanomembrane (upper panel). Also shown is the top view CL spectral peak mapping of the V-shaped nanomembrane. Red dotted arrows in (c) indicate the <111>A directions. Scale bar in (b) is 1 µm.

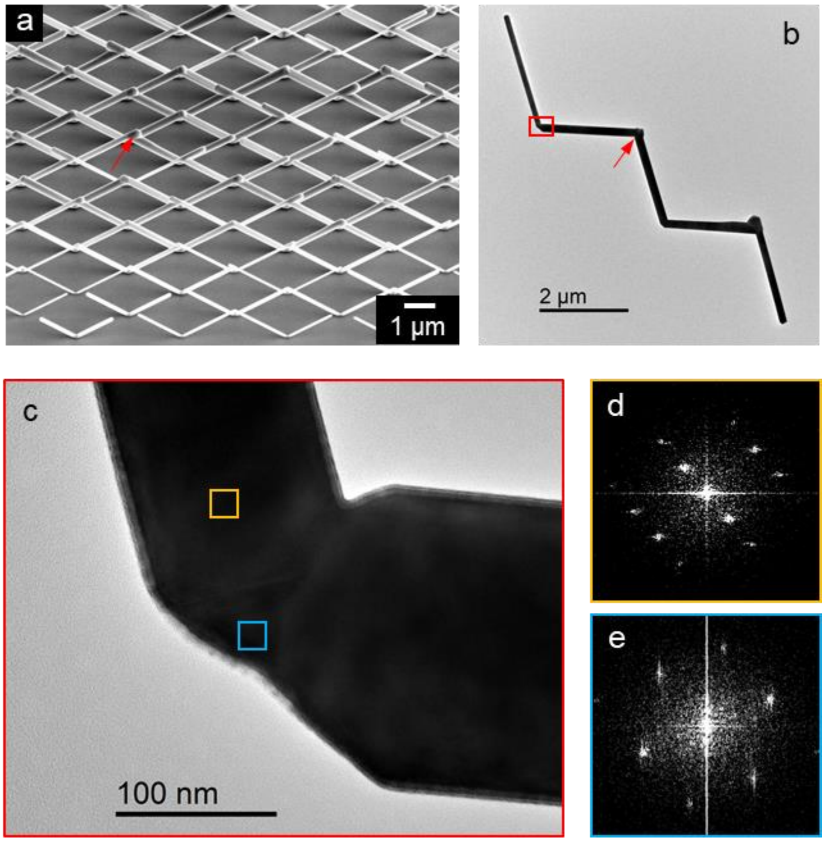

Figure 5.2: Electron micrographs of V-shaped InP nanowires grown on InP {100} substrate. (a) SEM image at 30° tilt and (b) low-magnification TEM image of V-shaped nanowires. Note that some of the nanowire branches merge, as indicated by the red arrows in (a,b). (c) High magnification TEM image from the rectangular area in (b) which is the bottom region of the V-shaped nanowire. (d,e) FFT patterns extracted from the corresponding areas in (c) indicate that the branches and intersection region of the V-shaped nanowires are of WZ and ZB phases, respectively.

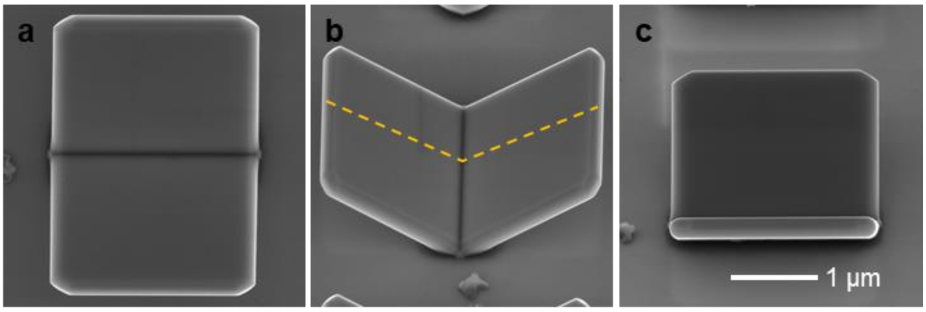

Top view 45° tilted view 56° tilted view

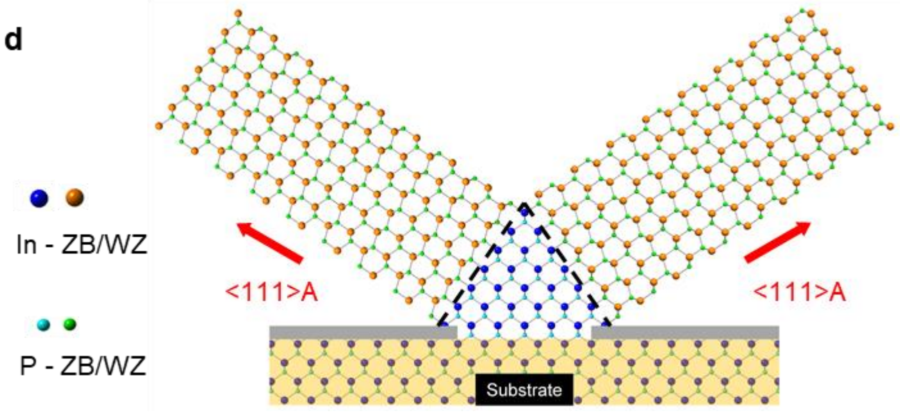

Figure 5.3: (a-c) SEM images at different view angles of a V-shaped nanomembrane grown from in-plane $\langle 10\bar{1}\rangle_{\perp}$ oriented nanoslot on InP {100} substrate. One of the branches seems to be vertical to the substrate at 56° tilted view which suggests that the branches of V-shaped nanomembrane are grown along the <111>A directions since the angle between [100] and [111] directions is 54.7°. (d) Atomistic model of the cross-section of the V-shaped nanomembrane, as indicated by the dotted line in (b). The scale bar in (c) applies to all SEM images.

In contrast, when opening array is along with the $\langle 10\bar{1}\rangle_{\parallel}$ direction, the nanostructures evolve differently in terms of shapes and crystal phases (see Figure 5.4). In the case of short nanoslots, in addition to the main morphology of V-shaped nanowires, two more symmetric structures (labeled as segment-II) can be seen at the bottom end near the intersection between the two nanowires (Figure 5.4b). CL spectral peak mapping in Figure 5.4f indicates that these segments are of WZ phase as well as the nanowire branches (labeled as segment-I), suggesting that they are formed due to epitaxial growth along the <111>A directions but interrupted by the substrate. In addition, CL examination shows the existence of a ZB phase region at the intersection area which is attributed to direct epitaxy on the InP {100} substrate at early stages of growth (Figure 5.4f). This ZB phase region forms four {111}A facets for subsequent growth of segments-I and II, as schematically indicated in Figure 5.5. The morphology changes in Figure 5.4b-e show that growth of segment-I along the <111>A directions is greatly reduced with the increase of nanoslot length. One of the segment-II disappears, followed by the exposure of the {111}B facet of the ZB region (marked by the colored area III), as confirmed by the CL spectral peak mapping (see Figure 5.4g,h).

The exposed {111}B facet and the remaining segment-II (Figure 5.4c) evolve in different ways with further increase of nanoslot length. Specifically, they both grow larger, but due to limited growth time, segment-II is truncated along the <111>A direction, resulting in (0001) facet as marked by the colored area IV (Figure 5.4d). For long nanoslot length, the truncated segment-II becomes thinner. Ultimately segment-II and the ZB region together form a tilted nanomembrane consisting of a pair of ZB and WZ layers (Figure 5.4e,h).

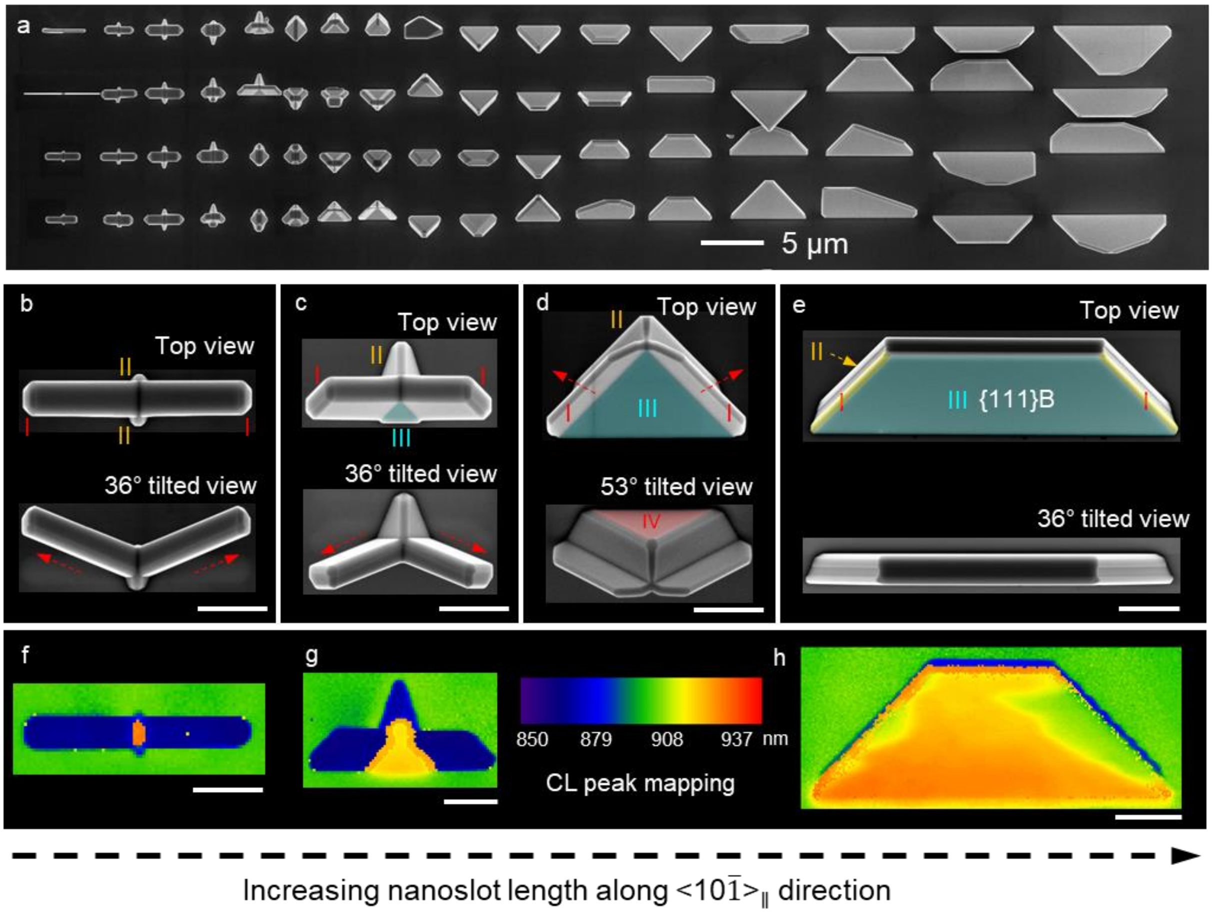

Figure 5.4: (a) Top view SEM image of InP nanostructure array with the increase of slot length along the $\langle 10\bar{1}\rangle_{\parallel}$ direction on InP {100} substrate, showing the shape evolution from V-shaped nanowire to inclined nanomembrane. (b-e) SEM images taken at different views of the nanostructures with increasing nanoslot length along the $\langle 10\bar{1}\rangle_{\parallel}$ direction. Red arrows indicate the <111>A directions. (f-h) Top view CL peak mapping of the nanostructures with morphologies similar to those in (b,c,e), respectively, indicating the evolution of the crystal phase. Note that CL characterization is not necessarily carried out on the same nanostructures shown in (b-e). Scale bars are 1 µm.

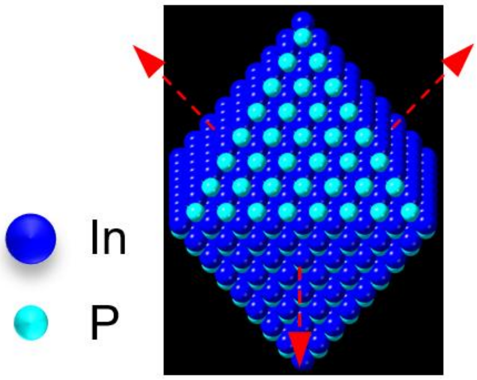

Figure 5.5: 3D atomistic model of a ZB InP crystal showing the possible {111} facets. Red arrows indicate the <111>A directions where the upward and downward ones correspond to growth directions of the nanowire branches (segment-I) and segment-II of the V-shaped nanowire in Figure 5.4b, respectively.

The detailed structure of the layered nanomembrane in Figure 5.4e was investigated by a Cs-corrected STEM, and the results are shown in Figure 5.6. The lamella was prepared by cutting the nanomembrane along the red dotted line using focused ion beam (see inset in Figure 5.6a). Figure 5.6a shows a low-magnification bright field STEM image of the cross-sectional nanomembrane along the <10$\bar{1}$> zone axis. The left- and right-hand regions are of WZ and ZB phases, respectively, as determined by the Fast Fourier transform (FFT) patterns extracted from the corresponding areas (Figure 5.6d,e). The layered nanomembrane is mainly bound by A-polar (0001) and B-polar {111}B side facets. Moreover, the top surfaces are dominated by {10$\bar{1}$0} and {111}B facets on the respective sides. An interface about two-thirds of the way from the edge of the nanomembrane can be seen due to the contrast caused by different crystal structures, indicated by the orange arrow in Figure 5.6a. This interface divides the nanomembrane into two different WZ and ZB layers which is further confirmed by the atomically-resolved HAADF images in Figure 5.6b,c. These structural investigations correspond to our CL analysis in Figure 5.4h in terms of the crystal phase distribution. Figure 5.6b,c also shows that a faulted ZB region with two stacking orientations is formed at the interface. In addition, we found that the interface extends from a region close to but outside of nanoslot opening (Figure 5.6a,c), suggesting that the WZ layer only forms after the opening is fully filled up with the ZB crystal. Careful TEM examination reveals a high quality WZ layer with a few planar defects, which is evidenced by the atomically-resolved HAADF STEM images from areas f and g in Figure 5.6a (see Figure 5.6f,g). In constrast, the ZB layer on the right-hand side of the faulted ZB region is free of twins or stacking faults except for a small area near the {111}B surface (Figure 5.6i,j). This also makes it difficult to locate the interface between ZB InP substrate and the epitaxial layers (Figure 5.6h). The coexistence of high quality WZ phase and defect-free ZB phase suggests that growth conditions of the two different crystal structures are not mutually exclusive.[27]

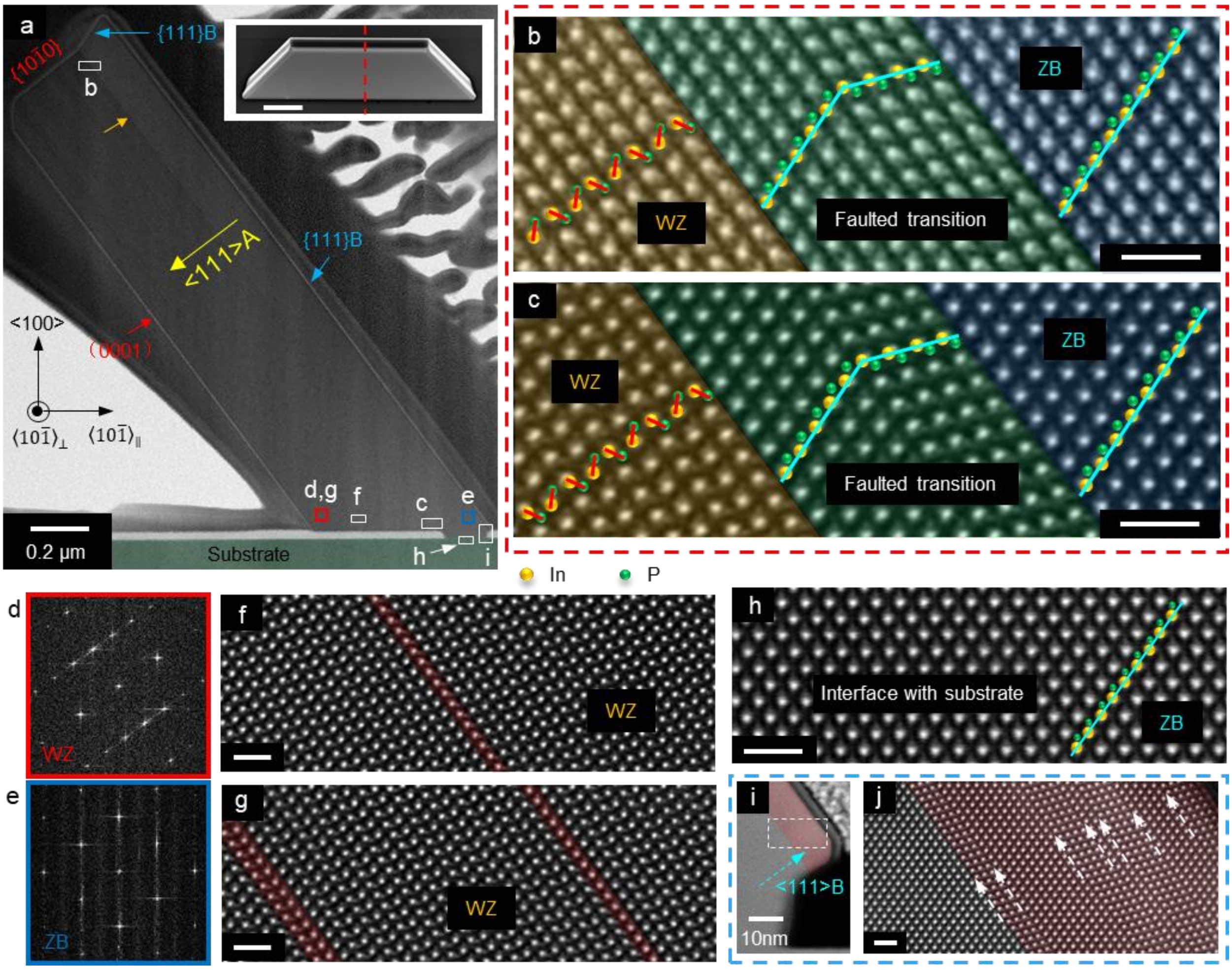

Figure 5.6: Crystallography of the layered WZ/ZB InP nanomembrane grown on InP {100} substrate. Top view SEM image in the inset of (a) shows a nanomembrane in which the dashed line indicates the direction and position where the TEM lamella is prepared. (a) Low-magnification bright field STEM image taken along the <10$\bar{1}$> zone axis. The orange arrow indicates the interface between ZB and WZ layers. (d,e) FFT patterns show WZ and ZB phases of the corresponding colored areas in (a). (b,c,f-h) Atomically-resolved HAADF STEM images from the corresponding regions marked in (a). The orange and green spheres representing indium and phosphorus atoms, respectively, are superimposed in (b,c,h), highlighting the atomic stacking sequence. (i) STEM image of area i in (a). (j) Atomically-resolved HAADF STEM image of the marked area in (i) in which the white arrows indicate twins. Scale bars: inset in (a) 1 µm; (b,c,f-h,j) 1 nm.

To understand how the different crystal phases are formed in the layered nanomembrane, a growth model is proposed and illustrated based on the structural analysis above (see Figure 5.7). Initially, pure ZB phase InP nucleates and fills up the nanoslot opening with the same stacking sequence as the ZB InP {100} substrate. After that, growth of nanomembrane with WZ/ZB homojunction proceeds via three different processes. Firstly, InP starts to grow along the <11$\bar{2}$> direction, forming a ZB layer with a thickness approximately the same as the width of nanoslot opening. This layer is free of planar defects since generally only growth along <111> directions forms twin planes or stacking faults, which is similar to the growth of pure ZB InP film[3] and GaAs nanowires[28] along non-<111> directions. Moreover, the growth along the <11$\bar{2}$> direction leads to the formation of {111}A and {111}B planes on each side facets. Secondly, on the newly formed {111}A side facet, WZ phase InP layer starts to grow along the <111>A direction as would InP nanostructures grown on InP {111}A substrate by SAE.[26, 29] Although a few faulted ZB layers are initially formed at the beginning of facet growth (see Figure 5.6b,c), subsequent growth results in a high quality WZ phase layer. Thirdly, growth is also occuring on the {111}B side facet along the <111>B direction resulting in the formation of a thin ZB layer with high density of twins, as indicated by the white dotted arrows in Figure 5.6j. Based on TEM analysis, in additon to the difference in crystal phases, the lateral growth rate along the <111>B direction is an order of magnitude lower than that along <111>A direction, i.e. the WZ facet is growing faster than the ZB facet. The growth of different crystal phases on the side facets of the nanomembrane as a result of different polarities essentially leads to the formation of the WZ/ZB homojunction nanomembrane. It demonstrates the possibility of tailoring the crystal phase by controlling growth directions and side facets.[27] WZ/ZB homojunction has been intensively investigated in III-V nanowires, in which they exhibit type-II band alignment and have a great significance in different applications.[30-33] Here, we expand the WZ/ZB homojunction structure from 1D nanowires to 2D nanomembranes, which can potentially provide additional functionality such as separation of charge carriers to the respective nanomembrane layer for high speed devices.

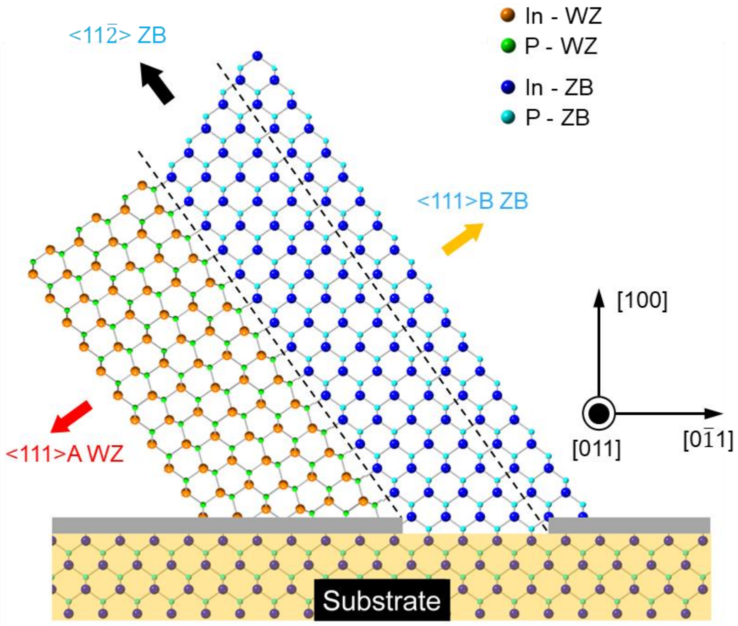

Figure 5.7: Atomistic model of the cross-section of layered nanomembranes grown on InP {100} substrate.

Compared with vertical and WZ nanowires, nanomembranes, and nanorings grown on InP {111}A substrates as discussed in Chapter 4, the unique InP nanostructure arrays on {100} substrate suggests that exploring growth behaviour on substrates of different orientations is vital in deepening the fundamental understanding of growth as well as producing more interesting heterostructures. Thus, we further investigate growth on InP {110}, {111}B, {112}A and {112}B substrates in the following sections.

5.3.2. InP {110} substrate

For InP {110} substrate, the opening array is designed along the <11$\bar{2}$> directions as schematically illustrated in Figure 5.8a. In this case, the {111} planes parallel to in-plane <11$\bar{2}$> oriented nanoslot is perpendicular to substrate. Vertical nanomembranes are expected according to the analysis of nanomembranes grown on {100} substrate, which is experimentally confirmed (see Figure 5.8b,d).

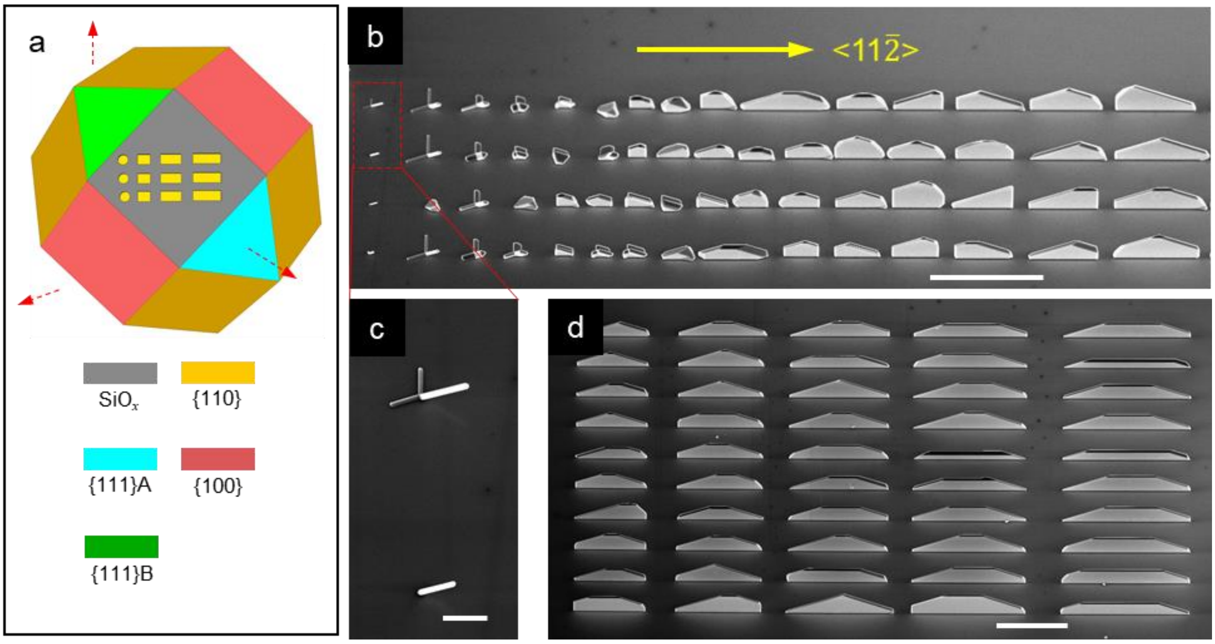

Figure 5.8: (a) Schematic diagram of the designed openings on InP {110} substrate and low-index {111}A, {111}B, {100} side planes closest to substrate top surface. Red dotted arrows indicate the <111>A directions. (b) SEM image at 30° tilted view of InP nanostructure array grown on InP {110} substrate, demonstrating the shape evolution from nanowire to vertical nanomembrane with the increase of slot length along the <11$\bar{2}$> directions. (c) Enlarged SEM image from the corresponding area in (b) showing that both tripod-like and unbranched nanowires can be formed when openings are nanoholes with small areas. (d) Vertical InP nanomembrane array with longer <11$\bar{2}$> oriented nanoslot length compared to those in (b). Scale bars: (b,d) 10 µm; (c) 1 µm.

Based on the crystallographic structure of cubic {110} substrate, there are two in-plane <111>A directions and one <111>A direction pointing upward (see Figure 5.8a). Since InP nanowires grown by SAE prefer to grow along the <111>A directions based on the analysis above, tripod-like nanowires are formed along these three directions from the nanoholes or short nanoslots (Figure 5.8b,c). Note that the in-plane <111>A oriented growth can be easily interrupted in the case of small opening, leading to the formation of unbranched nanowires (Figure 5.8b). With the increase of nanoslot length along the <11$\bar{2}$> direction, the nanostructures evolve from nanowires to vertical nanomembranes (Figure 5.8b). More details of the shape evolution can be found in Figure 5.9 where the enlarged SEM images of the representative nanostructures and the corresponding CL spectral peak mapping are demonstrated. CL peak wavelength image in Figure 5.9e indicates the three branched nanowires have WZ phase with a ZB phase at the intersection. Moreover, the ZB intersection region becomes longer and taller with increasing slot length, forming a vertical nanostructure bound by {111}B side facets, as highlighted by the teal coloured areas in Figure 5.9b,c and confirmed by the CL results (Figure 5.9f,g). Meanwhile, axial growth of the <111>A oriented nanowire branches gradually decreases (Figure 5.9a-c). When the nanoslot is longer than a critical length, branch I evolves into a WZ layer against the ZB part while the branches II and III tend to vanish, eventually leading to the formation of the vertical nanomembrane (Figure 5.9d).

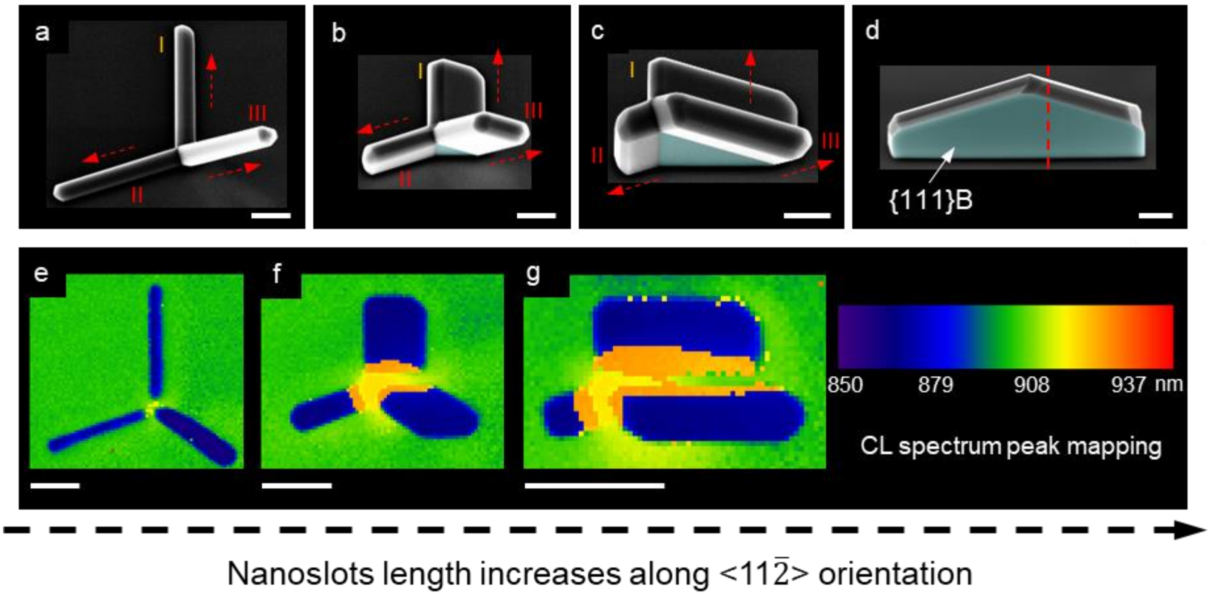

Figure 5.9: (a-d) 30° tilted SEM images of InP nanostructures grown on {110} InP substrate, demonstrating shape transformation from the tripod-like nanowire to vertical nanomembrane with the increase of slot length along the <11$\bar{2}$> direction. Red arrows indicate the <111>A directions. (e-g) Corresponding CL peak mapping of nanostructures in (a-c), indicating their crystal phase distribution. Scale bars: (a-d) 500 nm; (e-g) 1 µm.

Structural investigation of the vertical nanomembrane in Figure 5.9d suggests that its growth mechanism is the same as the layered nanomembrane grown on {100} substrates (see Figure 5.10). Figure 5.10a is a low-magnification STEM image of the cross-sectional nanomembrane where ZB and WZ phase layers can be identified by the different coloured areas, as confirmed by the FFT patterns in Figure 5.10b,c. Atomically-resolved HAADF STEM images from the areas d and e in Figure 5.10a confirms the formation of WZ/ZB homojunction (see Figure 5.10d,e). Careful STEM examination reveals that the ZB layer is free of planar defects and the WZ layer is of high quality with few defects, which are evidenced by the atomically-resolved STEM images from areas f, g and i in Figure 5.10a (see Figure 5.10f,g,i). Similar to inclined nanomembranes grown on {100} substrate, here, the main part of the ZB layer is formed due to epitaxial growth directly on the {110} substrate along the <10$\bar{1}$>

direction. The absence of planar defects is also due to the growth direction deviating from <111> orientations.[3] Meanwhile, the lateral growth along the <111>A and <111>B directions form a thick WZ layer and a thin ZB layer, respectively. Before the growth of the high quality WZ layer, a thin transition layer with twin planes is formed (Figure 5.10d,e), similar to the case of nanomembranes grown on {100} substrate. Note that the interface between ZB and WZ layers is close to but outside of opening as well (Figure 5.10a,h), which is similar to that the WZ layer is grown along the <111>A directions after the nucleation and filling up of opening with ZB InP crystal.

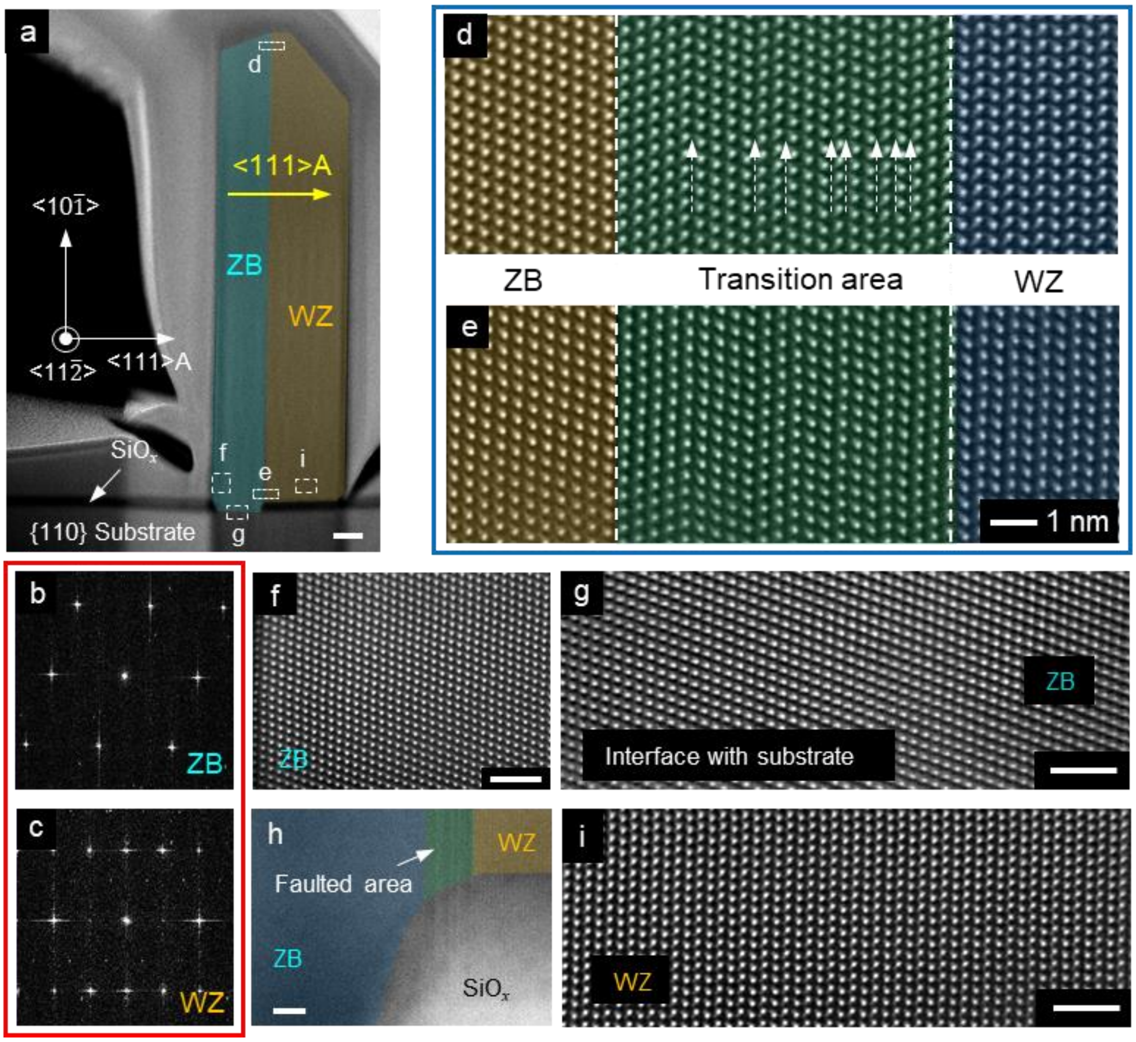

Figure 5.10: Structural investigation of a vertical InP nanomembrane grown from <11$\bar{2}$> oriented nanoslots on InP {110} substrate. (a) Low-magnification HAADF STEM image taken along the <11$\bar{2}$> zone axis of a nanomembrane cross-section from the region indicated by the red dashed line in Figure 5.9d. (b,c) FFT patterns extracted from the areas f and i in (a) showing the ZB and WZ phases, respectively. (d-g,i) Atomically-resolved HAADF STEM images taken along the <10$\bar{1}$> zone axis from the corresponding areas in (a). Scale bars: (a) 100 nm; (f,g,e) 2 nm; (h) 5 nm.

5.3.3. InP {111}B, {112}A and {112}B substrates

The above studies in Sections 5.3.1 and 5.3.2 demonstrate the possibility of simultaneously engineering the shape and crystal phase of InP nanostructures by changing the pattern design with consideration of the crystallographic nature of the adopted substrates. Similar shape evolution for nanomembranes grown on {100} and {110} substrates suggests the same growth fundamentals, which provides new insights into the design of nanostructure geometries, networks, and homo/hetero-structures for advanced devices. In short, InP nanostructures prefer to grow along the <111>A directions and form WZ phase. If <111>A oriented growth is restricted by the substrate and/or designed pattern, they could grow along other low-index orientations with a ZB phase. In the case of nanoslots which are parallel to {111} planes, nanomembranes are bound by {111}B and (0001) side facets. These growth behaviours help predict the shape and crystal phase of the InP nanostructures, for example, growth on InP {111}B, {112}A and {112}B substrates as will be discussed in this section.

The patterned openings on InP {111}B substrate are schematically illustrated in Figure 5.11a. It can be seen that nanoslots are designed to be aligned parallel with a {111}A side plane (i.e., along the <$10\bar{1}$> directions). Tripod-like nanowires along three <111>A directions are grown due to the weak confinement effect of nanoholes and short nanoslots (see Figure 5.11b,c), which has also been observed by Ikejiri et al.[34] As expected, the three branches in the tripod-like nanowires are WZ phase and their intersection region is ZB phase, which is confirmed by CL results (see Figure 5.12). Moreover, the ZB intersection region suggests that InP directly grown on InP {111}B substrate at the initial stage is of ZB phase.[34] With the increase of slot length along the <$10\bar{1}$> direction, nanostructures evolve from tripod-like nanowires to tilted nanomembranes when a strong confinement effect is imposed from nanoslots that are long (Figure 5.11b), similar to observed shape evolution of InP nanostructures on {100} and {110} substrates. These tilted nanomembranes are aligned parallel with {111} side planes, determined by the angle (70.5°) with respect to substrate (see Figure 5.11d). Figure 5.11e indicates that nanomembranes grown from long <$10\bar{1}$> oriented nanoslots have a high yield. Besides, CL examinations demonstrate that the inclined nanomembranes also form a pair of WZ and ZB layers as with the two other cases discussed earlier (Figure 5.13). Note that the WZ layer is grown upward.

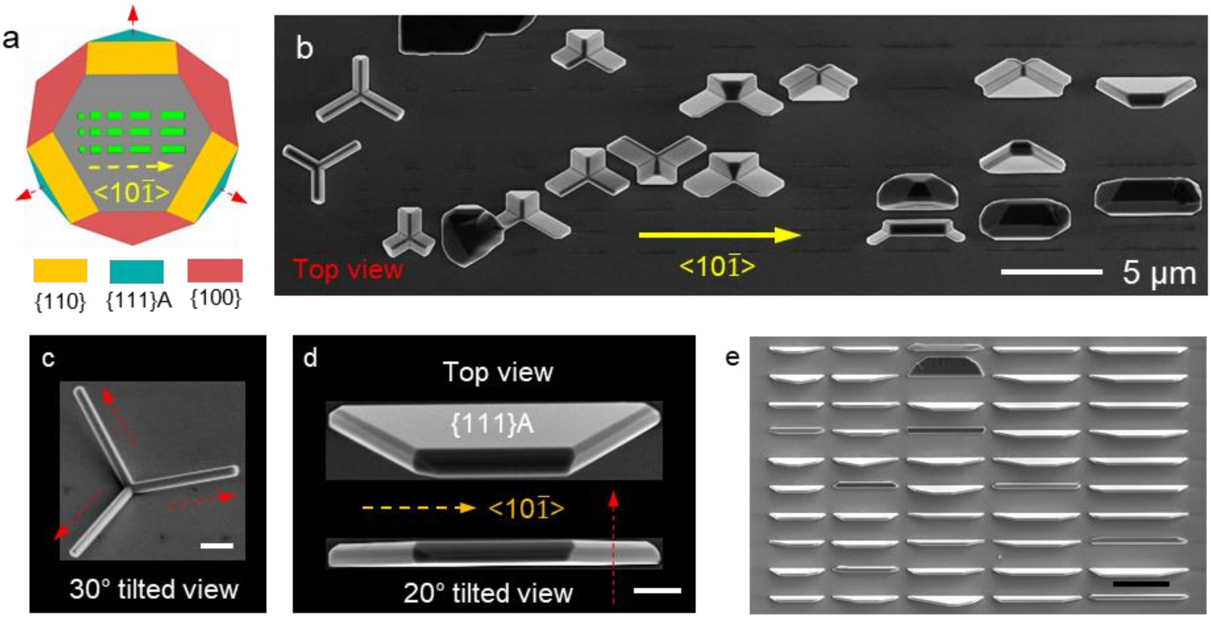

Figure 5.11: (a) Schematic diagram of the designed openings (i.e., nanoholes and <10$\bar{1}$> oriented nanoslots) on InP {111}B substrate. (b) Top view SEM image of InP nanostructures grown from the opening array showing the shape evolution from nanowires to inclined nanomembranes with the increase of slot length. Enlarged SEM images of (c) tripod-like nanowire and (d) tilted nanomembrane grown from a nanohole and a <10$\bar{1}$> oriented slot, respectively. Red arrows in (a,c,d) indicate the <111>A directions. (e) Top view SEM image of InP nanomembrane array demonstrating the high yield of nanomembranes. Scale bars: (c,d) 1 μm; (e) 10 μm.

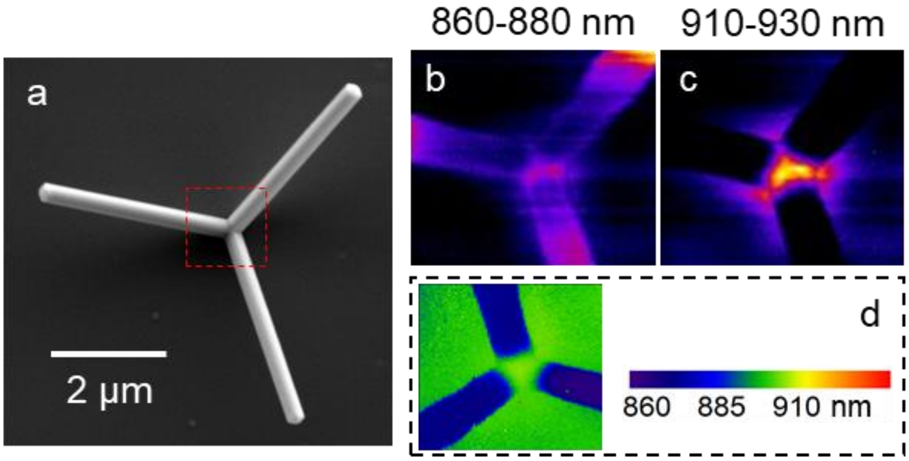

Figure 5.12: (a) Top view SEM image of a tripod-like InP nanowire grown on InP {111}B substrate. (b,c) False colour CL spectral mapping of the rectangular area in (a) at different wavelength range: (a) 860-880 nm, (c) 910-930 nm. (d) CL peak wavelength image.

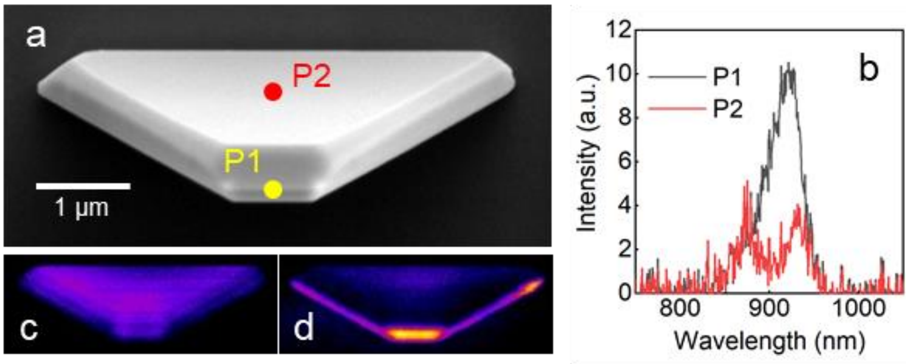

860-880 nm 910-930 nm

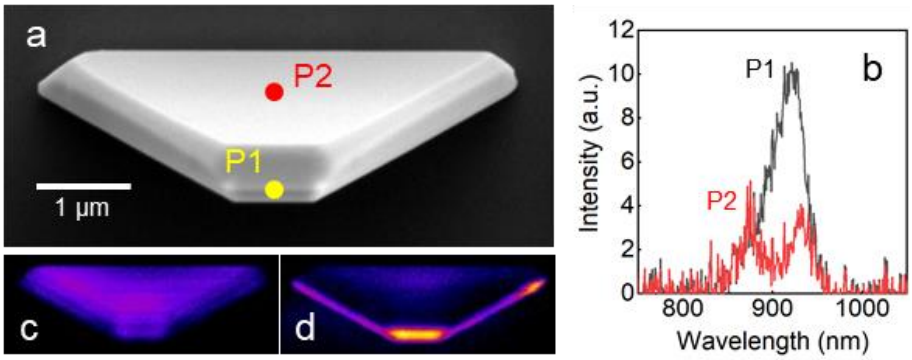

860-880 nm 910-930 nm

Figure 5.13: (a) Top view SEM image of InP nanomembrane grown from <10$\bar{1}$> oriented nanoslot on InP {111}B substrate. (b) CL spectra at the corresponding positions indicated in (a). (c,d) False colour CL spectral mapping at different wavelength range: (c) 860-880 nm, (d) 910-930 nm.

The upper panel of Figure 5.14a schematically depicts the opening array consisting of nanoholes and nanoslots on InP {112}A substrate. These nanoslots are designed along the in-plane <10$\bar{1}$> direction, and thus aligned parallel to two of {111}A planes with corresponding <111>A directions indicated by the dotted arrows. The two {111}A planes are either perpendicular or inclined with respect to {112}A substrate, referred to as the perpendicular and inclined {111}A planes, respectively. Figure 5.15a,b shows the shape evolution from V-shaped nanowire to vertical nanomembrane when InP nanostructures grow with the increase of opening along the <10$\bar{1}$> direction. The branches of V-shaped nanowire grow along both in-plane and out-of-plane <111>A directions, as indicated in the lower panel of Figure 5.14a. For long nanoslot length, vertical nanomembranes are formed. Note that the growth of nanomembranes parallel with the perpendicular {111}A plane is preferable compared to that parallel with the inclined {111}A plane. CL results indicate that these vertical nanomembranes also consist of both ZB and WZ layers (see Figure 5.15c-g). Moreover, CL panchromatic mode image shows an interface which is caused by the contrast between ZB and WZ layers (Figure 5.15d). CL spectral peak mapping in Figure 5.15e,f and spectra in Figure 5.15g confirm that the upper part of the nanomembrane is WZ phase while the lower part is of ZB phase.

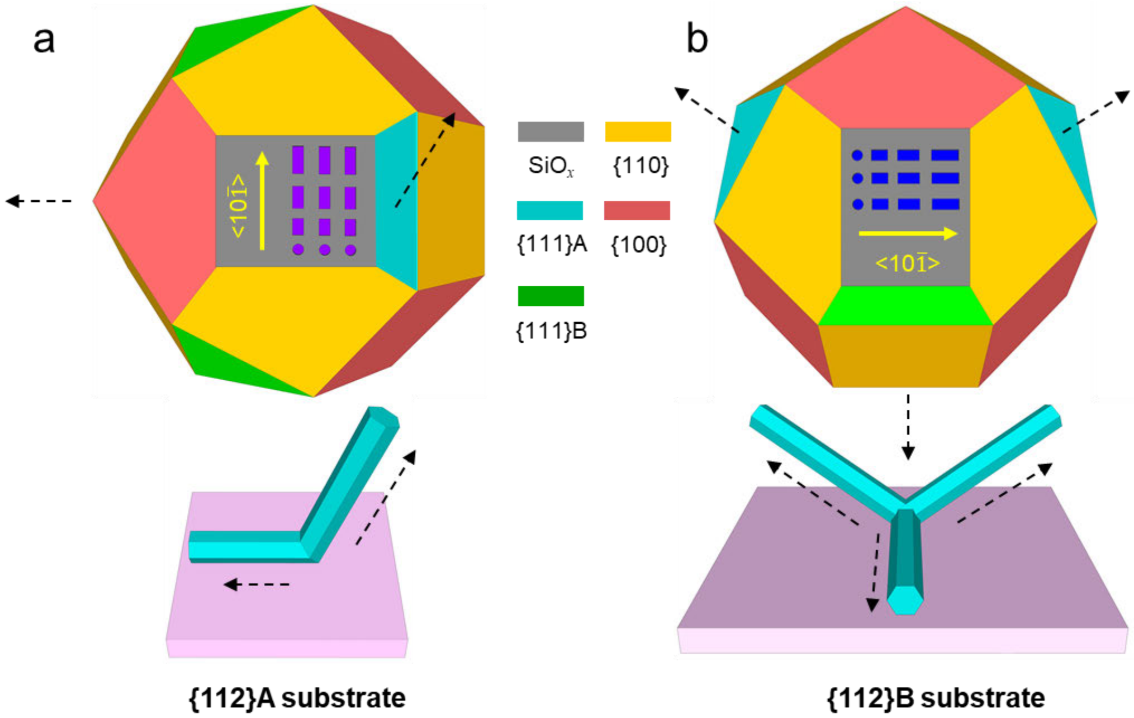

Figure 5.14: Schematic diagrams of the designed opening arrays and grown nanowires on (a) {112}A and (b) {112}B substrates, respectively. Opening arrays on both substrates consist of nanoholes and in-plane <10$\bar{1}$> oriented nanoslots with different length. Black dotted arrows indicate the <111>A directions. In addition to morphologies, the schematics of nanowires more clearly show the <111>A directions.

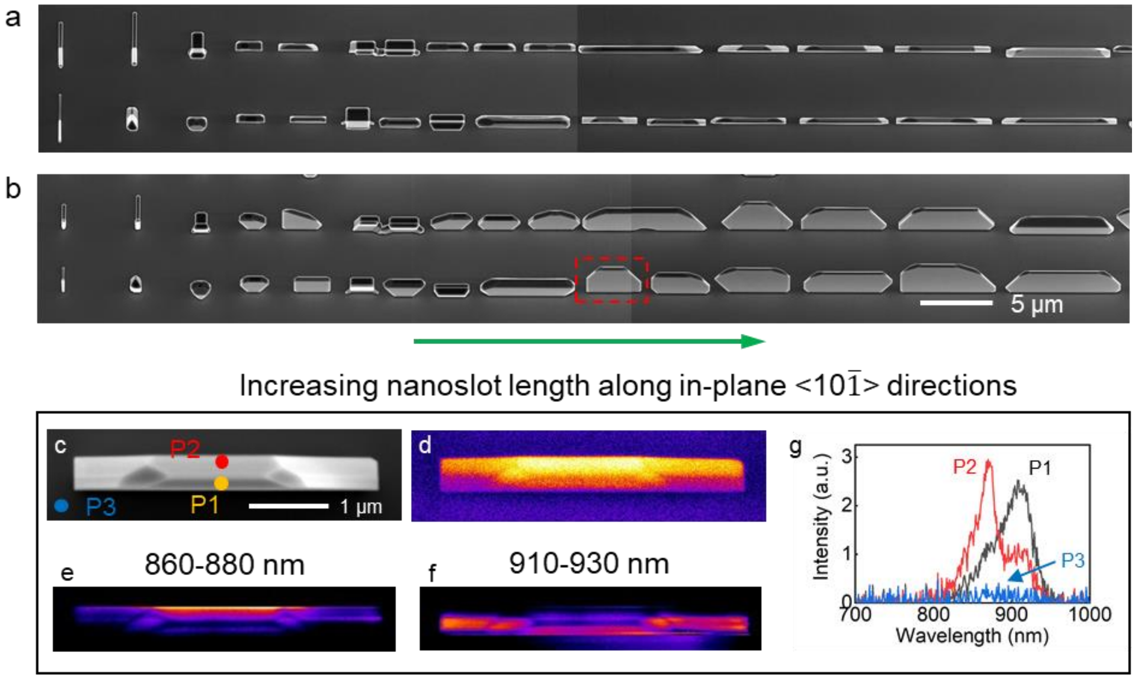

Figure 5.15: InP nanostructures grown on InP {112}A substrate. (a) Top view and (b) 30° tilted view SEM images of the nanostructures with the increase of slot length along the <10$\bar{1}$> directions, showing the shape evolution from V-shaped nanowire to vertical nanomembrane. (c-g) Further optical characterization of the nanomembrane highlighted in (b). (c) Top view SEM image. (d) Panchromatic mode CL image. (e,f) CL spectral mapping at different wavelength range: (e) 860-880 nm, (f) 910-930 nm. (g) CL spectra at the corresponding positions indicated in (c). Note that the scale bar in (b) applies to both SEM images in (a,b).

The designed openings on InP {112}B are schematically illustrated in the upper panel of Figure 5.14b. Likewise, the shape evolution from nanowire to nanomembrane are observed with the increase of opening along the <10$\bar{1}$> direction (Figure 5.16a). For nanoholes or short nanoslots, the tripod-like nanowires are grown. Their branches grow along an in-plane <111>A and two out-of-plane <111>A directions (see the lower panel in Figure 5.14b). For long <10$\bar{1}$> oriented nanoslots, either tilted or vertical (indicated by the orange arrow) nanomembranes grow. In comparison, the tilted nanomembranes are preferred. Both kinds of nanomembranes are aligned parallel to the {111} planes, demonstrating great similarity with the growth behaviours occurring on other substrates discussed above.

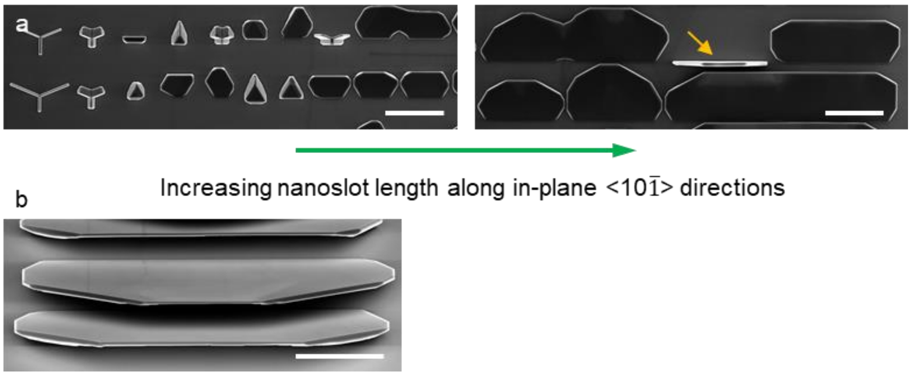

Figure 5.16: (a) Top view SEM image of InP nanostructures grown on InP {112}B substrate, showing the shape evolution from tripod-like nanowires to nanomembranes with the increase of opening along the <10$\bar{1}$> directions. (b) 55° tilted view SEM image of a few of the nanomembranes. Scale bars are 5 µm.

5.4. Growth models

The experimental results of InP nanostructures grown on InP substrates of different orientations have been investigated so far. However, to develop a unified understanding for SAE of InP arrays, the following questions need to be answered. Firstly, under identical growth conditions, how do different crystal phases form during nucleation along the <111>A and <111>B directions? Moreover, what is the underlying mechanism of shape transformation? The consistent growth behaviours on InP substrates of various orientations shown above as well as the growth on InP {111}A substrate discussed in Chapter 4 provide important information to help answer these questions. In the next sections, two models are established to address these questions.

5.4.1. Nucleation-based model on {111}A and {111}B substrates

5.4.1.1. Nucleus formation enthalpy

We first use a nucleation-based model to analyse the nucleation on both {111}A and {111}B planes. The formation enthalpy of an InP nucleus with *i* number of facets, Δ*G*, can be described by the following equation:[35]

$$\Delta G = -\Delta\mu N + \sum_{i=1}^{n} \gamma_i^{facet} \cdot A_i^{facet} + (\gamma_{int.} - \gamma_{base}) \cdot A_{base} \qquad (5.1)$$

where $\Delta\mu$ is the chemical potential change for nucleation per III-V pair; *N* is the number of III-V pairs for a given volume (V) of InP nucleus; γ_i^{facet}, $\gamma_{int.}$ and γ_{base} represent surface energy of the *i*-th exposed crystal facet, interfacial energy, and base (or substrate) surface energy, respectively; A_i^{facet} and A_{base} denote the surface area of the *i*-th exposed crystal facet and base surface area, respectively. $N = V/\Omega$ where $\Omega = {a_0}^3/4$ is the volume of a single III-V pair with a_0 as the InP lattice constant. The change in chemical potential per III-V pair, $\Delta\mu$, is calculated as follows:[36]

$$\Delta\mu = kT\left[\frac{P_{III}\,ln\frac{P_{III}}{P_{III,0}} + P_V\,ln\frac{P_V}{P_{V,0}}}{P_{III}+P_V}\right], \tag{5.2}$$

In equation (5.2), k and T are Boltzmann constant and the growth temperature, respectively; P_{III} and P_V are the partial pressures of In and P sources, respectively, while $P_{III,0}$ and $P_{V,0}$ are the equilibrium vapour pressures on solid InP surface at the given temperature T. Considering that the partial pressure of PH_3 is two orders of magnitude higher than that of TMIn, equation (5.2) could be simplified as[36]

$$\Delta\mu \approx kT\,ln\frac{P_V}{P_{V,0}} \tag{5.3}$$

Under the current growth condition, $\Delta\mu$ is calculated to be approximately 400 meV, which is comparable to chemical potential values that have been generally considered to be relatively low (group III-rich) for MOCVD growth.[35, 37]

Since crystal surface energies are known to change with surface reconstructions, which in turn depend on relative chemical potential during MOCVD growth, surface reconstruction has been taken into consideration while adopting crystal surface energies from the literature. The InP crystal surface energies used in this model are listed in Table 5.1, which are associated with surface reconstructions that are stable at low chemical potential conditions.[38, 39] In addition, all InP substrates have a ZB phase, hence $\gamma_{int.}$ is equal to 0 or $\gamma_{twin}$when nucleus is of ZB or WZ phases, respectively. Here γ_{twin} is the formation energy of the twin which causes the phase transition. The value of γ_{twin} is obtained from the literature, as listed in Table 5.1.[4] While most of values of facet surface energies are directly obtained from the literature, several assumptions are made since the surface energies of WZ facets are not well-reported. The surface energies of (0001) and $(000\bar{1})$ WZ facets are assumed to be similar to that of ZB $\{111\}$A and $\{111\}$B facets respectively, in consideration of the similar atomic configurations of their terminated surface.[40] On the other hand, while there is general agreement that the cleavage-type surface reconstruction of InP WZ $\{10\bar{1}0\}$ facet is stable under a wide range of relative chemical potentials,[41, 42] different calculated surface energies for this facet have been reported. In this model, we found that surface energy of $\{10\bar{1}0\}$ facet should be at least 4 eV/nm^2 for the calculation results to match experimental observations. Here, a value of 4.1 eV/nm^2 is used in this work, which is close to the calculated values reported in the literature.[41, 42]

Table 5.1: Values of surface energies of WZ and ZB InP facets and twin formation energy.[38, 39]

	{111}A	{111}B	{100}	(0001)	$(000\bar{1})$	$\{10\bar{1}\}$	$\{10\bar{1}0\}$	γ_{twin}
Surface energy (eV/nm^2)	5.0	5.8	6.2	5.0	5.8	5.5	4.1	0.056

5.4.1.2. Details of the investigated nuclei

Table 5.2: Details of the three different nuclei on {111}A and {111}B InP planes.

	{111}A base plane			{111}B base plane			Schematics
	Phase	Side facets	Top facets	Phase	Side facets	Top facets	
Case I	ZB	{111}B	{111}A or none	ZB	{111}A	{111}B or none	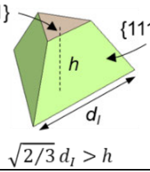 or 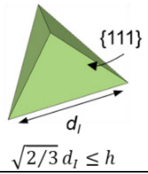
Case II	ZB	$\{10\bar{1}\}$	{111}A	ZB	$\{10\bar{1}\}$	{111}B	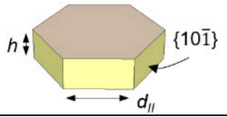
Case III	WZ	$\{10\bar{1}0\}$	(0001)	WZ	$\{10\bar{1}0\}$	$(000\bar{1})$	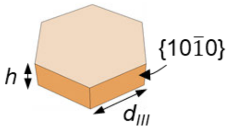

We restrict our model to the low-index facets according to the observed InP morphology: {111}A, {111}B, $\{10\bar{1}\}$, $\{10\bar{1}0\}$, (0001), and $(000\bar{1})$. The possible nuclei with different combinations of crystal phases, shapes and facets are listed in Table 5.2, categorized as Cases I, II and III. In this model, we consider that the nuclei have bilayer height of III-V pairs, given by $h = a_0\sqrt{3}/3$.[37] In Case I, the nucleus is of ZB phase, and have either truncated (when $\sqrt{6}/3\, d_I > h$) or ideal (when $\sqrt{6}/3\, d_I \le h$) tetrahedral geometry with {111} side facets, where d_I is the bottom side length of the tetrahedron. Although the intended nucleus shape for Case I is a truncated tetrahedron, the shape geometry becomes unphysical when d_I is shorter than a threshold related to the InP bilayer height ($d_I \le \sqrt{3/2}h$). Hence, for very small nucleus dimensions, Case I nucleus takes the shape of an ideal tetrahedron nucleus to avoid unphysical calculation results. Case II represents ZB nuclei with hexagonal geometry bound by $\{10\bar{1}\}$ side facets. In Case III, the nucleus has WZ phase and hexagonal geometry with six equivalent $\{10\bar{1}0\}$ side facets.

5.4.1.3. Calculations of free enthalpy formation of all the nuclei

Case I:

The volume of the nucleus in Case I (V_I) is given as follows:

$$V_I = \begin{cases} \frac{\sqrt{2}}{12} {d_I}^3, & \frac{\sqrt{6}}{3} d_I \le h \\ \frac{\sqrt{2}}{12}\left[{d_I}^3 - \left(d_I - \frac{\sqrt{6}}{2} h \right)^3 \right], & \frac{\sqrt{6}}{3} d_I > h \end{cases} ; \qquad (5.4)$$

According to equation (5.1), the formation enthalpy of a nucleus with ZB phase (ΔG_I) can be expressed as follow:

$$\Delta G_I = \begin{cases} -\Delta\mu \frac{V_I}{\Omega} + 3A_{side,I}\gamma_{side,I} - A_{base,I}\gamma_{base}, & \frac{\sqrt{6}}{3} d_I \le h \\ -\Delta\mu \frac{V_I}{\Omega} + 3A'_{side,I}\gamma_{side,I} + A_{top,I}\gamma_{top,I} - A_{base,I}\gamma_{base}, & \frac{\sqrt{6}}{3} d_I > h \end{cases} ; \qquad (5.5)$$

In equation (5.5), $A_{side,I} = A_{base,I} = \frac{\sqrt{3}}{4} {d_{\mathrm{I}}}^2$, $A'_{side,I} = \frac{3\sqrt{2}}{4} d_I h - \frac{3\sqrt{3}}{8} h^2$, $A_{top,I} = \frac{\sqrt{3}}{4}\left(d_I - \frac{\sqrt{6}}{2} h \right)^2$; $\gamma_{side,I} = \gamma_{\{111\}B}$ and $\gamma_{top,I} = \gamma_{base} = \gamma_{\{111\}A}$ in the case of {111}A substrate while $\gamma_{side,I} = \gamma_{\{111\}A}$ and $\gamma_{top,I} = \gamma_{base} = \gamma_{\{111\}B}$ in the case of {111}B substrate, where $\gamma_{\{111\}A}$ and $\gamma_{\{111\}B}$ are the corresponding surface energies of {111}A and {111}B facets.

Case II:

The volume of the nucleus in Case II (V_{II}) is given as follows:

$$V_{II} = \frac{3\sqrt{3}}{2} {d_{II}}^2 h \qquad (5.6)$$

where d_{II} is the hexagon side length, as shown in Table 5.2. In this model, the formation enthalpy of all the nuclei is calculated and compared under the condition of same volume. Thus, we have $V_I = V_{II}$. By substituting equation (5.6) into (5.4), d_{II} can be expressed in terms of d_I as follows:

$$d_{II} = \begin{cases} \sqrt{\frac{\sqrt{6} {d_I}^3}{54h}}, & \frac{\sqrt{6}}{3} d_I \le h \\ \sqrt{\frac{\sqrt{6}\left[{d_I}^3 - \left(d_I - \frac{\sqrt{6}}{2} h \right)^3 \right]}{54h}}, & \frac{\sqrt{6}}{3} d_I > h \end{cases} \qquad (5.7)$$

According to equation (5.1), the formation enthalpy of a nucleus with ZB phase in Case II (ΔG_{II}) can be expressed as follows:

$$\Delta G_{II} = -\Delta\mu \frac{V_{II}}{\Omega} + 6A_{side,II}\gamma_{side,II} \qquad (5.8)$$

where $A_{side,II} = d_{II}h$ and the surface energy of side facets $\gamma_{side,II} = \gamma_{\{10\bar{1}\}}$ in the case of both {111}A and {111}B substrates.

Case III:

The volume of the nucleus in Case III (V_{III}) is given as follow:

$$V_{III} = \frac{3\sqrt{3}}{2} {d_{III}}^2 h \tag{5.9}$$

where d_{III} is the hexagon side length, as shown in Table 5.2. Likewise, assuming that all the nuclei have the same volume, we have

$$d_{III} = d_{II} = \begin{cases} \sqrt{\frac{\sqrt{6}{d_I}^3}{54h}}, & \frac{\sqrt{6}}{3} d_I \leq h \\ \sqrt{\frac{\sqrt{6}\left[{d_I}^3 - \left(d_I - \frac{\sqrt{6}}{2}h\right)^3\right]}{54h}}, & \frac{\sqrt{6}}{3} d_I > h \end{cases} \tag{5.10}$$

According to equation (5.1), the formation enthalpy of a nucleus with WZ phase in Case III (ΔG_{III}) can be expressed as follows:

$$\Delta G_{II} = -\Delta\mu \frac{V_{III}}{\Omega} + 6A_{side,III}\gamma_{side,III} + A_{base,III}\gamma_{twin} \tag{5.11}$$

where $A_{side,III} = d_{III}h$, $A_{base,III} = \frac{3\sqrt{3}}{2} {d_{III}}^2$, the surface energy of the side facets $\gamma_{side,II} = \gamma_{\{10\bar{1}0\}}$ in the case of both {111}A and {111}B substrates.

Based on the calculations, the formation enthalpies (ΔG_I, ΔG_{II}, and ΔG_{III}) of all the nuclei grown on both {111}A and {111}B substrates with the increase of their feature size are plotted in Figure 5.17. The critical nucleus sizes are comparable to the values reported in the literature that are calculated based on the similar approaches, which supports the validity of this model. [36, 37]

For nucleation on {111}A planes, Δ*G* of the WZ phase nucleus (Case III) is much lower than its counterparts with ZB phase (Cases I and II), which explains why the growth of InP nanostructures along the <111>A directions forms the WZ phase. Moreover, the big difference of Δ*G* for Cases I/II and Case III suggests a low formation possibility of ZB segments which is consistent with high quality of all WZ phase nanostructures. On the contrary, the formation of ZB phase is preferred on {111}B planes due to the lowest Δ*G* of ZB phase nucleus (Case I). Δ*G* of a ZB nucleus in Case I on {111}B planes is only slightly lower than that of WZ nucleus in Case III, thus the sporadic formation of WZ phase is possible which is consistent with the observed twins in the thin ZB layer (Figure 5.6i,j). The preferred Case I nucleation mode on {111}B planes leads to the formation of three {111}A side facets where the nucleation mode of Case III on {111}A planes becomes energetically favourable. This explains the SAE of tripod-like nanowires with WZ branches and ZB intersection region grown on InP {111}B substrate.[34] In addition, for both {111}A and {111}B substrates, growth of vertical nanowire or nanomembrane with ZB phase is missing under the current growth conditions since they are not energetically favourable.

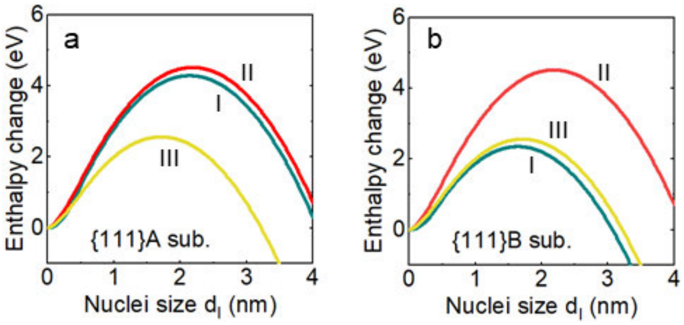

Figure 5.17: Formation enthalpies of three different nuclei on {111}A and {111}B InP planes as a function of their size.

5.4.2. Morphology transformation model

Following the nucleation-based model, another model is also proposed to explore the mechanism of shape evolution from nanowire to nanomembrane with the increase of nanoslot length. Since morphology change on InP substrates of different orientations is quite similar, only nanostructures grown on {100} substrates are discussed here (see Figure 5.4a-e). Based on the analysis above, InP initially fills up the opening and forms a shape bound by low-index facets, such as {111}A facets. Then, subsequent growth could occur along the <111>A directions with WZ phase or along other low-index orientations with ZB phase, eventually forming a nanostructure with different shapes. On InP {100} substrates, with increasing nanoslot length along the $\langle 10\bar{1}\rangle_{\parallel}$ direction, V-shaped nanowires evolve into an asymmetrical nanostructure (see Figure 5.18b,d). In other words, there are two different scenarios for growth from the $\langle 10\bar{1}\rangle_{\parallel}$ oriented nanoslots, namely the symmetrical V-shaped nanowire structure and the asymmetrical nanostructure, depending on the nanoslot length. In scenario 1, the ZB base of V-shaped nanowire consists of four {111}A facets and one top {100} facet, as schematically illustrated in Figure 5.18c, which is consistent with previous reports as well.[34, 43] In scenario 2, the ZB base has three {111}A, one {111}B and one {100} facets, as shown in Figure 5.18e. To compare the effective surface energies of the nanostructures in both scenarios under the assumption of identical volume, WZ phase segments on the three {111}A facets are considered in scenario 2 (see Figure 5.18f).

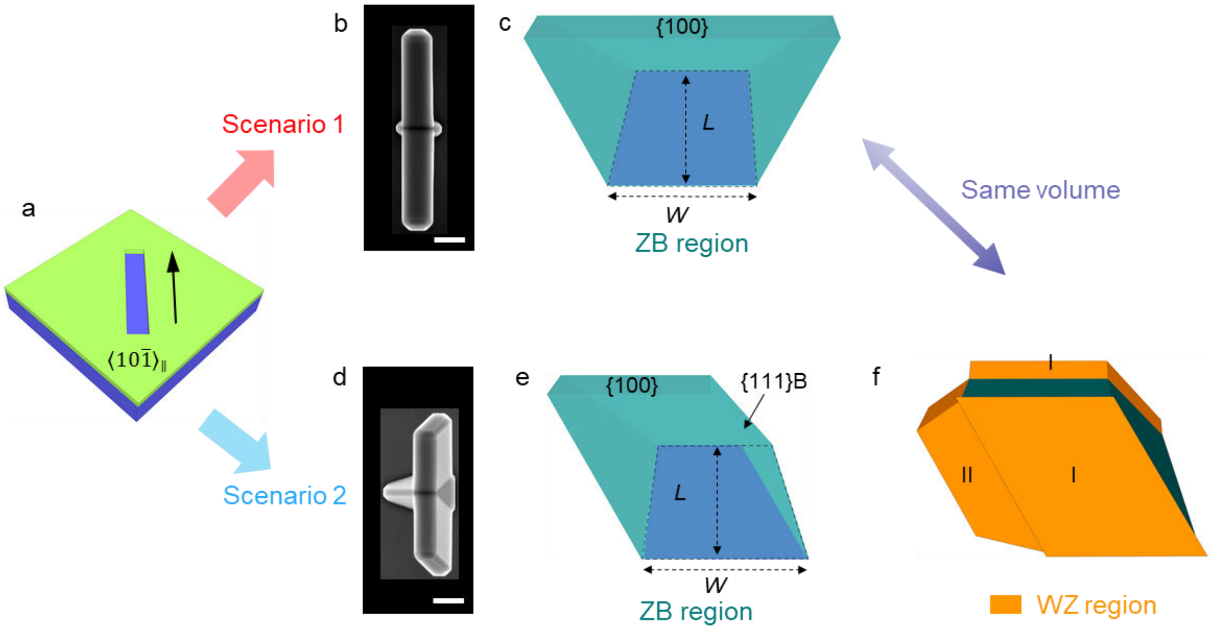

Figure 5.18: Shape transformation mechanism of InP nanostructures with the increase of nanoslot length along the $\langle 10\bar{1}\rangle_{\parallel}$ direction on InP {100} substrate. (a) Schematic of in-plane $\langle 10\bar{1}\rangle_{\parallel}$ oriented nanoslot. (b,d) SEM images of representative nanostructures demonstrate two different growth scenarios during the shape evolution. (c,e) Schematics of the corresponding ZB regions (e) with and (c) without {111}B facet. Nanoslot length and width are referred to as *L* and *W*, respectively. All unlabeled side facets are {111}A. (f) Schematic of the nanostructure grown on the ZB base in (e) with the same volume as the ZB region in (c). It shows that three WZ structures are grown on {111}A facets of the ZB base. Scale bars in (b,d) are 500 nm.

5.4.2.1. Effective formation enthalpy equation and base structure definition

In general, the formation enthalpy of an InP crystal could be expressed as equation (5.1). Under identical growth conditions and growth duration, it is assumed that the InP crystals grown in both scenarios have equal volume. As a result, the first term of equation (5.1) can be omitted in the following calculations. Furthermore, since the nanostructures in both scenarios have identical base interface with the substrate, the $\gamma_{base} \cdot A_{base}$ terms cancel out, and the effective formation enthalpy, $\Delta G'$, is finally simplified as follows:

$$\Delta G' = \sum_{i=1}^{n} \gamma_i^{facet} \cdot A_i^{facet} + \gamma_{int} \cdot A_{base} \; ; \qquad (5.12)$$

where $\gamma_{int} = \gamma_{twin}$ if the newly formed crystal has WZ phase, and $\gamma_{int} = 0$ if the newly formed crystal has ZB phase. γ_{twin} is obtained from the literature and listed in Table 5.1. Based on equation (5.12), the effective formation enthalpies in the two scenarios are calculated as a function of nanoslot length.

To simplify our calculations, it is postulated that the two nanostructures in both scenarios grow from a common base nanostructure, with its geometry shown in Figure 5.19. The base nanostructure is entirely in the ZB phase and has a truncated triangular shape, with three {111}A facets (coloured lime) and one {111}B facet (coloured brown) exposed on the sides, and one {100} facet exposed on top (coloured lavender). Figure 5.19b illustrates the truncated equilateral triangular {111}A facet on the left side of the structure, whereby the ratio between the truncated height *h* and untruncated height *H* (given by $H = \sqrt{3}L/2$, where L is the nanoslot length), *k*, is set to be 0.1. The consideration of a truncated {111} facet agrees with previously reported approaches to model nucleation at early growth stage.[34, 43] Further enthalpy calculations will only involve the exposed crystal facets of newly grown structure from the common base nanostructure.

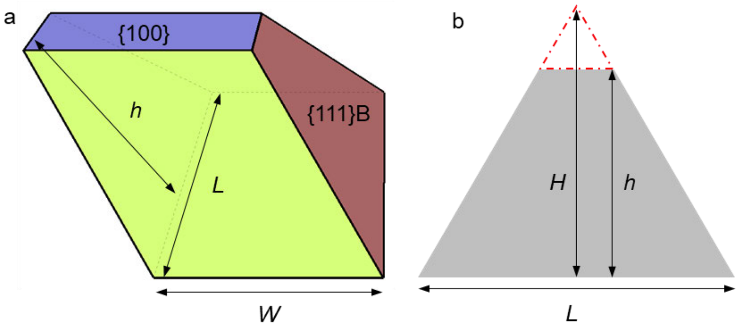

Figure 5.19: (a) 3D schematic of the ZB base nanostructure and (b) 2D view of the {111}A facet with truncated equilateral triangular geometry.

5.4.2.2. Effective formation enthalpy calculation

Scenario 1:

In scenario 1, further growth proceeds on the {111}B facet of the base nanostructure, until another {111}A facet is exposed (see Figure 5.20). The coloured region in Figure 5.20a highlights the newly formed ZB part, with its volume (V_1) given by the following equation:

$$V_1(L) = \frac{\sqrt{2}}{12}\left[L^3 - \left(L - \frac{2\sqrt{3}}{3}h\right)^3\right] - \frac{h\sqrt{6}}{6}\left(L - \frac{2\sqrt{3}}{3}h\right)^2 \qquad (5.13)$$

$$h(L) = k \cdot (\frac{\sqrt{3}}{2} L) \tag{5.14}$$

where $k = 0.1$, L and h are the nanoslot length and height of the truncated {111}A facet, respectively. As shown in Figure 5.20, the exposed facets of the newly formed part consist of three {111}A side facets and one {100} facet on top. The respective surface areas are labelled as $A_{a,ZB}$, $A_{b,ZB}$, and $A_{c,ZB}$ in Figure 5.20b. Based on equation (5.12), the effective formation enthalpy for scenario 1, $\Delta G_1'$, is described as follows:

$$\Delta G_1'(L) = (A_{a,ZB} + 2A_{b,ZB})\gamma_{\{111\}A} + A_{c,ZB}\gamma_{\{100\}}; \tag{5.15}$$

$$A_{a,ZB} = \left(L - \frac{\sqrt{3}h}{3}\right) h \ ; \tag{5.16}$$

$$A_{b,ZB} = \frac{\sqrt{3}}{3} h^2 \ ; \tag{5.17}$$

$$A_{c,ZB} = \left(\frac{2\sqrt{3}}{3} L - \frac{4}{3} h\right) h; \tag{5.18}$$

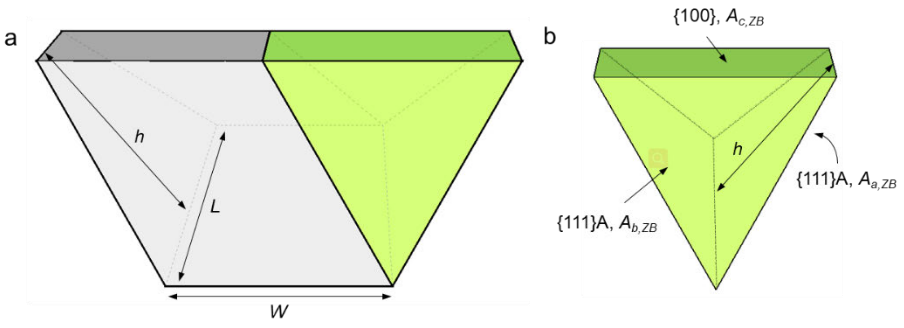

Figure 5.20: 3D schematics of the newly grown InP in scenario 1. $A_{a,ZB}$, $A_{b,ZB}$, and $A_{c,ZB}$ used in equations (5.15)-(5.18) are labelled in the figure.

Scenario 2:

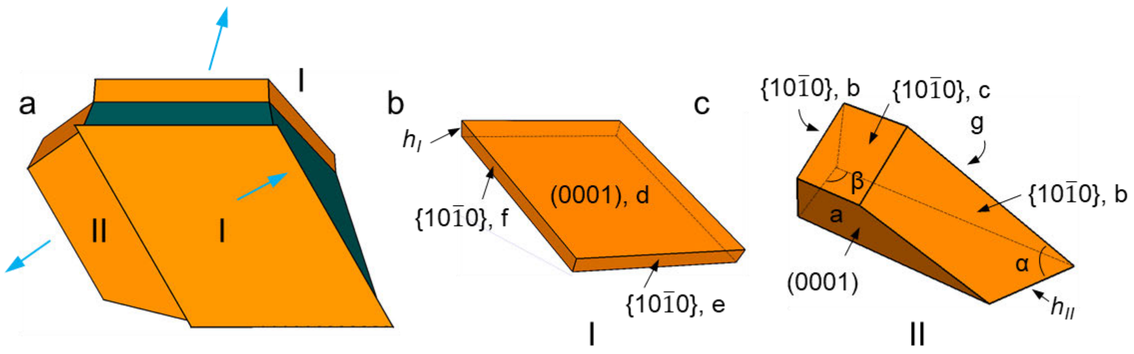

Figure 5.21: 3D schematics of the newly grown InP in scenario 2. Arrows in (a) indicate the <111>A directions.

Instead of the continued growth on the {111}B facet of the base nanostructure, three WZ segments grow from the three {111}A facets. As highlighted in Figure 5.21, the newly grown InP volume is distributed into two identical segments on both {111}A side facets (labelled V_2^I) and a single segment on the left {111}A side facet (labelled V_2^{II}). As indicated by the arrows in Figure 5.21a, the two symmetrical V_2^I segments grow in <111>A directions that are away from the substrate surface, while the V_2^{II} segment grows in <111>A direction pointing toward the substrate. The symmetrical V_2^I segment in Figure 5.21b has four $\{10\bar{1}0\}$ side facets (labelled as $A_{e,WZ}$ and $A_{f,WZ}$) and one (0001) facet (labelled as $A_{d,WZ}$) on top, whereas the V_2^{II} segment is surrounded by three $\{10\bar{1}0\}$ facets (labelled as $A_{b,WZ}$ and $A_{c,WZ}$) and terminated by a (0001) facet (labelled as $A_{a,WZ}$), as shown in Figure 5.21c. Two unique angles (α and β) formed between the edges of the $\{10\bar{1}0\}$ side facets with respect to substrate and {111}A growth front are determined to be 50.77° and 71.57°, respectively, based on the crystallographic calculations. The total newly grown volume in scenario 2 (V_2) is given by:

$$V_2 = 2V_2^I + V_2^{II} \tag{5.19}$$

$$V_2^I = \frac{2\sqrt{3}}{3} hWh_I \tag{5.20}$$

$$V_2^{II} = \frac{\sqrt{2}}{8}\left[L^3 - \left(L - \frac{\sqrt{10}}{5}h_{II}\right)^3\right] - \frac{3\sqrt{5}}{20}\left(L - \frac{2\sqrt{3}}{3}h\right)^2 h_{II} \tag{5.21}$$

where h_I and h_{II} are the lengths of the V_2^I and V_2^I segments, respectively (see Figure 5.21b,c), and W is the nanoslot width which is approximately 170 nm. Under equal volume consideration, $V_1 = V_2$. In other words, V_2 is distributed into two portions of V_2^I and one portion of V_2^{II}. With h known from equation (5.14), there are two unknown variables in V_2^I and V_2^{II}, namely h_I and h_{II}. To solve these variables, the volume distribution ratio between V_2^I and V_2^{II} has to be determined either analytically or through experimental measurements. Deriving an analytical solution for the volume distribution ratio as a function of slot length L would invoke a kinetic model that considers adatom diffusion on the growth mask and structure facets, which would introduce complications into this model. On the other hand, due to the relatively high growth rate in MOCVD, it is difficult to measure the distribution ratio experimentally. Based on the aforementioned considerations, a volume distribution ratio v is defined as follow to simplify the calculations of h_I and h_{II}:

$$v = \frac{V_2^{II}}{V_1}, 0 \le v \le 1 \tag{5.22}$$

$$V_2^I = \frac{V_1 \cdot (1 - v)}{2} \tag{5.23}$$

In this model, v is set to be 0.1. Note that the choice for the value of v is non-trivial and has physical significance in the model, which will be discussed later. With the volume distribution ratio defined, h_I and h_{II} are then solved by substituting equation (5.13), (5.22), and (5.23) into (5.20) and (5.21). Subsequently, the exposed facet surface areas that are unique to this scenario, labelled $A_{a,WZ}$, $A_{b,WZ}$, $A_{c,WZ}$, $A_{d,WZ}$, $A_{e,WZ}$, $A_{f,WZ}$, $A_{g,WZ}$ in Figure 5.21b,c, can be determined accordingly.

In addition to the exposed facets, the V_2^{II} segment, which is a laterally overgrown structure on top of the SiO$_x$ growth mask, also forms an interface with the mask. Figure 5.22 illustrates this InP-SiO$_x$ interfacial area, which is labelled as A_S.

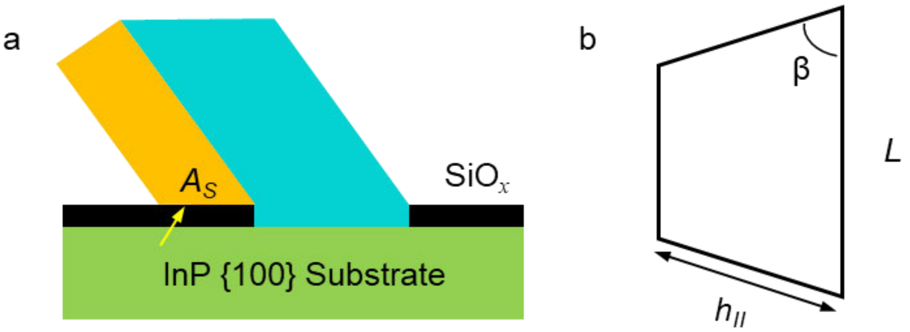

Figure 5.22: (a) Side view of lateral overgrowth of nanomembrane over SiO$_x$ growth mask. The interface of V_2^{II} segment and SiO$_x$ is indicated by the yellow arrow. Its interfacial area is A_S. (b) Top view of this interface surface area.

Finally, based on equation (5.12), the effective formation enthalpy for scenario 2 ($\Delta G_2'$) is described as follow:

$$\Delta G_2' = \left(A_{a,WZ} + 2A_{d,WZ}\right) \cdot \gamma_{(0001)} + \left(2A_{b,WZ} + A_{c,WZ} + 4A_{e,WZ} + 4A_{f,WZ}\right) \cdot \gamma_{\{10\bar{1}0\}} + \left(2A_{d,WZ} + A_{g,WZ}\right) \cdot \gamma_{twin} + \left(\gamma_{InP\{100\}-SiO_x} - \gamma_{SiO_x}\right) \cdot A_S \tag{5.24}$$

$$A_{a,WZ} = \frac{h - \frac{\sqrt{30}}{10} h_{II}}{2} \cdot \left(2L - \frac{2\sqrt{3}}{3} h - \frac{\sqrt{10}}{5} h_{II}\right) \tag{5.25}$$

$$A_{b,WZ} = \frac{\sqrt{15}}{5}\left(\frac{2\sqrt{3}}{3} h - \frac{\sqrt{10}}{5} h_{II}\right) h_{II} + \frac{\sqrt{6}}{10} {h_{II}}^2 \tag{5.26}$$

$$A_{c,WZ} = \frac{\sqrt{15}}{5}\left(L - \frac{2\sqrt{3}}{3} h\right) h_{II} \tag{5.27}$$

$$A_{d,WZ} = Wh \tag{5.28}$$

$$A_{e,WZ} = Wh_I \tag{5.29}$$

$$A_{f,WZ} = \frac{2\sqrt{3}}{3} h_I h \tag{5.30}$$

$$A_{g,WZ} = \left(L - \frac{h\sqrt{3}}{3}\right) h \qquad (5.31)$$

$$A_S = \frac{\sqrt{10}}{10}\left(L - \frac{3\sqrt{10}h_{II}}{10}\right)h_{II}\ ; \qquad (5.32)$$

In equation (5.24), $\gamma_{InP\{100\}-SiO_x}$ and γ_{SiO_x} are the interfacial energy between V_2^{II} segment and SiO$_x$ mask and surface energy of SiO$_x$, respectively, and A_s is the corresponding interface area.

Estimation of $\boldsymbol{\gamma_{InP\{100\}-SiO_x}}$ and $\boldsymbol{\gamma_{SiO_x}}$:

Due to the difficulty of confirming the exact oxide composition in the SiO$_x$ growth mask deposited by the PECVD system, we make a reasonable assumption of $x = 2$ in further analysis. First of all, it is widely accepted that III-V growth on amorphous material like SiO$_2$ follows the Volmer-Weber mode or 3D island growth mode with a negative Young-Dupré spreading parameter Ψ, as defined in equation (5.33) below[44]:

$$\Psi = \gamma_{SiO_2} - \gamma_{III-V} - \gamma_{III-V/SiO_2}; \qquad (5.33)$$

By applying the negative spreading parameter condition and taking $\gamma_{III-V} = \gamma_{InP\{100\}}$ in our case, an acceptable range for the $\gamma_{InP\{100\}-SiO_2} - \gamma_{SiO_2}$ term in equation (5.24) can be deduced:

$$\gamma_{InP\{100\}-SiO_2} - \gamma_{SiO_2} \geq -\gamma_{InP\{100\}}; \qquad (5.34)$$

In the literature, two different but close values of SiO$_2$ surface energies were reported, which were 1.6 and 1.8 eV/nm^2 respectively.[45, 46] Using Fowkes' Law[47] to determine the interfacial energy between InP {100} and SiO$_2$:

$$\gamma_{InP\{100\}-SiO_2} = \gamma_{InP\{100\}} + \gamma_{SiO_2} - 2\sqrt{\gamma_{InP\{100\}} \cdot \gamma_{SiO_2}}\ ; \qquad (5.35)$$

with $\gamma_{InP\{100\}} = 6.2\ eV/nm^2$ and $\gamma_{SiO_2} = 1.8\ eV/nm^2$, the $\gamma_{InP\{100\}-SiO_2} - \gamma_{SiO_2}$ term in equation (5.24) is approximately -0.5 eV/nm^2, which satisfies the condition in equation (5.34).

5.4.2.3. Results and discussion

In the case of segment II volume accounting for one-tenth of the total WZ volume (see Figure 5.18f), i.e. $v = 0.1$, effective total surface energies of scenarios 1 and 2 as a function of nanoslot length are calculated and plotted in Figure 5.23a. The effective total surface energy of scenario 1 is smaller than that of scenario 2 when nanoslot is short, suggesting that scenario 1 is energetically favourable. Conversely, scenario 2 is preferred when nanoslot is longer than a critical length. The calculated critical length is approximately 550 nm in this model which is comparable with the experimental results (Figure 5.4a). This model indicates that the driving force of shape transformation with the increase of nanoslot length could be attributed to minimization of the total surface energy. It is similar to our previous investigation of SAE growth of InP nanostructures on {111}A InP substrate.[26] Thus, in addition to confinement effect of opening, minimization of the total surface energy plays a key role in shape transformation of nanostructures grown on all InP substrates regardless of their orientations. As a significant parameter for determining the total surface energy of nanostructures, facet surface energy is strongly related to growth conditions.[48, 49] This model is established with respect to InP nanostructures grown at the optimized conditions provided in Section 5.2, but the principle can be applied to guide SAE of a wide range of III-V nanostructures under different growth conditions.

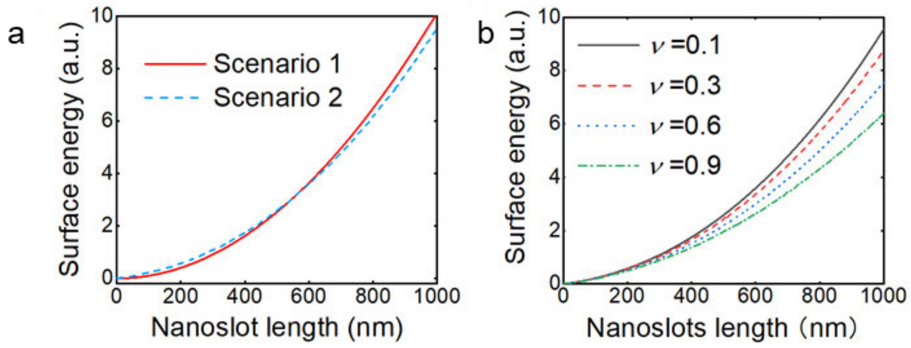

Figure 5.23: (a) Effective total surface energy of nanostructures in two scenarios as a function of nanoslot length when $v = 0.1$. (b) Effective total surface energy of the nanostructure in scenario 2 with the different v.

Effect of v:

The value of v defined in this model plays a role in determining $L_{critical}$. As v increases from 0.1 to 0.9, while the overall trend of $\Delta G_1'$ and $\Delta G_2'$ remains the same, $L_{critical}$ is found to decrease from approximately 550 to 280 nm. Since the value of v determines the surface areas of WZ segment V_2^{I} and V_2^{II}, the rate of increase of $\Delta G_2'$ will be affected by v. The $\Delta G_{II}'$-L plot with varying v values shown in Figure 5.23b illustrates this relationship. As mentioned previously, due to the technical complexity in determining the exact volumes of all the WZ segments in scenario 2, the value of $v = 0.1$ was chosen in such a way that our model provides the best representation of experimentally observed $L_{critical}$.

5.5. Summary

In this chapter, we demonstrated SAE of InP nanostructures with geometries evolving from wire-like to membrane-like shapes on InP substrates with various orientations. Based on in-depth investigation of the morphology and crystal structure of these nanostructures, unified growth fundamentals for SAE of InP arrays is established. We have revealed the relationship of the crystal structure to substrate orientations, growth directions and surface energies of the different crystallographic planes. At the initial nucleation stage on {100} and {110} substrates, epitaxial InP layers inherit the pure ZB crystal phase of the substrates. Our proposed nucleation model demonstrates that WZ and ZB phase nuclei are more energetically favorable on {111}A and {111}B substrates, respectively, which then results in formation of WZ and ZB phases along the <111>A and <111>B directions, respectively. In addition, crystal phase transition does not occur along other low-index directions, which leads to the formation of pure ZB phase layers along the $<11\bar{2}>$ and $<10\bar{1}>$ directions in the layered nanomembranes grown on {100} and {110} substrates, respectively. Dependence of crystal phase on growth directions provides an additional degree of freedom for crystal phase engineering, leading to formation of WZ/ZB homojunction in layered nanomembranes with a large interfacial area. They are unique platforms for investigating carrier transport in 2D systems and fundamental optical properties of type-II band alignment. By analyzing the shape evolution on substrates with different orientations, we also found that the morphology transformation is essentially determined by the confinement effect of the openings and minimization of the total surface energy. This work provides new insights for the design and growth of III-V nanostructures with sophisticated geometries beyond the nanowire geometry for new types of devices based on shapes and geometry.

References

1. P. Aseev, A. Fursina, F. Boekhout, F. Krizek, J. E. Sestoft, F. Borsoi, S. Heedt, G. Wang, L. Binci, S. Marti-Sanchez, T. Swoboda, R. Koops, E. Uccelli, J. Arbiol, P. Krogstrup, L. P. Kouwenhoven, and P. Caroff. Selectivity map for molecular beam epitaxy of advanced III-V quantum nanowire networks. *Nano Letters* 2019, vol. 19, no. 1, pp. 218-227.
2. S. Vaitiekenas, A. M. Whiticar, M. T. Deng, F. Krizek, J. E. Sestoft, C. J. Palmstrom, S. Marti-Sanchez, J. Arbiol, P. Krogstrup, L. Casparis, and C. M. Marcus. Selective-area-grown semiconductor-superconductor hybrids: A basis for topological networks. *Physical Review Letters* 2018, vol. 121, no. 14, p. 147701.
3. P. Staudinger, S. Mauthe, K. E. Moselund, and H. Schmid. Concurrent zinc-blende and wurtzite film formation by selection of confined growth planes. *Nano Letters* 2018, vol. 18, no. 12, pp. 7856-7862.

4. F. Krizek, J. E. Sestoft, P. Aseev, S. M. S. Anchez, S. Vaitiekenas, L. Casparis, S. A. Khan, Y. Liu, T. Stankevic, A. M. Whiticar, A. Fursina, F. Boekhout, R. Koops, E. Uccelli, L. P. Kouwenhoven, C. M. Marcus, J. Arbiol, and P. Krogstrup. Field effect enhancement in buffered quantum nanowire networks. *Physical Review Materials* 2018, vol. 2, no. 9, p. 093401.
5. C. Zhang, X. Miao, K. D. Chabak, and X. Li. A review of III–V planar nanowire arrays: selective lateral VLS epitaxy and 3D transistors. *Journal of Physics D: Applied Physics* 2017, vol. 50, no. 39, p. 393001.
6. F. Krizek, T. Kanne, D. Razmadze, E. Johnson, J. Nygård, C. M. Marcus, and P. Krogstrup. Growth of InAs wurtzite nanocrosses from hexagonal and cubic basis. *Nano Letters* 2017, vol. 17, no. 10, pp. 6090-6096.
7. J.-H. Kang, M. Galicka, P. Kacman, and H. Shtrikman. Wurtzite/Zinc-blende ‘k’-shape InAs nanowires with embedded two-dimensional wurtzite plates. *Nano Letters* 2017, vol. 17, no. 1, pp. 531-537.
8. S. Gazibegovic, D. Car, H. Zhang, S. C. Balk, J. A. Logan, M. W. A. de Moor, M. C. Cassidy, R. Schmits, D. Xu, G. Wang, P. Krogstrup, R. L. M. Op Het Veld, K. Zuo, Y. Vos, J. Shen, D. Bouman, B. Shojaei, D. Pennachio, J. S. Lee, P. J. van Veldhoven, S. Koelling, M. A. Verheijen, L. P. Kouwenhoven, C. J. Palmstrom, and E. Bakkers. Epitaxy of advanced nanowire quantum devices. *Nature* 2017, vol. 548, no. 7668, pp. 434-438.
9. T. Rieger, D. Rosenbach, D. Vakulov, S. Heedt, T. Schäpers, D. Grützmacher, and M. I. Lepsa. Crystal phase transformation in self-assembled InAs nanowire junctions on patterned Si substrates. *Nano Letters* 2016, vol. 16, no. 3, pp. 1933-1941.
10. L. Desplanque, M. Fahed, X. Han, V. Chinni, D. Troadec, M. Chauvat, P. Ruterana, and X. Wallart. Influence of nanoscale faceting on the tunneling properties of near broken gap InAs/AlGaSb heterojunctions grown by selective area epitaxy. *Nanotechnology* 2014, vol. 25, no. 46, p. 465302.
11. D. Car, J. Wang, M. A. Verheijen, E. P. Bakkers, and S. R. Plissard. Rationally designed single-crystalline nanowire networks. *Advanced Materials* 2014, vol. 26, no. 28, pp. 4875-4879.
12. J.-H. Kang, Y. Cohen, Y. Ronen, M. Heiblum, R. Buczko, P. Kacman, R. Popovitz-Biro, and H. Shtrikman. Crystal structure and transport in merged InAs nanowires MBE grown on (001) InAs. *Nano Letters* 2013, vol. 13, no. 11, pp. 5190-5196.
13. R. S. Dowdy, D. A. Walko, and X. Li. Relationship between planar GaAs nanowire growth direction and substrate orientation. *Nanotechnology* 2012, vol. 24, no. 3, p. 035304.

14. S. Conesa-Boj, E. Russo-Averchi, A. Dalmau-Mallorqui, J. Trevino, E. F. Pecora, C. Forestiere, A. Handin, M. Ek, L. Zweifel, L. R. Wallenberg, D. Ruffer, M. Heiss, D. Troadec, L. Dal Negro, P. Caroff, and A. Fontcuberta i Morral. Vertical "III-V" V-shaped nanomembranes epitaxially grown on a patterned Si[001] substrate and their enhanced light scattering. *ACS Nano* 2012, vol. 6, no. 12, pp. 10982-10991.
15. S. A. Fortuna, and X. Li. Metal-catalyzed semiconductor nanowires: a review on the control of growth directions. *Semiconductor Science and Technology* 2010, vol. 25, no. 2, p. 024005.
16. S. A. Fortuna, J. Wen, I. S. Chun, and X. Li. Planar GaAs Nanowires on GaAs (100) Substrates: Self-Aligned, Nearly Twin-Defect Free, and Transfer-Printable. *Nano Letters* 2008, vol. 8, no. 12, pp. 4421-4427.
17. M. Mattila, T. Hakkarainen, H. Jiang, E. I. Kauppinen, and H. Lipsanen. Effect of substrate orientation on the catalyst-free growth of InP nanowires. *Nanotechnology* 2007, vol. 18, no. 15, p. 155301.
18. M. Aagesen, E. Johnson, C. B. Sorensen, S. O. Mariager, R. Feidenhans'l, E. Spiecker, J. Nygard, and P. E. Lindelof. Molecular beam epitaxy growth of free-standing plane-parallel InAs nanoplates. *Nature Nanotechnology* 2007, vol. 2, no. 12, pp. 761-764.
19. L. Guniat, S. Marti-Sanchez, O. Garcia, M. Boscardin, D. Vindice, N. Tappy, M. Friedl, W. Kim, M. Zamani, L. Francaviglia, A. Balgarkashi, J. B. Leran, J. Arbiol, and I. M. A. Fontcuberta. III-V integration on si(100): Vertical nanospades. *ACS Nano* 2019, vol. 13, no. 5, pp. 5833-5840.
20. E. F. Pecora, G. F. Walsh, C. Forestiere, A. Handin, E. Russo-Averchi, A. Dalmau-Mallorqui, I. Canales-Mundet, I. M. A. Fontcuberta, and L. Dal Negro. Enhanced second harmonic generation from InAs nano-wing structures on silicon. *Nanoscale* 2013, vol. 5, no. 21, pp. 10163-10170.
21. Q. Gao, V. G. Dubrovskii, P. Caroff, J. Wong-Leung, L. Li, Y. Guo, L. Fu, H. H. Tan, and C. Jagadish. Simultaneous selective-area and vapor-liquid-solid growth of InP nanowire arrays. *Nano Letters* 2016, vol. 16, no. 7, pp. 4361-4367.
22. K. Ikejiri, J. Noborisaka, S. Hara, J. Motohisa, and T. Fukui. Mechanism of catalyst-free growth of GaAs nanowires by selective area MOVPE. *Journal of Crystal Growth* 2007, vol. 298, pp. 616-619.
23. M. Albani, L. Ghisalberti, R. Bergamaschini, M. Friedl, M. Salvalaglio, A. Voigt, F. Montalenti, G. Tutuncuoglu, A. F. I. Morral, and L. Miglio. Growth kinetics and

morphological analysis of homoepitaxial GaAs fins by theory and experiment. *Physical Review Materials* 2018, vol. 2, no. 9, p. 093404.

24. C. Y. Chi, C. C. Chang, S. Hu, T. W. Yeh, S. B. Cronin, and P. D. Dapkus. Twin-free GaAs nanosheets by selective area growth: implications for defect-free nanostructures. *Nano Letters* 2013, vol. 13, no. 6, pp. 2506-2515.
25. P. Staudinger, K. E. Moselund, and H. Schmid. Exploring the size limitations of wurtzite III-V film growth. *Nano Letters* 2020, vol. 20, no. 1, pp. 686-693.
26. N. Wang, X. Yuan, X. Zhang, Q. Gao, B. Zhao, L. Li, M. Lockrey, H. H. Tan, C. Jagadish, and P. Caroff. Shape engineering of InP nanostructures by selective area epitaxy. *ACS Nano* 2019, vol. 13, no. 6, pp. 7261-7269.
27. S. Lehmann, J. Wallentin, E. K. Martensson, M. Ek, K. Deppert, K. A. Dick, and M. T. Borgstrom. Simultaneous growth of pure wurtzite and zinc blende nanowires. *Nano Letters* 2019, vol. 19, no. 4, pp. 2723-2730.
28. M. Knoedler, N. Bologna, H. Schmid, M. Borg, K. E. Moselund, S. Wirths, M. D. Rossell, and H. Riel. Observation of twin-free GaAs nanowire growth using template assisted selective epitaxy. *Crystal Growth & Design* 2017, vol. 17, no. 12, pp. 6297-6302.
29. Q. Gao, D. Saxena, F. Wang, L. Fu, S. Mokkapati, Y. Guo, L. Li, J. Wong-Leung, P. Caroff, H. H. Tan, and C. Jagadish. Selective-area epitaxy of pure wurtzite InP nanowires: high quantum efficiency and room-temperature lasing. *Nano Letters* 2014, vol. 14, no. 9, pp. 5206-5211.
30. J. Bao, D. C. Bell, F. Capasso, J. B. Wagner, T. Martensson, J. Tragardh, and L. Samuelson. Optical properties of rotationally twinned InP nanowire heterostructures. *Nano Letters* 2008, vol. 8, no. 3, pp. 836-841.
31. K. Pemasiri, M. Montazeri, R. Gass, L. M. Smith, H. E. Jackson, J. Yarrison-Rice, S. Paiman, Q. Gao, H. H. Tan, C. Jagadish, X. Zhang, and J. Zou. Carrier dynamics and quantum confinement in type II ZB-WZ InP nanowire homostructures. *Nano Letters* 2009, vol. 9, no. 2, pp. 648-654.
32. N. Akopian, G. Patriarche, L. Liu, J. C. Harmand, and V. Zwiller. Crystal phase quantum dots. *Nano Letters* 2010, vol. 10, no. 4, pp. 1198-1201.
33. X. Yuan, L. Li, Z. Li, F. Wang, N. Wang, L. Fu, J. He, H. H. Tan, and C. Jagadish. Unexpected benefits of stacking faults on the electronic structure and optical emission in wurtzite GaAs/GaInP core/shell nanowires. *Nanoscale* 2019, vol. 11, no. 18, pp. 9207-9215.
34. K. Ikejiri, F. Ishizaka, K. Tomioka, and T. Fukui. Bidirectional growth of indium phosphide nanowires. *Nano Letters* 2012, vol. 12, no. 9, pp. 4770-4774.

35. F. Glas, J.-C. Harmand, and G. Patriarche. Why does wurtzite form in nanowires of III-V zinc blende semiconductors? *Physical Review Letters* 2007, vol. 99, no. 14, p. 146101.
36. K. Ikejiri, T. Sato, H. Yoshida, K. Hiruma, J. Motohisa, S. Hara, and T. Fukui. Growth characteristics of GaAs nanowires obtained by selective area metal-organic vapour-phase epitaxy. *Nanotechnology* 2008, vol. 19, no. 26, p. 265604.
37. H. J. Joyce, J. Wong-Leung, Q. Gao, H. H. Tan, and C. Jagadish. Phase perfection in zinc Blende and Wurtzite III-V nanowires using basic growth parameters. *Nano Letters* 2010, vol. 10, no. 3, pp. 908-915.
38. T. Akiyama, K. Nakamura, and T. Ito. Effects of surface and twinning energies on twining-superlattice formation in group III–V semiconductor nanowires: a first-principles study. *Nanotechnology* 2019, vol. 30, no. 23, p. 234002.
39. Q. Liu, N. Moll, M. Scheffler, and E. Pehlke. Equilibrium shapes and energies of coherent strained InP islands. *Physical Review B* 1999, vol. 60, no. 24, p. 17008.
40. N. Sibirev, M. Timofeeva, A. Bol’shakov, M. Nazarenko, and V. Dubrovskiĭ. Surface energy and crystal structure of nanowhiskers of III–V semiconductor compounds. *Physics of the Solid State* 2010, vol. 52, no. 7, pp. 1531-1538.
41. X. D. Yang, H. B. Shu, M. T. Jin, P. Liang, D. Cao, C. Li, and X. S. Chen. Crystal facet effect on structural stability and electronic properties of wurtzite InP nanowires. *Journal of Applied Physics* 2014, vol. 115, no. 21, p. 214301.
42. T. Yamashita, T. Akiyama, K. Nakamura, and T. Ito. Effects of facet orientation on relative stability between zinc blende and wurtzite structures in group III–V nanowires. *Japanese Journal of Applied Physics* 2010, vol. 49, no. 5R, p. 055003.
43. M. Fahed, L. Desplanque, C. Coinon, D. Troadec, and X. Wallart. Impact of P/In flux ratio and epilayer thickness on faceting for nanoscale selective area growth of InP by molecular beam epitaxy. *Nanotechnology* 2015, vol. 26, no. 29, p. 295301.
44. I. Lucci, S. Charbonnier, L. Pedesseau, M. Vallet, L. Cerutti, J. B. Rodriguez, E. Tournie, R. Bernard, A. Letoublon, N. Bertru, A. Le Corre, S. Rennesson, F. Semond, G. Patriarche, L. Largeau, P. Turban, A. Ponchet, and C. Cornet. Universal description of III-V/Si epitaxial growth processes. *Physical Review Materials* 2018, vol. 2, no. 6, p. 060401.
45. S. Brunauer, D. L. Kantro, and C. H. Weise. The Surface Energies of Amorphous Silica and Hydrous Amorphous Silica. *Canadian Journal of Chemistry* 1956, vol. 34, no. 10, pp. 1483-1496.
46. A. J. Kinloch. *Adhesion and adhesives: science and technology*. Springer: Netherlands, 1987.

47. M. Inoue. Structural integrity of metal–polymer adhesive interfaces in microelectronics. In *Advanced Adhesives in Electronics*. M. O. Alam; C. Bailey, Eds. Woodhead: 2011, pp. 157-198.

48. Y. Kitauchi, Y. Kobayashi, K. Tomioka, S. Hara, K. Hiruma, T. Fukui, and J. Motohisa. Structural transition in indium phosphide nanowires. *Nano Letters* 2010, vol. 10, no. 5, pp. 1699-1703.

49. X. M. Yuan, J. B. Yang, J. He, H. H. Tan, and C. Jagadish. Role of surface energy in nanowire growth. *Journal of Physics D: Applied Physics* 2018, vol. 51, no. 28, p. 283002.

CHAPTER 6

InAsP quantum wells in InP nanowires and nanomembranes

6.1. Introduction

In the last two chapters, we have demonstrated InP nanostructures with various morphologies grown by SAE technique and thoroughly investigated their structural and optical properties, as well as the mechanisms of shape transformation and phase transition regardless of substrate orientations. Based on these results, it is vital to further investigating the incorporation of quantum heterostructures, such as quantum wells (QWs) and quantum dots (QDs), since they are able to greatly improve the properties and functionality of III-V semiconductors. For instance, the radial QWs and axially embedded QDs in nanowires exhibit high emission efficiency thanks to the natural Fabry-Pérot cavity of nanowires themselves, and thus are widely applied in lasing,[1-3] single photon emission,[4] and infrared photodetection applications, etc.[5, 6] So far, despite the success of growing homogeneous III-V nanostructure arrays by SAE, the formation of heterostructures is less studied compared to the metal-catalysed heterostructure nanowires,[6-11] primarily due to the growth challenges of SAE, as it is harder to selectively control axial and lateral growth rates by only tuning growth conditions without the help of a catalyst. This situation leads to the insufficient understanding of heterostructure incorporation in III-V nanostructures grown by SAE. Especially, with increasing interests in a variety of nanoshapes and network structures, the limited understanding of heterostructure growth gained from nanowire research needs to be enhanced and, more importantly, extended to other types of nanostructures.

In this chapter, using pure WZ InP nanostructures grown on InP {111}A substrates with two kinds of morphologies, i.e. the conventional one dimensional nanowires and two dimensional nanomembranes, as templates, we systematically investigate the growth behaviours of InAsP QWs including crystal structure, morphology, polarity and composition. As discussed in the previous chapters, WZ InP nanowires are generally bound by $\{1\bar{1}00\}$ side facets, whereas WZ InP nanomembranes could be bound by either $\{1\bar{1}00\}$ or $\{11\bar{2}0\}$ side facets depending on the nanomembrane orientation. The use of InP nanowires and two different orientation nanomembranes allows us to investigate the effects of nanostructure shape and crystal facets on InAsP QWs growth. In Section 6.3, we first discuss the incorporation of InAsP QWs in nanowires and reveal an asymmetric growth on nonpolar $\{1\bar{1}00\}$ side facets. In Section 6.4, the similar asymmetric growth is observed in the $<1\bar{1}0>$-oriented nanomembranes with $\{1\bar{1}00\}$ side facets. On the other hand, InAsP growth on the dominant nonpolar $\{11\bar{2}0\}$ side facets of the $<11\bar{2}>$-oriented nanomembranes is quite uniform whilst the final QW nanomembranes present high symmetry. Moreover, bright and uniform emission from the nanomembrane QW heterostructures are achieved.

6.2. Experimental methods

InP/InAsP QW nanowires discussed in this chapter were grown in the horizontal MOCVD reactor. Trimethylindium (TMIn), arsine (AsH_3), phosphine (PH_3) were used as precursors for In, As and P elements, respectively. The reactor was first heated to 750 °C and maintained 10 min in the H_2 and PH_3 ambient to desorb possible contaminants. Subsequently, InP nanowires were grown at 730 °C with TMIn and PH_3 flow rates of 3.37×10^{-6} and 5.80×10^{-4} mol/min, respectively. After InP growth for 16 min, $InAs_{1-x}P_x$ QW was grown for 3 seconds by switching on the AsH_3 line with a flow rate of 1.02×10^{-4} mol/min to obtain a nominal composition of $InAs_{0.15}P_{0.85}$. Finally, an InP capping layer was grown for another 9 min under the same conditions as those of the initial InP nanowires. The above growth conditions are referred to as the standard growth conditions. In comparison, other growth conditions were also used which will be specified in Section 6.3.

SAE of InP/InAsP QW nanomembranes were carried out in the close coupled showerhead (CCS) MOCVD reactor. Two different orientation InP nanomembrane templates were grown at a surface temperature of 683 °C for 3 min with PH_3 and TMIn flow rates of 1.25×10^{-3} and 4.20×10^{-6} mol/min, respectively. A QW with nominal composition of $InAs_{0.3}P_{0.7}$ was then grown at the same conditions with an AsH_3 flow rate of 5.44×10^{-4} mol/min for 3 seconds, followed by the growth of an InP capping layer for 1.5 min under the same conditions as those used for InP templates. For the growth of multiple QWs, InP barrier layers were grown for 30 seconds between InAsP QWs.

The morphology of the nanostructures was characterized using an FEI Verios 460 scanning electron microscope (SEM). A Gatan MonoCL4 Elite cathodoluminescence (CL) spectroscopy equipped in the FEI Verios 460 SEM system, and CL spectroscopy and Moran scientific CL mapping system established in an FEI Quanta SEM system were used for CL characterisation. Structural and compositional analyses were carried out using a JEOL JEM-ARM200f aberration-corrected scanning transmission electron microscope (Cs-STEM) equipped with an energy dispersive X-ray spectroscopy system.

6.3. InP/InAsP quantum well nanowires

6.3.1. Morphological and structural analyses

Figure 6.1 shows the morphologies of InP/InAsP QW nanowire arrays grown at different conditions. For large diameter nanowires, they generally have a uniform triangular-like cross-section. The discontinuity of side facets is commonly observed due to the incorporation of InAsP QW, which in turn makes the QW position obvious, as indicated by the yellow arrows in Figure 6.1b-f. The similar morphology of these QW nanowires suggests that they have the same growth behaviour in a range of growth conditions. Consider that InP nanowire templates grown at the standard conditions are of pure WZ structure, i.e. free of planar defects, they will be used to further investigate the QW incorporation.

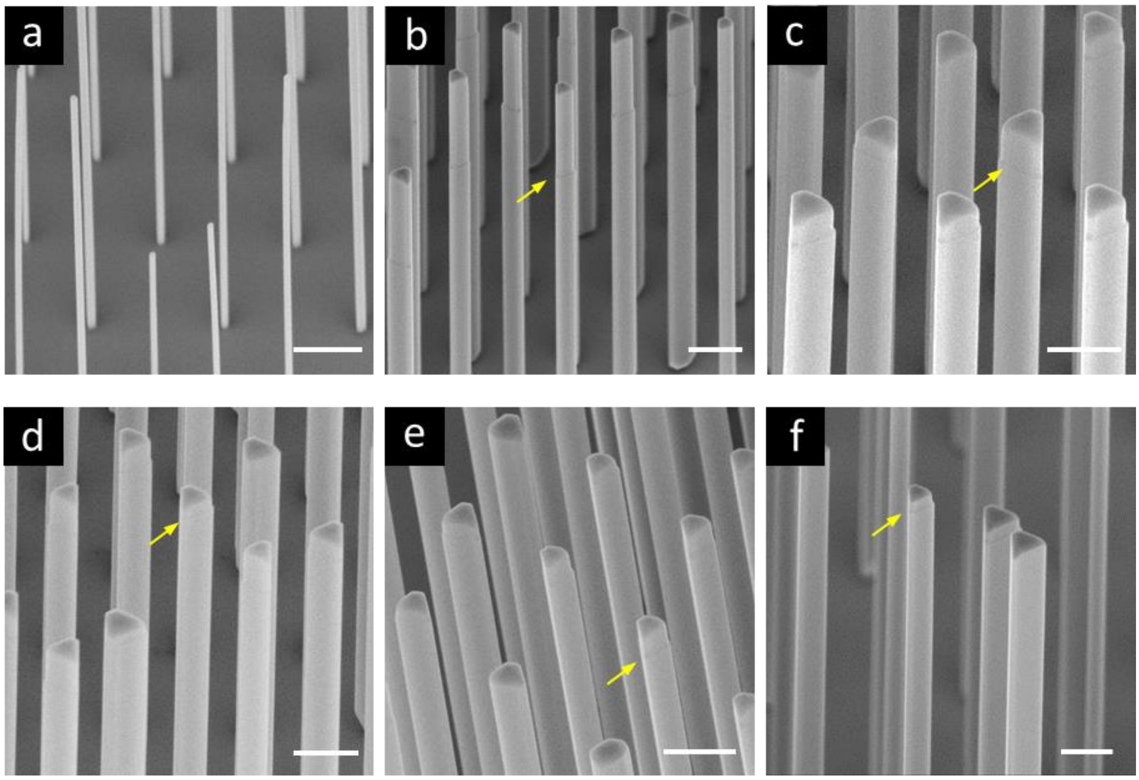

Figure 6.1: 45° tilted SEM images of InP/InAsP QW nanowire arrays grown at different conditions. Nanowire arrays in (a,b) are grown at the standard conditions (see Section 6.2) and their diameters are approximately 55 and 200 nm, respectively. Growth temperatures for (c-e) and (f) are 730 °C and 740 °C, respectively; TMIn flow rates for (c) and (d-f) are 4.048×10^{-6} and 3.373×10^{-6} mol/min, respectively; PH_3 flow rates for (c-e) and (f) are 5.804×10^{-4} and 6.25×10^{-4} mol/min, respectively; AsH_3 flow rates are (c) 5.804×10^{-4}, (d) 1.451×10^{-4}, (e) 2.859×10^{-4}, and (f) 1.563×10^{-4} mol/min, respectively, and thus the nominal composition of InAsP QWs is (c) $InAs_{0\ 5}P_{0\ 5}$, (d) $InAs_{0\ 2}P_{0\ 8}$, (e) $InAs_{0\ 33}P_{0\ 67}$, and (f) $InAs_{0\ 2}P_{0\ 8}$, respectively. InAsP QW growth time is (c) 5, (d) 3, (e) 3, and (f) 4 seconds, respectively. All scale bars are 500 nm.

InP/InAsP QW nanowire arrays shown in Figure 6.1a,b are grown at the standard conditions. Their diameters are approximately 55 and 200 nm, respectively. Normally, the nonpolar nature of $\{1\bar{1}00\}$ side facets leads to a hexagonal cross-section of WZ InP nanowires.[12, 13] The morphology transformation from hexagonal to triangular shape is caused by the growth of InAsP QW. The side facets of triangular-like InP/InAsP QW nanowires are still $\{1\bar{1}00\}$ which is determined by their angles with respect to the cleavage plane of the substrate. Thus, no facet rotation induced by QW growth is observed.[12] Figure 6.2a shows the low magnification HAADF image of a QW nanowire around the discontinuous position. The corresponding EDX mapping of P and As elements in Figure 6.2b,c confirms the incorporation of an axial QW at this position, as schematically shown in Figure 6.2d. Additionally, Figure

6.2c shows that the QW also forms radially on InP nanowire side facets. Furthermore, the As element signal on the left-hand side is broad and weak compared to that on the right-hand side that is narrow and strong. Considering the crystal symmetry, the QW distribution on the side facets is schematically described in Figure 6.2d, i.e. the QW alternately grows on the $\{1\bar{1}00\}$ side facets of the hexagonal InP nanowire template. Despite the current growth conditions being optimised for axial growth, the coexistence of both axial and radial InAsP QWs suggests that it is challenging to grow selectively either axial or radial QW nanowires using SAE technique, consistent with the reported SAE of InP/InGaAs[12, 14] and InP/AlInP[15] QW nanowires. Therefore, a thorough understanding of the QW growth behaviour would be highly valuable.

Atomically-resolved HAADF images in Figure 6.2e,f show the structural details of the QW nanowire. The atomic stacking sequence indicates that the axial InAsP QW is of ZB phase and grown on the top of WZ InP nanowire template along <111>A-polar direction, while the radial QW forming on the side facets inherits the WZ crystal structure of the InP nanowire. The crystal phase of the top InP segment switches back to WZ phase after InAsP QW growth, leading to an atomically sharp interface between axial ZB InAsP QW and WZ InP. Moreover, the axial InAsP QW forms inclined {111}B side facets (see Figure 6.2e) which confirms the cause of the discontinuous morphologies observed in Figure 6.1. The appearance of {111}B facets also suggests that the stable polarity of ZB InAsP {111} facets is B-polar, agreeing with reported InAsP nanowires.[16] InAsP QW growth alters subsequent InP growth. For example, the diameter of the top InP segments becomes smaller due to the formation of inclined side facets during InAsP QW growth (see Figure 6.2e). Besides, the axial growth rate of InP is reduced by a factor of 2.2 ± 0.2 after the QW growth, which could be due to an increased competition of lateral growth.

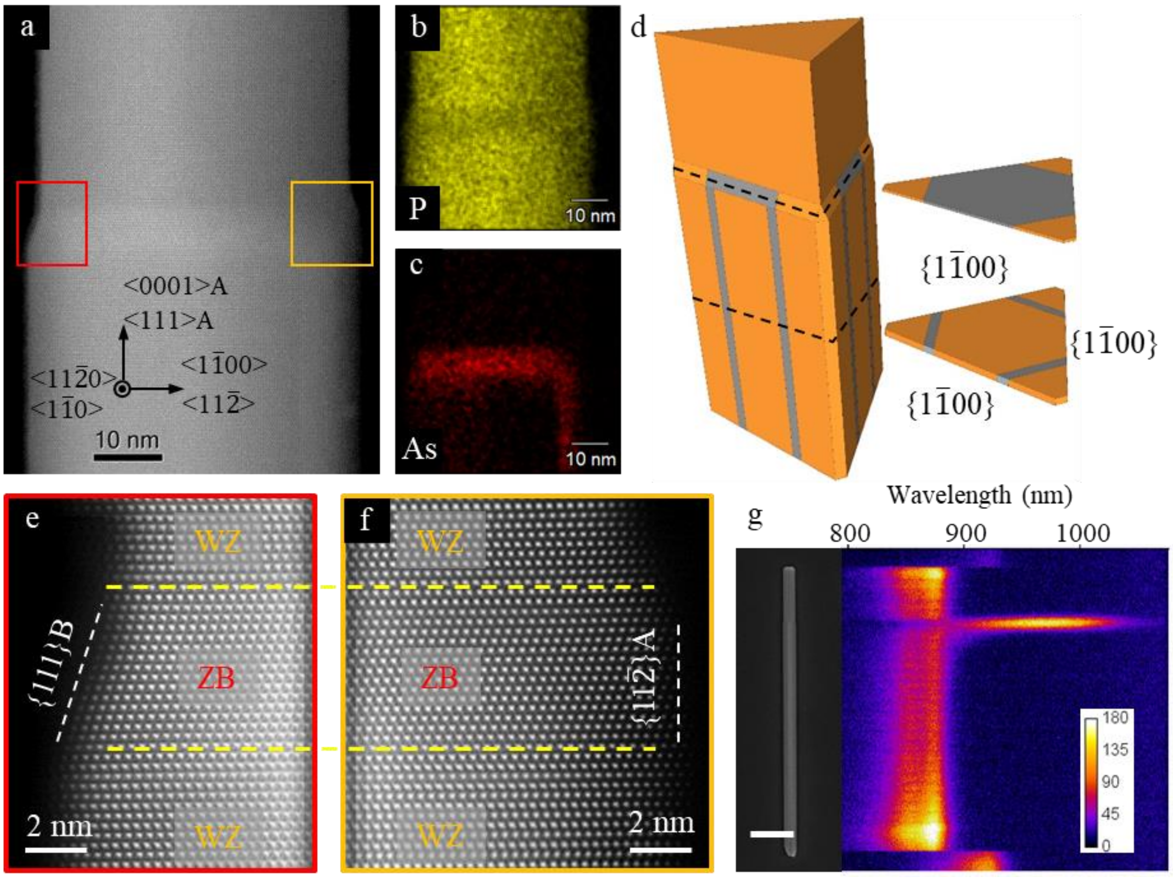

Figure 6.2: Structural, compositional and optical analyses of InP/InAsP QW nanowires grown at the standard conditions (see Section 6.2). (a) Low magnification HAADF image close to the axial QW area of a QW nanowire with a small diameter (48 nm) along the $\{11\bar{2}0\}$ zone axis. (b,c) EDX mapping of P and As elements. (d) Schematic illustration of the typical InP/InAsP QW nanowires, showing the morphology and distributions of axial and radial QWs. (e,f) Atomically resolved HAADF images from the corresponding areas in (a). (f) SEM image and CL line scan of an InP/InAsP nanowire. Scale bar in (g) is 1 µm.

6.3.2. Optical analysis

The CL result of an InP/InAsP QW nanowire shows strongest emission from the two ends due to a Fabry-Pérot cavity formed by the nanowire geometry.[17] Spectral information indicates emission from WZ InP along the nanowire. At the axial QW region, a strong but broad emission in the wavelength range of 900-1000 nm is observed. The broad emission peak width from our QW nanowire is unexpected in consideration of the sharp interface between InAsP and InP. One possible explanation is substantial composition fluctuation in the QW. Emission from the radial InAsP QW is not observed at room temperature most likely due to the very thin layer of the QW which results in poor confinement of carriers.

6.3.3. Asymmetric radial QW incorporation

Facet-selective growth has been widely observed during heterostructure formation because of the differences in surface energy and polarity.[18, 19] Thus, the asymmetric growth of the radial InAsP QW observed above is unexpected since the $\{1\bar{1}00\}$ side facets of InP nanowire templates are nonpolar and therefore identical. However, $\{11\bar{2}\}$ side facets of the axial ZB QW are polar. Taking this polarity into consideration, we found that the radial QW growth always occurs on the $<11\bar{2}>$A polar side of the axial QW. The detailed approach to determine the $<11\bar{2}>$A polar direction according to diffraction pattern can be found from Yuan *et al*.[20] and Zou *et al*.[21] As discussed in Section 2.4, crystal growth rate is greatly affected by the polarity and could be tuned by growth conditions.[12, 21] Yang *et al.* recently reported a triangular-like cross-section on the top of InP/InGaAs QW nanowires where the radial QW and InP barrier grow along both A- and B-polar $<11\bar{2}>$ directions driven by the axial ZB InGaAs QW.[22] Moreover, the triangular-like shape is an intermediate morphology and the preference for $\{1\bar{1}0\}$ sidewalls in axial ZB InGaAs QW finally leads to facet rotation of subsequent InP growth, forming a hexagonal InP top with $\{1\bar{1}0\}$ facets. Differently, in our case, the fast growth rate occurring on the $\{11\bar{2}\}$A polar side facets of the axial InAsP QW significantly facilitates the growth of radial InAsP QW and InP capping layer toward the $<11\bar{2}>$A polar direction, whereas the lateral growth on the $\{11\bar{2}\}$B polar sides is negligible, leading to the formation of triangular-like QW nanowires dominantly bound with $\{1\bar{1}00\}$side facets and the asymmetric incorporation of radial QWs.

6.4. InP/InAsP quantum well nanomembranes

InP nanowire templates used above have a six-fold symmetry, whereas InP nanomembranes have a two-fold symmetry. Different growth behaviours of InAsP QW are expected in these two kinds of nanostructures. More importantly, WZ InP nanomembranes can be bound by either $\{1\bar{1}00\}$ or $\{11\bar{2}0\}$ side facets. Thus, the investigation of QW nanomembranes is vital in understanding their growth behaviour and to improve optical properties.

6.4.1. Morphological and structural analyses

6.4.1.1. $<1\bar{1}0>$-oriented nanomembranes bound with $\{1\bar{1}00\}$ side facets

In Chapter 4, we demonstrate that $<1\bar{1}0>$-oriented InP nanomembranes are very uniform and have smooth $\{1\bar{1}00\}$ sidewalls. However, after the growth of InAsP QW, the uniformity of nanomembrane array is reduced and sidewalls are no longer smooth (see Figure 6.3a and Figure 6.4a). A TEM lamella is prepared by focused ion beam (FIB) milling along the white dotted line indicated in Figure 6.3a to expose the QW nanomembrane cross-section (Figure 6.3b) and heterostructure interface. In the Z-contrast STEM image viewed along the <$11\bar{2}0$> zone axis (see Figure 6.3c), the brighter areas are InAsP QW due to the incorporation of the heavier As element, which is confirmed by EDX mapping of As and P elements in Figure 6.3d,e. Figure 6.3c shows a similar QW formation as in the case of nanowires discussed above. Axially, the InAsP QW is grown as a ZB phase while radially it grows as a WZ phase, determined by the atomic stacking sequence and FFT pattern in Figure 6.3f,g. Moreover, the radial QW only forms on one $\{1\bar{1}00\}$ sidewall of the InP nanomembrane, and also on the <$11\bar{2}$>A polar side of the axial QW. The radial QW thickness reduces from top to bottom of the nanomembrane (Figure 6.3f,h,i). Besides, the larger dimension of nanomembranes leads to new growth behaviour. For instance, WZ InAsP is found to grow on $\{1\bar{1}02\}$ facets of the InP nanomembrane (see Figure 6.3f,j), which is similar to InP/InGaAs nanowire heterostructure with larger diameters.[22] This is a result of the top {0001} facet of the InP nanomembrane not joining the $\{1\bar{1}00\}$ sidewall at right angle, thus forming inclined $\{1\bar{1}02\}$ facets. Subsequent growth of InP after the axial QW remains ZB phase for ~6 nm before switching back to the preferred WZ phase (Figure 6.3f). Possible explanations are minor interdiffusion of As element and the larger surface energy of InAsP {111}A facet than the {111}B facet leading to ZB nucleation instead of the normally observed WZ phase. The lateral growth rate of InP capping layer is larger on the <$11\bar{2}$>A polar side of the axial InAsP QW as well as the radial QW in comparison to the near zero growth rate along the <$11\bar{2}$>B direction (see Figure 6.3b,c). The growth rate difference caused by polarity is commonly observed in III-V nanowire heterostructure growth.[23] Moreover, it can be seen that the thickness of lateral InP capping layer below the axial QW is also reduced from top to bottom, leading to formation of the inclined $\{1\bar{1}01\}$ side facet (Figure 6.3c). The above observations suggest that the asymmetric lateral growth of InAsP QW and InP capping layer on the nonpolar $\{1\bar{1}00\}$ side facets of <$1\bar{1}0$>-oriented InP nanomembrane template is due to the axial ZB InAsP QW which leads to the faster lateral growth along <$11\bar{2}$>A polar direction, similar to QW nanowires discussed in Section 6.3.[22]

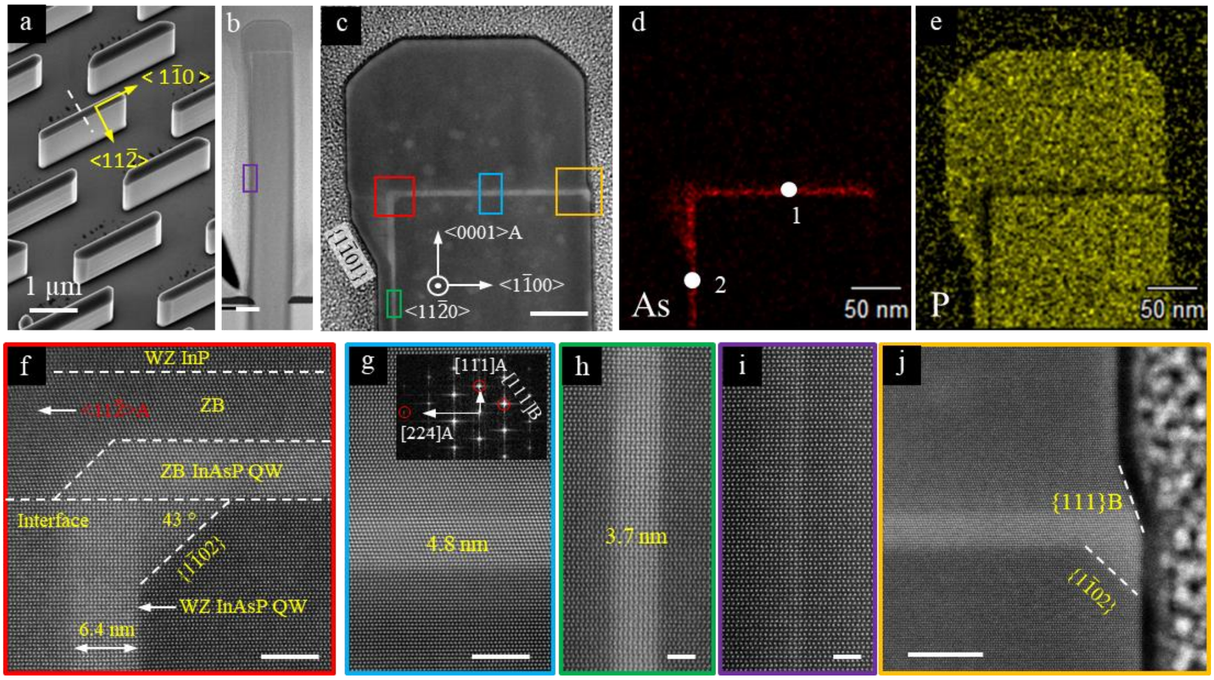

Figure 6.3: <1$\bar{1}$0>-oriented InP/InAsP single-QW nanomembranes. (a) 30° tilted SEM image of the QW nanomembrane array. The white dotted line indicates the ion milling direction and position for the TEM lamella preparation. (b,c) Low magnification HAADF images of the QW nanomembrane cross-section along <11$\bar{2}$0> zone axis. (d,e) EDX maps of As and P elements, respectively. (f-j) Atomically resolved HAADF images from the corresponding coloured areas in (b,c). FFT pattern inserted in (g) is extracted from the axial InAsP QW which confirms that it is ZB phase and indicates that the radial QW is located on the <11$\bar{2}$>A polar side of the axial QW. Scale bars: (b) 100 nm; (c) 50 nm; (f,g) 5 nm; (h,i) 2 nm; (j) 10 nm.

For the <1$\bar{1}$0>-oriented QW nanomembrane discussed above, despite the axial growth rate of InP capping layer being approximately 4.3 times slower than that of the initial InP nanomembrane due to the competition of lateral growth after InAsP QW growth, quite a thick InP segment is still grown on the top (Figure 6.3b). However, an interesting point to note is that, under the current growth conditions, the axial InP capping layer is absent in most cases, as shown in Figure 6.4a-h. In all cases, both axial ZB and radial WZ InAsP QWs are formed. Moreover, the radial QW forms asymmetrically on the <11$\bar{2}$>A polar side of the axial QW and its thickness reduces from top to bottom.

Further increasing the number of InAsP QWs deteriorates the uniformity of the nanomembrane, leading to the formation of a “protruding head” at one side of the nanomembrane (see Figure 6.4i). Z-contrast STEM image of the <1$\bar{1}$0>-oriented InP/InAsP nanomembrane heterostructure with 5 QWs in Figure 6.4i shows that InAsP QWs form on the

$\{0001\}$, $\{1\bar{1}00\}$ and $\{1\bar{1}01\}$ facets. The radial QWs are mostly formed on the <11$\bar{2}$>A polar side of the axial QW as well but with a significant thickness nonuniformity. Moreover, the inclined $\{1\bar{1}01\}$ facets consistently grow larger with the number of QWs, leading to the formation of the irregular “protruding head”.

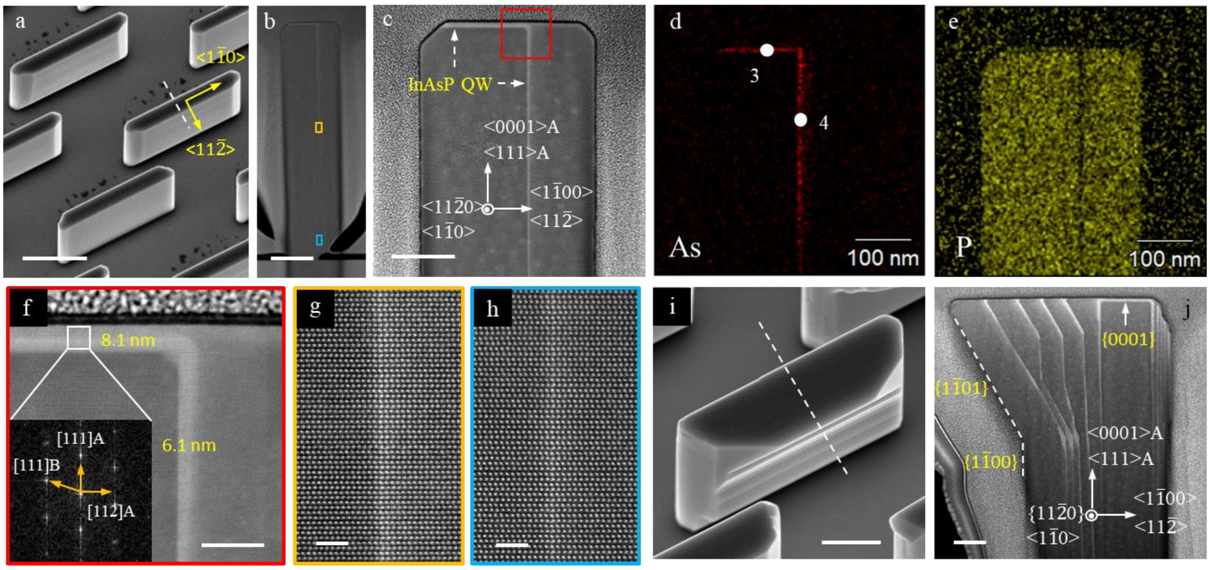

Figure 6.4: <1$\bar{1}$0>-oriented InP/InAsP single- and multiple-QW nanomembranes. (a) 30° tilted SEM image of the single-QW nanomembrane array. The white dotted line indicates the ion milling direction and position for the TEM lamella preparation. (b,c) Low magnification HAADF images of the single-QW nanomembrane cross-section along <11$\bar{2}$0> zone axis. (d,e) EDX maps of As and P elements, respectively. (f) HAADF image enlarged from the area marked in (c). The FFT pattern inserted in (f) is extracted from the axial QW, suggesting that the axial QW is of ZB phase and the radial QW is located on the <11$\bar{2}$>A polar side of the axial QW. (g,h) Atomically resolved HAADF images from the corresponding coloured areas in (b). (i,j) 30° tilted SEM and corresponding cross-sectional HAADF images of an InP/InAsP 5-QW nanomembrane. Scale bars: (a) 1 µm; (b) 200 nm; (c,j) 100 nm; (f) 20 nm; (g,h) 2 nm; (i) 500 nm.

6.4.1.2. <11$\bar{2}$>-oriented nanomembranes bound with $\{11\bar{2}0\}$ side facets

Figure 6.5a shows the <11$\bar{2}$>-oriented InP/InAsP single-QW nanomembrane array. It can be seen that even after InAsP QW growth they are highly uniform and no surface roughening is observed. The TEM lamella of an QW nanomembrane is prepared by FIB along the dotted line marked in Figure 6.5a. Low magnification HAADF image of the nanomembrane cross-section along $\{1\bar{1}00\}$ zone axis shows that radial QW grows on both $\{11\bar{2}0\}$ sidewalls (Figure 6.5b). The interface between QW and InP is quite sharp without any dislocations (see Figure 6.5e,f).

Moreover, the radial QW has a uniform thickness from top to bottom of the sidewalls with a thickness of ~2 nm. In comparison, the radial QW thickness in <11$\bar{2}$>-oriented nanomembrane is much thinner than both axial and radial QWs of <1$\bar{1}$0>-oriented nanomembranes (see Figure 6.3f-h and Figure 6.4f). After growing five InAsP QWs, the <11$\bar{2}$>-oriented nanomembranes still maintain a decent shape (Figure 6.5g-l). In addition, the axial QW growth rate is significantly reduced compared to the radial QW growth rate. Indeed, it may be even suppressed to near zero (see Figure 6.5k). These results show that {11$\bar{2}$0} facets are more desirable for multi-QW growth. One possible explanation is that {11$\bar{2}$0} and {1$\bar{1}$0} facets have similar atomic arrangement and InAsP prefers to form {1$\bar{1}$0} facets such as in SAE grown InAs and GaAs nanowires.

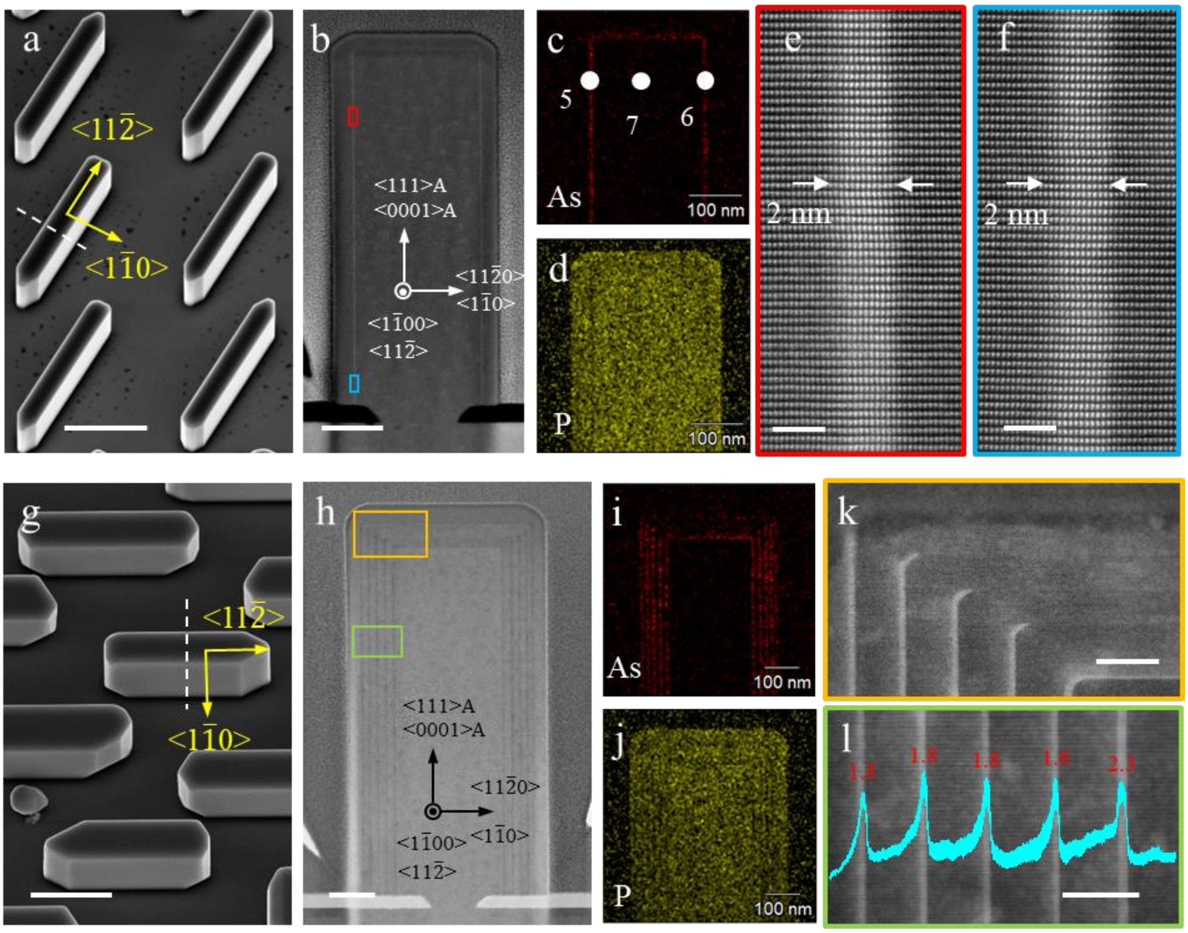

Figure 6.5: <11$\bar{2}$>-oriented InP/InAsP (a-f) single-QW and (g-l) 5-QW nanomembranes. (a,g) 30° tilted SEM images of nanomembrane arrays. The dotted lines indicate the direction and position for preparing TEM lamellae. (b,h) Low magnification HAADF images along {1$\bar{1}$00} zone axis showing the cross-section of these two nanomembranes. (c,d,i,j) EDX maps of As and P elements. (e,f,k,l) High magnification HAADF images from corresponding coloured areas in (b,h). Scale bars: (a,g) 1 µm; (b,h) 100 nm; (e,f) 2 nm; (k,l) 20 nm.

6.4.2. Compositional analysis

It can be seen from EDX maps of As and P elements shown in Figures 6.3-6.5 that the distribution of InAsP QW in the <11$\bar{2}$>-oriented QW nanomembranes exhibits not only high symmetry but also high uniformity compared with that in the <1$\bar{1}$0>-oriented nanomembranes. EDX spectra are extracted from a few positions 1-7 for quantitative composition analysis, as shown in Figure 6.6. By comparing the intensity of P element in InAsP QW with that from an InP reference, InAsP composition at the locations 1-6 is determined to be $InAs_{0.63}P_{0.37}$, $InAs_{0.79}P_{0.21}$, $InAs_{0.51}P_{0.49}$, $InAs_{0.68}P_{0.32}$, $InAs_{0.72}P_{0.28}$, and $InAs_{0.77}P_{0.23}$, respectively. The composition difference between the axial and radial QWs of the < 1$\bar{1}$0 >-oriented nanomembranes can reach 17%, suggesting QW composition is highly dependent on facets. The variation in composition could lead to different emission peaks and a complex emission behaviour. On the other hand, for the <11$\bar{2}$>-orientated InP nanomembranes, the radial QW has a uniform composition distribution.

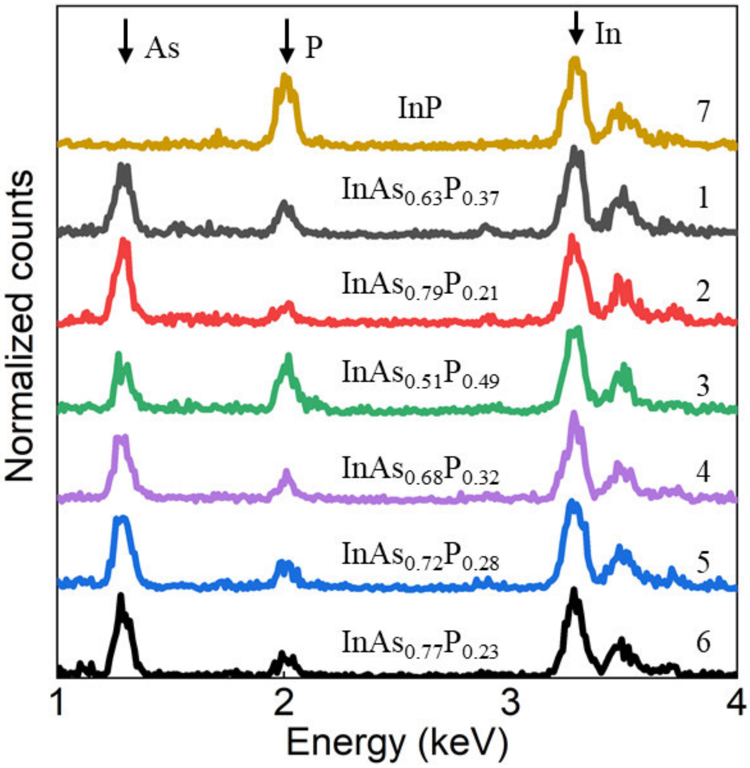

Figure 6.6: EDX spectra extracted from positions 1-7 marked in Figures 6.3-6.5.

6.4.3. CL analysis

CL characterisation was also performed on InP/InAsP QW nanomembranes that have been knocked down from their growth substrates to evaluate the QW emission. Based on the fracture at the bottom {111} plane, the growth direction of representative <1$\bar{1}$0>- and <11$\bar{2}$>-oriented QW nanomembranes is indicated by the yellow arrows in Figure 6.7a,e and Figure 6.8a,e, respectively. For the <1$\bar{1}$0>-oriented nanomembrane in Figure 6.7a, the CL emission spectra (Figure 6.7i) contain emissions from WZ InP (860-880 nm), radial InAsP QW (940-960 nm) and axial InAsP QW (1550-1570 nm). The emission maps for these wavelength regions are shown in Figure 6.7b-d, respectively. The emission from WZ InP and radial QW have similar intensity distribution and is strongest at the lower half of the nanomembrane. At the top half section, the emission is dominated by axial QW emission with a spectral range extending beyond 1.6 µm, close to the detection limit of our detector. Moreover, Figure 6.7f-h,j shows the CL maps and spectra of another <1$\bar{1}$0>-oriented nanomembrane. By comparing these two samples, we found that the emission wavelength and intensity of the axial and radial QWs significantly vary from one nanomembrane to another, which can be attributed to the inhomogeneous thickness distribution and composition variation of the QW.

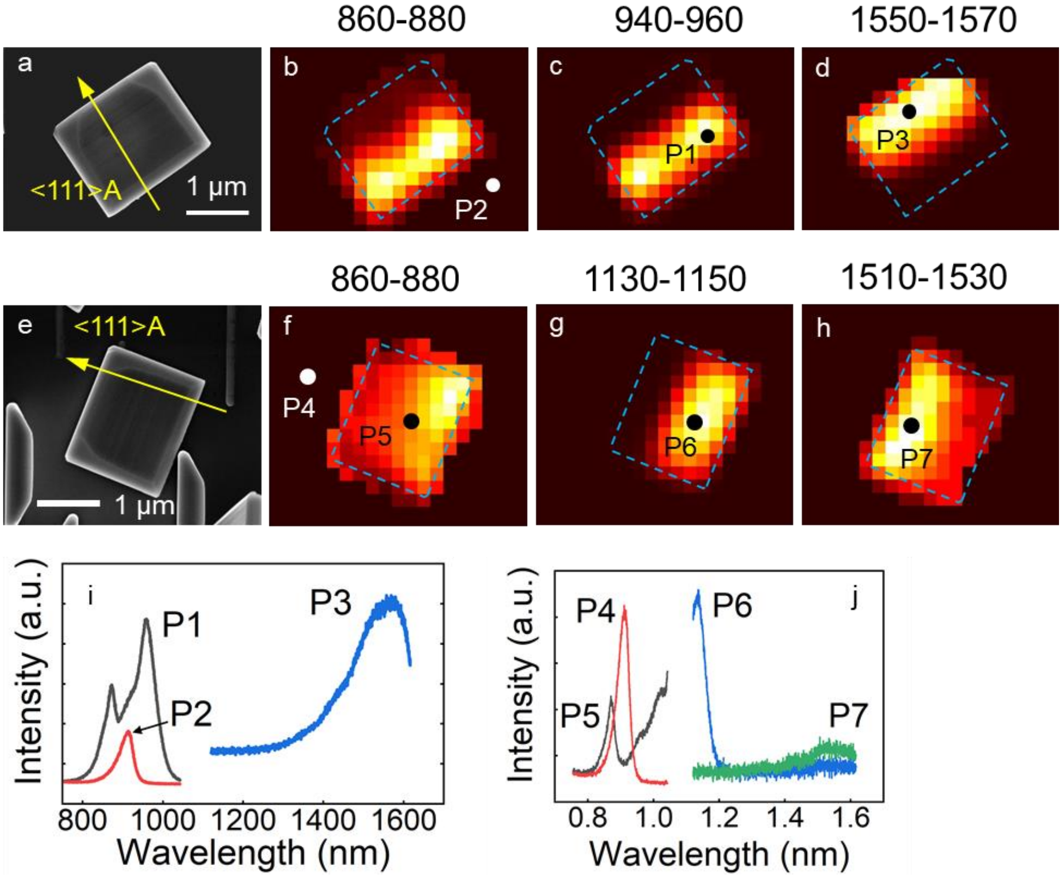

Figure 6.7: Spatially resolved CL emission of two representative <1$\bar{1}$0>-oriented InP/InAsP single-QW nanomembranes: (a-d,i) sample 1; (e-h,j) sample 2. (a,e) SEM images. (b-d,f-h) Normalized intensity maps at different wavelength ranges. (i,j) Corresponding CL spectra from positions indicated in (b-d,f-h).

Figure 6.8a-j shows CL results of two representative <11$\bar{2}$>-oriented single-QW nanomembranes. Compared with the <1$\bar{1}$0>-oriented single-QW nanomembranes in Figure 6.7, their QW emission is more uniform. Specifically, the signal from WZ InP nanomembranes is fairly uniform across the whole nanomembranes (Figure 6.8b,f). The radial QW emission spectra of these two nanomembranes can be deconvoluted into two peaks: 1286 and 1336 nm for the sample in Figure 6.8a,i; 1286 and 1352 nm for another sample in Figure 6.8e.j. The intensity distributions of these peaks are presented in Figure 6.8c,d,g,h, showing that despite of the slightly stronger emission intensity at one side, QW emissions are observed for the whole {11$\bar{2}$0} facets. The QW emission is fairly uniform across the array, showing a strong and broad emission peak around 1.3 µm (Figure 6.8k,l). No axial QW related emission is observed from the <11$\bar{2}$>-oriented nanomembranes. In addition, the results above also suggest that a slight composition and/or thickness variation occur during the radial QW growth on the {11$\bar{2}$0} sidewalls, and thus further growth optimisation is needed. Still, the <11$\bar{2}$>-oriented QW nanomembranes are greatly superior to the <1$\bar{1}$0>-oriented nanomembrane and nanowire counterparts.

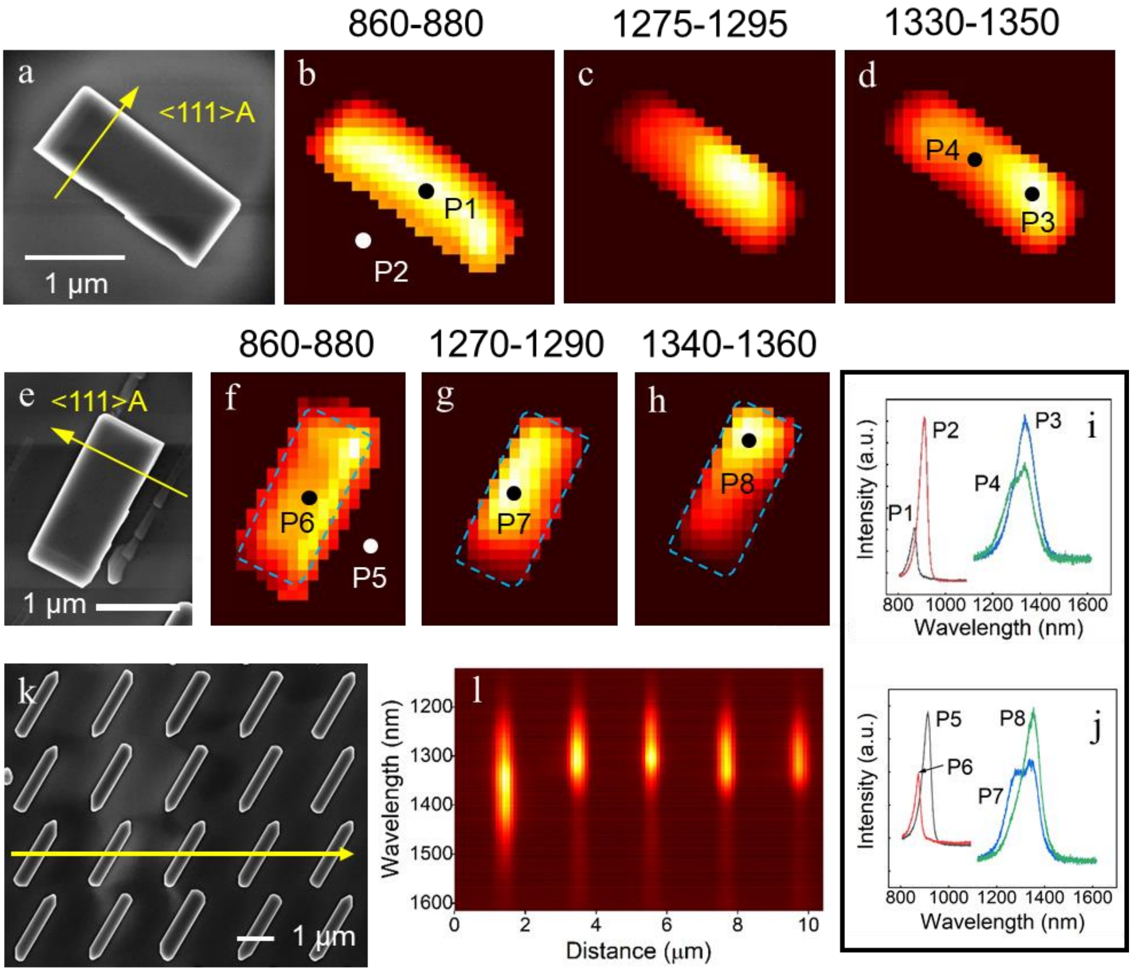

Figure 6.8: (a-j) Spatially resolved CL emission of two representative <11$\bar{2}$>-oriented InP/InAsP single-QW nanomembranes: (a-d,i) sample 1; (e-h,j) sample 2. (a,e) SEM images. (b,d,f-h) Normalized intensity maps at different wavelength ranges. (i,j) Corresponding CL spectra from positions indicated in (b-d,f-h). (k) SEM image of the <11$\bar{2}$>-oriented single-QW nanomembrane array. (l) CL line scan along the line indicated in (k).

6.5. Summary

In this chapter, we investigated the growth of InP/InAsP QW heterostructure in both nanowires and nanomembranes. The growth behaviour of InAsP QW was thoroughly studied, including crystal structure, composition, spatial distribution, and shape evolution. InAsP QWs grow both axially and radially, forming ZB and WZ structures, respectively on the InP nanowires and nanomembranes. Both axial and lateral QWs present a very sharp interface. Radial QW distribution varies on different sidewalls. QW formation on the {1$\bar{1}$00} side facets of nanowires and <1$\bar{1}$0>-oriented nanomembranes is asymmetric and nonuniform, and grows only on the <11$\bar{2}$>A polar side of the axial ZB QW. This asymmetric QW growth is due to the faster lateral growth rate along <11$\bar{2}$>A polar direction driven by the axial QW. Furthermore, the lateral growth rate decreases with distance from the axial QW, resulting in a nonuniform QW thickness. In comparison, QW grows uniformly on the $\{11\bar{2}0\}$ sidewalls of $<11\bar{2}>$-oriented nanomembranes even after growing five QWs. InAsP QW growth significantly affects subsequent InP growth. First, the axial growth rate of InP is greatly reduced due to competition from the lateral growth and can be suppressed to near zero. Moreover, the asymmetric growth deteriorates the symmetry of the nanowires and $<1\bar{1}0>$-oriented nanomembranes. The cross-section of QW nanowires transforms from a hexagonal to a triangular shape. For the $<1\bar{1}0>$-orientated nanomembranes, inclined $\{1\bar{1}01\}$ sidewalls are formed after QW growth, leading to the formation of a "protruding head" at the top. On the other hand, the $<11\bar{2}>$-oriented nanomembranes remain a high symmetry after QW growth.

In addition, a strong correlation between QW composition and growth direction is observed, which can be as high as 17% for As element. In the $<11\bar{2}>$-oriented nanomembranes, the axial growth rate of QW can be suppressed to near zero. Even though a composition fluctuation might exists in all QWs, the $<11\bar{2}>$-oriented nanomembranes are more uniform. Thus, while emission property from QW in nanowires and $<1\bar{1}0>$-oriented nanomembranes varies from one to another, strong and uniform emission at telecommunication wavelengths is observed from the $<11\bar{2}>$-oriented QW nanomembranes.

References

1. F. Qian, Y. Li, S. Gradečak, H.-G. Park, Y. Dong, Y. Ding, Z. L. Wang, and C. M. Lieber. Multi-quantum-well nanowire heterostructures for wavelength-controlled lasers. *Nature Materials* 2008, vol. 7, no. 9, pp. 701-706.
2. D. Saxena, N. Jiang, X. Yuan, S. Mokkapati, Y. Guo, H. H. Tan, and C. Jagadish. Design and room-temperature operation of GaAs/AlGaAs multiple quantum well nanowire lasers. *Nano Letters* 2016, vol. 16, no. 8, pp. 5080-5086.
3. G. Zhang, M. Takiguchi, K. Tateno, T. Tawara, M. Notomi, and H. Gotoh. Telecom-band lasing in single InP/InAs heterostructure nanowires at room temperature. *Science Advances* 2019, vol. 5, no. 2, p. eaat8896.
4. M. E. Reimer, G. Bulgarini, N. Akopian, M. Hocevar, M. B. Bavinck, M. A. Verheijen, E. P. Bakkers, L. P. Kouwenhoven, and V. Zwiller. Bright single-photon sources in bottom-up tailored nanowires. *Nature Communications* 2012, vol. 3, p. 737.
5. N. Erhard, S. Zenger, S. Morkötter, D. Rudolph, M. Weiss, H. J. Krenner, H. Karl, G. Abstreiter, J. J. Finley, G. Koblmüller, and A. W. Holleitner. Ultrafast photodetection in the

quantum wells of single AlGaAs/GaAs-based nanowires. *Nano Letters* 2015, vol. 15, no. 10, pp. 6869-6874.

6. M. Karimi, V. Jain, M. Heurlin, A. Nowzari, L. Hussain, D. Lindgren, J. E. Stehr, I. A. Buyanova, A. Gustafsson, L. Samuelson, M. T. Borgstrom, and H. Pettersson. Room-temperature InP/InAsP Quantum Discs-in-Nanowire Infrared Photodetectors. *Nano Letters* 2017, vol. 17, no. 6, pp. 3356-3362.
7. K. Tateno, G. Zhang, H. Gotoh, and T. Sogawa. VLS growth of alternating InAsP/InP heterostructure nanowires for multiple-quantum-dot structures. *Nano Letters* 2012, vol. 12, no. 6, pp. 2888-2893.
8. P. Kuyanov, and R. R. LaPierre. Photoluminescence and photocurrent from InP nanowires with InAsP quantum dots grown on Si by molecular beam epitaxy. *Nanotechnology* 2015, vol. 26, no. 31, p. 315202.
9. D. Dalacu, K. Mnaymneh, J. Lapointe, X. Wu, P. J. Poole, G. Bulgarini, V. Zwiller, and M. E. Reimer. Ultraclean emission from InAsP quantum dots in defect-free wurtzite InP nanowires. *Nano Letters* 2012, vol. 12, no. 11, pp. 5919-5923.
10. D. Dalacu, K. Mnaymneh, X. Wu, J. Lapointe, G. C. Aers, P. J. Poole, and R. L. Williams. Selective-area vapor-liquid-solid growth of tunable InAsP quantum dots in nanowires. *Applied Physics Letters* 2011, vol. 98, no. 25, p. 251101.
11. Z. Zhong, X. Li, J. Wu, C. Li, R. B. Xie, X. Yuan, X. Niu, W. Wang, X. Luo, G. Zhang, Z. M. Wang, H. H. Tan, and C. Jagadish. Wavelength-tunable InAsP quantum dots in InP nanowires. *Applied Physics Letters* 2019, vol. 115, no. 5, p. 053101.
12. I. Yang, X. Zhang, C. Zheng, Q. Gao, Z. Li, L. Li, M. N. Lockrey, H. Nguyen, P. Caroff, and J. Etheridge. Radial growth evolution of InGaAs/InP multi-quantum-well nanowires grown by selective-area metal organic vapor-phase epitaxy. *ACS Nano* 2018, vol. 12, no. 10, pp. 10374-10382.
13. Q. Gao, D. Saxena, F. Wang, L. Fu, S. Mokkapati, Y. Guo, L. Li, J. Wong-Leung, P. Caroff, H. H. Tan, and C. Jagadish. Selective-area epitaxy of pure wurtzite InP nanowires: high quantum efficiency and room-temperature lasing. *Nano Letters* 2014, vol. 14, no. 9, pp. 5206-5211.
14. I. Yang, Z. Li, J. Wong-Leung, Y. Zhu, Z. Li, N. Gagrani, L. Li, M. N. Lockrey, H. Nguyen, and Y. Lu. Multiwavelength single nanowire InGaAs/InP quantum well light-emitting diodes. *Nano Letters* 2019, vol. 19, no. 6, pp. 3821-3829.

15. F. Ishizaka, Y. Hiraya, K. Tomioka, J. Motohisa, and T. Fukui. Growth of all-wurtzite InP/AlInP core–multishell nanowire array. *Nano Letters* 2017, vol. 17, no. 3, pp. 1350-1355.
16. D. K. Ren, A. C. Farrell, B. S. Williams, and D. L. Huffaker. Seeding layer assisted selective-area growth of As-rich InAsP nanowires on InP substrates. *Nanoscale* 2017, vol. 9, no. 24, pp. 8220-8228.
17. Q. Gao, D. Saxena, F. Wang, L. Fu, S. Mokkapati, Y. Guo, L. Li, J. Wong-Leung, P. Caroff, H. H. Tan, and C. Jagadish. Selective-Area Epitaxy of Pure Wurtzite InP Nanowires: High Quantum Efficiency and Room-Temperature Lasing. *Nano Letters* 2014, vol. 14, no. 9, pp. 5206-5211.
18. T. J. Kempa, S.-K. Kim, R. W. Day, H.-G. Park, D. G. Nocera, and C. M. Lieber. Facet-selective growth on nanowires yields multi-component nanostructures and photonic devices. *Journal of the American Chemical Society* 2013, vol. 135, no. 49, pp. 18354-18357.
19. X. M. Yuan, J. B. Yang, J. He, H. H. Tan, and C. Jagadish. Role of surface energy in nanowire growth. *Journal of Physics D: Applied Physics* 2018, vol. 51, no. 28, p. 283002.
20. X. Yuan, P. Caroff, F. Wang, Y. Guo, Y. Wang, H. E. Jackson, L. M. Smith, H. H. Tan, and C. Jagadish. Antimony induced {112}A faceted triangular GaAs1-xSbx/InP core/shell nanowires and their enhanced optical quality. *Advanced Functional Materials* 2015, vol. 25, no. 33, pp. 5300-5308.
21. J. Zou, M. Paladugu, H. Wang, G. J. Auchterlonie, Y. N. Guo, Y. Kim, Q. Gao, H. J. Joyce, H. H. Tan, and C. Jagadish. Growth mechanism of truncated triangular III–V nanowires. *Small* 2007, vol. 3, no. 3, pp. 389-393.
22. I. Yang, X. Zhang, C. Zheng, Q. Gao, Z. Li, L. Li, M. N. Lockrey, H. Nguyen, P. Caroff, J. Etheridge, H. H. Tan, C. Jagadish, J. Wong-Leung, and L. Fu. Radial Growth Evolution of InGaAs/InP Multi-Quantum-Well Nanowires Grown by Selective-Area Metal Organic Vapor-Phase Epitaxy. *ACS Nano* 2018, vol. 12, no. 10, pp. 10374-10382.
23. M. Paladugu, J. Zou, Y.-N. Guo, X. Zhang, H. J. Joyce, Q. Gao, H. H. Tan, C. Jagadish, and Y. Kim. Polarity driven formation of InAs/GaAs hierarchical nanowire heterostructures. *Applied Physics Letters* 2008, vol. 93, no. 20, p. 201908.

CHAPTER 7

Conclusions and future outlook

7.1 Conclusions

This dissertation has investigated the SAE of InP nanostructures with diverse shapes, developed a thorough understanding of shape transformation and phase transition, and explored novel functional structures and InAsP quantum well heterostructure growth for future optoelectronic applications. It expands the research interests of III-V compound semiconductors from 1D nanowires to nanostructures with higher-order 2D/3D shapes.

Firstly, shape engineering of InP nanostructures grown on {111}A InP substrates using SAE technique was investigated in Chapter 4. The preference for {111} substrate as a starting point is due to vertical growth of III-V nanostructures such as nanowires. To control the nanostructure shapes, openings with different geometries and dimensions were elaborately designed and patterned on a dielectric mask layer over InP substrates, including nanoholes, nanoslots with different orientations and nanorings. Subsequently, InP nanowires, nanomembranes/nanoprisms and nanorings were achieved from these three types of openings, suggesting the significance of confinement afforded by the mask pattern in shape engineering. The morphology and optical properties of nanomembranes and nanoprisms with different growth temperatures and V/III ratios were systematically investigated to optimise the structural and optical properties, such as nanostructure regularity and uniformity, minority carrier lifetime, and photon emission intensity and uniformity. At low temperatures, trenches were commonly observed on the top surfaces due to inefficient diffusion of indium adatoms, as explained by a kinetic model. It was shown that higher temperatures were required to grow these nanostructures with high crystal and optical qualities. At optimal conditions, InP nanostructure arrays with different shapes, i.e. nanomembranes, nanoprisms and nanorings, exhibited high uniformity. Moreover, the detailed structural and optical results revealed that they had pure WZ crystal phase, and strong and uniform photon emission across an array, regardless of their shapes. For nanoslots with different low- and high-index orientations, shape evolution with increasing slot length and growth time has been investigated. $\{10\bar{1}0\}$, $\{11\bar{2}0\}$ and high index facets (thermal stability $\{10\bar{1}0\} > \{11\bar{2}0\} >$ high index facets) can coexist, but metastable $\{11\bar{2}0\}$ and high index facets eventually evolve into $\{10\bar{1}0\}$ facets. A theoretical model was proposed to explore the fundamental mechanism of shape transformation. It has been found that in addition to confinement from the mask, shape transformation is essentially determined by minimisation of nanostructure total surface energy.

In Chapter 5, InP nanostructures with different shapes grown on {100}, {110}, {111}B, {112}A and {112}B InP substrates were investigated, aiming to build a unified understanding for SAE of InP nanostructures and explore more structural possibilities. Shape evolution from V-shaped/tripod-like nanowires to bilayer nanomembranes with the increase of nanoslot length along specific crystal orientations was demonstrated on all the above non-{111}A substrates. In-depth analyses revealed that while these nanowires consisted of two/three WZ phase branches along the <111>A directions and one ZB intersection region against the substrate, the bilayer nanomembranes comprised of one WZ layer along the <111>A directions and one ZB layer grown along the <111>B or other non-<111> low-index directions. These results together with the growth of InP nanostructures on {111}A substrates indicated that crystal phase of nuclei and subsequent nanostructures was highly dependent on substrate orientation/polarity and growth directions. The crystal phase of nuclei on non-{111} substrates inherits a ZB phase of the underlying substrates and grew along non-<111> oriented low-index directions, due to phase transition which generally occurs with the formation of planar defects along the <111> crystal directions. The polarity difference for nuclei on A- and B-polar {111} substrates and growth along A- and B-polar <111> directions led to formation of respective WZ and ZB structures, which was energetically favourable as confirmed by a proposed model. Besides, the similar shape evolution with increasing nanoslot length on the substrates of various orientations suggests an identical mechanism for shape transformation, which can also be attributed to pattern confinement and minimisation of total surface energy, as explained by a theoretical model. More surprisingly, the bilayer InP nanomembranes with a large size WZ/ZB homojunction was achieved, which provided a new class of nanostructures with potential in optoelectronic applications.

Finally, Chapter 6 investigated the growth of InAsP QW in pure WZ InP nanowires and two types of $<1\bar{1}0>$- and $<11\bar{2}>$-oriented nanomembranes to facilitate the optoelectronic applications of shape-engineered InP nanostructures. Structural examination by Cs-corrected STEM revealed that InAsP QW could grow axially and radially with a sharp interface, and form

ZB and WZ phases, respectively. For InP nanowires and <1$\bar{1}$0>-oriented nanomembranes, although they were bound by nonpolar {1$\bar{1}$00} side facets and the incorporation of the radial QW was asymmetric. Detailed analysis showed that the radial QW grew selectively on sidewalls at the <11$\bar{2}$>A side of the axial ZB QW, suggesting that the axial QW increased the growth rate of radial QW along the <11$\bar{2}$>A directions. Furthermore, the driving force became weaker with distance from the axial QW, leading to slower growth rate of the radial QW and uneven thickness distribution from the top to bottom. The axial ZB QW also affected subsequent radial growth of InP capping layer in the same way as radial QW, resulting in morphology transformation of nanowires from hexagonal shape to triangular shape, asymmetric <1$\bar{1}$0>-oriented QW nanomembranes, and even the formation of a “protruding head” after the growth of 5 QWs. After the incorporation of QW, the axial growth of InP was significantly suppressed due to the competition from lateral growth, and in most cases could be reduced to near zero. On the other hand, InAsP QW can uniformly formed on both sides of the <11$\bar{2}$>-oriented InP nanomembranes bound by {11$\bar{2}$0} side facets from the top to bottom and maintaining a high symmetry even after growing 5 QWs. Compared with the radial QWs, growth of the axial QWs were greatly reduced. In addition, the QW composition and its optical properties were thoroughly studied. It was shown that the QW composition was highly dependent on the crystal facets. In case of the <1$\bar{1}$0>-oriented QW nanomembranes, the difference between axial and radial QWs could reach up to 17% for the As element. In comparison, QW composition in the <11$\bar{2}$>-oriented QW nanomembranes are much more uniform. CL maps and spectra revealed that the axial and radial QWs in the <1$\bar{1}$0>-oriented QW nanomembranes emitted with inhomogeneous intensity at different wavelength range, and vary from one sample to another. On the other hand, <11$\bar{2}$>-oriented QW nanomembranes demonstrated strong and quite uniform emission at the telecommunication wavelength range around 1.3 µm, making them promising platform for future optoelectronic devices.

7.2 Future research directions

In this thesis, the shape transformation mechanism of InP nanostructures has been investigated in detail, and nanostructures with a number of shapes, such as nanowires, nanomembranes, nanoprisms and nanorings, have been demonstrated. Next, one of the compelling follow-on works is to explore the application of these tunable nanoshapes in metasurfaces/meta-optics. Numerical simulations are needed to design these nanostructures in terms of shapes, dimensions and arrangement in an array. Moreover, a few aspects with respect to epitaxial growth remain to be tackled. For example, InP nanostructures with more different shapes and ordered array comprising of various shapes need to be investigated to meet the simulation results. Moreover, shape engineering of nanostructures can also be investigated on other III-V semiconductors, such as GaAs and InAs, to compare and expand the operation wavelength range. In addition to the application in metasurfaces/meta-optics, the expansion of research interests to other III-V semiconductors is inevitable in consideration of the great potential in fundamental science, and electronic/optoelectronic applications.

Some chemicals, such as ZEP520A and HMDS, currently used during substrate preparation are toxic, which need to be replaced in the long term. Besides, EBL system is used to fabricate openings on SiO_x/substrates, which is time-consuming and impractical for mass production. Thus, a new fabrication processing using other techniques is highly desirable, such as nanoimprint lithography.

InP-based nano/microrings are worthy of further investigation for lasing application. Nano/microring cavities can support optical modes (usually whispering gallery modes) and generate lasing when gain is present in the material. For simplicity, the investigation of ring laser can be first carried out on {111}A InP substrates through a series of steps. Firstly, a professional simulation tool can be used to design the required structure and study its mode characteristics. Subsequently, the growth conditions can be investigated to control the facets and dimensions of the ring, incorporation of axial and radial quantum well heterostructures (e.g. InGaAs), and doping. A thick SiO_x dielectric mask layer is required to minimise the optical losses to substrates. Lastly, the optical properties and lasing action can be studied using various optical characterisation techniques.

A novel bilayer InP nanomembranes with WZ/ZB homojunction have been demonstrated in this work. They have high crystal quality for each layer, a large and atomically sharp WZ/ZB interface. These unique features make them different from their nanowire counterparts. Carrier dynamics in this bilayer nanomembranes has been thoroughly investigated by a collaborator (Dr. Zhicheng Su, ANU), revealing type-II band alignment and 2D carrier localization. Next, a very promising research direction is to fabricate this type of nanomembranes into devices, such as solar cells and photodetectors. In addition, further investigation is required to improve the uniformity of these interesting InP nanostructures grown on non-{111}A InP substrates to enable their practical applications over a large scale.

The superior structural and optical properties of InP/InAsP quantum well heterostructure nanomembranes have been demonstrated. Still, further growth studies are needed to realise doping, control the incorporation of axial and radial quantum wells, obtain a higher uniformity of composition and photon emission, and tune the emission wavelength, even when multiple quantum wells are grown. It would then be very interesting to move the research focus to device applications, such as optically or even electrically pumped lasers.

Growing III-V semiconductors on Si has always been a hot topic because of the low cost of Si and most importantly, the great significance in integration of III-V devices with Si-based microelectronics. For example, InP nano/mcrorings can provide an efficient light source for Si photonics. The small footprint of nanostructures greatly reduces the intrinsic growth challenges caused by the mismatch of lattice and thermal expansion and antiphase domains. Still, it is difficult to grow InP nanostructures on Si but considering the great opportunities of integrating InP nanodevices onto Si chip, this topic is worthy of further investigation. Amongst different growth approaches such as modification of Si surface properties and controlling the surface polarity by pre-flowing group III or group V precursors, epitaxial lateral overgrowth, and aspect ratio trapping methods definitely deserve further studies.